ANNUAL REPORTS ON NMR SPECTROSCOPY

Volume 36

- NMR study of active sites in paramagnetic haemoproteins
- Empirical versus non-empirical evaluation of secondary structure of fibrous and membrane proteins by solid-state NMR: a practical approach
- Xenon NMR

ACADEMIC PRESS

ANNUAL REPORTS ON

NMR SPECTROSCOPY

This Page Intentionally Left Blank

ANNUAL REPORTS ON

NMR SPECTROSCOPY

Edited by

G. A. WEBB

Department of Chemistry, University of Surrey, Guildford, Surrey, England

VOLUME 36

ACADEMIC PRESS

San Diego ● London ● Boston
New York ● Sydney ● Tokyo ● Toronto

This book is printed on acid-free paper.

Copyright © 1998 by ACADEMIC PRESS

All Rights Reserved

No part of this publication may be reproduced or transmitted in any form or by any means electronic or mechanical, including photocopy, recording, or any information storage and retrieval system, without permission in writing from the publisher.

Academic Press
525 B Street, Suite 1900, San Diego, California 92101-4495, USA
http://www.apnet.com

Academic Press Limited
24–28 Oval Road, London NW1 7DX, UK
http://www.hbuk.co.uk./ap/

ISBN 0-12-505336-3

A catalogue record for this book is available from the British Library

Typeset by Keyset Composition, Colchester, Essex
Printed in Great Britain by MPG Books Ltd, Bodmin, Cornwall

98 99 00 01 02 03 MP 9 8 7 6 5 4 3 2 1

List of Contributors

Akira Naito, *Department of Life Science, Himeji Institute of Technology, Harima Science Garden City, Kamigori, Hyogo, Japan 678-12*

Christopher I. Ratcliffe, *Steacie Institute for Molecular Sciences, National Research Council of Canada, Ottawa, Ontario, Canada K1A 0R6*

Hazime Saitô, *Department of Life Science, Himeji Institute of Technology, Harima Science Garden City, Kamigori, Hyogo, Japan 678-12*

Satoru Tuzi, *Department of Life Science, Himeji Institute of Technology, Harima Science Garden City, Kamigori, Hyogo, Japan 678-12*

Yasuhiko Yamamoto, *Department of Chemistry, University of Tsukuba, Tsukuba 305, Japan*

This Page Intentionally Left Blank

Preface

It is a great pleasure for me to introduce volume 36 of *Annual Reports on NMR Spectroscopy* which consists of reports from three very different areas of molecular science. Each of which serves to demonstrate the widespread importance of NMR spectroscopy.

The first report by Y. Yamamoto deals with the NMR Study of Active Sites in Paramagnetic Haemoproteins, Empirical versus Non-empirical Evaluations of the Secondary Structure of Fibrous and Membrane Proteins by Solid-state NMR are reviewed by H. Saitô, S. Tuzi and A. Naito and finally, C. I. Ratcliffe reports on Applications of Xenon NMR.

I am very grateful to all of these authors for the very considerable efforts which they have invested in the preparation of their manuscripts and for delivering them punctually. Such devotion is necessary for the continued success of this series as is the generous support and assistance provided by the production staff at Academic Press (London).

University of Surrey
Guildford, Surrey
England

G. A. WEBB
May 1997

This Page Intentionally Left Blank

Contents

NMR Study of Active Sites in Paramagnetic Haemoproteins

YASUHIKO YAMAMOTO

Department of Chemistry, University of Tsukuba, Tsukuba 305, Japan

NMR studies of paramagnetic haemoproteins are reviewed with special emphasis on characterization of both structural and dynamic properties of haem active site. In the past decade, the development of NMR methodologies for detecting the connections between hyperfine shifted signals has contributed greatly to establishing systematic and reliable strategies for the signal assignments of paramagnetic haemoproteins. The use of reconstituted haemoprotein is a characteristic of the study of b-type haemoproteins and NMR studies on reconstituted myoglobins and haemoglobins are described in some detail. Additionally, nonequivalence in haem electronic structure between the two

ANNUAL REPORTS ON NMR SPECTROSCOPY
VOLUME 36 ISBN 0-12-505336-3

Copyright © 1998 Academic Press Limited
All rights of reproduction in any form reserved

different subunits in human adult haemoglobin enables one to characterize the individual subunits in intact tetramers using NMR, and the advantages in studying tetrameric haemoglobin by NMR are also described.

1. INTRODUCTION

The use of paramagnetic ions as extrinsic shift and relaxation probes for investigating the structure of biological molecules in solution has not been as fully exploited as originally expected. This is due to the presence of rapid averaging of nonspecific interaction between the ions and molecules, which complicates the interpretation of NMR parameters.[1] Paramagnetic metalloproteins, however, already contain internal paramagnetic ion(s) at specific site(s) of the molecule. Consequently, taking advantage of the properties of unpaired electron(s), resonances arising from nuclei located in the close proximity of the paramagnetic centre exhibit hyperfine shifts and hence appear outside of the diamagnetic envelope where signals due to the protein overlap severely. Hyperfine shifted signals are extremely sensitive to structural properties of molecules, as has been fully described elsewhere.[1–20] NMR studies of paramagnetic metalloproteins have provided a wealth of information for characterizing structure–function relationships of proteins.[12–15,21,22] One of the major drawbacks in the NMR study of paramagnetic molecules is obviously fast nuclear relaxation. Since there is no way to slow down the relaxation without losing the hyperfine shift, we have to accept it. Paramagnetic-induced relaxation substantially diminishes the development of the nuclear Overhauser effect or coherence in two-dimensional (2D) NMR. All the connectivities that should be observable if the molecule were diamagnetic are not always expected to be detected. However, the major 2D experiments are found to be surprisingly effective in detecting both scalar and dipolar connectivities.[23–25] The applicability of various NMR methodologies to paramagnetic molecules possessing a wide range of shifts, line widths and T_1 values has been examined in detail from both the experimental and theoretical points of view.[9,23–39]

In the present chapter, NMR studies of paramagnetic haemoproteins are reviewed with special emphasis on characterization of both structural and dynamic properties of the haem active site. As in the previous review by Satterlee,[12] an initial attempt is made to assign the signals of the paramagnetic haemoprotein to specific nuclei in the molecule by isotope labelling or comparison with model systems. This is restricted to the resonances arising from coordinated ligands.[40] In the past decade, the development of NMR methodologies for detecting the connectivities between hyperfine shifted signals has contributed greatly to the establishment of systematic and reliable strategies for signal assignment.[26,41–53] In particular, the observation of the dipolar connectivity between the resonances of paramagnetic haemoproteins

not only permits the assignments of the resonances arising from haem peripheral side-chains as well as those from non-coordinated amino acid residues, but also provides information on the cross relaxation rate between selected proton pairs, which can be interpreted in terms of internal motion of the interproton vector.[54–56]

Haemoproteins are composed of a protein moiety (globin) and a prosthetic group (haem). The haem is incorporated into a pocket, called the haem pocket, at the final step of biosynthesis of *b*-type haemoprotein. This process can easily be implemented *in vitro*. Globins are isolated from the corresponding haemoproteins by removing the haem at an acidic pH, under controlled experimental conditions.[57,58] Reaction of apoprotein with haem yields holoprotein. This reaction is called reconstitution of haemoprotein and the holoprotein prepared by the reaction is called a reconstituted protein. The reconstitution of haemoproteins allows replacement of the naturally occurring haem in the protein with a chemically modified haem. Reconstituted proteins with a variety of modified haems have been shown to be of considerable importance in the study of structure–function relationships in haemoproteins because the haem–globin interaction, which is thought to be responsible for controlling the function of the molecule, can be systematically altered in these proteins.[59–65] The use of reconstituted protein is characteristic of the study of haemoproteins, and NMR studies on reconstituted myoglobins (Mbs) and haemoglobins (Hbs) are described in some detail. Additionally, nonequivalence in haem electronic structure between the two different subunits in tetrameric Hb results in the appearance of two sets of NMR signals, one set arising from each subunit. This enables one to characterize the individual subunits in intact tetramer using NMR.[10,66] The advantages of studying tetrameric Hb by NMR are also described.

2. HAEMOPROTEINS

Haemoproteins are probably the most studied group of proteins. This is due not only to their wide distribution and abundance, but also to their many unique physicochemical properties arising from the presence of a haem group, usually iron protoporphyrin IX (Fig. 1). Haem is found as the prosthetic group of a number of proteins possessing quite different functions, i.e., electron transport proteins (cytochromes), oxidase enzymes (peroxidase, catalase) and oxygen transport/storage proteins (Hb/Mb). Since the proteins all contain the same prosthetic group at their active sites, their functional differences are thought to arise from differences in the way that the proteins interact with the haems.

Myoglobin is a monomeric haemoprotein of about 17 kDa and consists of eight helices, labeled A to H from the amino to the carboxyl terminus. The helices are folded to form an ellipsoidal molecule of approximate dimensions

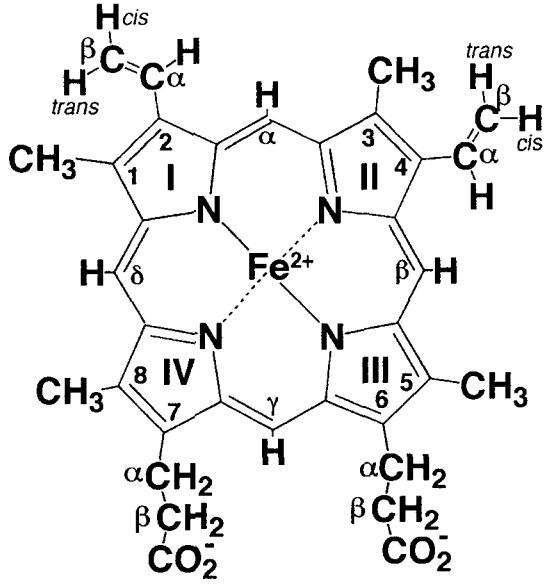

Fig. 1. Structure and numbering system of haem.

$4.4 \times 4.4 \times 2.5$ nm. Human adult haemoglobin (called Hb A) is a globular protein with a diameter of about 6.4 nm and a molecular mass of about 65 kDa. The protein moiety consists of two pairs of polypeptide chains, usually called subunits, two α subunits and two β subunits and the tertiary structure of the subunits resembles that of Mb. The four Mb-like subunits are assembled in a tetrahedral array to form a roughly spherical molecule.[67]

The porphyrin ring of haem is formed by four pyrrole rings connected by methine bridges, α–δ, and substituted with different groups, i.e., two vinyl, two propionic acid and four methyl groups, as illustrated in Fig. 1. The central position in the porphyrin ring is occupied by an iron atom, which is coordinated to the pyrrole nitrogens. The haem is inserted into the haem pocket between the E and F helices with the propionic acid side-chains of the haem oriented toward the exterior. The haem–globin linkage is stabilized by coordination of the proximal histidine (His) imidazole to the haem iron (Fig. 2) and by many van der Waals contacts between the haem and globin in the haem pocket. In some proteins, the propionic acid side-chains are bound to the globin through salt bridges.[67] In spite of the tight binding of the haem to the globin, the haem pocket exhibits considerable flexibility as reflected in various dynamic properties.[55,68,69] Internal motion is though to be indispensable for accommodating external ligands at the binding site in the pocket,[70] because X-ray crystallographic studies do not reveal any ligand entry pathways.

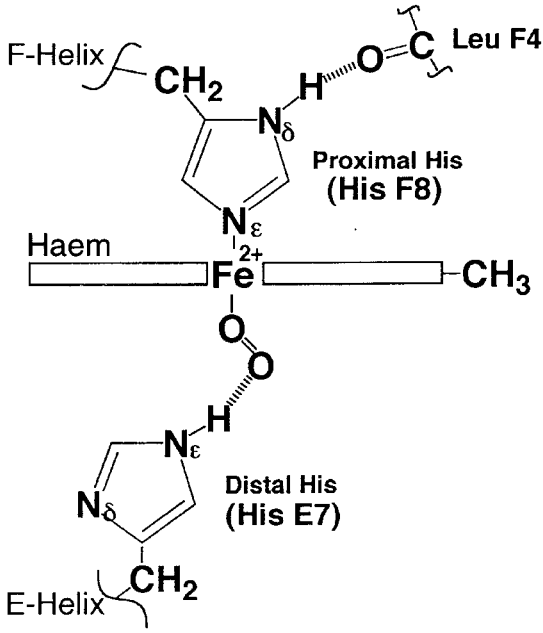

Fig. 2. The structure of the ligand-binding site in sperm whale Mb. The iron-bound O_2 is stabilized by the hydrogen bond with the side-chain of the distal His E7.[67]

Generally, haem iron in Hb and Mb is in either the ferrous or ferric state. The number of electrons in 3d orbitals of ferrous and ferric iron are six and five, respectively. The total spin quantum number S is integer and half-integer in ferrous and ferric haems, respectively. Depending on the degree of spin pairing of electrons in 3d orbitals, ferrous haem iron can have 4, 2 or 0 unpaired electrons corresponding to $S = 2, 1$, or 0, respectively, and ferric haem iron can have $S = 5/2, 3/2$ or $1/2$ with 5, 3 or 1 unpaired electron, respectively. Based on an octahedral ligand field, the energy levels of five 3d orbitals of the iron atom split into two groups in such a way that the d_{z^2} and $d_{x^2-y^2}$ orbitals are higher in energy than the other three orbitals, d_{xy}, d_{yz} and d_{xz} (Fig. 3). The spin state of a haemoprotein depends on the chemical nature of the ligand. For ferrous haem iron, the deoxy (no ligand) form is pentacoordinated with a high-spin configuration $S = 2$ and the oxy (O_2) or carbon monoxy (CO) form possesses the low-spin configuration $S = 0$. On the other hand, binding of ligands with a relatively weak field strength, such as H_2O, to ferric haem iron gives the high-spin state $S = 5/2$ (met-aquo form). The low-spin state $S = 1/2$ is achieved with a strong ligand such as CN^- (met-cyano form). There are some ferric haemoproteins such as met-hydroxyl, met-azido and met-imidazole haemoproteins that exhibit intermediate values of magnetic susceptibility

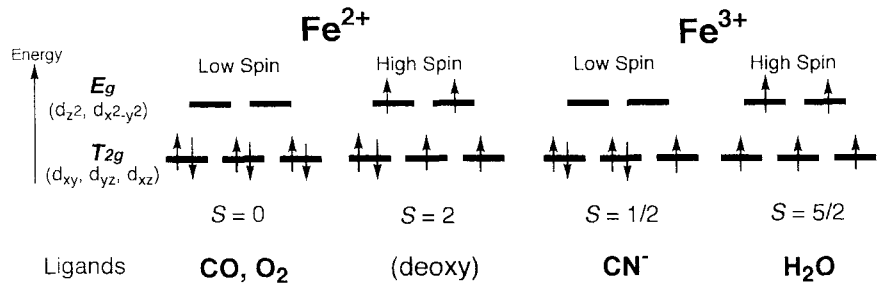

Fig. 3. Iron oxidation/spin states of Mb.

between those of the high-spin and low-spin states. Each of the proteins with the intermediate magnetic susceptibility is found to be a mixture of high-spin and low-spin states.[71–75]

3. NMR PARAMETERS

The gyromagnetic ratio of the electron is about 660 times greater than that of the proton. The large magnetic moment due to the unpaired electron(s) on the haem iron leads to a dramatic influence on the NMR spectrum of a paramagnetic haemoprotein. The theory behind NMR parameters in paramagnetic systems has been treated in detail elsewhere.[11,14,20,76–79] Only a qualitative description of paramagnetic shifts and relaxation, which suffices to provide an appreciation of the data presented, is given here.

3.1. Paramagnetic shifts

The observed chemical shift due to the presence of a paramagnetic centre (δ_{obs}) is expressed as in Eq. (1), where δ_{dia} and δ_{para} are the diamagnetic and paramagnetic contributions, respectively.

$$\delta_{obs} = \delta_{dia} + \delta_{para} \tag{1}$$

δ_{dia} is the shift that would have been observed if the molecule contained no unpaired electron(s), and the shift found for a suitable diamagnetic compound is usually used as δ_{dia}. δ_{para} is due to the permanent magnetic moment of the unpaired electron(s). δ_{para} is divided into three terms as in Eq. (2),

$$\delta_{para} = \delta_c + \delta_{pc}^{L} + \delta_{pc}^{M} \tag{2}$$

where δ_c is the contact shift and δ_{pc}^{L} and δ_{pc}^{M} are the ligand- and metal-centred

pseudo-contact shifts. The latter are due to the magnetic dipolar field arising from delocalized electrons and the unpaired electrons on the haem iron, respectively. In the ideal case of a singly populated level for the iron, which approximates most of the cases to be considered, δ_c is given by[76,78,80–82]

$$\delta_c = \frac{A}{\hbar} \frac{g\beta S(S+1)}{3\gamma_N kT} \tag{3}$$

where A is the hyperfine coupling constant, $\hbar$ the Planck's constant divided by 2π, g is the electronic g factor, β is the Bohr magneton, S is the total electron spin number, γ_N is the gyromagnetic ratio of the nucleus of interest, k is the Boltzmann constant, and T is the absolute temperature. A is related to the spin density ρ on the resonating nucleus and, for the haem propionate α-proton, is expressed as[83]

$$A = \frac{Q_{CCH}\rho}{2S} \tag{4}$$

where Q_{CCH} is the parameter that accounts for the transfer of the unpaired electron density in the p_z orbital of the pyrrole carbon to the proton of interest and ρ is the unpaired electron density. Q_{CCH} depends on θ, the dihedral angle between the C–C_α–H plane and the normal to the haem plane according to[3,84]

$$Q_{CCH} = B_0 + B_2 \cos^2 \theta \tag{5}$$

where B_0 and B_2 are coefficients. Since B_0 is much smaller than B_2,[3] the magnitude of the δ_c value, to the first approximation, is assumed to be proportional to $\cos^2 \theta$. In the case of the haem methyl proton resonance, only a single signal for the haem methyl protons is observed, because the frequency of the haem methyl rotation is much higher than the A value.[85] Each of the protons interacts with ρ, as for the haem propionate α-proton the average A value for the three methyl protons is expressed as[83,86]

$$A = \frac{Q_{CCH_3}\rho}{2S} \tag{6}$$

where Q_{CCH_3} accounts for the transfer of the unpaired electron density in the p_z orbital of the pyrrole carbon to the methyl proton through hyperconjugation and hence possesses no angular dependence. Since Q_{CCH_3} is positive,[3] δ_c is a high-frequency shift (for a typical ferric low-spin complex such as met-cyano Mb, +5 to +20 ppm) for the haem methyl proton resonance. Therefore, haem methyl proton signals of the ferric low-spin complex are generally observed in the high-frequency hyperfine shifted region. Each of the pyrrole groups of the porphyrin ring of the haem carries a methyl group. The δ_c values of all of the four haem methyl proton resonances represent the ρ values of the individual

pyrrole rings, which reflect an in-plane asymmetry of the electronic structure of the haem.

For a system with a single unpaired electron, δ_{pc}^{M} is given in terms of the magnetic anisotropy for the unpaired electron spin in Eq. (7),[76]

$$\delta_{pc}^{M} = \frac{1}{24\pi r_M^3}[(3\cos^2\theta - 1)(2\chi_{zz} - \chi_{xx} - \chi_{yy}) + 3\sin^2\theta\cos 2\Omega\,(\chi_{xx} - \chi_{yy})] \quad (7)$$

where χ_{ii} are the principal components of the molecular magnetic susceptibility tensor, r_M is the metal–nucleus distance, and θ and Ω are the angles between the r_M and the molecular z axes and between the projection of r_M into the xy plane and the molecular x axis, respectively. Provided that the principal magnetic axes with respect to the haem are known, although this is not trivial for most paramagnetic haemoproteins, δ_{pc}^{M} can be calculated for a nucleus from its coordinates using Eq. (7). Conversely, the coordinates for a nucleus with respect to the principal axes can be inferred from its δ_{pc}^{M} value. δ_{pc}^{M} of a nucleus is extremely sensitive to the values of the coordinates with respect to the principal molecular magnetic axes (see Fig. 4): for met-cyano Mb, a nucleus located at 700 pm away from the haem iron exhibits a δ_{pc}^{M} value of -5 to $+10$ ppm. On the other hand, in the case of a ferric high-spin system, the anisotropic magnetic moment caused by zero-field splitting at the metal ion creates δ_{pc}^{M}, although it is absent for the $S = 1/2$ system.[14] Similarly to the δ_{pc}^{M}, the value of δ_{pc}^{L} is also expressed in terms of the dipolar interaction between a nucleus and a delocalized unpaired electron, and is assumed to be directly proportional to ρ.

For resonances of non-coordinated amino acid residues, δ_{para} is essentially equal to δ_{pc}^{M} because δ_c and δ_{pc}^{L} are neglected. Therefore the quantitative analysis of the δ_{pc}^{M} based on Eq. (7) provides an estimate of the molecular structure of the haem active site. However, for resonances of coordinated ligands, it is realized from Eq. (2) that the relative contributions of the three terms to δ_{para} have to be determined in order to interpret δ_{para} in terms of the electronic/molecular structure of the haem active site. Separation of δ_{para} into its individual components generally demands the determination of the principal magnetic susceptibility tensor axes with respect to the molecule. Several procedures have been proposed to locate these axes. One is based on the components of the diagonal susceptibility tensor obtained from measurements of the low-temperature g values of the lowest Kramer doublets.[88–90] Even for ideal magnetic behaviour, however, questions remain about the applicability of solid-state data in interpreting solution NMR results.[11,91] The least-squares search for the orientation of the principal magnetic axes with respect to the molecule has been used commonly and satisfactorily for various haemoproteins such as ferric low-spin forms of mitochondrial cytochrome c,[92]

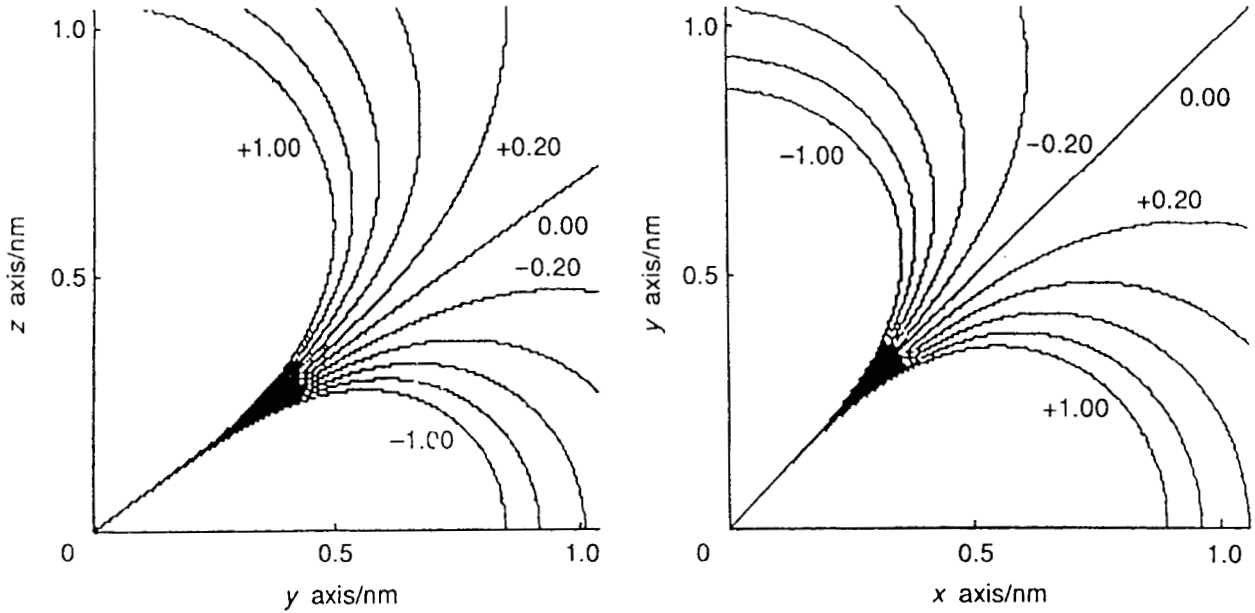

Fig. 4. The δ^{M}_{pc} values calculated for horse heart ferric cytochrome-*c* at 20°C. The axial and rhombic terms of Eq. (7) are plotted separately and δ^{M}_{pc} at any point in space is the sum of these terms. The numbers on the plots are shifts in ppm (positive sign indicates a high frequency shift).[87]

sperm whale Mb[91] and its mutants,[93–95] *Aplysia* Mb,[96] bovine cytochrome b_5,[97] horse heart cytochrome c[98–100] and its mutant,[101] yeast cytochrome c,[102,103] bacterial cytochrome c[104] and horseradish peroxidase.[105] Furthermore, the δ_{pc}^{M} value in met-aquo Mb due to the zero-field splitting is also similarly determined.[106] However, this method requires not only the X-ray co-ordinates of the protein, but also the unambiguous assignments of many NMR resonances for both paramagnetic and diamagnetic forms of the protein. In the limit of validity of the axially symmetric magnetic property, although it is not generally the case for paramagnetic haemoproteins, the equation for δ_{pc}^{M} can be determined analytically from the combined analysis of the paramagnetic shifts of the haem methyl carbon and of the attached proton.[87,107,108]

3.2. Paramagnetic relaxation

Similarly to the shift, the relaxation rate (R_{obs}) of an NMR signal in a paramagnetic system is expressed as the sum of diamagnetic (R_{dia}) and paramagnetic (R_{para}) terms,

$$R_{obs} = R_{dia} + R_{para} \tag{8}$$

R_{para} arises solely from the interaction of the nucleus with the unpaired electron. R_{para} is composed of four terms,

$$R_{para} = R_M + R_L + R_C + R_c \tag{9}$$

where R_M and R_L are the metal-centred and ligand-centred dipolar terms which account for modulation of the dipole–dipole interaction between the nucleus and the unpaired electron spin on the metal and between the nucleus and the delocalized unpaired electron spin on the ligand, respectively. R_C is the Curie spin relaxation term which depends upon $[S(S+1)]^2$ and the square of the applied field strength.[109,110] R_C represents modulation of the contact hyperfine interaction. Using the Solomon–Bloembergen equations,[111–115] the paramagnetic relaxation times $T_{1,para}$ and $T_{2,para}$ of the haem methyl proton in a ferric low-spin complex are written as

$$\begin{aligned} R_{1,para} = (T_{1,para})^{-1} = {} & \frac{2}{15}\gamma_H^2 g^2 \beta^2 S(S+1)(r_M^{-6} + \rho^2 r_L^{-6}) \\ & \times \left[\frac{\tau_{c_2}}{1+(\omega_I - \omega_S)^2 \tau_{c_2}^2} + \frac{3\tau_{c_1}}{1+\omega_I^2 \tau_{c_1}^2} + \frac{6\tau_{c_2}}{1+(\omega_I + \omega_I)^2 \tau_{c_2}^2} \right] \\ & + \frac{2}{3} S(S+1) \left(\frac{A}{\hbar} \right)^2 \left[\frac{\tau_{e_2}}{1+(\omega_I - \omega_S)^2 \tau_{e_2}^2} \right] \end{aligned} \tag{10}$$

$$R_{2,\text{para}} = (T_{2,\text{para}})^{-1} = \frac{1}{15}\gamma_H^2 g^2 \beta^2 S(S+1)(r_M^{-6} + \rho^2 r_L^{-6})$$

$$\times \left[\frac{4\tau_{c_1} + 3\tau_{c_2}}{1 + (\omega_I - \omega_S)^2 \tau_{c_2}^2} + \frac{3\tau_{c_1}}{1 + \omega_I^2 \tau_{c_1}^2} + \frac{6\tau_{c_2}}{1 + \omega_S^2 \tau_{c_1}^2} + \frac{6\tau_{c_2}}{1 + (\omega_I + \omega_S)^2 \tau_{c_2}^2} \right]$$

$$+ \frac{1}{3} S(S+1) \left(\frac{A}{\hbar} \right)^2 \left[\tau_{e_1} + \frac{\tau_{e_2}}{1 + (\omega_I - \omega_S)^2 \tau_{e_2}^2} \right] \tag{11}$$

$$\tau_{c_1}^{-1} = T_{1e}^{-1} + \tau_r^{-1} + \tau_{ex}^{-1} \tag{12}$$

$$\tau_{c_2}^{-1} = T_{2e}^{-1} + \tau_r^{-1} + \tau_{ex}^{-1} \tag{13}$$

$$\tau_{e_1}^{-1} = T_{1e}^{-1} + \tau_{ex}^{-1} \tag{14}$$

$$\tau_{e_2}^{-1} = T_{2e}^{-1} + \tau_{ex}^{-1} \tag{15}$$

where r_M is the metal–nucleus distance, r_L is the distance between the nucleus and the delocalized spin density. ω_I and ω_S are the Larmor frequencies of nucleus and electron, respectively. T_{1e} and T_{2e} are the electron longitudinal and transverse relaxation times, respectively, τ_r is the correlation time of overall molecular tumbling, and τ_{ex} is the electron exchange time. In the above equations, the effects of magnetic anisotropy[116] are not included. In larger molecules with highly resolved NMR spectra, T_{1e}, $T_{2e} \ll \tau_r$, τ_{ex}, and at high magnetic field, $\omega_I^2 T_{1e}^2 \ll 1$, $\omega_S^2 T_{1e}^2 > 1$, and $\omega_S^2 T_{2e}^2 > 1$, Eqs. (10) and (11) are reduced to Eqs. (16) and (17), respectively,[117,118]

$$R_{1,\text{para}} = (T_{1,\text{para}})^{-1} = \frac{6}{15}\gamma_H^2 g^2 \beta^2 S(S+1)(r_M^{-6} + \rho^2 r_L^{-6}) T_{1e} \tag{16}$$

$$R_{2,\text{para}} = (T_{2,\text{para}})^{-1} = \frac{7}{15}\gamma_H^2 g^2 \beta^2 S(S+1)(r_M^{-6} + \rho^2 r_L^{-6}) T_{1e}$$

$$+ \frac{1}{3} S(S+1) \left(\frac{A}{\hbar} \right)^2 T_{1e} \tag{17}$$

Equation (16) shows that $R_{1,\text{para}}$ is proportional to ρ^2. Since the magnitude of δ_c is proportional to ρ (see above), the reciprocal of the observed T_1 value for the haem methyl protons is proportional to the square of their δ_c values. From the plot of $(T_1)^{-1}$ versus $(\delta_c)^2$, T_{1e} can be calculated from the slope and the intercept to $(\delta_c)^2 \rightarrow 0$ indicates $T_{1,\text{para}}$ of the proton with a value of $r_M = 620$ pm.[85,118]

Since the contribution of $\rho^2 r_L^{-6}$ to $(T_{1,\text{para}})^{-1}$ of the amino acid resonances can be neglected, their T_1 values are simply proportional to r_M^6 and hence the ratio of the T_1 values for protons is equal to the sixth power of the ratio of their r_M values. Consequently, if T_1 and r_M are known for a proton, for example, the

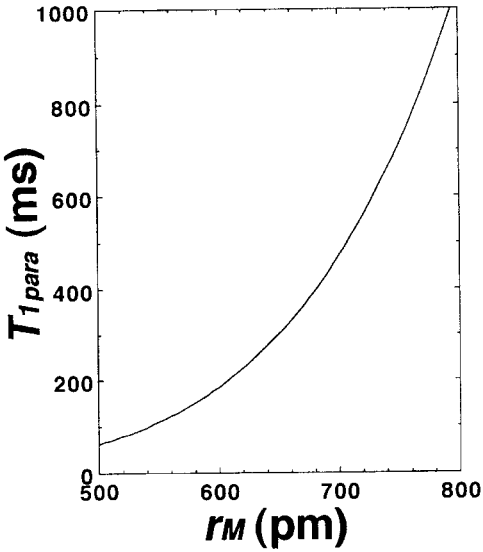

Fig. 5. Plot of ^1H $T_{1,para}$ against the metal–nucleus distance (r_M). The plots are based on haem methyl proton T_1 for shark met-cyano Mb.[119] According to the relationship $T_{1,para} \propto r_M^6$, +12% difference in r_M leads to the doubling of $T_{1,para}$.

haem methyl proton is often used for reference because of its fixed r_M;[12,118,119] the r_M values for the other protons can be obtained from their T_1 values (see Fig. 5). It should be noted that the condition, $R_{dia} \ll R_{para}$, has to be fulfilled for this analysis to be applicable. The ^1H and ^{13}C T_1 data for a ferric low-spin complex indicate that such a condition is satisfied for a nucleus located at <750 pm from the iron.[120] The region where R_{para} dominates in R_{obs}, for protons of a paramagnetic haemoprotein, is found to be even more restricted. For sperm whale met-cyano Mb, the r_M values of the selected protons (r_M = 400–700 pm) of Ile FG5 and Phe CD1 side-chains, as determined from their T_1 values, are smaller than the corresponding value calculated from the X-ray coordinates and the discrepancy between the corresponding values obtained from the two different methods tends to become larger for protons removed farther away from the haem iron.[119] Although the solution structure of the protein is not necessarily identical to the crystal structure, the observed systematic errors strongly suggested that R_{para} is no longer an overwhelming relaxation mechanism for these protons.

Furthermore, in a macromolecule exhibiting cross relaxation, the recovery of magnetization is not by means of a single exponential and a T_1 value can only be extracted from the initial linear portion of a semilogarithmic plot of $(\mu_I - \mu_{I_0})$, where μ_{I_0} is the magnetic moment of a spin i at the thermal equilibrium, as a function of time.[24,121,122] A spin i with intrinsic spin–lattice

relaxation rate ρ_i, interacting with a spin j with magnetic moment μ_J via cross-relaxation rate σ_{ij}, obey the equation,

$$\frac{d\mu_I}{dt} = -\rho_i(\mu_I - \mu_{I_0}) - \sigma_{ij}(\mu_J - \mu_{J_0}) \tag{18}$$

The initial linear portion of nonselective and selective T_1 experiments yield recovery rates of, respectively,

$$^{\text{nonsel}}R_{1,\text{obs}} = \rho_i + \sigma_{ij} \tag{19}$$

and

$$^{\text{sel}}R_{1,\text{obs}} = \rho_i \tag{20}$$

Since σ_{ij} is negative for a macromolecule, we always have $^{\text{nonsel}}\rho_i < {}^{\text{sel}}\rho_i$, while $^{\text{nonsel}}R_{1,\text{obs}}$ is close to $^{\text{sel}}R_{1,\text{obs}}$ in a small molecule or in a molecule where the paramagnetic contribution to ρ_i is much larger than σ_{ij}. Consequently, $^{\text{nonsel}}T_1$ should not be used for the structural analysis of macromolecules.[24]

Practically, the use of $R_{1,\text{para}}$ is mainly in determining r_M. Information about the dynamic properties of a molecule is usually inferred from R_{dia} as in the case of usual diamagnetic molecules.[85] Consequently, the determination of the relative contributions of R_{dia} and R_{para} to R_{obs} is essential in order to interpret the relaxation data of paramagnetic molecules.

4. SIGNAL ASSIGNMENT STRATEGIES

Although, for paramagnetic molecules, the build-up of connectivities through magnetization or coherent transfer is largely diminished by paramagnetic relaxation, multidimensional NMR techniques have been effectively used to assign hyperfine shifted resonances. These have combined the use of conventional magnitude–mode COSY[123] and NOESY[124] and have provided the signal assignments for most of the haem peripheral protons (see Fig. 6).[125–127] On the other hand, in the case of very rapidly relaxing systems, the 1D NOE difference experiment is of great practical use in detecting the dipolar connectivity, as fully described earlier.[53] Furthermore, when detection of connectivities is impossible in practice, the signal assignments often rely on the isotope labelling or comparison with a model compound study.

4.1. Assignment by scalar connectivities

In the ^{1}H NMR spectra of paramagnetic haemoproteins, the resonances resolved from the diamagnetic envelope generally arise from protons located

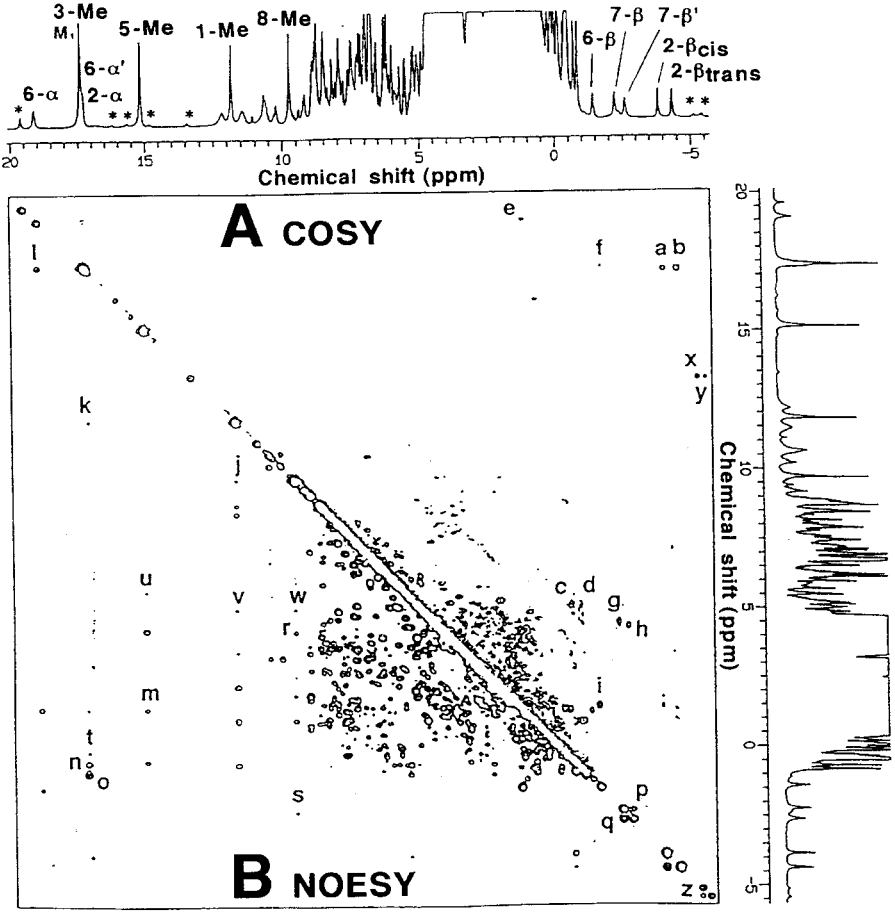

Fig. 6. (A) COSY and (B) NOESY spectra of mollusc *Dolabella* met-cyano Mb at 30°C in ^2H_2O (p^{2}H 8.1). The cross peaks used for the signal assignments are labelled alphabetically. a, (2-α, 2-β_{cis}); b, (2-α, 2-β_{trans}); c, (4-α, 4-β_{cis}); d, (4-α, 4-β_{trans}); e, (6-α, 6-β'); f, (6-α', 6-β); g, (7-α, 7-β); h, (7-α', 7-β'); i, (6-β, 6-β'); j, (1-Me, 8-Me); k, (1-Me, 2-α); l, (6-α, 6-α'); m, (5-Me, 6-β); n, (3-Me, 4-β_{cis}); o, (3-Me, 4-β_{trans}); p, q, (7-β, 7-β'); r, (7-α', 8-Me); s, (7-β, 8-Me); t, (3-Me, α-*meso*); u, (5-Me, β-*meso*), v, (1-Me, δ-*meso*); x, y, z, (the reversed haem vinyl α, β). Signals indicated by an asterisk arise from the reversed haem (see Section 6.1). (Reprinted from Y. Yamamoto and T. Suzuki, *Biochim. Biophys. Acta*, 1993, **1163**, 287, with kind permission of Elsevier Science – NL, Sara Burgerhartstraat 25, 1055 KV, Amsterdam, The Netherlands.)

at <1 nm from the haem iron and their line widths are usually >5 Hz. Consequently, in paramagnetic systems, the line widths, in most cases, are larger than scalar spin–spin couplings (J) and hence the multiplets are not observed except for the haem vinyl β-proton resonances (see the haem structure in Fig. 1) of ferric low-spin complexes of monomeric proteins.[128,129] The spectrum of haemin dicyano complex indicates that $^3J_{\alpha\beta_{trans}}$, $^3J_{\alpha\beta_{cis}}$, and $|^2J_{\beta_{cis}\beta_{trans}}|$ are ~15, ~10, and ~3 Hz, respectively, and the line widths of vinyl α- and β-proton resonances in the ferric low-spin form of Mb are generally ~40 and ~10 Hz, respectively. Therefore, the splitting of β_{trans}-proton resonance due to $^3J_{\alpha\beta_{trans}}$ can be observed only if it is resolved from the diamagnetic envelope.

The applicability of COSY experiments to paramagnetic molecules has been examined in detail.[24,25,29,31,130] Successful application of COSY to paramagnetic haemoproteins has been reported mostly for ferric low-spin forms of the proteins such as the met-cyano forms of various wild-type Mbs[119,125,127,130–135] and monomeric Hb[136,137] and Mb mutants[93,94,138,139], the CN^- adducts of horseradish,[23,140] lignin,[141,142] manganese[143] and cytochrome c[144–146] peroxidases and various ferric cytochromes.[128,147–151] The rotating-frame scalar correlation experiment (TOCSY)[152,153] has also been applied to ferric low-spin forms of Mbs,[130,132,136] cytochromes c,[154,155] manganese peroxidase,[156] and horseradish peroxidase isoenzyme C[157] and the ferrous high-spin form of Mb, i.e., deoxy Mb.[158] For the haem peripheral proton resonances, through-bond connectivities can be observed among the hyperfine shifted resonances arising from the vinyl and propionic acid side-chains. Characteristics of the cross-peaks among proton signals of each side-chain are that they are relatively far away from the diagonal because of the large chemical shift separation of the signals.

The haem vinyl proton signals have previously been assigned from either isotope labelling[12] or a characteristic anti-Curie behaviour of their shifts.[2] However, the scalar coupling network among the vinyl protons of ferrous high-spin and ferric low-spin complexes can easily be identified from a characteristic cross-peak pattern, due to the isolated three-spin system, in the COSY spectrum.[119,125,129,130] Two COSY cross-peaks between α- and β_{cis}- and between α- and β_{trans}-proton resonances exhibit unequal intensities. The facts that $^3J_{\alpha\beta_{cis}} < {}^3J_{\alpha\beta_{trans}}$ and that the vinyl $C_\beta H_2$ geminal protons exhibit similar relaxation rates[131] strongly suggest the assignment of the cross-peak with the largest intensity to the connectivity between α- and β_{trans}-proton resonances and hence of the cross-peak with the smallest intensity to the other pair. The specific assignments of vinyl $C_\beta H_2$ proton resonances can be confirmed by the detection of dipolar connectivity with the α proton or the near-by haem methyl proton.[129] The connectivity between the $C_\beta H_2$ geminal proton resonances is not usually observed in the COSY spectra, because of small J couplings, but can be clearly detected in the single relayed coherence transfer (RCOSY)[159,160] spectrum illustrated in Fig. 7.[131] This result indicates that the coherence transfer

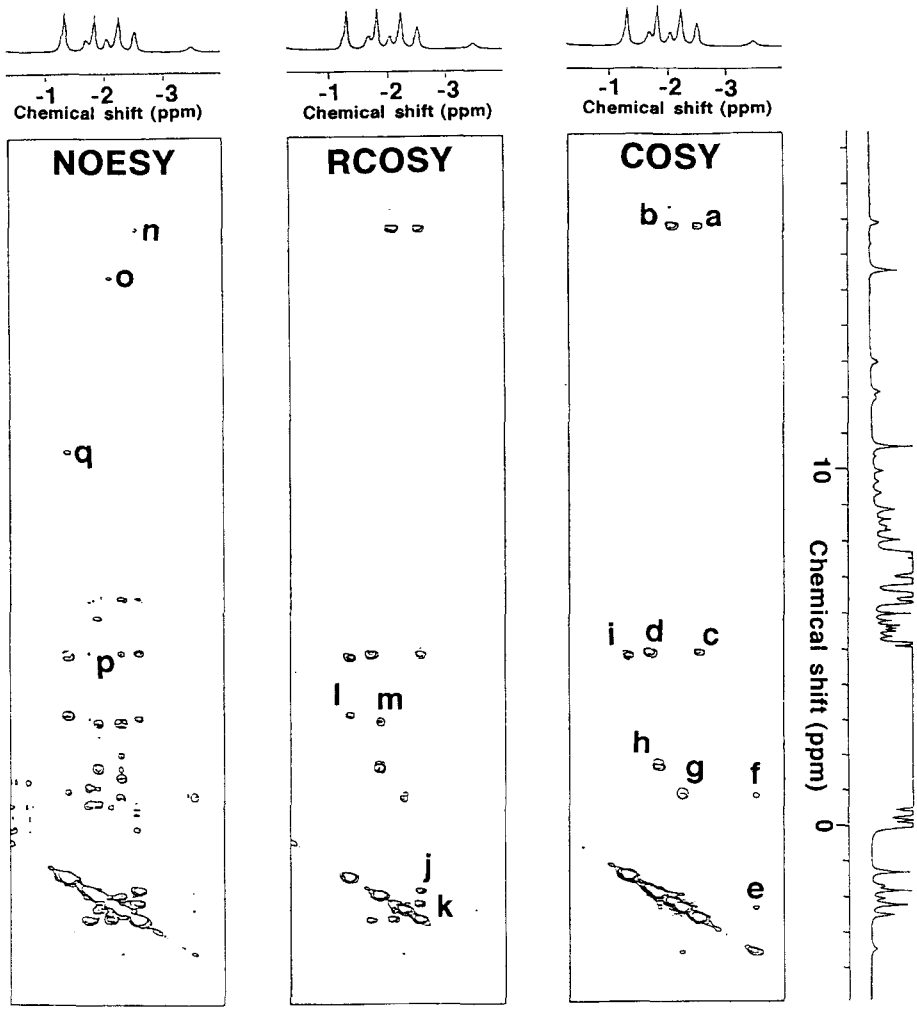

Fig. 7. Portions of COSY (right), RCOSY (centre) and NOESY (left) spectra of shark *Galeorhinus* met-cyano Mb at 45°C in ^2H_2O (p^{2}H 8.5). The cross peaks used for the signal assignments are labelled alphabetically. a, (2-α, 2-β_{cis}); b, (2-α, 2-β_{trans}); c, (4-α, 4-β_{cis}); d, (4-α, 4-β_{trans}); e, (Ile FG5 γ-CH, Ile FG5 γ-CH′); f, (Ile FG5 γ-CH, Ile FG5 δ-CH); g, (Ile FG5 γ-CH′, Ile FG5 δ-Me); h, (Ile FG5 γ-Me, Ile FG5 β-CH); i, (Thr E10 γ-Me, Thr E10 β-CH); j, (2-β_{cis}, 2-β_{trans}); k, (4-β_{cis}, 4-β_{trans}); l, (Thr E10 γ-Me, Thr E10 α-CH); m, (Ile FG5 γ-Me, Ile FG5 α-CH); n, (2-α, 2-β_{cis}); o, (2-β_{trans}, 1-Me); p, (4-α, Ile FG5 δ-Me): q, (Thr E10 γ-Me, 8-Me).[131] (Reprinted from Y. Yamamoto, K. Iwafune, N. Nanai, R. Chûjô, Y. Inoue and T. Suzuki, *Biochim. Biophys. Acta*, 1992, **1120**, 173, with kind permission of Elsevier Science – NL, Sara Burgerhartstraat 25, 1055 KV, Amsterdam, The Netherlands.)

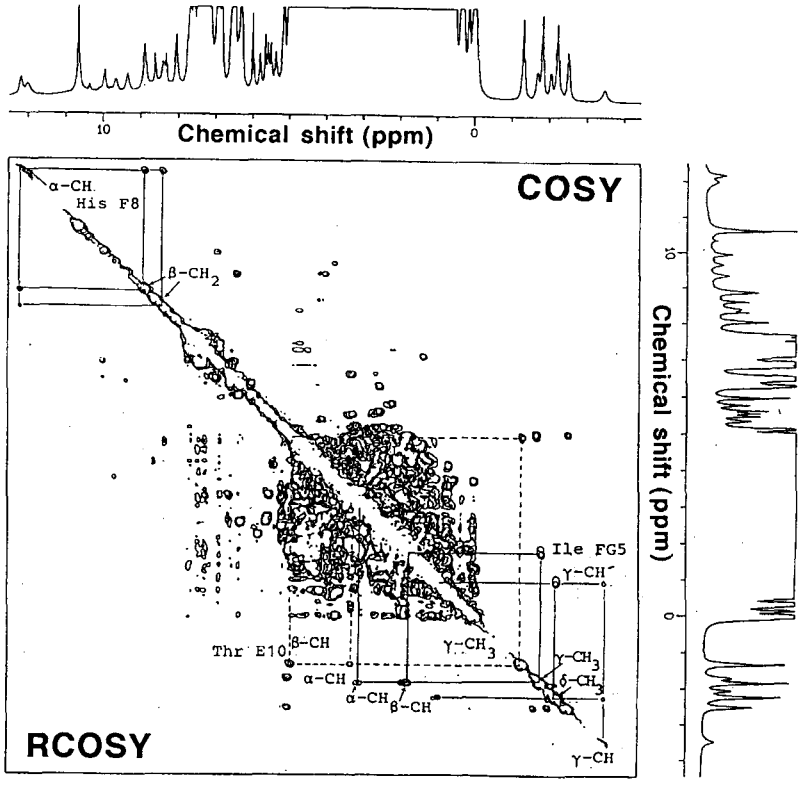

Fig. 8. Portions of COSY and RCOSY spectra of shark *Galeorhinus* met-cyano Mb at 45°C in ^2H_2O (p^2H 7.0). The connectivities are indicated by lines.[119]

between the $C_\beta H_2$ geminal protons takes place through the $C_\alpha H$ proton. RCOSY spectra are also useful in identifying the spin system of amino acid side-chains as illustrated in Fig. 8.[119]

The magnitude–mode COSY spectra of larger paramagnetic metalloproteins recorded at high magnetic field are shown to exhibit not only through-bond connectivities, but also cross peaks due to "relaxation allowed coherence transfer", i.e., cross correlation between interproton dipolar coupling and Curie relaxation.[33,161,162] These two types of cross peaks can be readily distinguished on the basis of their differential phase properties relative to the diagonal peaks in the phase-sensitive COSY spectrum.[31,33,163] In addition, the relaxation-allowed coherence transfer is absent in TOCSY experiments.[34,140]

Since the magnitude of the heteronuclear scalar spin–spin coupling between ^1H and ^{13}C, $^1J_{^1H^{13}C}$, is much larger than that of the homonuclear scalar

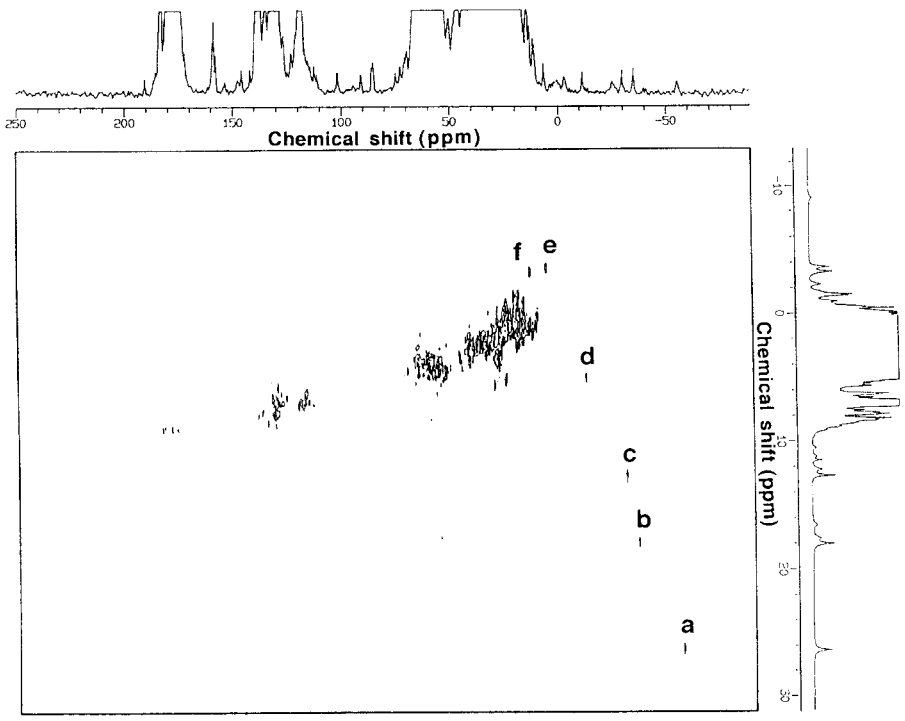

Fig. 9. ^{1}H-^{13}C COSY spectrum of sperm whale met-cyano Mb at 35°C in $^{2}H_2O$ ($p^{2}H$ 8.5). The cross peaks used for the signal assignments are indicated. a, 5-Me; b, 1-Me; c, 8-Me; d, 3-Me; e, Ile FG5 δ-Me; f, Ile FG5 γ-Me.[131] (Reprinted from Y. Yamamoto, K. Iwafune, N. Nanai, R. Chûjô, Y. Inoue and T. Suzuki, *Biochim. Biophys. Acta*, 1992, **1120**, 173, with kind permission of Elsevier Science – NL, Sara Burgerhartstraat 25, 1055 KV, Amsterdam, The Netherlands.)

coupling between protons, $^{n}J_{^{1}H^{1}H}(n > 2)$, coherence is strongly developed in heteronuclear ^{1}H-^{13}C COSY experiments.[164–166] Successful application of ^{1}H-^{13}C COSY to ferric low-spin haemoproteins[44,46,131,167,168] and a model haem complex[45] at natural abundance has been reported. An example for sperm whale met-cyano Mb is illustrated in Fig. 9. Since the haem methyl carbon resonances are usually resolved in the low-frequency hyperfine shifted region, the ^{1}H-^{13}C COSY connectivities identify all of the haem methyl proton resonances even if the attached proton signal resonates in the diamagnetic envelope.[131] The sensitivity has been shown to improve significantly for ^{1}H detection.[48,169] Potential utility of ^{13}C hyperfine shift data in characterizing haem electronic structure has been demonstrated in studies on both model compounds[11,170–178] and proteins.[179–182] The analysis of the haem methyl ^{13}C relaxation in met-cyano Mb revealed that the paramagnetic contribution is

30–55% and <10% for the T_1 and T_2 processes, respectively, and that the rotational correlation time of the methyl group is ≤3 ps,[85] which is typical for methyl group rotations.[183] In the limiting case of axial symmetry such as found in a model compound, δ_{pc}^{M} can be determined quantitatively from the combined analysis of δ_{para} for the haem methyl ^1H and ^{13}C resonances.[107]

4.2. Assignment by dipolar connectivities

The time evolution of an NOE in a two-spin system can be presented by[121]

$$\mathrm{NOE}(t)_{j\to i} = \frac{\sigma_{ij}}{\rho_i}[1 - \exp(-\rho_i t)] \tag{21}$$

where σ_{ij} and ρ_i are the cross relaxation rate between the interacting protons, i and j and the intrinsic spin–lattice relaxation rate of spin i, respectively. σ_{ij} is given by

$$\sigma_{ij} = \frac{\hbar^2 \gamma_H^4}{10r^6}\left[\frac{6\tau_c}{1 + 4\omega_I^2 \tau_c^2} - \tau_c\right] \tag{22}$$

where γ_H is the gyromagnetic ratio of the proton, r is the distance between the protons, τ_c is the correlation time which modulates the dipolar interaction between the two spins, and ω_I is the Larmor frequency. For a short saturation time of spin j, the truncated NOE results in

$$\mathrm{NOE}(t)_{j\to i} = \sigma_{ij} t \tag{23}$$

Equation (23) indicates that the NOE is independent of paramagnetic relaxation.[24,184] In the limit of a long saturation time, the steady-state NOE is given

$$\mathrm{NOE}(t)_{j\to i} = \frac{\sigma_{ij}}{\rho_i} \tag{24}$$

For a paramagnetic molecule, $\rho_i = \rho_{dia} + \rho_{para}$ (ρ_{dia} and ρ_{para} are the diamagnetic and paramagnetic contributions to ρ_i, respectively) and, for a dominant paramagnetic relaxation ($\rho_{dia} \ll \rho_{para}$), the steady state NOE is considerably reduced through "paramagnetic leakage". Although the magnitude is relatively small, the observation of NOEs has been reported for most accessible oxidation and spin states of paramagnetic haemoproteins with a variety of molecular size such as ferric high-spin forms of Mb[26,185–188] and horseradish peroxidase,[189] low-spin forms of Mbs,[23,54–56,93–96,125–127,129–135,190–195] monomeric Hbs,[136,137,196,197] cytochromes,[97–99,102,128,151,156,198–204] and various

peroxidases[23,140–146,154–157,205–221] and ferrous high-spin form of Mbs.[158,222] Furthermore, at high field and with a long correlation time, the molecular motion occurs in the slow motion limit ($\omega_I^2 \tau_c^2 \gg 1$), and Eq. (22) reduces to

$$\sigma_{ij} = -\frac{\hbar^2 \gamma_H^4 \tau_c}{10 r^6} \tag{25}$$

Substitution of Eq. (25) into Eq. (23) yields

$$\mathrm{NOE}(t)_{j \to i} = -\left(\frac{\hbar^2 \gamma_H^4 \tau_c}{10 r^6}\right) t \tag{26}$$

Thus the magnitude of the truncated NOE is simply proportional to both t and τ_c. These results imply that an NOE study is more likely to be successful for a paramagnetic haemoprotein than for a model compound, provided that they possess the same number of unpaired electron(s). For a diamagnetic system with a large ω_I or τ_c, however, the spin diffusion plays a dominant role in relaxation and renders NOEs completely nonspecific.[223] In contrast, for a macromolecule possessing unpaired electron(s), spin diffusion is conveniently suppressed by paramagnetic relaxation, although the degree of the suppression decreases sharply as the protons are farther removed from the paramagnetic centre.[24,224] Furthermore, in the slow motion limit, ρ_{dia} and ρ_{para} are proportional to τ_c and $r_M^6 T_{1e}$, respectively,[1,184] and it has been shown experimentally that T_{1e} is independent of τ_c.[85,118,120,184] Consequently, as long as a dominant paramagnetic relaxation occurs, steady-state NOE in the slow motion limit is proportional to τ_c.

The first successful application of NOESY to a paramagnetic molecule[43] was largely based on the above consideration. When haemin dicyano complex is dissolved in methanol, the low viscosity of the solvent yields $\omega_I^2 \tau_c^2 \sim 0.2$, leading to a quenching of NOEs. However, dissolving the sample in a viscous solvent, which places the system in the slow motion limit ($\omega_I^2 \tau_c^2 \gg 1$), renders NOEs detectable. Even in the case of paramagnetic protein, the increase in the solvent viscosity largely enhances both the magnitude and build-up rate of NOEs.[184] Although the addition of organic cosolvents to increase viscosity is useful for the NOE study of a paramagnetic protein, it also appears to perturb the structure of the haem active site, as reflected in subtle changes to hyperfine shifted resonances. Effects of cosolvent on protein structure are not fully understood.

The time evolution of the intensity (volume), a_{ij}, of a NOESY cross-peak between proton i and j is given by[225]

$$a_{ij}(t_m) = \frac{n_i n_j}{n_i + n_j} \frac{V_0 |\sigma_{ij}|}{2D} [1 - \exp(-2Dt_m)] \times \exp[-(R - D)t_m] \tag{27}$$

$$D = \left[\frac{(\rho_i - \rho_j)^2}{4 + \sigma_{ij}^2}\right]^{1/2} \tag{28}$$

$$R = \frac{(\rho_i + \rho_j)}{2} \tag{29}$$

where t_m is the mixing time, n_i, n_j and ρ_i, ρ_j are intensities and intrinsic relaxation rates for the corresponding proton signals, respectively, and $V_0(=V_{0i} + V_{0j})$ is the total magnetization (total intensity or volume of the diagonal peaks for i and j at $t_m = 0$). The optimization of experimental parameters in NOESY experiment on rapidly relaxing systems, where the cross relaxation is much smaller than the nuclear relaxation rate, has been fully discussed previously.[53] It is clear from Eq. (27) that the cross peak intensity depends on the cross relaxation rate between protons, their signal intensities and nuclear relaxation rates. In the spectra of paramagnetic molecules, fast relaxing signals exhibit sizeable hyperfine shifts and hence are resolved outside of the diamagnetic envelope. The detection of dipolar connectivities between a rapidly relaxing signal and a slowly relaxing one, which is buried in the diamagnetic envelope, can be much more efficiently performed by conventional 1D NOE difference spectroscopy. Such an example is illustrated in Fig. 10. Shark Mb possesses Gln at the distal E7 position instead of the usual His.[226–228] In the met-cyano form of shark Mb, iron-bound CN^- is stabilized by the hydrogen bond with the $N_\varepsilon H$ proton of Gln E7.[194] The $N_\varepsilon H$ proton is located at about 400 pm from the iron and its intrinsic spin–lattice relaxation time ($^{sel}T_1$) is about 10 ms. In the assumption of an extended side-chain conformation of Gln, non-exchangeable protons of the side-chain are at least 250 pm away from the $N_\varepsilon H$ proton and hence $|\sigma_{ij}| < 2$ is estimated with the assumption of $\tau_r = 8$ ns, calculated from the Stokes–Einstein equation.[121] The irradiation of the $N_\varepsilon H$ signal for 50 ms yields a clear NOE to the $C_\gamma H$ proton signal with a $^{sel}T_1$ of about 70 ms. Furthermore, the analysis of the time-dependent 1D NOE connectivity between the $C_\gamma H_2$ geminal proton signals provides not only the cross relaxation rate between them but also the intrinsic spin–lattice relaxation rate of the $C_\gamma H'$ proton.

The rotating-frame 2D NOE experiment (ROESY)[229,230] was utilized to distinguish between dipolar and exchange cross-peaks in the spectra of a paramagnetic model complex[231] and cytochrome c_3.[232] However, this experiment has not been used as much as NOESY in the study of paramagnetic molecules. 3D NOE[49] and a combination of 1D NOE and NOESY experiments[50] have been used to provide assignments of hyperfine shifted resonances of a paramagnetic haemoprotein, which had not been accessible by conventional NMR methods.

4.3. Assignment by saturation transfer

The saturation transfer experiment is useful for relating resonances that are connected by a dynamic exchange process with a suitable time scale. If the

assignments are known in one form, saturation transfer connectivity identifies the same resonance in the other form. The first application of saturation transfer to a paramagnetic haemoprotein was demonstrated for establishing correlations between reduced and oxidized cytochrome *c*.[41,233–235] Subsequently, it has been demonstrated that the magnetization is transferred through the exogenous ligand exchange process of the protein.[205,236–240]

The Fe(III) high-spin form of Mb (metMb) possesses either pentacoordinated haem iron[185,241–243] or hexacoordinated haem iron[244] with H_2O as an iron-bound ligand and binds exogenous ligands such as CN^-, N_3^-, OH^- and imidazole. The ligand binding of metMb results in a change of S of the haem iron from ferric high-spin ($S = 5/2$) to ferric low-spin ($S = 1/2$) (see Fig. 3). Since the hyperfine shift is proportional to $S(S+1)$,[76] there is an enormous difference in the resonance frequency between the two different spin states of Mb. In the presence of less than the stoichiometric amount of an exogenous ligand relative to metMb, the signals from each form are observed separately. In the spectrum of metMb, a large contact interaction leads to the resolution of most haem peripheral proton signals, and the previous assignments in various metMbs[185–188,241,243] have demonstrated that the haem methyl paramagnetic shift pattern in metMb is independent of the protein. Hence, the haem methyl proton signals in ferric low-spin Mb can be straightforwardly assigned through saturation transfer connectivities upon the saturation of the corresponding resonances in metMb (Fig. 11), and the magnitude of the magnetization transfer provides the kinetics of ligand exchange (see Section 7.1). A 2D exchange experiment[245] can also be used to detect the connectivities (Fig. 12).

Fig. 10. (**A**) NOE connectivity between His F8 $N_\delta H$ and amide NH proton resonances. (a) High-frequency portion of the 400 MHz ^1H NMR spectrum of *Galeorhinus* met-cyano Mb in 90% H_2O/10% ^2H_2O at pH 7.10 and 25°C. (a′) The saturation of His F8 $N_\delta H$ proton resonance for 50 ms exhibits an NOE to the amide NH proton resonance. (b) High-frequency portion of the 400 MHz ^1H NMR spectrum of *Mustellus* met-cyano Mb in 90% H_2O/10% ^2H_2O at pH 7.13 and 35°C. (b′) The saturation of His F8 NH proton resonance for 50 ms exhibits an NOE to the amide NH proton resonance. (**B**) NOE connectivity between Gln E7 $N_\varepsilon H$ and γ-H proton resonances. (c) High-frequency portion of the 400 MHz ^1H NMR spectrum of *Galeorhinus* met-cyano Mb in 90% H_2O/10% ^2H_2O at pH 7.10 and 25°C. (c′) The saturation of Gln E7 $N_\delta H$ proton resonance for 50 ms exhibits an NOE to the γ-H proton resonance. (d) High-frequency portion of the 400 MHz ^1H NMR spectrum of *Mustellus* met-cyano Mb in 90% H_2O/10% ^2H_2O at pH 7.13 and 35°C. (d′) The saturation of Gln E7 $N_\delta H$ proton resonance for 50 ms exhibits an NOE to the γ-H proton resonance. The signal due to the off-resonance saturation is indicated by an asterisk. (e) High-frequency portion of the 400 MHz ^1H NMR spectrum of shark *Mustellus* met-cyano Mb in 100% ^2H_2O at p^{2}H 7.13 and 35°C. (Reprinted from Y. Yamamoto and T. Suzuki, *Biochim. Biophys. Acta*, 1996, **1129**, 129, with kind permission of Elsevier Science – NL, Sara Burgerhartstraat 25, 1055 KV, Amsterdam, The Netherlands.)

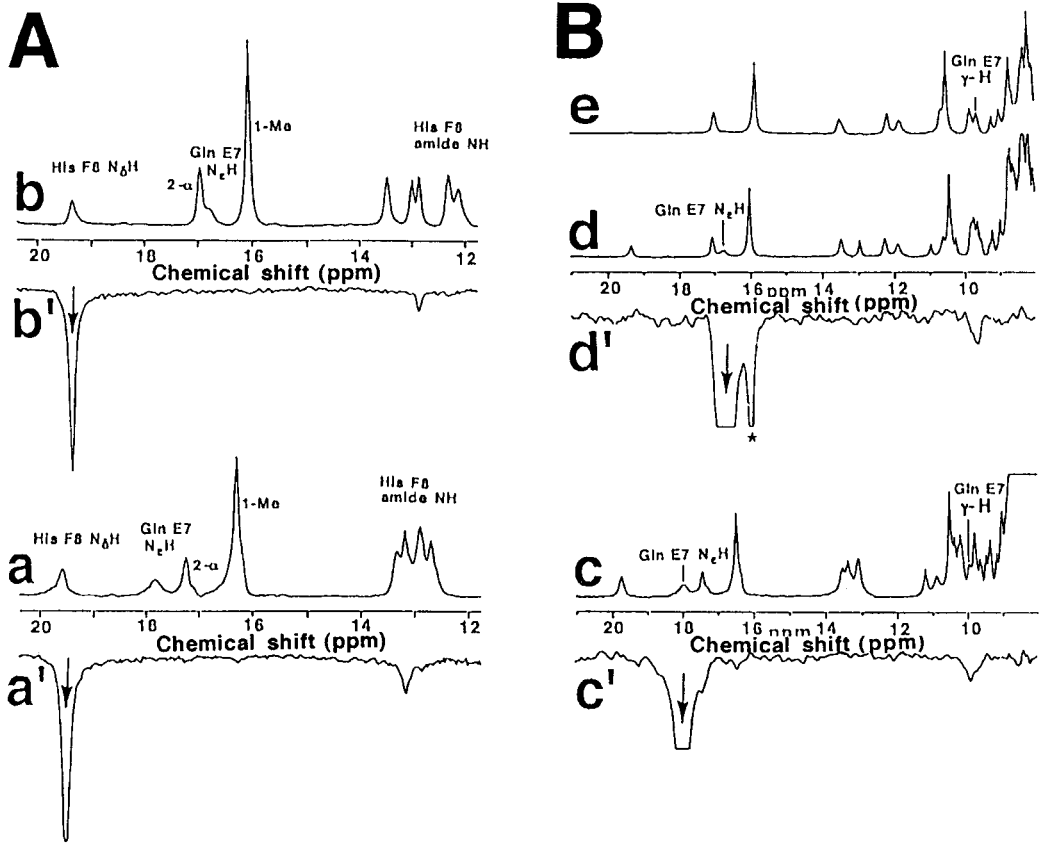
A
b
His F8 NδH
2-α
Gln E7 NεH
1-Me
His F8 amide NH
20
18
16
14
12
Chemical shift (ppm)
b'
a
His F8 NδH
Gln E7 NεH
2-α
1-Me
His F8 amide NH
20
18
16
14
12
Chemical shift (ppm)
a'
B
e
Gln E7 γ-H
d
Gln E7 NεH
20
18
16 ppm
14
12
10
Chemical shift (ppm)
d'
*
c
Gln E7 NεH
Gln E7 γ-H
20
18
16 ppm
14
12
10
Chemical shift (ppm)
c'

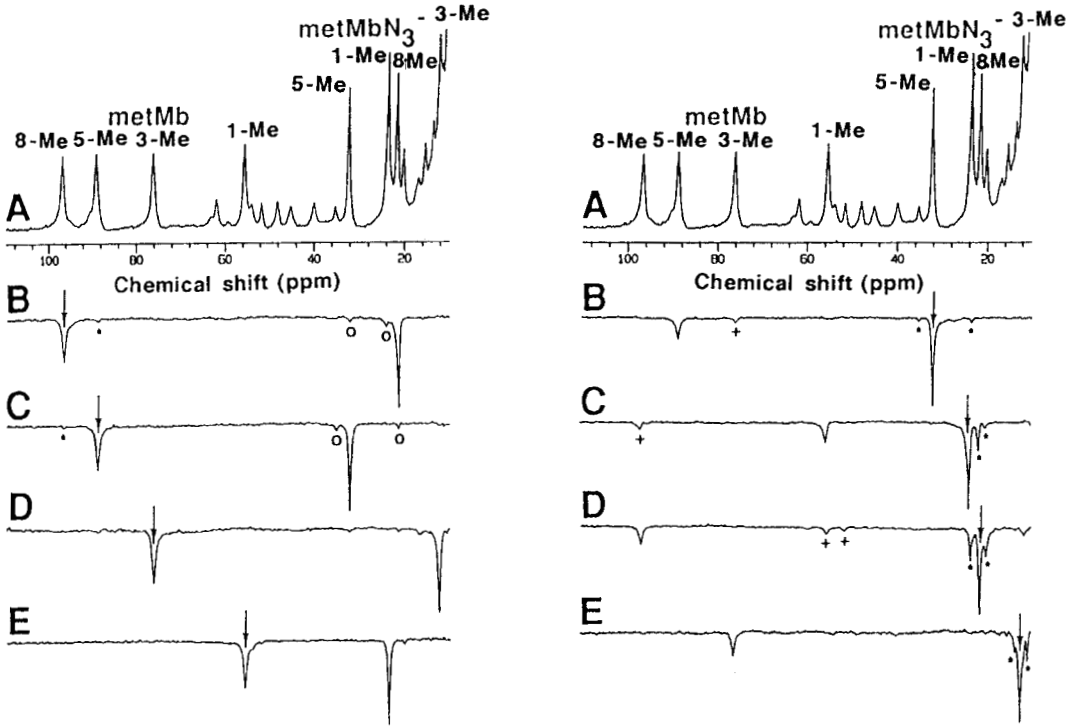
metMbN3 - 3-Me
1-Me
8Me
5-Me
metMb
8-Me 5-Me 3-Me
1-Me
A
100
80
60
40
20
Chemical shift (ppm)
B
C
D
E

The transition of hexacoordinated metMb to met-hydroxyl Mb is fast compared with the NMR time scale (Fig. 13). The NMR saturation transfer technique is not applicable to a system dynamically exchanging faster than the NMR time scale. Using thiocyanate iron as a mediator ligand, the resonances of metMb can be connected to the corresponding resonance of met-hydroxyl Mb, because thiocyanate ion competes with H_2O and OH^- for the binding to the haem iron with the regime of slow exchange on the NMR time scale, as illustrated in Fig. 14.[238] This study demonstrates the potential applicability of a mediator ligand in the spectral assignments of paramagnetic haemoproteins by saturation transfer.

4.4. Assignment by comparison with model compounds

The iron–His bonding interaction in haemoproteins has been of particular interest because the electronic control of the haem iron reactivity is proposed to be exerted through this bond.[246] The proximal His imidazole resonance provides a sensitive probe for characterizing this bonding interaction. The ^{13}C NMR spectrum of horse deoxy Mb[247] is illustrated in Fig. 15. Several resonances are resolved in the high-frequency region. The study of ferrous high-spin model compound demonstrated that the axial His imidazole ring C_δ and C_ε resonate at ~400 and ~900 ppm, respectively.[178] Hence the peaks a and b at 235.3 and 686.3 ppm, respectively, possibly arise from proximal His C_δ and C_ε, respectively. Considering the line widths of about 200 Hz for these resonances, the widths of the signals of the attached protons, i.e., $C_\delta H$ and $C_\varepsilon H$, could be as large as ~4 kHz owing to paramagnetic relaxation. Consequently, the detection of ^1H-^{13}C COSY connectivity is practically impossible for these CH fragments. The assignments of peaks a and b to C_δ and C_ε, respectively, was confirmed by the detection of the spin–spin couplings $^1J_{^1H^{13}C}$. The removal of

---

Fig. 11. High-frequency hyperfine shifted portions of the 270 MHz ^1H NMR spectrum and saturation-transfer difference spectra of the mixture of *Dolabella* metMb and met-azido Mb at p^2H 7.24 and 30°C. [met-azido Mb]/[metMb] = 1.2. An arrow indicates the peak being saturated and the signal due to off-resonance saturation is indicated by an asterisk. A circle or + sign shows the saturation-transfer connectivity from the resonances other than that indicated with an arrow. Saturation-transfer spectra observed upon saturation of haem methyl proton resonance of metMb are shown on the left. (A) Reference spectrum. The difference spectra upon saturation of (B) 8-Me, (C) 5-Me, (D) 3-Me and (E) 1-Me signals of metMb. Saturation-transfer spectra observed upon saturation of haem methyl proton resonance of met-azido Mb are shown on the right. (A) Reference spectrum. The difference spectra upon saturation of (B) 5-Me, (C) 1-Me, (D) 8-Me and (E) 3-Me signals of met-azido Mb. The corresponding resonances of the two forms are unambiguously connected via the saturation-transfer connectivities.[237]

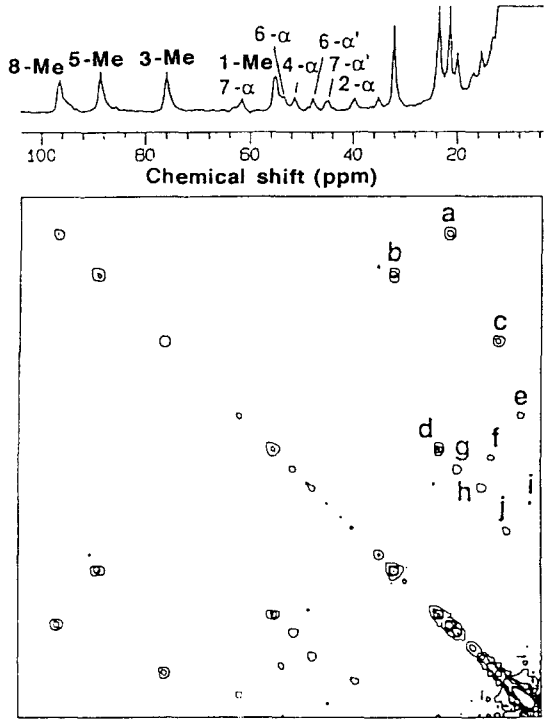

Fig. 12. Portion of the 2D exchange spectrum of the mixture of *Dolabella* metMb and met-azido Mb at p^2H 7.24 and 30°C. [met-azido Mb]/[metMb] = 1.2. A mixing time of 5 ms was used. The cross-peaks a–j indicate the connectivities between the haem peripheral proton resonances of the two forms. a, 8-Me; b, 5-Me; c, 3-Me; d, 1-Me; e, 7-α; f, 6-α; g, 4-α; h, 6-α′; i, 7-α′; j, 2-α.[237]

the decoupling field yields the lineshape of B′ and C′ for peaks a and b, respectively. Peak b splits into two and the width of peak a increases by 20 Hz. These results are consistent with the $^1J_{^1H^{13}C}$ values of 190 and 208 Hz for the C_δ–H and C_ε–H bonds, respectively, in imidazole.[248]

The 50 MHz ^{15}N NMR spectrum of horse Mb(Im)[249] is shown in Fig. 16. In the spectrum, there are two ^{15}N signals observed at 177.2 and 250.3 ppm (referenced to the signal of neat nitromethane). The 27 MHz ^{15}N NMR of Fe(III) tetraphenylporphyrin–imidazole complex[251] in Fig. 17 exhibits two resonances at 124.8 and −2115.2 ppm (referenced to the signal of neat nitromethane) with widths of 52 and 708 Hz, respectively, besides the single signal arising from free imidazole at 172.6 ppm due to rapid tautomerization reaction at ambient temperature.[252] Considering the exchange rate of 14 s^{-1} of imidazole between its free and bound states,[253] it is reasonable to assume that these two resonances arise from the bound imidazole. Since the iron–nucleus

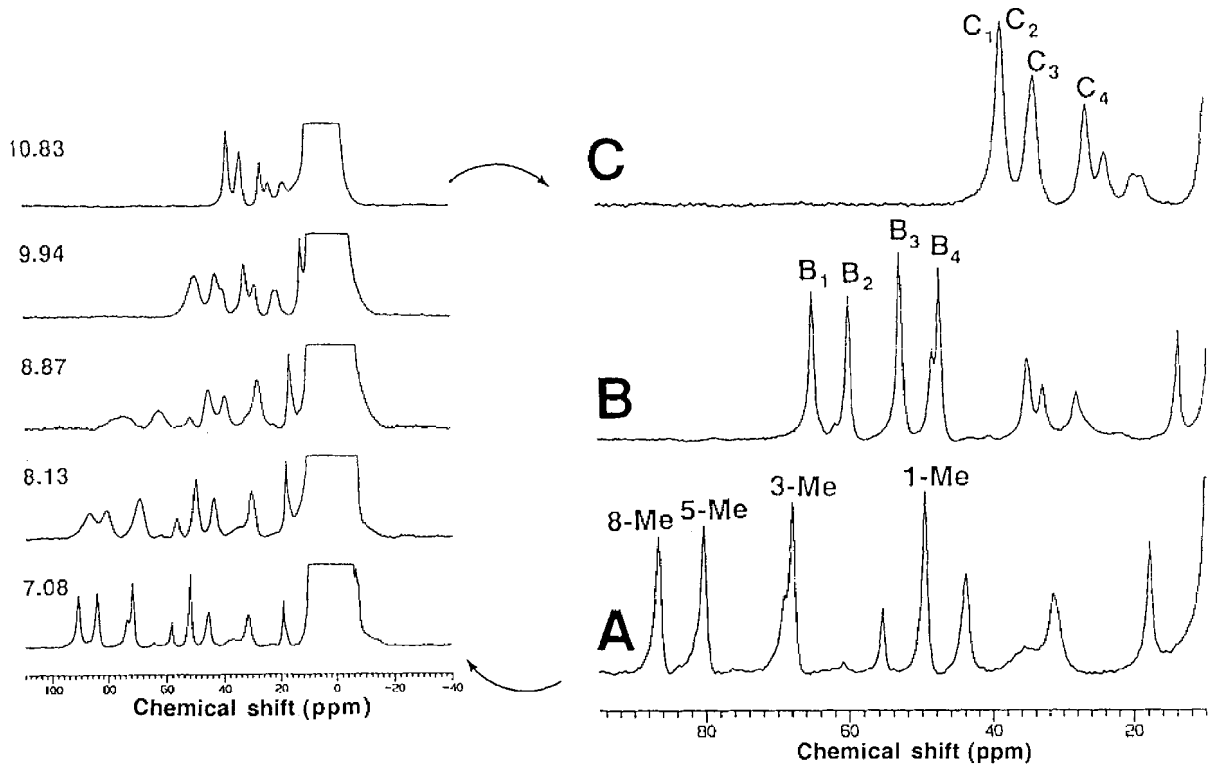

Fig. 13. High-frequency hyperfine shifted portion of the 270 MHz ^{1}H NMR spectra of (A) horse metMb in ^2H_2O, p^{2}H 6.80, (B) met-thiocyanate Mb in ^2H_2O, p^{2}H 7.56 and (C) met-hydroxyl Mb in ^2H_2O, p^{2}H 11.31 at 45°C. Signals labelled B_1–B_4 and C_1–C_4 arise from haem methyl protons. A series of spectra illustrated on the left-hand side shows the spectra of metMb at the indicated p^{2}H.[238]

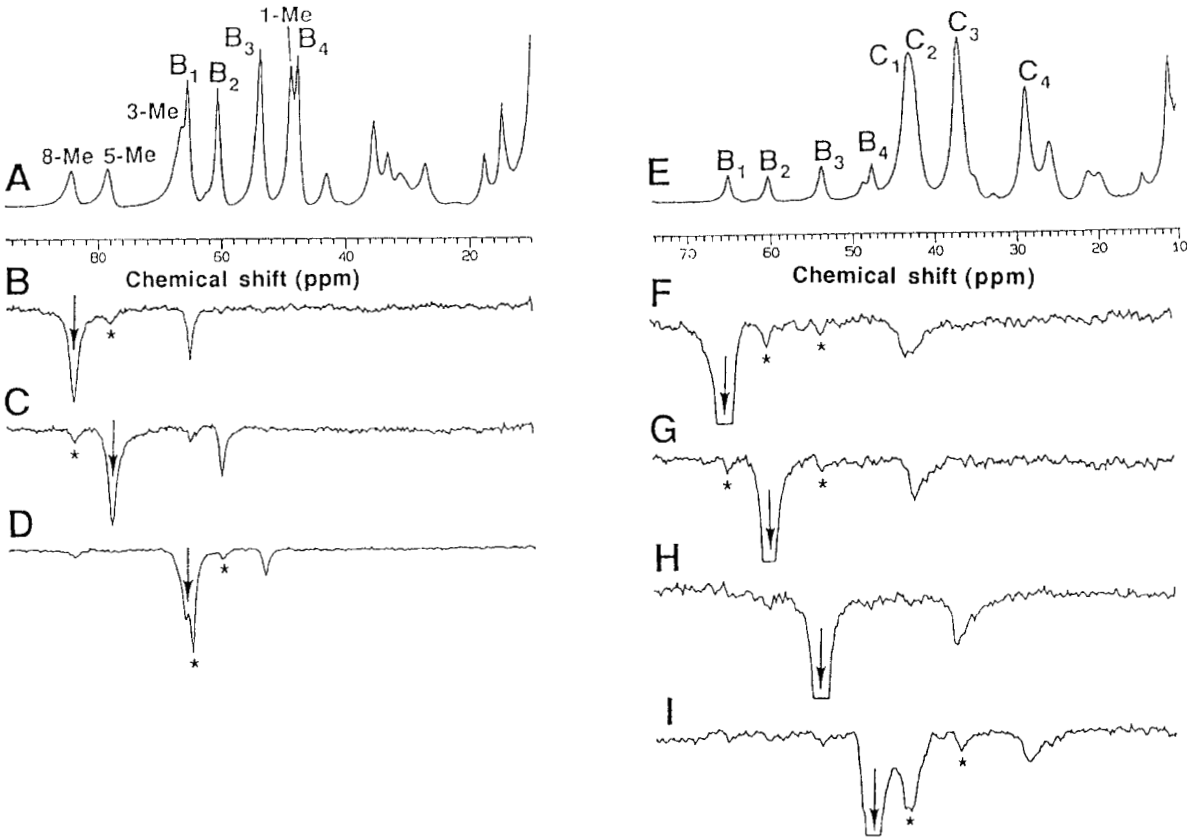
A
8-Me
5-Me
3-Me
B1
B2
B3
1-Me
B4
80
50
40
20
Chemical shift (ppm)
B
C
D
E
B1
B2
B3
B4
C1
C2
C3
C4
70
60
50
40
30
20
10
Chemical shift (ppm)
F
G
H
I

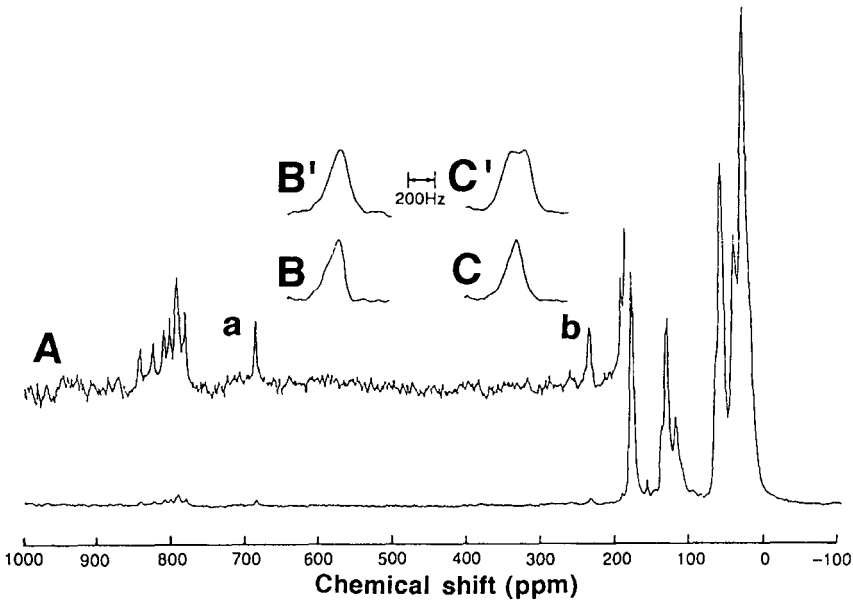

Fig. 15. The 67.8 MHz coupled ^{13}C NMR spectrum of horse deoxy Mb in $^{2}H_2O$ at 35°C. (A) The *Y*-scale is expanded by a factor of 10. The signals arising from C_ε and C_δ carbons are labelled a and b, respectively. (B), (C) and (B'), (C') are the resonances with and without ^{1}H decoupling, respectively.[247]

distances (r_M) are 400 and 200 pm for $N_{(1)}$ and $N_{(3)}$ of iron-bound imidazole, respectively,[254] the difference in the line widths strongly supports the assignments shown with the spectrum. Thus, the ^{15}N signals of the bound and unbound imidazole are separated by more than 2000 ppm. Hence the observation of only a single peak for the bound ligand in the spectrum of Mb(Im) (Fig. 16) is not due to a rapid exchange of the ligand, but to the extensive broadening

---

Fig. 14. The 270 MHz ^{1}H NMR and saturation-transfer difference spectra of horse metMb complexes at 45°C. (A) High-frequency hyperfine shifted portion of the spectrum of the mixture of metMb and met-thiocyanate Mb in $^{2}H_2O$, $p^{2}H$ 7.32. Saturation of (B) 8-Me, (C) 5-Me and (D) 3-Me signals of metMb. The observed saturation-transfer connectivities provide the assignments of met-thiocyanate Mb, B_1 (8-Me), B_2 (5-Me) and B_3 (3-Me) and hence B4 (1-Me). (E) High-frequency hyperfine shifted portion of the spectrum of the mixture of met-thiocyanate Mb and met-hydroxyl Mb in $^{2}H_2O$, $p^{2}H$ 10.39. In the traces (F)–(I), the connectivities between haem methyl proton resonances of the two forms are shown. The results indicate the haem methyl proton signal assignments of met-hydroxyl Mb, i.e. C_1 (8-Me), C_2 (5-Me), C_3 (3-Me) and C_4 (1-Me). An arrow indicates the peak being saturated and peaks due to off-resonance saturation are indicated by an asterisk.[238]

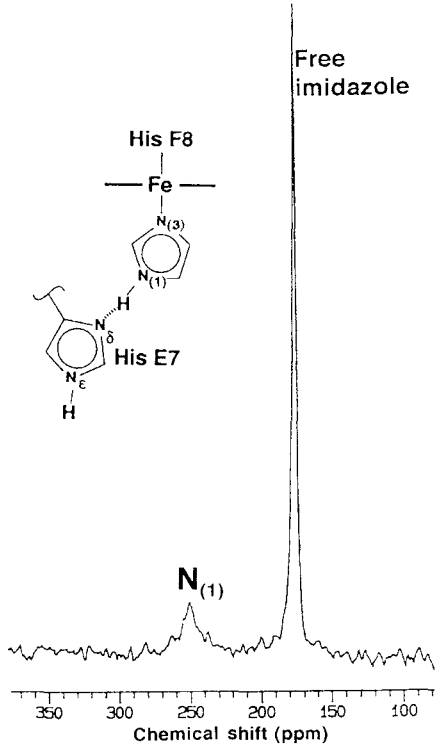

Fig. 16. The 50 MHz ^{15}N NMR spectrum of met-imidazole Mb in $^{2}H_2O$, p^{2}H 7.94, at 12°C. The numbering system of the imidazole ring and the hydrogen bond[250] between the bound ligand and His E7 are indicated in the inset. Chemical shifts are given relative to the signal of neat nitromethane.[249]

of the $N_{(3)}$ signal. This is supported by the value of ~14 for the ratio of the line widths of the $N_{(1)}$ and $N_{(3)}$ signals in the spectrum of a model compound and the width of the $N_{(1)}$ signal (~510 Hz) dictates that the width of the $N_{(3)}$ signal for Mb(Im) could be as large as ~7 kHz.

5. DETERMINATION OF HAEM ACTIVE-SITE STRUCTURE

Hyperfine shifted resonances observed in the spectra of paramagnetic proteins provide sensitive probes for the haem environments. Since the shifts and the relaxation rates are quantitatively interpretable in terms of the interaction between the nucleus and the unpaired electron(s), the molecular and electronic structures of the haem active site can be directly inferred from the analysis of these data.

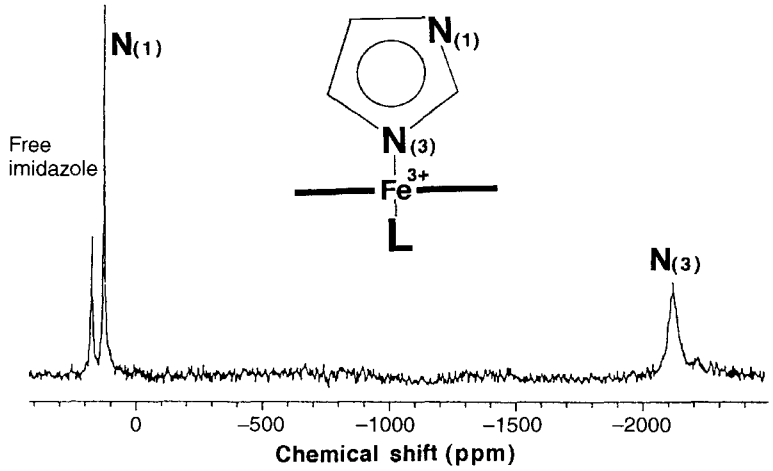

Fig. 17. The 27 MHz ^{15}N NMR spectrum of iron(III) tetraphenyl porphyrin-imidazole in C^2HCl_3 at 30°C. The numbering system of the imidazole ring is indicated in the inset. Chemical shifts are given relative to the signal of neat nitromethane.[251]

5.1. Iron–His bonding interaction

A minor alteration in the iron–proximal His imidazole binding interaction leads to drastic changes in the electronic structure of the haem and hence in the reactivity of the haem iron. The iron–His imidazole bond in the haemoprotein can be modulated by both the steric interaction and the hydrogen-bonding interaction of the $N_\delta H$ proton of His F8 with the protein acceptor (see Fig. 2). The former interaction simply compresses or extends the Fe–N_ε bond and the latter modulates the Fe–N_ε bond through the alteration of the imidazole basicity. A few spectroscopic probes have been used to specifically monitor the Fe–N_ε bond in haemoprotein. Resonance Raman spectroscopy[255] provides the Fe–N_ε stretching frequency, which can be directly interpreted in terms of the bonding energy. X-ray absorption spectroscopy[256] allows a direct observation of the Fe–N_ε distance. ^1H NMR gives the hyperfine shift of the $N_\delta H$ proton, which provides useful information about the unpaired electron delocalization and the strength of the hydrogen bond between the $N_\delta H$ and the acceptor.[257,258] Combined analysis of these data allows the separation of the steric and hydrogen-bonding contributions to the Fe–N_ε bond.[259]

An alternative method for characterizing the electronic structure of the proximal His imidazole is the observation of the imidazole ^{15}N resonances because both the steric and hydrogen-bonding interactions can be monitored simultaneously through the electronic structure of the axial imidazole. These

Table 1. Separation of δ_{hf} into δ_{pc} and δ_c contributions for ^{15}N NMR resonances of the bound imidazole in iron(III) tetraphenyl porphyrin–imidazole complex in $CDCl_3$ at 30°C.[251]

Resonance	δ_{obs}[a]	δ_{dia}[a,b]	δ_{hf}[a]	GF[c]	δ_{pc}[a]	δ_c[a]
$N_{(1)}$	124.8	150.5	−25.7	27.58	23.7	−49.4
$N_{(3)}$	−2115.2	231.5	−2346.7	260.01	223.1	−2569.8

[a]Shifts in ppm.
[b]The value at $T^{-1} \rightarrow 0$ obtained from the Curie plot.
[c]Geometric factor, $(3\cos^2\theta - 1)/r^3$, in units of 10^{-6} nm^3.

signals in a model compound are observed as demonstrated in Fig. 17. Using the values at $T^{-1} \rightarrow 0$ for their Curie plots gives δ_{dia}, together with the δ_{pc}^{M} values calculated from the reported data;[176] the contributions to their δ_{para} values are thus separated as in Table 1.[251] A remarkable difference in their δ_c values demonstrates the magnitude of polarization of this imidazole ring. Thus δ_c of the $N_{(3)}$ signal could be used as an indicator of the Fe–$N_{(3)}$ covalency.

5.2. Orientation of axial His imidazole with respect to haem

Among the hyperfine shifted signals, the haem methyl proton and carbon resonances are of considerable importance because their shifts sharply and directly reflect the haem electronic structures of the proteins.[7,8,12,13,168,179–182,260–262] The fact that the spread of the four haem methyl proton signals in the protein is always much larger than that for the corresponding model complex[8] indicates that asymmetry of the haem electronic structure in the protein is mainly due to an asymmetric haem–protein interaction.

There are two major factors responsible for the in-plane asymmetry in the haem electronic structure. One is the nature of the axial ligands and their orientation with respect to the haem[168,260–264] and the other is the nonequivalent haem peripheral substituents whose electronic natures are also altered by interaction with the neighbouring amino acids.[8,265] The former factor modulates the haem electronic structure via the interaction of the p_π orbital of imidazole with the highest energy d_π metal orbital where the unpaired electron most probably resides. The latter is through the molecular orbital containing the unpaired electron. Since the interaction between the π-systems of the haem vinyl group and the porphyrin ring is influenced by the orientation of the vinyl group with respect to the haem plane, the electronic structure of the haem can be altered by the orientation of the vinyl.[266] Furthermore, the difference in the interaction between the iron-bound cyanide ion and the distal residue is also reported to perturb the hyperfine shifted haem methyl

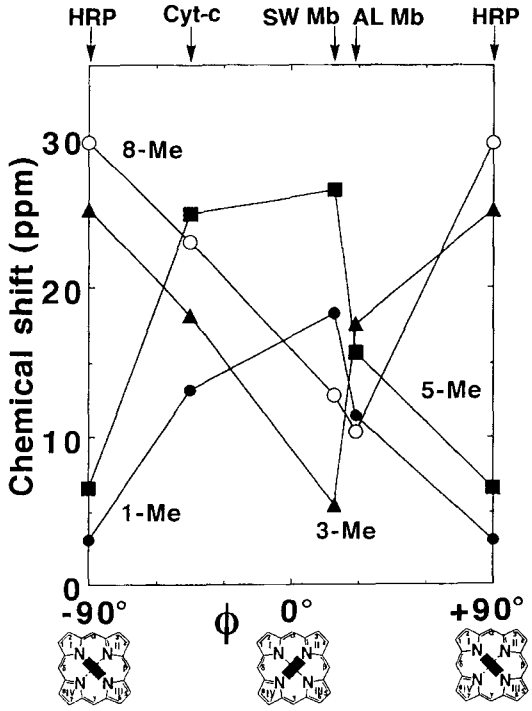

Fig. 18. Plots of the haem methyl proton hyperfine shifts of some met-cyano haemoproteins at 35°C against the dihedral angle, ϕ, between the projection of the proximal His imidazole plane onto the haem plane and the N_{II}–Fe–N_{IV} axis. The ϕ values are 19° for sperm whale Mb (SW Mb),[67] 29° for *Aplysia* Mb (AL Mb),[192] −45° for horse heart cytochrome *c* (Cyt-c),[268] and 90° for horseradish peroxidase (HRP).[269] (From Ref. 168.)

resonances.[267] But such minor perturbations on the haem electronic structure cannot account for the large difference in the hyperfine shifts for the haem methyl ^{13}C resonances found between the met-cyano Mbs from different species.[168] In Fig. 18, the haem methyl ^{1}H hyperfine shifts of some haemoproteins are plotted against the angle (ϕ) between the projection of the proximal histidyl imidazole plane onto the haem plane and the N_{II}–Fe–N_{IV} axis. The spread of the haem methyl ^{1}H resonances, which in turn reflects the asymmetric nature of the haem electronic structure, is smaller for the CN^- complex of ferric cytochrome *c*[167] and *Aplysia* met-cyano Mb[192] and larger for sperm whale[190] and shark[168] met-cyano Mbs or the CN^- complex of horseradish peroxidase,[205] where the imidazole plane is roughly along the N_{II}–Fe–N_{IV} axis. Such ϕ dependency of the in-plane asymmetry in the electronic structure of the porphyrin ring has been analysed in detail using model

compounds.[263] The bond length between the haem iron and the bound imidazole is found to be essentially independent of the imidazole orientation in the model compounds[263] as well as in haemoproteins.[67] Thus, in the case of the ferric low-spin complex, the haem methyl hyperfine shift pattern correlates well with the axial imidazole orientation with respect to the haem.

The temperature dependence of haem methyl proton or carbon hyperfine shifts has been used to investigate the electronic and molecular structures of the active site as a function of temperature.[127,192,270,271] Since there is no angular dependence in the delocalization of an unpaired electron from the porphyrin π-system to a haem methyl group (Eq. (6)), the haem methyl hyperfine shifts generally obey the Curie law. There are two cases reported so far where haem methyl proton shifts exhibit anti-Curie behaviour, i.e. where the hyperfine shift increases with increasing temperature. One is the case where an external ligand with an intermediate field strength, such as N_3^-, imidazole or OH^-, binds to a ferric haem iron. Such a complex exhibits a thermal spin equilibrium between high-spin, $S = 5/2$, and low-spin $S = 1/2$ states,[71–75] and the haem methyl hyperfine shift pattern at a given temperature is mainly determined by the equilibrium population of the two spin states.[193,272–275] The other is the case where dynamic averaging over multiple structures with somewhat different haem methyl hyperfine shift patterns takes place and the populations change with temperature.[127,192,265]

It has been reported that two haem methyl proton resonances in horse heart ferric cytochrome *c* exhibit anti-Curie behaviour, whereas its haem methyl carbon resonances all obey the Curie law.[271] Similar anti-Curie behaviour of haem methyl proton resonances has been reported for other *c*-type haemoproteins.[271,276–279] It has been proposed that such anti-Curie behaviour is due to the thermal mixing of two different electronic structures of the haem.[271,280] For the ferric low-spin complex, overlap of the e-symmetry π orbitals of a symmetrical porphyrin ring and the d_π orbitals of the metal produces two low-energy molecular orbitals, for which the equilibrium populations vary with temperature. An alternative interpretation[281] of the anti-Curie behaviour of the haem methyl proton shift in the CN^- adduct of ferric cytochrome-*c* is based on the temperature dependence of the angle ϕ in Fig. 18. In the case of the $S = 1/2$ system, where zero-field splitting is absent,[14] provided that the geometrical coordinates of the nucleus with respect to the molecular axes are independent of temperature, δ_{pc}^M is simply proportional to T^{-1}. To a first approximation, δ_{pc}^L is directly proportional to ρ.[11,176] δ_{pc}^M and δ_{pc}^L are negative for both haem methyl proton and carbon resonances. Since the temperature dependence of δ_{dia} can be quite small, compared with that of δ_{para}, the slope of the Curie plot, i.e., δ_{obs} vs T^{-1}, is expressed from Eqs. (1) and (2) as

$$\frac{\partial(\delta_{obs})}{\partial(T^{-1})} = \frac{\partial(\delta_c)}{\partial(T^{-1})} + \frac{\partial(\delta_{pc}^M)}{\partial(T^{-1})} + \frac{\partial(\delta_{pc}^L)}{\partial(T^{-1})} \tag{30}$$

For a haem methyl proton resonance, the first term of Eq. (30) is positive, whereas the last two terms are negative. Therefore, as long as $|\partial(\delta^{M}_{pc})/\partial(T^{-1}) + \partial(\delta^{L}_{pc})/\partial(T^{-1})| < |\partial(\delta_c)/\partial(T^{-1})|$, the Curie plot for a haem methyl proton resonance exhibits a positive slope. Alternatively, for the haem methyl carbon resonances, the slope of their Curie plots is always negative. Thus the anti-Curie behaviour for a haem methyl proton resonance could arise from competition in the temperature dependence between δ_c and $\delta_{pc}(=\delta^{M}_{pc} + \delta^{L}_{pc})$. As illustrated in Fig. 18, distribution of the delocalized unpaired electron is considerably affected by the angle ϕ and therefore the anti-Curie behaviour observed for ferric cytochrome-*c* might be due to the occurrence of the haem rotational displacement about the iron–His bond. Rotation of the haem, with respect to the protein moiety, in the haem pocket of various reconstituted Mbs has been investigated in detail.[270,282–289] Although, owing to the presence of the covalent bonds between the haem and the protein moiety in *c*-type haemoprotein, the change in the ϕ value is rather restricted, the ϕ value could be modulated through conformational alteration of the haem–protein linkage.

5.3. Coordination of a sixth ligand in the ferric high-spin form

Although the haem in ferric high-spin haemoprotein is usually hexacoordinated with the sixth ligation site occupied by a water molecule, some metMbs and metHbs possess a pentacoordinated active site, i.e., the sixth ligation site is vacant.[185,188,241–243,290] Since the bound water molecule is stabilized by the hydrogen-bonding interaction with the distal E7 amino acid residue in these proteins, the ligation state of ferric high-spin haemoproteins depends crucially on the nature of the E7 residue.[188,241,243,290]

It has been shown from a study on a model compound that the haem meso-proton resonances of the model compound system appear to low frequency (~ -50 ppm) for the pentacoordinated system and to high frequency (40 ppm) for the hexacoordinated haem.[291] The validity of the use of the meso-proton chemical shift as a probe for determining the coordination system of the haem iron in ferric high-spin haemoproteins has been confirmed from the study of *Aplysia* metMb.[185]

Furthermore, in the ferric high-spin complexes, the relaxation process for the haem peripheral side-chain proton resonances has been shown to be modulated mainly by T_{1e}, which in turn is detected by modulation of the zero-field level of the complex.[292,293] The narrower resonances (line width $\sim$200 Hz) observed for shark metMb compared with those (line width 350–400 Hz) for vertebrate metMbs (see Fig. 19) indicate the larger zero-field splitting in the former protein. This result is consistent with the lower symmetry in the ligand field around the haem iron, as a result of the pentacoordinated haem in shark metMb.[243]

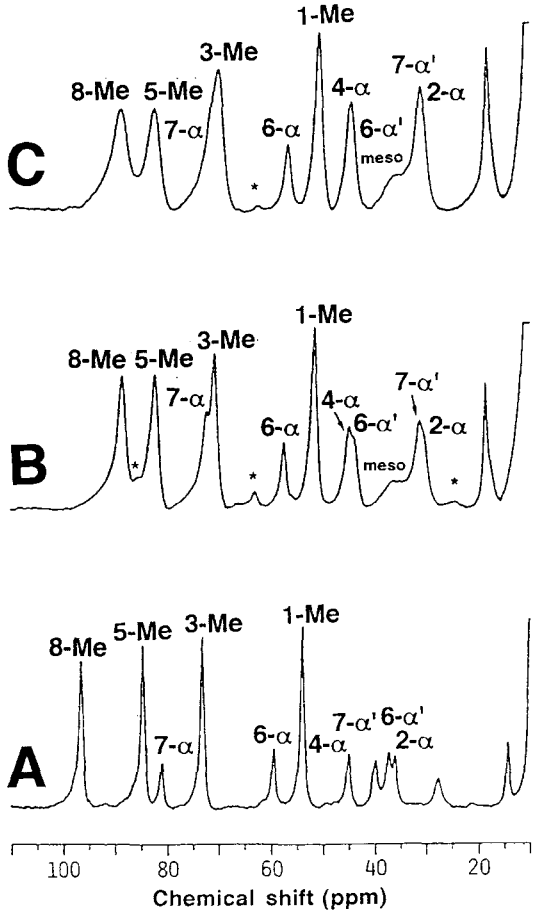

Fig. 19. High-frequency hyperfine shifted portions of the 270 MHz ^{1}H NMR spectra of (A) shark, (B) sperm whale and (C) horse metMbs in ^2H_2O, p^{2}H 7.0, at 35°C. Peaks indicated by an asterisk arise from the reversed haem.[243]

Additionally, it has been reported that the shifts and the widths of the hyperfine shifted haem peripheral methyl proton resonances in the spectra of ferric high-spin haemoproteins are influenced by solvent isotope composition through hydrogen-bonding interactions between the coordinated water molecule and a distal amino acid residue.[244] Larger hyperfine shifts and paramagnetic line widths in ^2H_2O than in H_2O for metMb and metHb hexacoordinated with the bound water molecule have been attributed to a stronger axial ligand field in the former solvent owing to the strong hydrogen bond between the bound ^2H_2O and the distal residue. Therefore, these isotope

effects can also be used as probes for the presence of an iron-bound water molecule in ferric high-spin haemoproteins.

5.4. Interaction of an iron-bound ligand with a distal amino acid residue

In the distal pocket of oxygen-binding haemoproteins, an amino acid residue capable of being a hydrogen-bond donor is generally located in close proximity to the ligand binding site of haem, and this residue has been shown to play important roles in the molecular mechanisms for controlling the ligand affinity of the active sites. In most vertebrate Mbs and Hbs, His at the E7 helical position is highly conserved and has been shown to act as a proton donor to stabilize the bound ligand in a variety of ligation states such as the oxy,[294] met-cyano,[68,194] and met-fluoro[295] forms. Furthermore, it has been proposed that His E7 also acts as a proton acceptor to stabilize the iron-bound ligand in the met-aquo[244,296] and met-imidazole[250] forms. A survey[297] of 226 natural globin sequences revealed that, besides His E7, Gln most frequently occupies the E7 position, i.e., in elephant Mb,[298] shark Mb,[227] hagfish Hb,[299] opossum Hb α subunit[300] and clam Hb.[301] Since side-chains of His and Gln are similar in both their molecular size and ability to participate in a hydrogen bond as a proton donor as well as a proton acceptor, Gln E7 is expected to play similar roles to His E7 in vertebrate Mbs and Hbs.

The hydrogen-bonding interaction between a distal amino acid residue and an iron-bound ligand can be investigated by NMR through characterization of the exchange behaviour of the labile proton directly involved in the interaction.[68,194,302–304] Rates of exchange can be measured by the saturation transfer method.[68,302,305] The extent of spin saturation transferred from the irradiated solvent signal to the exchangeable proton resonances was determined as follows. First, a spectrum is recorded without water suppression; then the decoupler is applied off-acquisition on the H_2O transition. The pair of spectra so obtained yield the needed signal intensities I, observed when the solvent is saturated, and I_0, the intensity in the absence of saturation. The corresponding saturation factor I/I_0 is then determined. The rate of exchange (k) is related to I/I_0 by the formula

$$\frac{I}{I_0} = \frac{\rho_i}{\rho_i + k} \tag{31}$$

where ρ_i is the intrinsic relaxation rate of the resonance whose I/I_0 is evaluated and, under the condition that $\rho_i \gg k$, ρ_i can be obtained using a selective saturation recovery experiment with a selective excitation pulse sequence.[306–310] If ρ_i remains constant over the pH range, the exchange rate is obtainable from

$$k = \frac{\rho_i[1 - (I/I_0)]}{I/I_0} \tag{32}$$

Exchange rates of $1–10^3\ s^{-1}$ at physiological pH and ambient temperature have been reported for NH protons of His E7 in various mammalian met-cyano Mbs[68,302–304] and Gln E7 in shark met-cyano Mbs.[194] Slow exchange for these NH protons strongly supports the view that they are donated to iron-bound CN^- through a hydrogen-bonding interaction. Mb from a gastropod mollusc belonging to the *Aplysiidae* possesses Val E7,[311–314] but exhibits relatively high oxygen affinity.[315,316] An NMR study of *Dolabella* met-cyano Mb revealed that a guanidino NH proton of Arg E10 is located at 410 pm from the haem iron and exhibits the exchange rate of $<10\ s^{-1}$ at neutral pH.[316] These results strongly suggest the presence of a hydrogen-bonding interaction between a guanidino NH proton of Arg E10 and iron-bound CN^-. The presence of a hydrogen bond between Arg E10 and iron-bound CN^- has been identified in analogous *Aplysia* metMb.[317] Thus the mollusc Mb possesses a molecular basis for the ligand stabilization that is completely different from that for mammalian Mb.[132,316–318]

Furthermore, the ^{15}N NMR signal of iron-bound $C^{15}N^-$ is sensitive to the nature of the hydrogen-bonding interaction between the coordinated ligand and the distal residue.[319] Unpaired metal electron density delocalized to the bound ligand is also transferred to the NH proton of the distal residue through the hydrogen-bonding interaction. The analysis of shark met-cyano Mbs revealed that unpaired electron density at the nitrogen of the bound CN^- decreases with a strengthening of the hydrogen-bonding interaction and the density transferred to the Gln E7 $N_\varepsilon H$ proton increases with the strength of the interaction.[194] Thus combined analyses of the $N_\varepsilon H$ proton exchange rate and the ^{15}N shift of the bound $C^{15}N^-$ have led to a detailed characterization of the hydrogen-bonding interaction between the bound ligand and Gln E7 in shark met-cyano Mb.

5.5. Conformation of haem peripheral side-chains

The functional properties of a haemoprotein depend on the haem molecular/electronic structure. Interaction between the π-system of the peripheral vinyl group and the π-conjugated system of the haem is thought to influence the haem electronic structure.[266,320] The conformations of the propionate groups have been shown to be important for the haem–globin interaction.[288,289,321,322]

It has been demonstrated that the conformation of the propionic acid side-chain of the soybean carbon monoxy leghaemoglobin (molecular mass ~15 kDa) can be uniquely determined from the analyses of NOESY cross-peaks and J couplings.[323] For large haemoproteins, however, increased line widths render the measurements of J coupling constants difficult. The determination of interproton distances from the measurement of cross-relaxation rate using the time evolution of NOESY cross-peaks could possibly lead to a

conformational determination of the haem peripheral side-chains in paramagnetic haemoproteins.[324] In the slow motion limit, σ_{ij} yields the interproton distance r_{ij} through Eq. (25). At very small values of t_m, $t_m \ll 1/2D$, $1/(R-D)$, Eq. (27) is simplified to

$$a_{ij}(t_m) = \frac{n_i n_j}{(n_i + n_j)} V_0 |\sigma_{ij}| t_m \tag{33}$$

The internuclear distances are extracted from this initial linear slope of the NOESY cross-peak build-up. The methodology was applied to cyanide-inhibited horseradish peroxidase (~44 kDa).[324] NOESY spectra, as a function of t_m, demonstrated that quantitatively accurate rise curves can be obtained and that primary and secondary NOEs can be clearly differentiated even among the most strongly relaxed protons, but this requires very short t_m values in the range of 0.5–3.0 ms. The time evolution of the cross-peak intensities, although it is linear to only a few milliseconds, is shown to yield cross relaxation rates and internuclear distances.

The conformations of three characteristic fragments in the active site of a haemoprotein are depicted in Fig. 20 and they are defined by single dihedral angles χ, ψ, and ζ as illustrated in the figure. Equation (23) dictates that NOE build-up rate is simply proportional to σ_{ij}. Provided that two interproton vectors undergo identical motion, Eq. (25) implies that the ratio of the σ values, σ_1 and σ_2, for the two systems is simply expressed as that of the interproton distances, r_{M_1} and r_{M_2}, as in Eq. (34).

$$\frac{\sigma_1}{\sigma_2} = \left(\frac{r_{M_2}}{r_{M_1}}\right)^6 \tag{34}$$

Since the time scale for haem methyl rotation is at least three orders of magnitude smaller than that for haem vinyl and propionate mobility,[55,85,186,193] the centre of mass for the methyl proton is used to calculate distances. In Fig. 21, the distances between selected protons for each fragment are plotted as functions of the dihedral angles defined in Fig. 20.

The conformation around the C_α–C_β bond of His F8 (see Fig. 20A) can be determined uniquely from the interproton distances between the α- and β-protons and between the α- and β'-protons. The NOE difference spectra upon saturation of the His F8 α-proton signal of *Galeorhinus* met-cyano Mb for a variety of saturation times are shown in Fig. 22A. The initial build-up slopes yield σ values of -0.58 ± 0.01 and $-0.81 \pm 0.02\ s^{-1}$ for the β- and β'-protons, respectively. Using Eq. (34), these σ values yield 0.95 ± 0.01 for the ratio of the α–β' and α–β interproton distances, which corresponds to the χ values of $75 \pm 5°$ and $130 \pm 5°$ in Fig. 21A. The NOE difference spectra upon saturation of the His F8 β-proton signal for a variety of times are illustrated

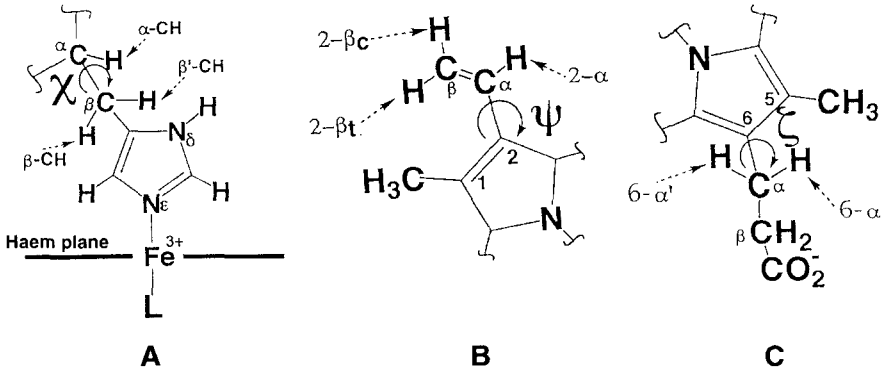

Fig. 20. (A) Dihedral angle χ is defined by the atoms $HC_\alpha C_\beta H$ of His F8; $\chi = 0°$ for $C_\alpha H$ eclipsed by $C_\beta H$. The C_β methylene proton located closest to haem iron is labelled β and the other β'. The rotation direction for χ is positive when the viewer is located on the C_α atom and observes a clockwise rotation around the C_α–C_β bond. (B) Dihedral angle ψ is defined as the angle between the 2-vinyl plane and the normal to the haem plane; $\psi = 0°$ for the vinyl plane orthogonal to the haem plane with the 2-β_{trans}-proton oriented in the His F8 side with respect to the haem plane and +90° for C_α–C_β *cis* to C^2-C^1. (C) Dihedral angle ζ is defined as the angle between the plane comprising C^6, C_α, C_β and the normal to the haem plane; $\zeta = 0°$ for the C^6, C_α, C_β plane orthogonal to the haem plane and +90° for C_α–C_β *cis* to C^6–C^5.

in Fig. 22B. The initial build-up slopes yield σ values of -0.63 ± 0.03 and $-6.8 \pm 0.1\ s^{-1}$ for the α- and β'-protons, respectively. These σ values provide a value of 0.26 ± 0.01 nm for the α–β distance, which corresponds to a χ value of about $\pm 80°$ in Fig. 21B. Consequently, the value of about +80° satisfies the results from the analyses of the two sets of time-dependent NOE data shown in Fig. 22.

The determination of haem vinyl conformation, with respect to the haem, demands a knowledge of the σ values between the β_{cis}- and β_{trans}- or the α-protons and between one of the vinyl protons and the nearby methyl protons. Similarly the σ values between the propionate α-CH_2 geminal protons and between one of the propionate α-protons and the nearby methyl protons are needed to determine the orientation of the haem propionate α-CH_2 groups with respect to the haem. The NOE build-up on the 1-Me-, 2-α-, and 2-β_{cis}-proton signals upon saturation of the 2-β_{trans}-proton signal of shark met-cyano Mb is illustrated in Fig. 23. The plots in the inset yield σ values of -0.090 ± 0.01 and $-1.3 \pm 0.1\ s^{-1}$ for 1-Me- and 2-β_{cis}-protons, respectively. The fact that the initial build-up slope for the 2-α-proton signal vanishes at $t > 0$ indicates that the NOE between the 2-α- and 2-β_{trans}-protons is secondary. Using the geminal proton distance of 0.177 nm, the ratio of the σ values for the 1-Me- and 2-β_{cis}-protons yields the interproton distance of 0.28 ± 0.01 nm

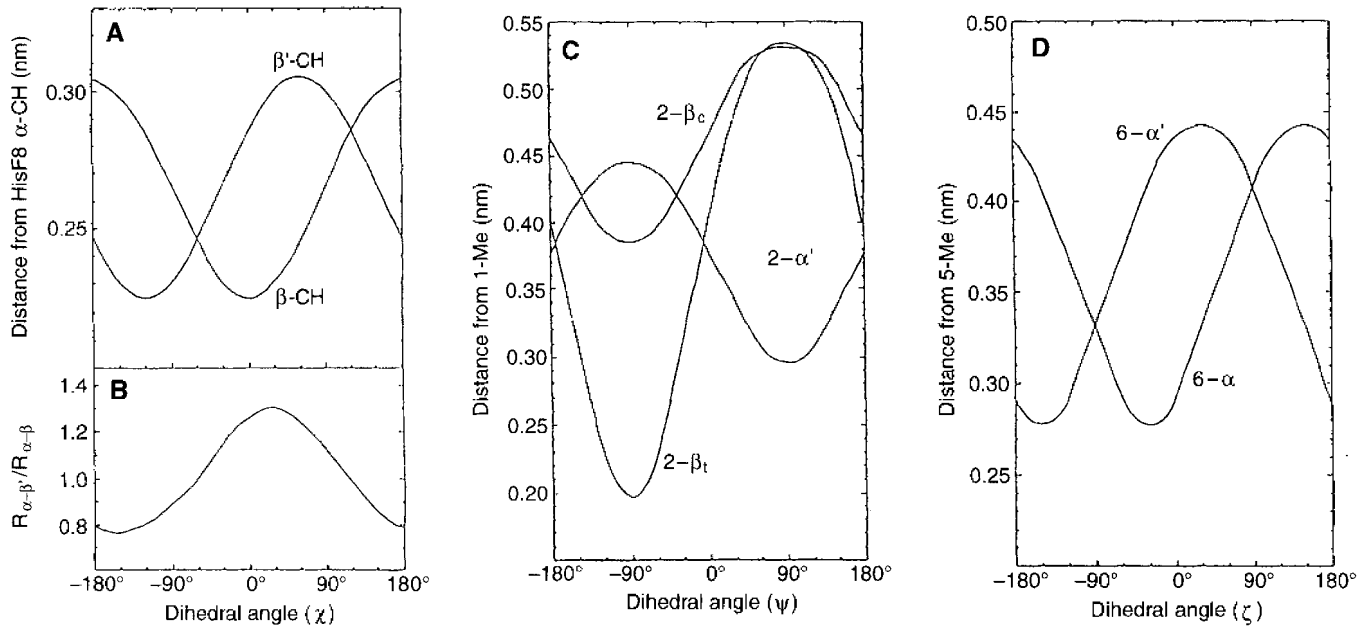

Fig. 21. (A) Plot of χ versus the distances of His F8 β- and β'-protons from the α-proton. (B) Plot of χ versus the ratio of the α–β' and α–β distances, $R_{\alpha-\beta'}/R_{\alpha-\beta}$. (C) Plot of ψ versus the distances of the 2-vinyl protons from the 1-Me proton. (D) Plot of ζ versus the distances of the 6-propionate α-protons from the 5-Me proton.[195]

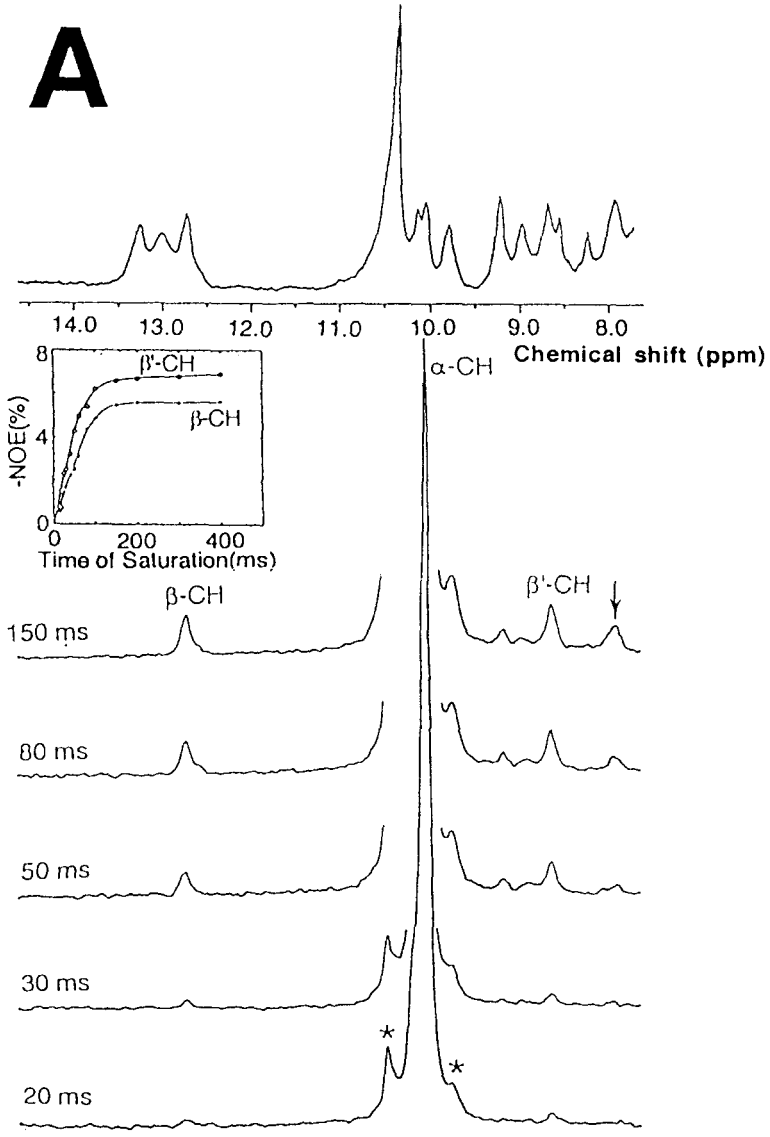

Fig. 22. Time-dependent NOE difference spectra of *Galeorhinus* met-cyano Mb at 30°C. (A) Observed upon saturation of His F8 α-proton signal for the indicated time. The intensity of the α-proton signal is kept constant. The time evolution of the NOEs observed for the His F8 β- and β'-proton signals is illustrated in the inset and the initial build-up slopes provide σ values of -0.58 ± 0.01 and $-0.81 \pm 0.01\ s^{-1}$ for β- and β'-protons, respectively. (B) Observed upon saturation of His F8 β-proton signal for the indicated time. The time evolution of the NOEs observed for the His F8 α- and

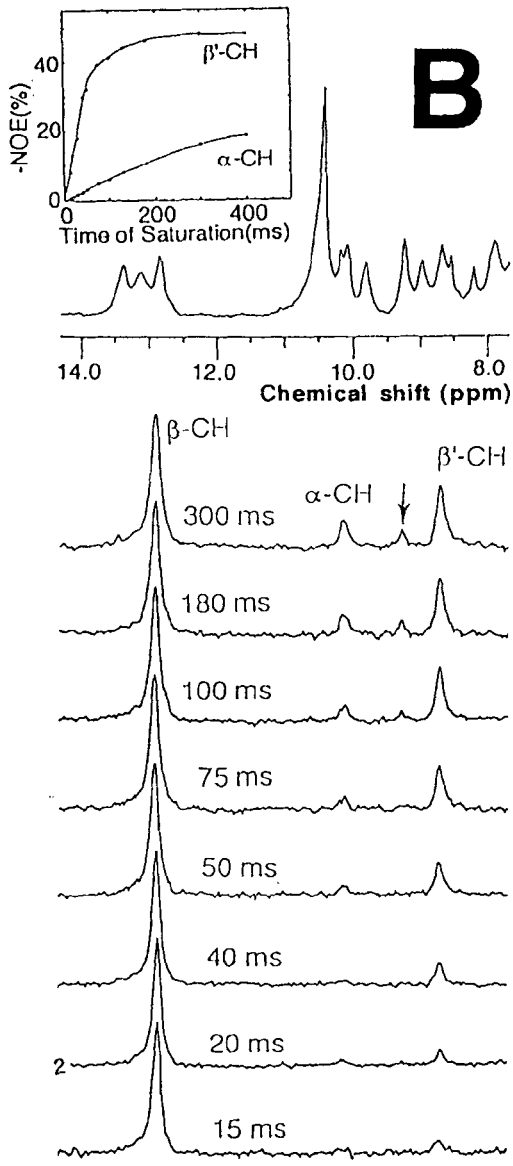

Fig. 22. continued
β'-proton signals are indicated in the inset. The initial build-up slopes provide σ values of -0.63 ± 0.03 and $-6.8 \pm 0.1\ s^{-1}$ for α- and β-protons, respectively. Peaks indicated by an arrow are due to a secondary NOE.[195]

between the 1-Me- and 2-α-protons through Eq. (34). This distance corresponds to ψ values of about $-40°$ and $-140°$ in Fig. 21C. The NOE build-up on the 6-α'- and 5-Me-proton signals upon saturation of the 6-α-proton signal is shown in Fig. 24. The time evolution of the NOE observed on the 6-α'- and 5-Me-proton signals, illustrated in the inset of Fig. 24, yields σ values of -0.47 ± 0.01 and $-0.020 \pm 0.005\ s^{-1}$ for the 6-α'- and 5-Me-protons, respectively. The substitution of these σ values, together with the internuclear distance between the geminal protons, into Eq. (34) yield the value of 0.30 ± 0.01 nm for the distance between the 5-Me- and 6-α-protons, which corresponds to ζ values of about $-70°$ and $+110°$ in Fig. 21D. Thus, analysis of interproton distances leads to two possible conformations for these haem peripheral side-chains owing to the symmetric nature of these fragments. The analysis of hyperfine shifts provides complementary structural information to that obtained from the analysis of the interproton distances.[195] For example, in the case of the vinyl side-chain, the difference in the δ_{para} value between the β-CH_2 geminal protons is primarily attributed to that in their δ^M_{pc} values.[131] Using the principal magnetic axes determined for this protein,[131] the δ^M_{pc} values for the 2-β_{trans}- and 2-β_{cis}-proton signals as a function of ψ can be calculated and the difference in their shifts, $\delta^M_{pc}(\beta_{trans}) - \delta^M_{pc}(\beta_{cis})$, is plotted against ψ in Fig. 25. The shift difference of -0.13 ppm, i.e. δ_{obs} and δ_{dia} values are -2.6 and 5.85 ppm, respectively, for the β_{trans}-proton signal and -3.0 and 5.58 ppm, respectively, for the β_{cis}-proton signal, yields ψ values of $-36°$ and $+10°$ in Fig. 25. Consequently a ψ value of about $-40°$ satisfies the results from the analysis of both the NOE and the δ_{para} data. However, in the analysis of the haem propionate conformation, the δ_c values of the 6-α- and 6-α'-proton signals are interpreted in terms of the angle ζ using Eqs. (4) and (5). Since δ_c generally dominates for their δ_{para} values, the larger contact shift for the 6-α than for the 6-α' signal indicates that the θ value for the 6-α-proton is smaller than that of the 6-α'-proton. Hence the value of $+10°$ for ζ is consistent with the results obtained from the analysis of the NOE and the δ_{para} data. Thus, combined analysis of both interproton distances and hyperfine shifts leads to the specific determination of the haem side-chain conformations.

Fig. 23. Time-dependent NOEs observed upon saturation of 2-β_{trans}-proton signal of *Galeorhinus* met-cyano Mb at 45°C. The *Y*-scale for the 2-α- and 1-Me-proton signals is expanded by a factor of 10 and these signals are apodized with a larger line broadening factor to improve the signal-to-noise ratio. Peaks labelled by an asterisk are due to off-resonance saturation. The time evolution of the NOEs observed for the 1-Me-, 2-α- and 2-β_{cis}-proton signals are indicated in the inset. The initial build-up slopes provide σ values of -0.090 ± 0.01 and $-1.3 \pm 0.1\ s^{-1}$ for 1-Me- and 2-β_{cis}-protons, respectively. The fact that the initial NOE build-up slope for 2-α-proton signal vanishes at $t > 0$ indicates that the NOE for this proton is secondary. Peaks indicated by an arrow are due to a secondary NOE.[195]

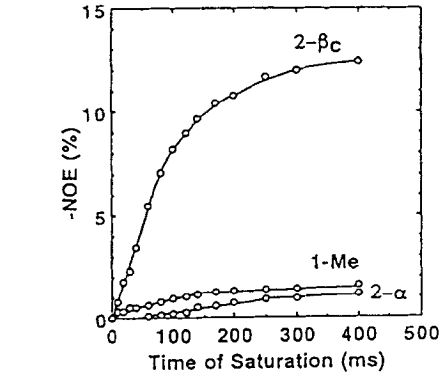
15
10
5
0
-NOE (%)
2-βc
1-Me
2-α
0
100
200
300
400
500
Time of Saturation (ms)

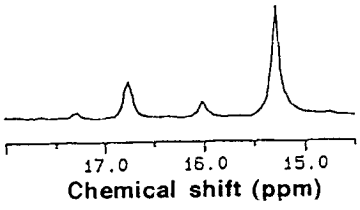
17.0
16.0
15.0
Chemical shift (ppm)

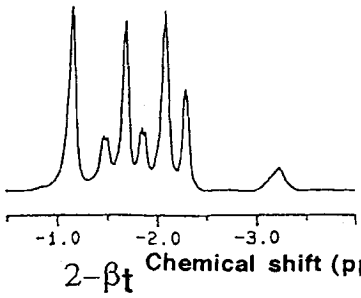
-1.0
-2.0
-3.0
2-βt
Chemical shift (ppm)

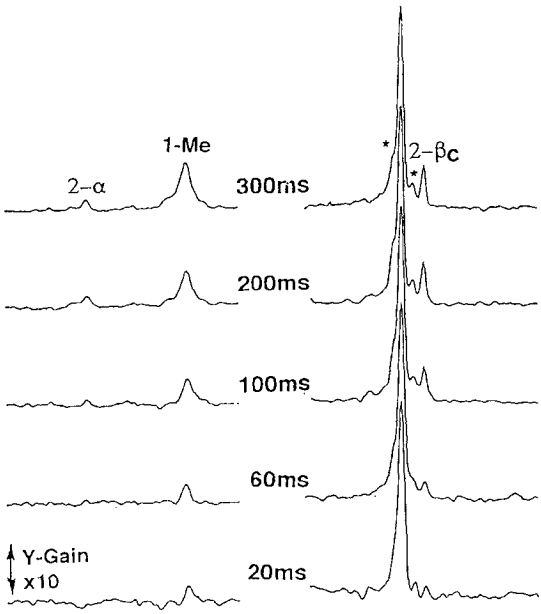
1-Me
2-α
300ms
*
2-βc
200ms
100ms
60ms
Y-Gain
x10
20ms

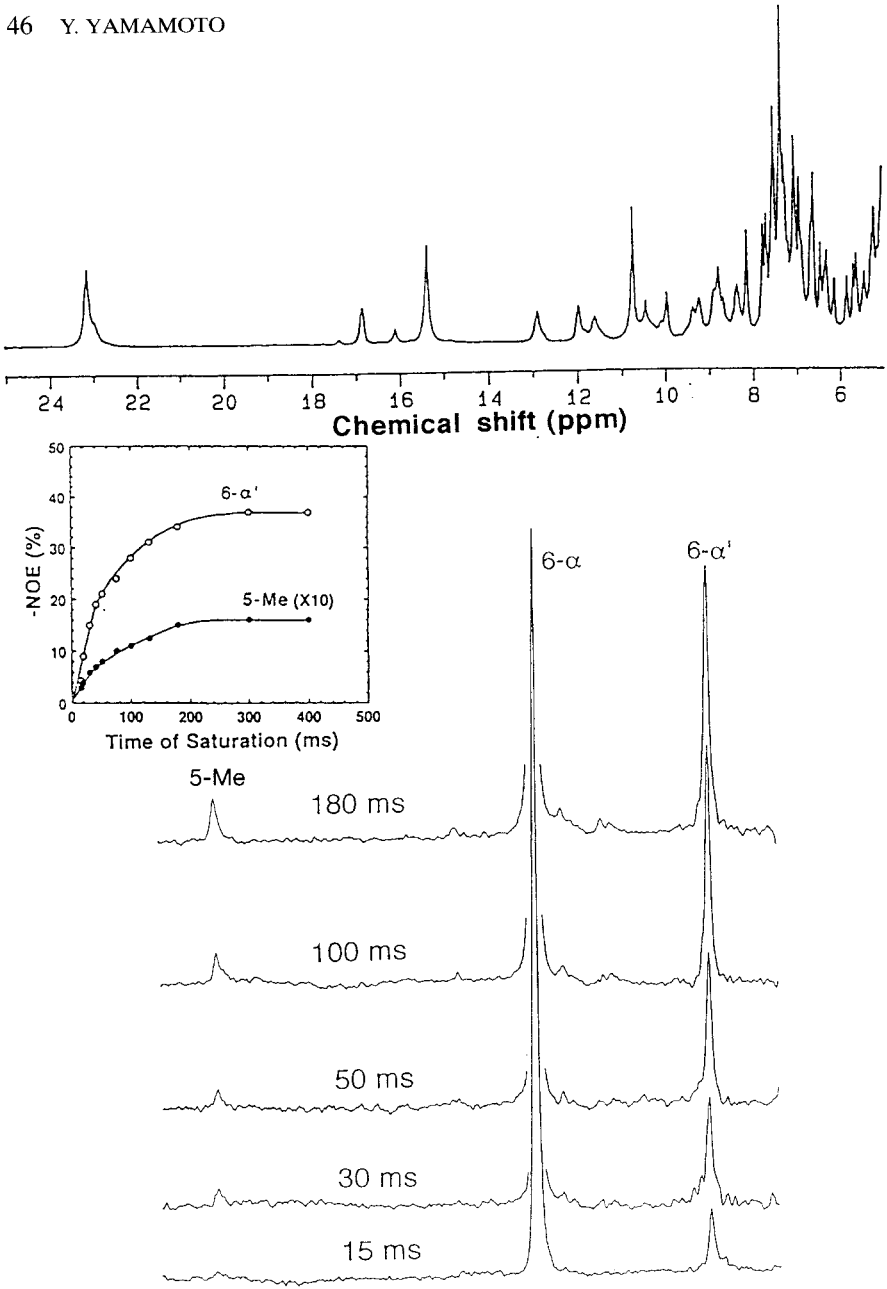

Fig. 24. Time-dependent NOE observed upon saturation of 6-α-proton signal of *Galeorhinus* met-cyano Mb at 45°C. In the difference spectra, the intensity of the 6-α-proton signal is kept constant. The time evolution of the NOEs observed on the 6-α'- and 5-Me-proton signals is illustrated in the inset. The initial build-up slopes provide σ values of -0.47 ± 0.01 and $-0.020 \pm 0.005\ s^{-1}$ for 6-α'- and 5-Me-protons, respectively.[195]

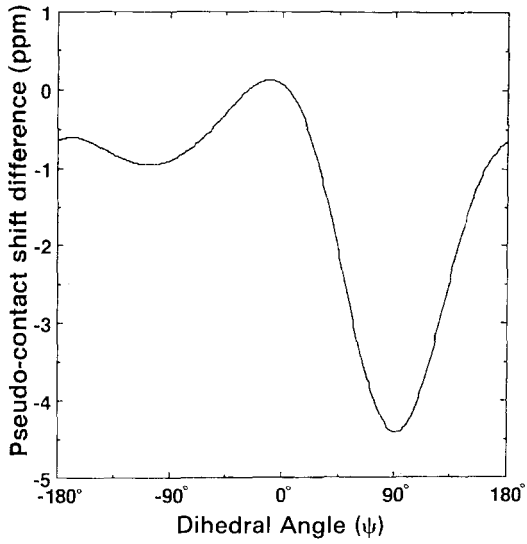

Fig. 25. Plot of ψ versus the difference in the metal-centred pseudo-contact shift, $\delta^{M}_{pc}(2\text{-}\beta_{trans}) - \delta^{M}_{pc}(2\text{-}\beta_{cis})$.[195]

6. HAEM POCKET DYNAMICS

Proteins possess a variety of internal motions about an equilibrium structure and such fluctuations appear to be relevant to their functional properties. Mb is a typical example, in this respect, since X-ray crystallography does not reveal any pathways for ligand entry in oxygen-binding haemoproteins; therefore, structural fluctuations are essential for the accommodation of ligands in the binding sites of these proteins. NMR studies of paramagnetic haemoproteins have been utilized in detailed analyses of a variety of dynamic processes of the haem pocket with a time scale spanning 10^{-12}–10^{7} s.

6.1. Reorientation of haem about its pseudo-C_2 axis

Perhaps one of the most striking results obtained from the NMR study of paramagnetic haemoproteins is the discovery of the "haem orientation disorder" (Fig. 26), which demonstrates that *b*-type haemoprotein exists as a mixture of isomers, i.e. the protein is structurally inhomogeneous.[325] The haem is incorporated into the haem pocket at the final step of biosynthesis of *b*-type haemoproteins. This process can be easily carried out *in vitro* by mixing apoprotein and haem. The kinetic analysis of this reaction, i.e. reconstitution

of *b*-type haemoprotein, indicates that the reaction between haem and apoprotein yields native holoprotein within a time scale of a millisecond.[326,327] Since X-ray studies have strongly supported the unique orientation of the haem in the protein, the reaction of the haem with apoprotein has been thought to proceed in a specific manner and to yield the native holoprotein instantaneously. The solution ^{1}H NMR spectra of both native and reconstituted paramagnetic Mbs, however, reveal that the reaction of the haem and apoprotein initially yields ~1:1 mixture of two isomers and both components are still present in the native protein.[325,328] The time course of the ^{1}H NMR spectrum of reconstituted protein demonstrates that one form is converted to the other, thermodynamically favoured, form and the rate at which the equilibrium mixture is attained is on the hour or day rather than the millisecond time scale as originally thought. Structural identification of two isomers initially formed from the reaction of the haem with apoprotein has been carried out based on the comparison of haem methyl hyperfine shift patterns for these isomers.[325] The high-frequency hyperfine shifted portion of the ^{1}H NMR spectrum of freshly reconstituted sperm whale met-azido Mb (Fig. 27), exhibited twice the number of haem methyl peaks as observed in the native protein (trace 27A). Comparison between the two spectra yields a clear differentiation of the resonances arising from the two forms. The unambiguous assignments of the individual haem resonances were obtained using the reconstitution of the apoprotein with haemins specifically deuterated at positions of the 1-Me and 3-Me or the 1-Me and 5-Me groups (see traces 27C

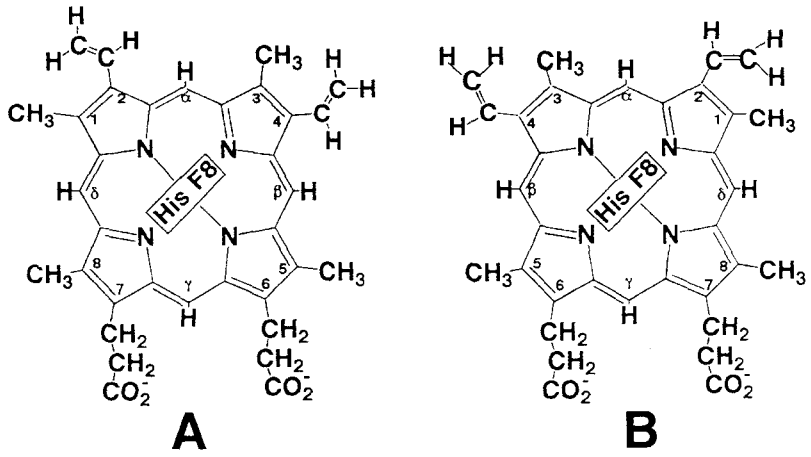

Fig. 26. Orientation of haem relative to the His F8 imidazole plane viewed from the proximal side: (A) as found in the crystal structure[67] and (B) rotated by 180° about α, γ-*meso* axis.

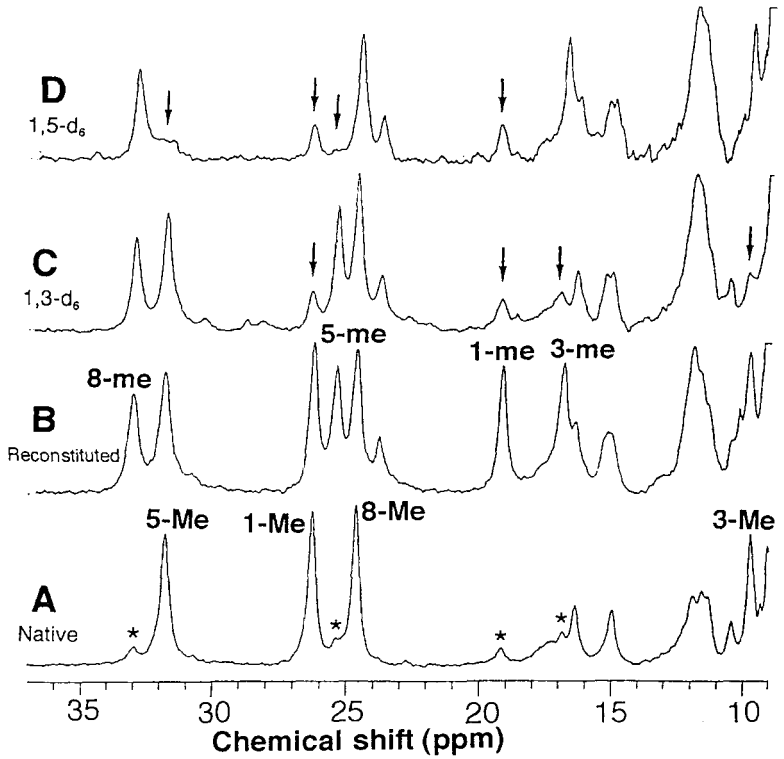

Fig. 27. Haem methyl proton signal assignments for freshly reconstituted sperm whale met-azido Mb. High-frequency hyperfine shifted portions of the 360 MHz ^{1}H NMR spectra of sperm whale met-azido Mb in ^2H_2O at 25°C. (A) Native Mb, p^{2}H 7.5; (B) freshly reconstituted Mb, p^{2}H 7.4; (C) freshly reconstituted Mb with 1-Me and 3-Me deuterated haemin, p^{2}H 7.3; and (D) freshly reconstituted Mb with 1-Me and 5-Me deuterated haemin, p^{2}H 7.8. Peaks with reduced intensities due to deuteration are marked with an arrow. Peaks indicated by an asterisk in (A) originate from the reversed haem in the native protein.[329]

and 27D).[329] The peaks that disappear in both traces 27C and 27D are attributed to the 1-Me proton. In contrast, the peaks present in both traces are assigned to the 8-Me proton. The other two peaks that disappear in traces 27C and 27D are assigned to the 3-Me and 5-Me protons, respectively. As described in Section 5.2, the haem methyl hyperfine shift pattern for the major component is consistent with the haem orientation found in a single crystal (this isomer is called the native form). For another conformational state (the disordered form), the 5-Me and 8-Me signals appear at almost the same position as those for the 8-Me and 5-Me signals of the native form, i.e. the 5-Me and 8-Me signals exhibit pairwise exchange. Similar chemical shifts of the 5-Me

signal of the native form (or the disordered form) and of the 8-Me signal of the disordered form (or the native form) indicates that these methyl groups are in similar chemical environments. However, the 1-Me and 3-Me signals from both forms are not quite related by pairwise exchange as observed between the 5-Me and 8-Me signals. This means that the 1-Me and 3-Me groups are in different chemical environments in the individual forms of the protein. These results can be interpreted on the basis of symmetry of haem. The haem molecular structure has a pseudo-twofold rotation axis passing through the α, γ-*meso* axis. Simple 180° rotation about this axis places the 5-Me group in the chemical environment previously held by the 8-Me group and vice versa. Therefore, a pairwise exchange relationship appears between 5-Me and 8-Me signals. Since the rotation only exchanges the position of the 1-Me $\leftrightarrow$ 4-vinyl and the 3-Me $\leftrightarrow$ 2-vinyl groups, perfect exchange of the chemical environments between the 1-Me and 3-Me groups cannot be achieved by 180° rotation about the α, γ-*meso* axis. These results convincingly suggest the reversed haem orientation in the disordered form. The fact that the reconstituted protein with symmetric haems, protohaem III or XIII, shows only one set of haem methyl signals[330] is also supportive of this interpretation. In the case of Mb, this conclusion has been confirmed by the detection of NOE connectivities between the haem peripheral proton and amino acid proton resonances in the two forms.[331]

A ^{1}H NMR study of human adult haemoglobin (Hb A) further identified the degree of the haem orientation disorder within the individual subunits.[329,332,333] Similarly to the case for met-azido Mb, the ^{1}H NMR spectrum of reconstituted met-azido Hb A clearly demonstrates the doubling of the number of peaks compared with that in the spectrum of native met-azido Hb A (Fig. 28). Although random haem disorder in the subunits of Hb A yields 10 structural isomers involving permutation of haem orientations, the fact that only two sets of comparably intense methyl signals are observed in the initial product of the reconstitution of apoHb with haemin indicates that the hyperfine shift pattern in each subunit is determined solely by the haem orientation within that subunit. Therefore, the hyperfine shifts in met-azido Hb A appear not to detect any influence of a given haem orientation in one subunit with that of the haem orientation in another subunit. The fact that ^{1}H NMR spectrum of Hb A, which is quickly converted to the met-azido complex from oxy Hb A prepared from freshly drawn blood, indicates ~2% and ~10% disorder in the α and β subunits, respectively. The equilibration in met-aquo form (the equilibration rate in the met-aquo form is much larger than that in the met-azido form (see below)) results in the disappearance of the resonances arising from the disorder in the α subunit, while there is essentially no change for the disorder in the β subunit. Thus, freshly isolated oxy Hb A contains haem disorder in both subunits. The observation of the disorder in the α subunit in freshly prepared Hb A, which disappears when converted to met-aquo Hb A or stored for long periods of time as in oxy Hb A, suggests that more extensively

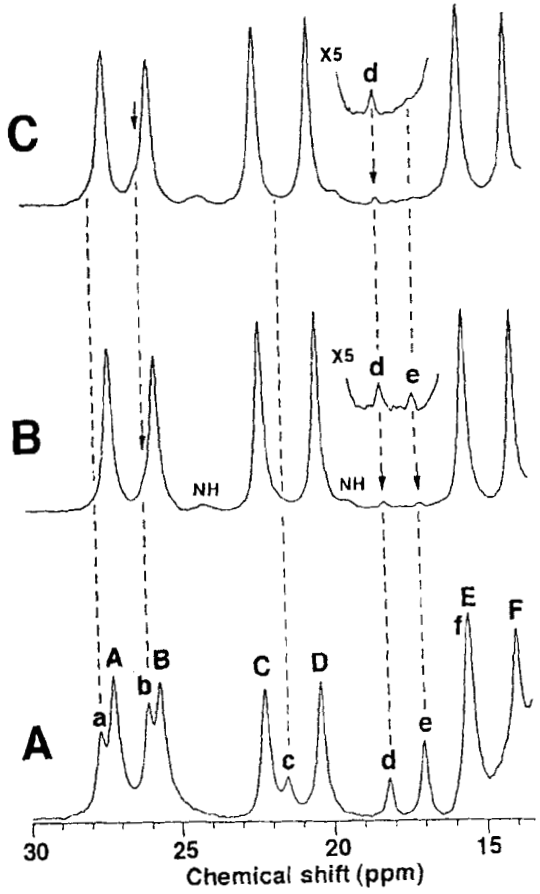

Fig. 28. High-frequency hyperfine shifted portions of the 360 MHz ^{1}H NMR spectra of native and reconstituted Hb A as the met-azido complex at 35°C. (A) Freshly reconstituted Hb A in ^2H_2O, p^{2}H 8.3. (B) Met-azido Hb A in H_2O, pH 8.03, prepared from freshly drawn blood. (C) Met-azido Hb A in H_2O, pH 8.03; Hb A isolated from freshly drawn blood was kept in the met-aquo form, pH 7.85, at 25°C for 20 hours and then azide was added. Peaks labelled NH are due to exchangeable protons. Signal assignments: A, 5-Me(α); B, 5-Me(β); C, 1-Me(α); D, 1-Me(β); E, 8-Me(α); F, 8-Me(β); a, 8-Me(α); b, 8-Me(β); c, 4-α(α); d, 4-α(β); e, 5-Me(α); f, 5-Me(β). α or β in parentheses indicates the subunit and signals A–F and a–f arise from the native and disordered forms, respectively. (Reprinted with permission from Ref. 332. © 1985 American Chemical Society.)

disordered Hb A exists *in vivo*. These results indicate that the disordered protein is initially formed in the biosynthesis of Hb A. The half-life for the haem reorientation of >30 days at 5°C in the physiologically active forms of Hb A, together with the known ~120-day lifetime of erythrocytes, permits the detection of the metastable states in blood. The spectrum in Fig. 28 demonstrates that a significant degree of equilibrium haem disorder exists within the β subunits.

Simple doubling of the number of peaks is not observed for the spectra of reconstituted deoxy, carbon monoxy, and met-cyano Hb A. But the presence of the 10 possible permutational isomers in disordered Hb A causes the loss of spectral resolution owing to the appearance of several shoulders and/or an increase in the line width. These results could be indicative of the haem–haem interaction, i.e., the environment of a given orientation in one subunit affects those of the other subunits.[333]

Although the molecular mechanism of the haem reorientation is not yet clear, it is obvious that there is not enough space within the active site of the protein for haem, with its diameter of >1.1 nm, to rotate about the pseudo-C_2 axis. Hence the rate of haem reorientation is likely to be related to the dynamic nature of the haem pocket. The analysis of the time dependence of the ^{1}H NMR spectra of reconstituted Mb and Hb A allows the determination of the rate of the interconversion from the disordered form to the native form.[333,334] The results obtained for Mb indicate that the reaction exhibits both acid- and base-catalyses with the minimum rate at neutral pH, and that the interconversion rate depends crucially on the type of haemin used, i.e. relative rates are 1:~12:~200 for protohaemin:mesohaemin:deuterohaemin.[334] Similar kinetic analyses for reconstituted Hb A demonstrate that the dynamics of equilibration are pH-dependent in both subunits in a fashion that allows selective equilibration in either subunit.[333] The pH value at the minimum rate differs for the two subunits, α (pH 7.5–7.7) and β (pH 6.7–6.8). The isoelectric points, p*I*, of the isolated α and β subunits of Hb A are 7.8 and 6.7, respectively.[335] Although these values cannot be determined for the individual subunits in Hb A, they are unlikely to be altered significantly in the tetramer assembly. Therefore, the pH values at the minimum rates for the two subunits are thought to reflect their effective isoelectric points in the tetramer. Since the interconversion rates in the two subunits are essentially the same at their minimum values, the inherent dynamic stabilities of the haem pocket are likely to be similar in the two subunits.

The rates are found to be quite different in met-aquo and met-azido Hb A, so that nonequilibrium mixtures of isomers can be kinetically trapped for periods of several months. The rate of interconversion in met-aquo Hb A is slightly higher than that in sperm whale met-aquo Mb at neutral pH. Replacement of H_2O by N_3^- decreases the rate by a factor of ~300 in Hb A. This ratio of the rates is essentially the same as found for the same two complexes of Mb. These results indicate that quaternary structure is not

important relative to the nature of the axial ligand in determining the rate of haem reorientation.

In sperm whale Mb, competition experiments between haem reorientation and haem replacements reveal that the former is slightly faster.[334] This is interpreted as indicating that reorientation of the haem involves an apparent unimolecular reaction, i.e. the haem dissociates from apoprotein but does not leave a protein "cage", and then haem is incorporated into the same haem pocket after rotation about the α, γ-*meso* axis. In Hb A, the rate of 10^{-4}–10^{-5} s^{-1} at pH 7 and 37°C has been reported for haem dissociation in the met-aquo form.[336] This is quite similar to the rate of the haem reorientation determined for the same complex. Thus the rate-determining step in haem reorientation in Hb A is most likely to be the dissociation of the subunit into haem and apoprotein. The significant decrease in the haem reorientation rate in low-spin bound Hb A is also consistent with the results that indicate that haem in oxy or met-cyano Hb A cannot be abstracted by another apoprotein within a time compatible with that of the stability of the apoprotein.[336]

The haem disorder is found to be present in most of the *b*-type haemoproteins studied by NMR,[127,192,325,328,337–348] with the equilibrium population of the two forms ranging from a few per cent to essentially a completely disordered system such as that found for *Chironomus* Hb[337] and rat cytochrome b_5,[338] which contain 40% and 45% haem disorder, respectively. The functional consequences of the disordered form varies with the protein. Two forms of sperm whale Mb exhibit essentially the same CO affinities,[349,350] while the Bohr effect of *Chironomus* Hb[351] and the redox potential of cytochrome b_5[352] are largely affected by the haem orientation. Furthermore, the rate of autoxidation is slightly higher for the disordered form than for the native form in both subunits of Hb A and the N_3^- affinity in the β subunit is significantly lower for the disordered form than for the native form.[353] The proximal His F8 $N_\delta H$ and distal His E7 $N_\varepsilon H$ proton resonances for the two forms of sperm whale met-cyano Mb are observed separately. Analysis of the exchange kinetics of these labile protons by the saturation transfer method reveals that the exchange rate of the distal His E7 $N_\varepsilon H$ in the disordered form is 3–5 times higher than that in the native form, while the rate for the proximal His F8 $N_\delta H$ proton is essentially unchanged in the two forms. Since the breaking of the hydrogen bond between the distal His E7 $N_\varepsilon H$ proton and the bound ligand is likely to be a rate-determining step for the exchange reaction, the higher rate of the distal His $N_\delta H$ proton exchange for the disordered form indicates that the hydrogen bond between the distal His and the ligand is weaker in the disordered form. The detailed structural comparison between the two forms of the protein reveals that the rotation of haem about the α, γ-*meso* axis causes not only alterations in the contact between the haem peripheral side-chains of pyrroles I and II and the protein, but also the slide of the haem relative to the surrounding protein. Therefore, considering the structure–function relationship in haemoprotein, these structural differences

between the two forms are likely to result in an alteration of functional properties. In the case of tetrameric Hb, the molecular mechanism of cooperativity has been proposed to involve transmission of structural information among subunits by altering the contacts between Val FG5 and the 4-vinyl group of haem.[353,354] Therefore, the replacement of the 4-vinyl group by the smaller 1-Me group due to the haem rotation alters this important contact considerably and hence leads to a significant change in cooperativity. Thus, a complete understanding of this haem orientational disorder in Hb A is highly relevant to the interpretation of the physicochemical measurements made on not only reconstituted Hb A but also native Hb A. Additionally, a difference in patterns of haem peripheral proton shifts between the two haem orientations within haemoprotein may provide further insight into the electronic and magnetic environments of the haem pocket.

Various native and genetically prepared apoproteins were reconstituted with a wide variety of chemically modified haems in order to gain insight into the effects of the haem orientation on the haem–protein contacts and the haem electronic structure.[289,321,322,330,334,340–342,355–369] The studies indicate that a repulsive interaction between haem vinyl groups and the protein is the major determinant for controlling the haem orientations.[361] Additionally, besides the haem orientational disorder due to 180° rotation about the α, γ-*meso* axis, a new type of haem disorder involving rotation about a N–Fe–N axis has been discovered in cytochrome-b_5 reconstituted with monopropionate haemin.[362]

6.2. Rotation of haem about the iron–His bond

Fe(III) meso-tetraalkylporphyrins with methyl (TMeP(Fe^{3+})), ethyl (TEtP(Fe^{3+})), or n-propyl groups (TPr^{n}P(Fe^{3+})) can be incorporated into apoMb,[270,282] and the CO binding kinetics of the reconstituted proteins have been characterized.[285] A ^{1}H NMR spectrum of met-cyano Mb containing TMeP(Fe^{3+}) exhibits only a single resonance for the eight pyrrole protons, which is an indication of the absence of in-plane asymmetry of the electronic structure of the porphyrin ring. Since in-plane asymmetry of the electronic structure of the porphyrin in haemoprotein is largely accounted for by the fixed orientation of the axial ligands (see Section 5.2), this result can be interpreted as rapid rotation of either the axial imidazole or the porphyrin ring about the iron–His F8 bond, which results in the eight pyrrole protons becoming magnetically equivalent to give a single resonance owing to motional averaging of the spin delocalization over the porphyrin ring. The appearance of only a single resonance for the pyrrole protons of bisimidazole adduct of Fe(III) tetraphenylporphyrin has been attributed to free rotation of the axial

ligands.[370] In the case of Mb, however, the rotation of the His F8 imidazole with respect to the porphyrin ring about the iron–His F8 bond is restricted by the covalent linkage. Consequently, the in-plane symmetric nature of the electronic structure of the porphyrin ring in the met-cyano complex of Mb containing TMeP(Fe^{3+}) has been attributed to the presence of dynamic rotational motion of the porphyrin ring about the iron–His F8 bond. As the bulkiness of the alkyl side-chain increases, multiple signals emerge for the pyrrole protons because of poor motional averaging of in-plane asymmetry of the unpaired electron delocalization.[270] This indicates that the rotation of the porphyrin ring about the iron–His F8 bond is largely hindered by steric interaction between the haem peripheral side-chains. Multiple signals for the pyrrole protons, observed in the spectrum of reconstituted Mb with TEtP(Fe^{3+}) or TPrP(Fe^{3+}), merge into a single peak at ~60°C, confirming the presence of free rotation of the prosthetic group about the Fe–N(His F8) bond within the protein. Similar rotational motion of the prosthetic group has also been found for sperm whale Mb reconstituted with Fe(III) porphine.[287] These results suggest that incorporation of these modified haemins totally disrupts the highly specific haem–globin interaction, making the prosthetic haem mobile in the protein.

The rotational motion of haem about the Fe–N(His F8) bond is found to be affected by modulation of the salt bridges between the haem propionate groups and the protein.[285,288,289,360–363] NMR spectra of sperm whale and horse met-cyano Mbs reconstituted with a synthetic haemin, heptamethyl-monopropionate-porphine-iron(III), have been studied in order to characterize the relative importance of the two haem propionate salt bridges to the protein matrix in determining the equilibrium orientation preference.[288] Two sets of hyperfine shifted resonances are observed in the spectra of the reconstituted proteins. There are two positions available for the single propionate group of this haemin to form salt bridges: one is the position where the salt bridge with the interior FG3 residue (His for both Mbs) is possible and the other is the position where the propionate group is close to the surface CD3 residue (Arg for sperm whale Mb and Lys for horse Mb) to form the salt bridge. Therefore, the two positions for the sole propionate group of the haem interexchange with each other by a 180° rotation of the haem about the α, γ-*meso* axis. NOE connectivities between the haem methyl groups and amino acid side-chains determine the orientation of a given haem incorporated into an essentially unperturbed haem pocket. Based on the signal intensities for the resonances arising from the two forms, the preference for occupying the position of the salt bridge to FG3 over that of the other position for the salt bridge to CD3 is found to be ~1:2 for the sperm whale protein and ~3:2 for the horse protein. Therefore, the haem propionate–Lys CD3 salt bridge in horse Mb is less stable by ~2.7 kJ/mol than the propionate–Arg CD3 interaction in sperm whale Mb.[288] Additionally, the hyperfine shifted

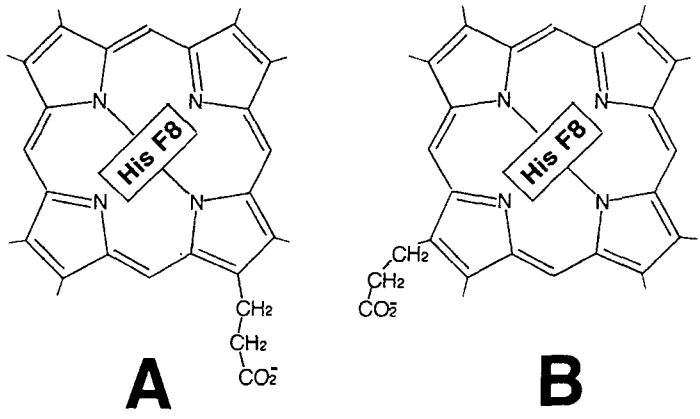

Fig. 29. Two different orientations of a synthetic haemin, heptamethyl-monopropionate-porphine-iron(III), relative to the His F8 imidazole plane viewed from the proximal side. The interconversion between (A) and (B) involves 90° rotational hopping of the haem about the iron–His bond.[288]

resonances in the spectra of the haem oriented isomer with a propionate situated as A in Fig. 29 exhibit anomalous line broadening with increasing temperature. This is indicative of exchange in the slow-exchange limit.[288] Analysis of the qualitative pattern of the exchange broadening among the five resolved methyl resonances identifies the isomers that interexchange between the two haem orientations illustrated in Fig. 29. Each of the monopropionate haemins reveals that the orientational isomer with a propionate situated at A in Fig. 29 is in dynamic equilibrium ($\sim 10^3\ s^{-1}$) with the orientation given in Fig. 29B. The interconversion involves simply a 90° rotational hopping of the haem about the iron–His bond, and this process is found to be significantly faster in horse Mb than in sperm whale Mb. Similar rotational hopping of the haem about the intact Fe–N(His F8) has been observed for the products of reconstitution of sperm whale apoMb with a series of synthetic haemins possessing a wide variety of substitution patterns for two and three propionate groups on the methyl-containing haem periphery.[289] In reconstituted Mbs with coprohaemin-type derivatives, hopping rates of $1–10\ s^{-1}$ at ambient temperature are found from measurements of saturation transfer factors and selective relaxation rates.[321] Quantitative analysis of variable-temperature data for a coprohaemin complex yields an activation barrier of ~4.1 kJ/mol. The results are consistent with a unimolecular process. The rate of rotational hopping of the despropionate haemin is found to be ~3 times higher than for sperm whale met-cyano Mb, confirming that the propionate residue–CD3 salt bridge is more stable for the Arg CD3 in sperm whale Mb than the Lys CD3 in horse Mb.

Table 2. The internal mobility of haem peripheral and His F8 side-chains in various paramagnetic haemoproteins.

Protein	Molecular Mass (kDa)	τ_r(ns)	Fragment	τ(ns)	Reference
Sperm whale met-cyano Mb	17	11	2-Vinyl $C_\beta H_2$	2.5	55
Sperm whale met-cyano Mb			His F8 $C_\beta H_2$	8	377
Bovine ferricytochrome b_5	13	10	7-Propionate $C_\alpha H_2$	8	198
Horseradish peroxidase CN^- complex	44	21	7-Propionate $C_\alpha H_2$	20	205
			His F8 $C_\beta H_2$	21	206
Shark met-cyano Mb	17	11	2-Vinyl $C_\beta H_2$	1.9	131
			2-Vinyl $C_\alpha H$-$C_\beta H_c$	1.9	131
			4-Vinyl $C_\beta H_2$	2.4	131
			His F8 $C_\beta H_2$	3.6	131
Shark met-cyano Mb	17	11	6-Propionate $C_\alpha H_2$	11.3	186
			7-Propionate $C_\alpha H_2$	11.7	186
Shark met-azido Mb			6-Propionate $C_\alpha H_2$	8.7	193
			7-Propionate $C_\alpha H_2$	5.1	193
Dolabella met-cyano Mb	17	11	2-Vinyl $C_\beta H_2$	1.5	127
			6-Propionate $C_\alpha H_2$	5.4	127
			6-Propionate $C_\beta H_2$	3.7	127
			7-Propionate $C_\beta H_2$	4.2	127

6.3. Mobility of haem peripheral side-chains

NMR has been utilized extensively to characterize the internal fluctuations of the haemoproteins. NMR relaxation studies[371–374] facilitate the quantitative determination of the internal motion of specific groups. Particularly, ^{2}H NMR quadrupolar relaxation measurements on the proteins reconstituted with ^{2}H-labelled haemins provide information about the dynamic nature of the haem as well as of the haem peripheral side-chains.[375,376] One of the advantages of using ^{2}H NMR relaxation data for characterizing haem molecular motion in haemoproteins arises from the dominance of the quadrupolar relaxation process, even in paramagnetic systems, although ambiguity in quadrupolar coupling constants may hamper a quantitative interpretation.

Time-dependent NOE studies provide the internal motion of the haem peripheral side-chain groups and the side-chain of the coordinated His residue.[55,127,131,186,193,198,205,206,377] NOEs are observed with a variety of saturation times (or t_m in NOESY) and are analysed with Eqs. (21)–(26). The τ_c value for an interproton vector, with a known r, can be calculated from σ using Eq. (22) or Eq. (25), and the values reported for paramagnetic haemoproteins are summarized in Table 2. The τ_c value for the overall Mb motion has been reported to be about 10 ns.[371–373,378] The immobility of haem in Mb is confirmed from the observation that haem exhibits a similar τ_c value.

6.4. Internal mobility of amino acid side-chains

The side-chain ring proton signals for the highly conserved Phe residue at CD1 in Mb are resolved in the high-frequency hyperfine shifted region of the spectrum of sperm whale met-cyano Mb.[379] The two $C_\varepsilon H$ proton signals of Phe CD1 remain degenerate to give a single peak over the temperature range 5–45°C, but this peak broadens considerably at lower temperature, demonstrating that the motional averaging of these proton signals is in the regime of rapid exchange on the NMR time scale. A quantitative estimate of exchange contributions to the line width of the average $C_\varepsilon H$ proton resonances of the ring, as a function of temperature, yields a ring reorientation rate of $\sim 10^5\ s^{-1}$ at 25°C and an activation barrier of 3.3 ± 1 kJ/mol.[379] The barrier is consistent with a low activation process indicative of local concerted structural fluctuations of the CD corner.

The mobility of the $C_\gamma H_2$ group of Gln E7 in shark met-cyano Mb has been analysed from time-dependent NOE measurements.[194] The τ_c value of 3.1 ns obtained for this fragment indicates that the Gln E7 side-chain possesses some conformational mobility, even if its $N_\varepsilon H$ proton is hydrogen-bonded to the Fe-bound CN^-. The shift difference of about 2.5 ppm between the Gln E7 $C_\gamma H_2$ geminal proton signals suggests that the amplitude of librational motion of the $C_\gamma H_2$ methylene group is relatively small.

6.5. Labile proton exchange of proximal and distal amino acid residues

The exchange of a labile proton buried in the protein matrix results from low activation energy fluctuations of the structure that expose its site transiently to the solvent. The rate (k) of such an exchange can be measured by the saturation transfer method as described in Section 5.4. In the case of met-cyano Mb, labile proton signals arising from the His F8 $N_\delta H$ and amide NH protons and an NH proton that is hydrogen-bonded to Fe-bound CN^- are generally resolved in the high-frequency hyperfine shifted region.[68,194,302–304,316] Since their $^{sel}T_1 (= \rho^{-1})$ values are 10–150 ms, k values of $1–10^3\ s^{-1}$ can be determined through the saturation factor using Eq. (32). The rate profiles of Arg E10 NH and His F8 $N_\delta H$ protons in *Dolabella* met-cyano Mb are compared with those for the His E7 $N_\varepsilon H$ and His F8 $N_\delta H$ of horse met-cyano Mb in Fig. 30.[316] The behaviour of the His residues is informative for the mechanism of hydrogen exchange, as H^+ (or H_3O^+) and OH^- catalyses involve an attack at different positions of the neutral imidazole side-chain. Acid attack necessarily proceeds at the free nitrogen; in contrast, base-catalysed exchange requires a direct attack of OH^- at the nitrogen that carries a proton. The NH exchange rate profiles for the two different types of His imidazole rings in horse Mb clearly reflect such reaction mechanisms (see Fig. 30). Since His F8 imidazole is coordinated to the haem iron, its $N_\delta H$ exchange rate is not affected by

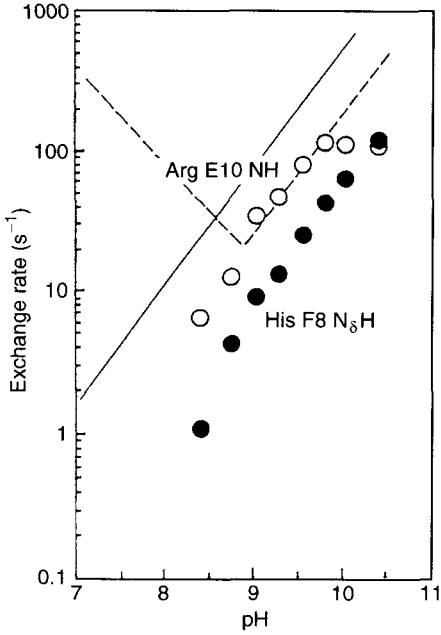

Fig. 30. Plot of the exchange rates as a function of pH at 30°C for Arg E10 NH (open circles) and His F8 N_δH (filled circles) in *Dolabella* met-cyano Mb. The rate profiles[68] for His E7 N_εH and His F8 N_δH protons of horse met-cyano Mb at 40°C are indicated by broken and continuous lines, respectively, for comparison.[316]

acid-catalysis and increases monotonically with pH. On the other hand, the profile of His E7 imidazole NH shows both acid- and base-catalyses with a minimum rate appearing near to neutral pH. In the case of the Arg side-chain NH proton exchange, only base-catalysed exchange is operative.[380]

In the spectra of deoxy Mb and Hb, the His F8 N_δH proton signals are resolved at 60–80 ppm (see Fig. 31).[222,381–386] The exchange of this proton in Hb A is relatively slow (10^{-4}–10^{-5} s^{-1}), so that the kinetics can be followed directly through the measurement of the signal intensity as a function of time after dilution of the sample with H_2O.[387,388] The studies reveal that the exchange rates in the two different subunits in Hb tetramer are different from each other. Furthermore, the rates for the two subunits in the R quaternary structure are found to be much larger than those in the T state. Since the exchange of these protons takes place through the EX_2 mechanism,[389] this result indicates that the dynamic nature of the haem cavities of the individual subunits is closely related to the quaternary structure of Hb.

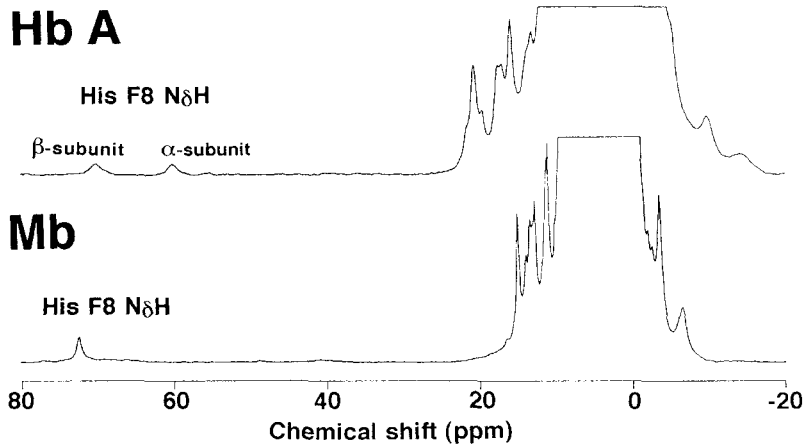

Fig. 31. The 400 MHz ^1H NMR spectra of sperm whale deoxy Mb (pH 6.41) and deoxy Hb A (pH 6.44) in 90% H_2O/10% ^2H_2O at 44.5°C. His F8 $N_\delta H$ proton signal is observed at 60–80 ppm.

7. DYNAMICS AND THERMODYNAMICS

7.1. Acid–alkaline transition

The acid–alkaline transition in ferric Mb has been of importance in understanding the structure–function relationship of Mb because it reflects the characteristics of the structural and ligand-binding properties of the haem active site. Upon changing from the acidic form to the alkaline form in the ferric state of mammalian Mb, the iron-bound ligand changes from H_2O to OH^- with concomitant change of the spin state from $S = 5/2$ to $S = 1/2$.[390] The rapid transition in mammalian Mb has been interpreted in terms of a protonation/deprotonation process of the distal His imidazole bound to the iron-bound ligand via a hydrogen bond (see Fig. 32, Type I).[391] In contrast, the Mbs from the sea hare *Aplysia limacina*,[185] the sharks *Galeorhinus japonicus*[243] and *Musterus japonicus*,[188] and the mollusc *Dolabella auricularia*[188] exhibit a relatively slow transition, which has been attributed to the absence of bound H_2O in the acidic form (Fig. 32, Type II). Hence, the acid–alkaline transition in these Mbs leads to simultaneous changes in both the coordination and the spin states of the haem iron. The thermodynamics of the acid–alkaline transition in ferric haemoproteins have been analysed in detail using a variety of physicochemical methods. But the kinetics of the transition have not been fully investigated because of the lack of a methodology to yield quantitative kinetic parameters. The saturation transfer experiment allows quantitative

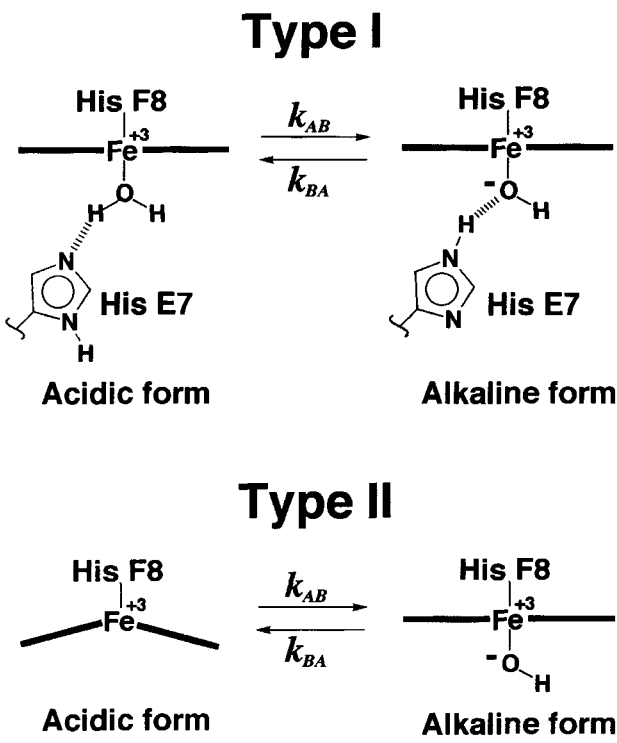

Fig. 32. The acid–alkaline transition in hexacoordinated metMb (type I) and pentacoordinated metMb (type II).

characterization of the kinetics of the acid–alkaline transition in Mb, provided that the transition rate is comparable to the paramagnetic relaxation rate of the haem peripheral side-chain proton of ferric Mb.[187,188,236] Saturation of haem methyl proton signals of the acidic form exhibits clear saturation transfer to the corresponding methyl signal of the alkaline form, as shown in Fig. 33, Hence, the haem methyl proton assignments can easily be obtained for the alkaline form from the known assignments for the acidic form. Similarly to the determination of the labile proton exchange rate (Section 5.4), the transition rate between the two exchanging states can be calculated from the saturation transfer factor and the selective spin–lattice relaxation time ($^{sel}T_1$) using Eq. (32). Equation (31) implies that the detection of the saturation factor I/I_0 is easier for the signal with the smallest value of ρ (longest $^{sel}T_1$) between the two forms if k_{AB} and k_{BA} are comparable with each other. Additionally, the adjustment of the pH value of the sample is necessary to remove one of the components so that the $^{sel}T_1$ value, which is free from the effect of the transition, can be obtained. Once either one of the reaction rates is determined,

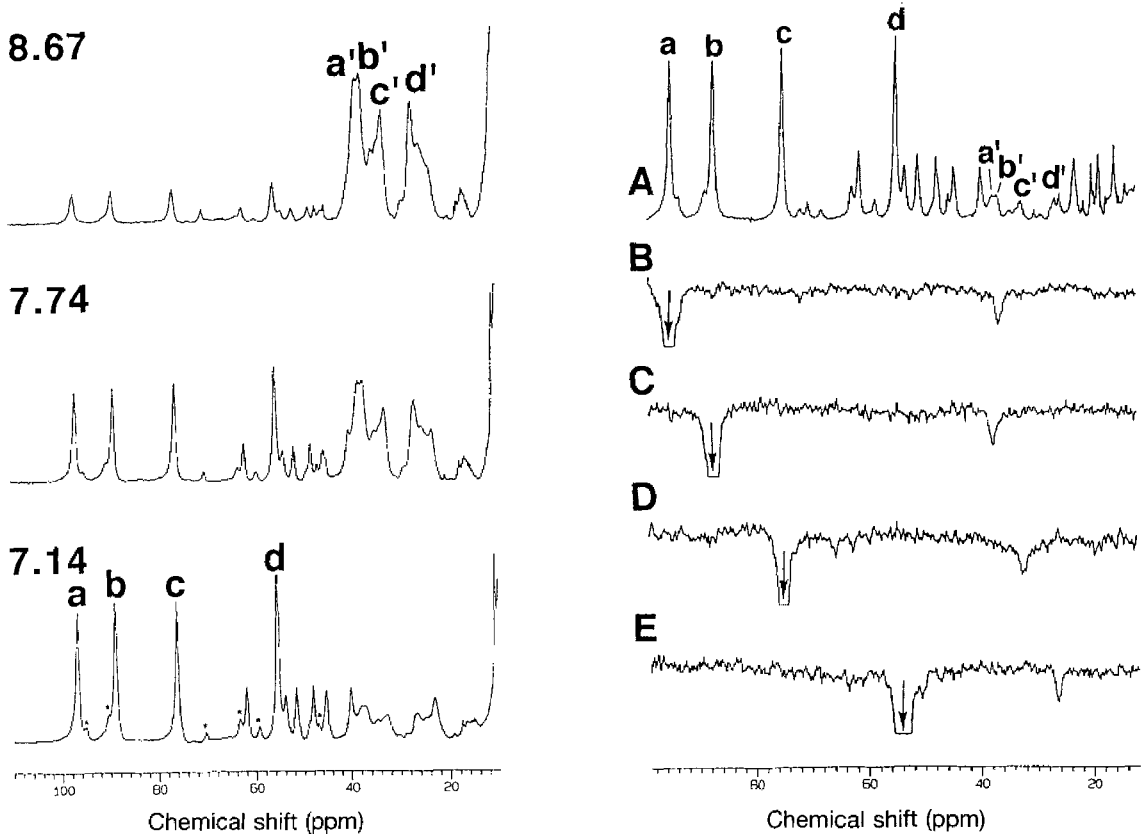

Fig. 33. High-frequency hyperfine shifted portions of the 500 MHz ^{1}H NMR spectra of *Dolabella* metMb in ^2H_2O. *Left*: pH dependence at 30°C. *Right*: Saturation-transfer difference spectra at 35°C and p^{2}H 6.9. (A) reference spectrum and saturation of a, 8-Me (B); b, 5-Me (C); c, 3-Me (D); d, 1-Me (E). The connectivities provide the assignments of haem methyl proton signals of met-hydroxyl form; a′, 5-Me; b′, 8-Me; c′, 3-Me; d′, 1-Me.[236]

the other can be calculated from the equilibrium constant ($=k_{AB}/k_{BA}$), which is manifested in the ratio of the signal intensities for the two forms.[188] The temperature dependence study of these kinetic data yielded the activation energy for the transition, which is related to the stabilization of the iron-bound OH^- in Mb.[188]

7.2. Redox potentials of tetrahaem protein

Cytochrome c_3 is a relatively small protein (molecular mass ~14 kDa) which carries four *c*-type haem groups. This protein is involved in the electron-transport system as a partner of hydrogenase in bacteria. Owing to the presence of four redox centres within a molecule, five macroscopic oxidation states appear during the redox process from the fully oxidized state to the fully reduced state. Additionally, in the states between these two extreme macroscopic oxidation states, the scrambling of electron(s) among the haems yields 14 different redox species. Therefore a total of 32 microscopic formal potentials can be defined between these 16 redox species. Paramagnetic NMR techniques have been utilized extensively to investigate the redox process of this protein and to characterize the degree of oxidation of each haem, for which the redox potential is influenced by interaction with the other haems.[232,392–406] Haem methyl proton signals are sensitive to the oxidation state of the haem iron and hence can be used as probe signals to monitor the redox process of the protein. The fact that the hopping rate of electron(s) between the haems is higher than the relevant NMR time scale in the intermediate redox states results in the observation of only one set of the signals for each of the five macroscopic oxidation states. Therefore, their intensities sharply reflect the concentration of each species and their shifts remain essentially constant throughout the reduction process. The saturation transfer experiment allows the identification of a particular resonance in the five different macroscopic oxidation states and the probability of the electron distribution at each haem in the individual oxidation states is estimated directly from the chemical shifts.[393–399,405] Furthermore, 32 microscopic reduction potentials are estimated from the combined analyses of both the electron distribution probability derived from the shift data and the macroscopic redox potentials measured by electrochemical methods.[395]

7.3. Stability of protein folding

Irrespective of the presence of unpaired electron(s), the signal arising from a His imidazole NH proton that is buried in the protein matrix and involved in an internal hydrogen bond is largely deshielded and resolved outside of the diamagnetic envelope.[407] Two such His side-chain NH proton signals in

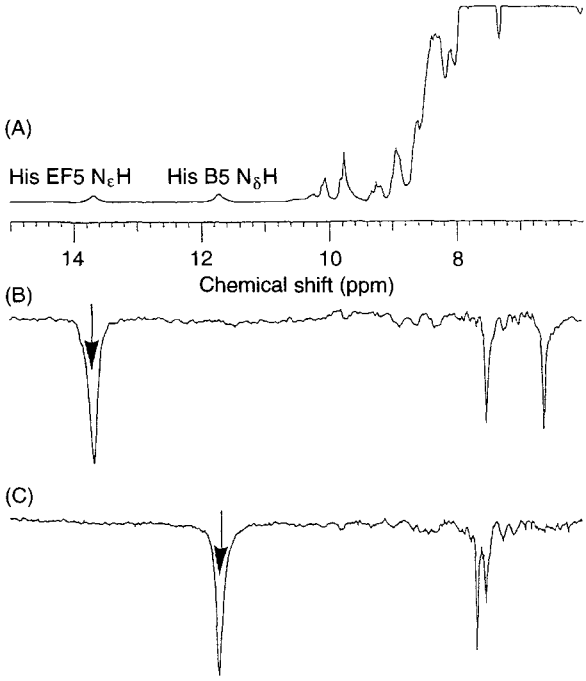

Fig. 34. The high-frequency portions of the 400 MHz ^1H NMR spectrum of sperm whale carbon monoxy Mb in 90% H_2O/10% ^2H_2O, pH 8.46, at 35°C. The NOE difference spectra result from saturation of the His EF5 $N_\varepsilon H$ (B) and His B5 $N_\delta H$ (C) proton signals. The peaks at 6.54 and 7.46 ppm in (B) arise from the His EF5 $C_\delta H$ and $C_\varepsilon H$ protons, respectively, and those at 7.47 and 7.61 ppm in (C) from the His B5 $C_\varepsilon H$ and amino NH protons, respectively.[408]

mammalian Mbs have been assigned.[408,409] One is the signal for His B5 $N_\delta H$ proton, which is located in a unique triad hydrogen-bonding network, Asp B1–His B5–His GH1. In this network, the $N_\varepsilon H$ proton of His GH1 is hydrogen-bonded to the N_ε of His B5 and the $N_\delta H$ proton of His B5 interacts with the peptide carbonyl oxygen of Asp B1.[296] These hydrogen bonds contribute to the structural stabilization of the interface between the B helix and the GH corner. The other is the signal for the His EF5 $N_\varepsilon H$ proton, which is hydrogen-bonded to O_δ of Asp H18.[296] This hydrogen bond stabilizes the interface between the EF corner and the H helix. The signal assignments have been based on the spectral comparison and 1D NOE measurements (see Fig. 34). Their resonance frequencies indicate that the exchange rate of these protons is $\ll 3 \times 10^3\ s^{-1}$. Their line widths are sensitive to temperature, pH and the concentration of denaturant. The comparison of the pH-dependent line width of the His EF5 $N_\varepsilon H$ proton signal between horse and sperm whale carbon

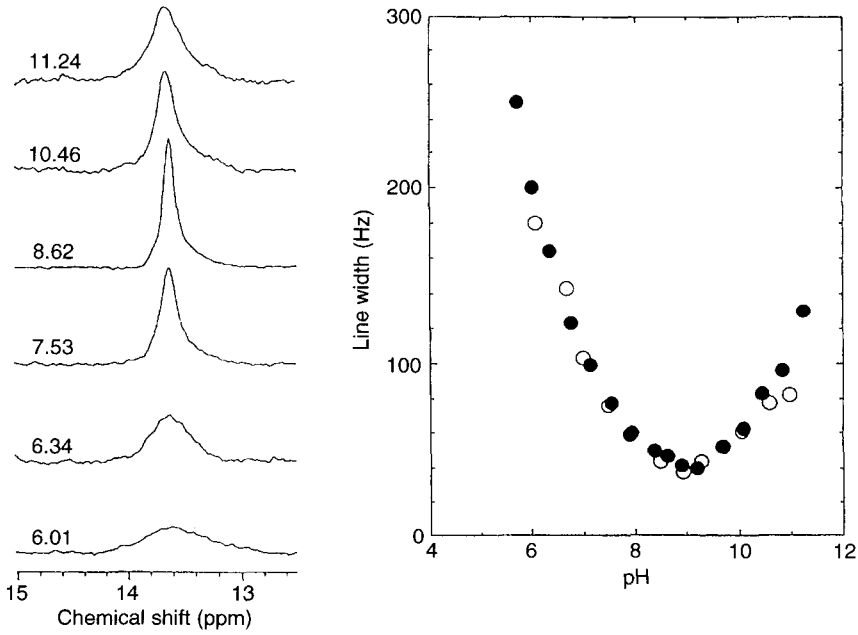

Fig. 35. The signal of His EF5 $N_\varepsilon H$ proton of horse carbon monoxy Mb in 90% H_2O/10% ^2H_2O at 25°C and the indicated pH (left) and plot of the line width for the signal of horse (filled circles) and sperm whale (open circles) Mbs against pH (right).[408]

monoxy Mbs reveals that the exchange rates of this proton in these proteins are essentially identical, suggesting the similarity in the structural stability of the EF–H interface between the two Mbs (see Fig. 35).[408] The effects of the addition of a denaturant, guanidine hydrochloride, on these His NH proton signals of sperm whale carbon monoxy Mb are illustrated in Fig. 36. Both the NH proton signals are shifted to low frequency and are broadened with an increase in the denaturant concentration, although no significant shift change is observed for the other signals of these imidazole rings.[408] The differential exchange broadening of these resonances, induced by the addition of the denaturant, is in sharp contrast to the results from the temperature-dependent study, which demonstrate that both of the signals are similarly broadened with increasing temperature. These results strongly suggest that the hydrogen bond between His EF5 and Asp H18 is more susceptible to the denaturant than that between Asp B1 and His B5. Thus the analyses of these His NH proton resonances provide useful information about local conformation, which in turn relates to the protein folding. A similar structural study using His imidazole NH proton signals as probes should be possible for other proteins.

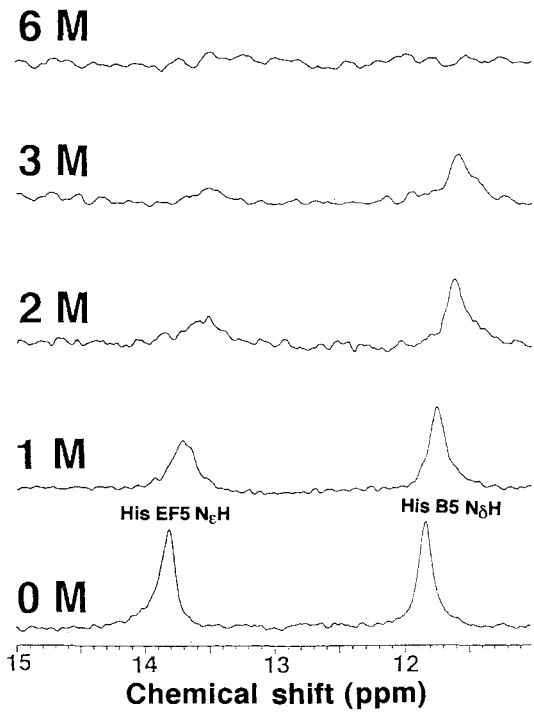

Fig. 36. The high-frequency portions of the 400 MHz ^1H NMR spectra of sperm whale carbon monoxy Mb in 90% H_2O/10% ^2H_2O, pH 8.65, at 25°C in the presence of the indicated concentration of guanidine hydrochloride.[408]

ACKNOWLEDGEMENT

This work was supported by University of Tsukuba, Research Projects.

REFERENCES

1. O. Jardetzky and G. C. K. Roberts, *NMR in Molecular Biology*, Academic Press, New York, 1981.
2. K. Wüthrich, *Struct. Bonding*, 1970, **8**, 53.
3. G. N. La Mar, in *NMR of Paramagnetic Molecules, Principles and Applications* (ed. G. N. La Mar, W. Dew. Horrocks, Jr and R. H. Holm), Ch. 3, Academic Press, New York, 1973.
4. J. S. Morrow and F. R. N. Gurd, *CRC Crit. Rev. Biochem.*, 1975, **3**, 221.
5. R. G. Shulman, in *ESR and NMR of Paramagnetic Species in Biological and Related Systems* (ed. I. Bertini and R. S. Drago), p. 135, Reidel, New York, 1979.
6. K. Wüthrich, *NMR in Biological Research: Peptide and Proteins*, Ch. 6, North-Holland, Amsterdam, 1976.

7. I. Morishima, S. Ogawa, T. Inubushi and T. Iizuka, *Adv. Biophys.*, 1978, **11**, 217.
8. G. N. La Mar, in *Biological Application of Magnetic Resonance* (ed. R. G. Shulman), p. 305, Academic Press, New York, 1979.
9. R. M. Keller and K. Wüthrich, in *Biological Magnetic Resonance*, Vol. 3 (ed. L. J. Berliner and J. Reuben), p. 1, Plenum Press, New York, 1981.
10. C. Ho and I. M. Russu, *Methods Enzymol.*, 1981, **76**, 278.
11. H. M. Goff, in *Iron Porphyrins*, Part 1 (ed. A. B. P. Lever and H. B. Gray), p. 239, Addison-Wesley, Reading, Mass., 1983.
12. J. D. Satterlee, *Annu. Rep. NMR Spectrosc.*, 1986, **17**, 79.
13. J. D. Satterlee, *Metal Ions Biol. Syst.*, 1986, **21**, 121.
14. I. Bertini and C. Luchinat, *NMR of Paramagnetic Molecules in Biological Systems*, Benjamin/Cummings, Menlo Park, CA, 1986.
15. I. Bertini, P. Turano and A. J. Vila, *Chem. Rev.*, 1993, **93**, 2833.
16. F. A. Walker and U. Simonis, in *Biological Magnetic Resonance*, Vol. 12 (ed. L. J. Berliner and J. Reuben), p. 133, Plenum Press, New York, 1993.
17. J. D. Satterlee, S. Alam, Q. Yi and J. E. Erman, in *Biological Magnetic Resonance*, Vol. 12 (ed. L. J. Berliner and J. Reuben), p. 275, Plenum Press, New York, 1993.
18. J. Mispelter, M. Momenteau and J. Lhoste, in *Biological Magnetic Resonance*, Vol. 12 (ed. L. J. Berliner and J. Reuben), p. 299, Plenum Press, New York, 1993.
19. C. Luchinat and S. Ciurli, in *Biological Magnetic Resonance*, Vol. 12 (ed. L. J. Berliner and J. Reuben), p. 357, Plenum Press, New York, 1993.
20. I. Bertini and C. Luchinat, *Coord. Chem. Rev.*, 1996, **150**, 1.
21. L. Banci, M. Piccioli and A. Scozzafava, *Coord. Chem. Rev.*, 1992, **120**, 1.
22. A. T. Smith, P. Du and G. H. Loew, in *Nuclear Magnetic Resonance of Paramagnetic Macromolecules* (ed. G. N. La Mar), p. 75, Kluwer Academic Publishers, Dordrecht, 1995.
23. J. S. de Ropp, L. P. Yu and G. N. La Mar, *J. Biomol. NMR*, 1991, **1**, 175.
24. G. N. La Mar and J. S. de Ropp, in *Biological Magnetic Resonance*, Vol. 12 (ed. L. J. Berliner and J. Reuben), p. 1, Plenum Press, New York, 1993.
25. A. V. Xavier, D. L. Turner and H. Santos, *Method Enzymol.*, 1993, **227**, 1.
26. S. W. Unger, J. T. J. Lecomte and G. N. La Mar, *J. Magn. Reson.*, 1985, **64**, 521.
27. J. T. J. Lecomte, S. W. Unger and G. N. La Mar, *J. Magn. Reson.*, 1991, **94**, 112.
28. I. Bertini, F. Capozzi, C. Luchinat and P. Turano, *J. Magn. Reson.*, 1991, **95**, 244.
29. D. L. Turner, *J. Magn. Reson. A*, 1993, **104**, 197.
30. L. Banci, in *Biological Magnetic Resonance*, Vol. 12 (ed. L. J. Berliner and J. Reuben), p. 79, Plenum Press, New York, 1993.
31. I. Bertini, C. Luchinat, M. Piccioli and D. Tarchi, *Concepts Magn. Reson.*, 1994, **6**, 307.
32. M. Sette, A. Desider, G. Rotilio and M. Paci, *J. Magn. Reson.*, 1994, **B105**, 91.
33. C. Luchinat and M. Piccioli, in *Nuclear Magnetic Resonance of Paramagnetic Macromolecules* (ed. G. N. La Mar), p. 1, Kluwer Academic, Dordrecht, 1995.
34. G. N. La Mar, Z. Chen and J. S. de Ropp, in *Nuclear Magnetic Resonance of Paramagnetic Macromolecules* (ed. G. N. La Mar), p. 55, Kluwer Academic, Dordrecht, 1995.
35. S. L. Alam, D. P. Dutton and J. D. Satterlee, in *Nuclear Magnetic Resonance of Paramagnetic Macromolecules* (ed. G. N. La Mar), p. 123, Kluwer Academic, Dordrecht, 1995.
36. Z. Wang and L. Que, Jr, in *Nuclear Magnetic Resonance of Paramagnetic Macromolecules* (ed. G. N. La Mar), p. 193, Kluwer Academic, Dordrecht, 1995.
37. L. Banci and R. Oierattelli, in *Nuclear Magnetic Resonance of Paramagnetic Macromolecules* (ed. G. N. La Mar), p. 281, Kluwer Academic, Dordrecht, 1995.
38. Y. K. Chae, B. Xia, H. Cheng, B.-H. Oh, L. Skjeldal, W. M. Westler and J. L. Markley, in *Nuclear Magnetic Resonance of Paramagnetic Macromolecules* (ed. G. N. La Mar), p. 297, Kluwer Academic, Dordrecht, 1995.
39. A. J. Macedo and J. G. Moura, in *Nuclear Magnetic Resonance of Paramagnetic Macromolecules* (ed. G. N. La Mar), p. 319, Kluwer Academic, Dordrecht, 1995.

40. G. N. La Mar, T. Jue, K. Nagai, K. M. Smith, Y. Yamamoto, R. J. Kauten, V. Thanabal, K. C. Langry, R. K. Pandey and H.-K. Leung, *Biochim. Biophys. Acta*, 1987, **952**, 131.
41. R. J. Gupta and A. G. Redfield, *Science*, 1970, **169**, 1204.
42. J. Trewhella, P. E. Wright and C. A. Appleby, *Nature (London)*, 1980, **180**, 87.
43. C. Yu, S. W. Unger and G. N. La Mar, *J. Magn. Reson.*, 1986, **67**, 346.
44. H. Santos and D. L. Turner, *FEBS Lett.*, 1986, **194**, 73.
45. Y. Yamamoto and N. Fujii, *Chem. Lett.*, 1987, 1703.
46. Y. Yamamoto, *FEBS Lett.*, 1987, **222**, 115.
47. B. G. Jenkins and R. B. Lauffer, *J. Magn. Reson.*, 1988, **80**, 328.
48. R. Timkovich, *Inorg. Chem.*, 1991, **30**, 37.
49. L. Banci, W. Bermel, C. Luchinat, R. Pierattelli and D. Tarchi, *Magn. Reson. Chem.*, 1993, **31**, s3.
50. I. Bertini, A. Dikiy, C. Luchinat, M. Piccioli and D. Tarchi, *J. Magn. Reson.*, 1994, **B103**, 278.
51. I. Bertini, C. Luchinat, R. Macinai, M. Piccioli, A. Scozzafava and M. S. Viezzoli, *J. Magn. Reson.*, 1994, **B104**, 95.
52. I. Bertini, F. Capozzi, C. Luchinat, M. Piccioli and A. J. Vila, *J. Am. Chem. Soc.*, 1994, **116**, 651.
53. L. Banci, I. Bertini and C. Luchinat, *Methods Enzymol.*, 1994, **239**, 485.
54. R. D. Johnson, S. Ramaprasad and G. N. La Mar, *J. Am. Chem. Soc.*, 1983, **105**, 7205.
55. S. Ramaprasad, R. D. Johnson and G. N. La Mar, *J. Am. Chem. Soc.*, 1984, **106**, 3632.
56. S. Ramaprasad, R. D. Johnson and G. N. La Mar, *J. Am. Chem. Soc.*, 1984, **106**, 5330.
57. F. W. Teal, *Biochim. Biophys. Acta*, 1959, **35**, 543.
58. F. Ascoli, M. R. R. Fanelli and E. Antonini, *Methods Enzymol.*, 1981, **48**, 177.
59. T. Yonetani and T. Asakura, *J. Biol. Chem.*, 1968, **243**, 4715.
60. R. Makino and I. Yamazaki, *Arch. Biochem. Biophys.*, 1973, **157**, 356.
61. R. Makino and I. Yamazaki, *Arch. Biochem. Biophys.*, 1974, **165**, 485.
62. H. Yamada, R. Makino and I. Yamazaki, *Arch. Biochem. Biophys.*, 1975, **169**, 344.
63. M. Sono and T. Asakura, *J. Biol. Chem.*, 1976, **250**, 5227.
64. T. Inubushi and T. Yonetani, *Methods Enzymol.*, 1981, **76**, 88.
65. R. Makino, T. Iizuka, K. Sakaguchi and Y. Ishimura, in *Oxygenases and Oxygen Metabolism* (ed. M. Nozaki, S. Yamamoto, Y. Ishimura, M. J. Coon, L. Ernster and W. R. Estabrook), p. 467, Academic Press, New York, 1982.
66. C. Ho and J. R. Perussi, *Methods Enzymol.*, 1994, **232**, 97.
67. R. E. Dickerson and I. Geis, *Hemoglobin: Structure, Function, Evolution and Pathology*, Benjamin/Cummings, New York, 1983.
68. J. T. J. Lecomte and G. N. La Mar, *Biochemistry*, 1985, **24**, 7388.
69. G. N. La Mar, H. Toi and R. Krishnamoorthi, *J. Am. Chem. Soc.*, 1988, **106**, 6395.
70. D. A. Case and M. Karplus, *J. Mol. Biol.*, 1979, **132**, 343.
71. P. George, J. Beetlestone and J. S. Griffith, *Rev. Mod. Phys.*, 1964, **36**, 441.
72. J. Beetlestone and P. George, *Biochemistry*, 1964, **3**, 707.
73. T. Iizuka and M. Kotani, *Biochim. Biophys. Acta*, 1968, **154**, 417.
74. T. Iizuka and M. Kotani, *Biochim. Biophys. Acta*, 1969, **181**, 295.
75. T. Iizuka and M. Kotani, *Biochim. Biophys. Acta*, 1969, **194**, 351.
76. J. P. Jesson, in *NMR of Paramagnetic Molecules, Principles and Applications* (ed. G. N. La Mar, W. Dew. Horrocks, Jr and R. H. Holm), Ch. 1, Academic Press, New York, 1973.
77. G. N. La Mar and F. A. Walker, in *The Porphyrins* (ed. D. Dolphin), Ch. 2, Academic Press, New York, 1979.
78. J. D. Satterlee, *Concepts Magn. Reson.*, 1990, **2**, 69.
79. J. D. Satterlee, *Concepts Magn. Reson.*, 1990, **2**, 119.
80. K. J. Kurland and B. R. McGarvey, *J. Magn. Reson.*, 1970, **2**, 286.
81. H. M. McConnel and R. E. Robertson, *J. Chem. Phys.*, 1958, **29**, 1361.

82. I. Bertini and P. Turano, in *Nuclear Magnetic Resonance of Paramagnetic Macromolecules* (ed. G. N. La Mar), p. 29, Kluwer Academic, Dordrecht, 1995.
83. H. M. McConnel, *J. Chem. Phys.*, 1956, **24**, 764.
84. A. D. McLachlan, *Mol. Phys.*, 1958, **1**, 233
85. Y. Yamamoto, *J. Magn. Reson.*, 1994, **B103**, 72.
86. H. M. McConnel and D. B. Chestnut, *J. Chem. Phys.*, 1958, **28**, 107.
87. Y. Yamamoto, K. Komori, N. Nanai, R. Chûjô and Y. Inoue, *J. Chem. Soc., Dalton Trans.*, 1992, 1813.
88. W. D. Horrocks and E. S. Greenberg, *Biochim. Biophys. Acta*, 1973, **322**, 38.
89. H. Hori, *Biochim. Biophys. Acta*, 1971, **251**, 227.
90. H. Hori and H. Morimoto, *Biochim. Biophys. Acta*, 1979, **200**, 581.
91. S. D. Emerson and G. N. La Mar, *Biochemistry*, 1990, **29**, 1556.
92. G. Williams, N. J. Clayden, G. R. Moore and R. J. P. Williams, *J. Mol. Biol.*, 1985, **183**, 447.
93. K. Rajarathnam, G. N. La Mar, M. L. Chiu and S. G. Sligar, *J. Am. Chem. Soc.*, 1992, **114**, 9048.
94. K. Rajarathnam, J. Qin, G. N. La Mar, M. L. Chiu and S. G. Sligar, *Biochemistry*, 1994, **33**, 5493.
95. X. Zhao, K. Vyas, B. D. Nguyen, K. Rajarathnam, G. N. La Mar, T. Li, G. N. Phillips, Jr, R. F. Eich, J. S. Olson, J. Ling and D. F. Bocian, *J. Biol. Chem.*, 1995, **270**, 20763.
96. J. Qin, G. N. La Mar, F. Ascoli and M. Brunori, *J. Mol. Biol.*, 1993, **231**, 1009.
97. N. C. Veitch, D. Whitford and R. J. P. Williams, *FEBS Lett.*, 1990, **269**, 297.
98. Y. Feng, Two-dimensional NMR study of the structure of ferricytochrome c, University of Pensylvania, 1989.
99. Y. Feng, H. Roder and S. W. Englander, *Biochemistry*, 1990, **29**, 3494.
100. P. X. Qi, R. A. Beckman and A. J. Wand, *Biochemistry*, 1996, **35**, 12275.
101. M. Gochin and H. Roder, *Protein Sci.*, 1995, **4**, 296.
102. Y. Gao, J. Boyd, G. J. Pielak and R. J. P. Williams, *Biochemistry*, 1991, **30**, 1928.
103. Y. Gao, G. McLendon, G. J. Pielak and R. J. P. Williams, *Eur. J. Biochem.*, 1992, **204**, 337.
104. R. Timkovich and M. Cai, *Biochemistry*, 1993, **32**, 11516.
105. G. N. La Mar, Z. Chen, K. Vyas and A. D. McPherson, *J. Am. Chem. Soc.*, 1995, **117**, 411.
106. Y. -H. Kao and J. T. J. Lecomte, *J. Am. Chem. Soc.*, 1993, **115**, 9754; *J. Am. Chem. Soc.*, 1994, **116**, 6991.
107. Y. Yamamoto, N. Nanai, Y. Inoue and R. Chûjô, *Bull. Chem. Soc. Jpn.*, 1989, **62**, 1771.
108. Y. Yamamoto, N. Nanai and R. Chûjô, *J. Chem. Soc., Chem. Commun.*, 1990, 1556.
109. M. Gueron, *J. Magn. Reson.*, 1975, **19**, 58.
110. A. J. Vega and D. Fiat, *Mol. Phys.*, 1976, **31**, 347.
111. I. Solomon, *Phys. Rev.*, 1955, **99**, 559.
112. N. Bloembergen, *J. Chem. Phys.*, 1957, **27**, 572.
113. N. Bloembergen and C. O. Morgan, *J. Chem. Phys.*, 1961, **34**, 842.
114. H. P. W. Gottieb, M. Barfield and D. M. Doddrell, *J. Chem. Phys.*, 1977, **67**, 3785.
115. D. M. Doddrell, P. C. Healy and M. R. Bendall, *J. Magn. Reson.*, 1978, **29**, 163.
116. H. Sternlicht, *J. Chem. Phys.*, 1965, **42**, 2250.
117. T. J. Swift, in *NMR of Paramagnetic Molecules, Principles and Applications* (ed. G. N. La Mar, W. Dew. Horrocks, Jr and R. H. Holm), Ch. 2, Academic Press, New York, 1973.
118. S. W. Unger, T. Jue and G. N. La Mar, *J. Magn. Reson.*, 1985, **61**, 448.
119. Y. Yamamoto, K. Iwafune, N. Nanai, A. Osawa, R. Chûjô and T. Suzuki, *Eur. J. Biochem.*, 1991, **198**, 299.
120. Y. Yamamoto, N. Nanai, R. Chûjô and Y. Inoue, *Bull. Chem. Soc. Jpn.*, 1991, **64**, 3199.
121. J. H. Noggle and R. E. Schirmer, *The Nuclear Overhauser Effect*, Academic Press, New York, 1971.
122. D. Neuhaus and M. Williamson, *The Nuclear Overhauser Effect in Structural and Conformational Analysis*, VCH, New York, 1989.

123. W. P. Aue, J. Karhan and R. R. Ernst, *J. Chem. Phys.*, 1976, **64**, 2229.
124. A. Kumar, R. R. Ernst and K. Wüthrich, *Biochem. Biophys. Res. Commun.*, 1980, **95**, 1.
125. S. D. Emerson and G. N. La Mar, *Biochemistry*, 1990, **29**, 1545.
126. D. H. Peyton, *Biochem. Biophys. Res. Commun.*, 1991, **175**, 515.
127. Y. Yamamoto and T. Suzuki, *Biochim. Biophys. Acta*, 1993, **1163**, 287.
128. S. J. McLachlan, G. N. La Mar and K.-B. Lee, *Biochim. Biophys. Acta*, 1988, **957**, 430.
129. Y. Yamamoto, A. Osawa, Y. Inoue and R. Chûjô, *FEBS Lett.*, 1989, **247**, 263.
130. L. P. Yu, G. N. La Mar and K. Rajarathnam, *J. Am. Chem. Soc.*, 1990, **112**, 9527.
131. Y. Yamamoto, K. Iwafune, N. Nanai, R. Chûjô, Y. Inoue and T. Suzuki, *Biochim. Biophys. Acta*, 1992, **1120**, 173.
132. J. Qin, G. N. La Mar, F. Ascoli, M. Bolognesi and M. Brunori, *J. Mol. Biol.*, 1992, **224**, 891.
133. J. Qin and G. N. La Mar, *J. Biomol. NMR*, 1992, **2**, 597.
134. K. Vyas, K. Rajarathnam, L. P. Yu, S. D. Emerson, G. N. La Mar, R. Krishnamoorthi and H. Mizukami, *J. Biol. Chem.*, 1993, **268**, 14826.
135. C. T. Allocatelli, F. Cutruzzolá, A. Brancaccio, M. Brunori, J. Qin and G. N. La Mar, *Biochemistry*, 1993, **32**, 6041.
136. W. Zhang, G. N. La Mar and K. Gerzonde, *Eur. J. Biochem.*, 1996, **237**, 841.
137. S. L. Alam and J. D. Satterlee, *Biochemistry*, 1994, **33**, 4008.
138. K. Rajarathnam, J. Qin, G. N. La Mar, M. L. Chiu and S. G. Sligar, *Biochemistry*, 1993, **32**, 5670.
139. J. Qin, G. N. La Mar, Y. Dou, S. J. Admiraal and M. Ikeda-Saito, *J. Biol. Chem.*, 1994, **269**, 1083.
140. Z. Chen, J. S. de Ropp, G. Hernández and G. N. La Mar, *J. Am. Chem. Soc.*, 1994, **116**, 8772.
141. J. S. de Ropp, G. N. La Mar, H. Wariishi and M. H. Gold, *J. Biol. Chem.*, 1991, **266**, 15001.
142. L. Banci, I. Bertini, P. Turano, M. Tien and K. Kirk, *Proc. Natl. Acad. Sci. USA*, 1991, **88**, 6956.
143. L. Banci, I. Bertini, E. A. Pease, M. Tien and P. Turano, *Biochemistry*, 1992, **31**, 10009.
144. L. Banci, I. Bertini, P. Turano, J. C. Ferrer and A. G. Mouk, *Inorg. Chem.*, 1991, **30**, 4510.
145. J. C. Ferrer, P. Turano, L. Banci, I. Bertini, I. K. Morris, K. M. Smith, M. Smith and A. G. Mauk, *Biochemistry*, 1994, **33**, 7819.
146. P. Turano, J. C. Ferrer, M. R. Cheesman, A. J. Thomson, L. Banci, I. Bertini and A. G. Mauk, *Biochemistry*, 1995, **34**, 13895.
147. Y. Feng, H. Roder and S. W. Englander, *Biochemistry*, 1989, **28**, 195.
148. J. Wu, G. N. La Mar, L. P. Yu, K.-B. Lee, F. A. Walker, M. L. Chiu and S. G. Sligar, *Biochemistry*, 1991, **30**, 2156.
149. J. D. Satterlee, D. J. Russel and J. E. Erman, *Biochemistry*, 1991, **30**, 9072.
150. L. Banci, I. Bertini, P. Turano and M. V. Oliver, *Eur. J. Biochem.*, 1992, **204**, 107.
151. H. S. Costa, H. Santos and D. L. Turner, *Eur. J. Biochem.*, 1993, **215**, 817.
152. L. Braushweiler and R. R. Ernst, *J. Magn. Reson.*, 1983, **53**, 521.
153. C. Griesinger, G. Otting, K. Wüthrich and R. R. Ernst, *J. Am. Chem. Soc.*, 1988, **110**, 7870.
154. L. Banci, I. Bertini, M. T. Cambria, F. Capozzi and A. Dikiy, *Eur. J. Biochem.*, 1994, **219**, 663.
155. L. Banci, I. Bertini, T. Bini, M. Tien and P. Turano, *Biochemistry, 1993*, **32**, 5825.
156. N. C. Veitch, R. J. P. Williams, N. M. Bone, J. F. Burke and A. T. Smith, *Eur. J. Biochem.*, 1995, **233**, 650.
157. K. L. Bren, H. B. Gray, L. Banci, I. Vertini and P. Turano, *J. Am. Chem. Soc.*, 1995, **117**, 8067.
158. S. C. Busse and T. Jue, *Biochemistry*, 1994, **33**, 10934.
159. G. W. Eich, G. Bodenhausen and R. R. Ernst, *J. Am. Chem. Soc.*, 1982, **104**, 3731.
160. A. Bax and G. Drobny, *J. Magn. Reson.*, 1985, **61**, 306.
161. S. Wimperis and G. Bodenhausen, *Mol. Phys.*, 1989, **66**, 897.

162. I. Bertini, C. Luchinat and D. Tarchi, *Chem. Phys. Lett.*, 1993, **203**, 445.
163. J. Qin, F. Delaglio, G. N. La Mar and A. Bax, *J. Magn. Reson. B.*, 1993, **102**, 332.
164. A. A. Maudsley and R. R. Ernst, *Chem. Phys. Lett.*, 1977, **50**, 368.
165. A. A. Maudsley, L. Muller, R. R. Ernst, *J. Magn. Reson.*, 1977, **28**, 463.
166. G. Bodenhausen and R. Freeman, *J. Magn. Reson.*, 1977, **28**, 471.
167. Y. Yamamoto, N. Nanai, Y. Inoue and R. Chûjô, *Biochem. Biophys. Res. Commun.*, 1988, **151**, 262.
168. Y. Yamamoto, N. Nanai, R. Chûjô and T. Suzuki, *FEBS Lett.*, 1990, **264**, 113.
169. L. Banci, I. Bertini, R. Pierattelli and A. J. Vila, *Inorg. Chem.*, 1994, **33**, 4338.
170. K. Wüthrich and R. Baumann, *Helv. Chim. Acta*, 1973, **56**, 585.
171. K. Wüthrich and R. Baumann, *Helv. Chim. Acta*, 1974, **57**, 336.
172. H. Goff, *J. Am. Chem. Soc.*, 1977, **99**, 7723.
173. H. Goff, *J. Chem. Soc., Chem. Commun.*, 1978, 777.
174. H. M. Goff, *Biochim. Biophys. Acta*, 1978, **542**, 348.
175. M. A. Phillipi and H. M. Goff, *J. Chem. Soc., Chem. Commun.*, 1980, 455.
176. H. M. Goff, *J. Am. Chem. Soc.*, 1981, **103**, 3714.
177. H. M. Goff, E. T. Shimomura and M. A. Phillipi, *Inorg. Chem.*, 1983, **22**, 66.
178. A. Shirazi, E. Leum and H. M. Goff, *Inorg. Chem.*, 1983, **22**, 360.
179. H. Santos and D. L. Turner, *Eur. J. Biochem.*, 1992, **206**, 721.
180. D. L. Turner, *Eur. J. Biochem.*, 1995, **227**, 829.
181. L. Banci, R. Pierattelli and D. L. Turner, *Eur. J. Biochem.*, 1995, **232**, 522.
182. D. L. Turner, C. A. Salguerio, P. Schenkels, J. LeGall and A. V. Xavier, *Biochim. Biophys. Acta*, 1995, **1246**, 24.
183. F. R. N. Gurd and T. M. Rothgeb, *Adv. Protein Chem.*, 1979, **33**, 73.
184. L. B. Dugad, G. N. La Mar and S. W. Unger, *J. Am. Chem. Soc.*, 1990, **112**, 1386.
185. U. Pande, G. N. La Mar, J. T. J. Lecomte, F. Ascoli, M. Brunori, K. M. Smith, R. K. Pandey, D. W. Parish and V. Thanabal, *Biochemistry*, 1986, **25**, 5638.
186. Y. Yamamoto, Y. Inoue, R. Chûjô and T. Suzuki, *Eur. J. Biochem.*, 1990, **189**, 567.
187. J. Qin, U. Pande, G. N. La Mar, F. Ascoli, P. Ascenzi, F. Cutruzzolá, C. Travaglini-Allocatelli and M. Brunori, *J. Biol. Chem.*, 1993, **268**, 24012.
188. Y. Yamamoto, T. Suzuki and H. Hori, *Biochim. Biophys. Acta*, 1993, **1203**, 267.
189. V. Thanabal, J. S. de Ropp and G. N. La Mar, *J. Am. Chem. Soc.*, 1986, **108**, 4244.
190. G. N. La Mar, S. D. Emerson, J. T. J. Lecomte, U. Pande, K. M. Smith, G. W. Craig and L. A. Kehres, *J. Am. Chem. Soc.*, 1986, **108**, 5568.
191. M. J. Chatfield, G. N. La Mar, W. O. Parker, Jr, K. M. Smith, H.-K. Leung and I. K. Morris, *J. Am. Chem. Soc.*, 1988, **110**, 6352.
192. D. H. Peyton, G. N. La Mar, F. Ascoli, K. M. Smith, P. K. Pandey, D. W. Parish, M. Bolognesi and M. Brunori, *Biochemistry*, 1989, **28**, 4880.
193. Y. Yamamoto, R. Chûjô and T. Suzuki, *Eur. J. Biochem.*, 1991, **198**, 285.
194. Y. Yamamoto and T. Suzuki, *Biochim. Biophys. Acta*, 1996, **1293**, 129.
195. Y. Yamamoto, *J. Chem. Soc., Dalton Trans.*, 1995, 3281.
196. J. T. J. Lecomte, G. N. La Mar, J. D. G. Smith, K. H. Winterhalter, K. M. Smith, K. C. Langry and H.-K. Leung, *J. Mol. Biol.*, 1989, **209**, 235.
197. D. H. Peyton, G. N. La Mar and K. Gersonde, *Biochim. Biophys. Acta*, 1988, **954**, 82.
198. S. J. McLachlan, G. N. La Mar and E. Sletten, *J. Am. Chem. Soc.*, 1986, **108**, 1285.
199. J. D. Satterlee and S. Moench, *Biophys. J.*, 1987, **52**, 101.
200. S. J. Moench, T.-M. Shi and J. D. Satterlee, *Eur. J. Biochem.*, 1991, **197**, 631.
201. I. Bertini, G. Gori, C. Luchinat and A. J. Vila, *Biochemistry*, 1993, **32**, 776.
202. S. J. Moench and J. D. Satterlee, *J. Biol. Chem.*, 1989, **264**, 9923.
203. K.-B. Lee, S. J. McLachlan and G. N. La Mar, *Biochim. Biophys. Acta*, 1996, **1208**, 22.
204. W. Shao, G. Liu, X. Huang, H. Wu and W. Tang, *Biochim. Biophys. Acta*, 1996, **1295**, 44.
205. V. Thanabal, J. S. de Ropp and G. N. La Mar, *J. Am. Chem. Soc.*, 1987, **109**, 265.

206. V. Thanabal, J. S. de Ropp and G. N. La Mar, *J. Am. Chem. Soc.*, 1987, **109**, 7516.
207. V. Thanabal, J. S. de Ropp and G. N. La Mar, *J. Am. Chem. Soc.*, 1988, **110**, 3027.
208. V. Thanabal and G. N. La Mar, *Biochemistry*, 1989, **28**, 7038.
209. N. C. Veitch, R. J. P. Williams, R. C. Bray, J. F. Burke, S. A. Sanders, R. N. F. Thorneley and A. T. Smith, *Eur. J. Biochem.*, 1992, **207**, 521.
210. L. B. Dugad, G. N. La Mar, H. C. Lee, M. Ikeda-Saito, K. S. Booth and W. S. Caughey, *J. Biol. Chem.*, 1990, **265**, 7173.
211. J. D. Satterlee and J. E. Erman, *Biochemistry*, 1991, **30**, 4398.
212. L. B. Dugad and H. M. Goff, *Biochim. Biophys. Acta*, 1992, **1122**, 63.
213. S. J. Moench, S. Chroni, B.-S. Lou, J. E. Erman and J. D. Satterlee, *Biochemistry*, 1992, **31**, 3661.
214. N. C. Veitch, R. J. P. Williams, R. C. Bray, J. F. Burke, S. A. Sanders, R. N. F. Thorneley and A. T. Smith, *Eur. J. Biochem.*, 1992, **207**, 521.
215. L. Banci, I. Bertini, T. Bini, M. Tien and P. Turano, *Biochemistry*, 1993, **32**, 5825.
216. L. Banci, I. Bertini, I.-C. Kuan, M. Tien, P. Turano and A. J. Vila, *Biochemistry*, 1993, **32**, 13483.
217. J. D. Satterlee, S. L. Alam, J. M. Mauro, J. E. Erman and T. L. Poulos, *Eur. J. Biochem.*, 1994, **224**, 81.
218. P. Turano, J. C. Ferrer, M. R. Cheesman, A. J. Thomson, L. Banci, I. Bertini and A. G. Mauk, *Biochemistry*, 1995, **34**, 13895.
219. S. L. Alam, J. D. Satterlee, J. M. Mauro, T. L. Poulos and J. E. Erman, *Biochemistry*, 1995, **34**, 15496.
220. N. C. Veitch, Y. Gao and K. G. Welinder, *Biochemistry*, 1996, **35**, 14370.
221. L. Banci, I. Bertini, S. Marconi and R. Pierattelli, *Eur. J. Biochem.*, 1993, **215**, 431.
222. Y. Yamamoto, K. Iwafune, R. Chûjô, Y. Inoue, T. Suzuki and K. Imai, *J. Biochem.*, 1992, **112**, 414.
223. A. Kalk and H. J. C. Berendsen, *J. Magn. Reson.*, 1976, **24**, 343.
224. A. J. Duben and W. C. Hutton, *J. Magn. Reson.*, 1990, **88**, 60.
225. R. R. Ernst, G. Bodenhausen and A. Wakaun, *Principles of Nuclear Magnetic Resonance in One and Two Dimensions*, Ch. 9, Clarendon Press, Oxford, 1987.
226. T. Suzuki and T. Kisamori, *Comp. Biochem. Physiol.*, 1984, **78B**, 163.
227. T. Suzuki, T. Suzuki and T. Yata, *Aust. J. Biol. Sci.*, 1985, **38**, 347.
228. T. Suzuki, *Biochim. Biophys. Acta*, 1987, **914**, 170.
229. A. A. Bothner-By, R. L. Stephens, J. Lee, C. D. Warren and R. W. Jeanloz, *J. Am. Chem. Soc.*, 1984, **106**, 811.
230. A. Bax and D. G. Davis, *J. Magn. Reson.*, 1985, **63**, 207.
231. U. Simonis, J. D. Dallas and F. A. Walker, *Inorg. Chem.*, 1992, **31**, 5349.
232. C. A. Salguerio, D. L. Turner, H. Santos, J. LeGall and A. V. Xavier, *FEBS Lett.*, 1992, **314**, 155.
233. R. M. Keller and K. Wüthrich, *Biochem. Biophys. Res. Commun.*, 1978, **83**, 1132.
234. H. Senn, R. M. Keller and K. Wüthrich, *Biochem. Biophys. Res. Commun.*, 1980, **92**, 1362.
235. Y. Feng, H. Roder and S. W. Englander, *Biophys. J.*, 1990, **57**, 15.
236. Y. Yamamoto, R. Chûjô, Y. Inoue and T. Suzuki, *FEBS Lett.*, 1992, **310**, 71.
237. Y. Yamamoto, Y. Inoue and T. Suzuki, *Magn. Reson. Chem.*, 1993, **31**, S8.
238. Y. Yamamoto, *Biochem. Biophys. Res. Commun.*, 1993, **196**, 348.
239. Y. Yamamoto, T. Suzuki and H. Hori, *Biochim. Biophys. Acta*, 1995, **1248**, 149.
240. Y. Yamamoto, *Bull. Chem. Soc. Jpn.*, 1996, **69**, 2947.
241. K. Rajarathnam, G. N. La Mar, M. L. Chiu, S. G. Sligar, J. P. Singh and K. M. Smith, *J. Am. Chem. Soc.*, 1991, **113**, 7886.
242. M. Bolognesi, A. Coda, G. Batti, P. Ascenzi and M. Brunori, *J. Mol. Biol.*, 1985, **183**, 113.
243. Y. Yamamoto, A. Osawa, Y. Inoue, R. Chûjô and T. Suzuki, *Eur. J. Biochem.*, 1990, **192**, 225.

244. G. N. La Mar, M. J. Chatfield, D. H. Peyton, J. S. de Ropp, W. S. Smith, R. Krishnamoorthi, J. D. Satterlee and J. E. Erman, *Biochim. Biophys. Acta*, 1988, **956**, 267.
245. J. Jeener, B. H. Meier, P. B. Bachmann and R. R. Ernst, *J. Chem. Phys.*, 1979, **71**, 4546.
246. M. F. Perutz, *Br. Med. Bull.*, 1976, **32**, 195.
247. Y. Yamamoto and R. Chûjô, *J. Chem. Soc., Chem. Commun.*, 1992, 87.
248. K. Wüthrich, *NMR in Biological Research: Peptide and Proteins*, Ch. 5, North Holland, Amsterdam, 1976.
249. Y. Yamamoto, *Gazz. Chim. Ital.*, 1994, **124**, 475.
250. C. Lionetti, M. G. Guanziroli, F. Frigerio, P. Ascenzi and M. Bolognesi, *J. Mol. Biol.*, 1991, **217**, 409.
251. Y. Yamamoto, N. Nanai, Y. Inoue and R. Chûjô, *J. Chem. Soc., Chem. Commun.*, 1989, 1419.
252. A. N. Nesmeyanov, E. B. Zavelovich, V. N. Babin, N. S. Kochetkova and E. I. Fedin, *Tetrahedron*, 1975, **31**, 1461.
253. J. D. Satterlee and G. N. La Mar, *J. Am. Chem. Soc.*, 1976, **98**, 2804.
254. D. M. Collins, R. Countryman and J. L. Hoard, *J. Am. Chem. Soc.*, 1972, **94**, 2066.
255. K. Nagai, T. Kitagawa and H. Morimoto, *J. Mol. Biol.*, 1980, **136**, 271.
256. R. Sinclair, S. Hallam, M. Chen, B. Chance and L. Power, *Biochemistry*, 1996, **35**, 15120.
257. G. N. La Mar, K. Nagai, T. Jue, D. L. Budd, K. Gersonde, H. Sick, T. Kagimoto, T. Hayashi and F. Taketa, *Biochem. Biophys. Res. Commun.*, 1980, **96**, 1172.
258. S. Takahashi, A. K.-H. Lin and C. Ho, *Biochemistry*, 1980, **19**, 5196.
259. G. N. La Mar and J. S. de Ropp, *J. Am. Chem. Soc.*, 1982, **104**, 5203.
260. R. G. Shulman, S. H. Glarum and M. Karplus, *J. Mol. Biol.*, 1971, **57**, 93.
261. T. G. Traylor and A. P. Berzinis, *J. Am. Chem. Soc.*, 1980, **102**, 2844.
262. M. Smith and G. McLendon, *J. Am. Chem. Soc.*, 1981, **103**, 4912.
263. S. M. Soltis and C. E. Strouse, *J. Am. Chem. Soc.*, 1988, **110**, 5644.
264. H. Senn and K. Wüthrich, *Biochim. Biophys. Acta*, 1983, **746**, 48.
265. G. N. La Mar, D. B. Viscio, K. M. Smith, W. S. Caughey and M. L. Smith, *J. Am. Chem. Soc.*, 1978, **100**, 8085.
266. J. D. Satterlee and J. E. Erman, *J. Biol. Chem.*, 1983, **258**, 1050.
267. J. T. J. Lecomte and G. N. La Mar, *J. Am. Chem. Soc.*, 1987, **109**, 7219.
268. T. Takano and R. E. Dickerson, *J. Mol. Biol.*, 1981, **153**, 79.
269. B. C. Finzel, T. L. Poulos and J. J. Kraut, *J. Biol. Chem.*, 1984, **259**, 13027.
270. S. Neya and N. Funasaki, *J. Biol. Chem.*, 1987, **262**, 6725.
271. D. L. Turner, *Eur. J. Biochem.*, 1993, **211**, 563.
272. T. Iizuka and I. Morishima, *Biochim. Biophys. Acta*, 1974, **371**, 1.
273. I. Morishima, S. Neya, T. Inubushi, T. Yonezawa and T. Iizuka, *Biochim. Biophys. Acta*, 1978, **534**, 307.
274. S. Neya and N. Funasaki, *Biochemistry*, 1986, **25**, 1221.
275. Y. Yamamoto and G. N. La Mar, *Biochim. Biophys. Acta*, 1989, **996**, 187.
276. C. C. McDonald and W. D. Phillips, *Biochemistry*, **12**, 3170.
277. Y. H. Chao, R. Bersohn and P. Asisen, *Biochemistry*, 1979, **18**, 774.
278. G. M. Smith, *Biochemistry*, 1979, **18**, 1628.
279. R. Timkovich, M. S. Cork and P. V. Taylor, *Biochemistry*, 1984, **23**, 3526.
280. N. V. Shokhirev and F. A. Walker, *J. Phys. Chem.*, 1995, **99**, 17795.
281. Y. Yamamoto, *J. Biochem.*, 1996, **119**, 16.
282. S. Neya and N. Funasaki, *Biochim. Biophys. Acta*, 1988, **952**, 150.
283. S. Neya and N. Funasaki, *Biochim. Biophys. Acta*, 1989, **996**, 226.
284. S. Neya and N. Funasaki, *Biochim. Biophys. Acta*, 1992, **1117**, 243.
285. T. Sato, N. Tanaka, S. Neya, N. Funasaki, T. Iizuka and Y. Shiro, *Biochim. Biophys. Acta*, 1992, **1121**, 1.
286. T. Sato, N. Tanaka, H. Moriyama, O. Matsumoto, A. Takenaka, S. Neya and N. Funasaki, *Bull. Chem. Soc. Jpn.*, 1992, **65**, 739.

287. S. Neya, N. Funasaki, T. Sato, N. Igarashi and N. Tanaka, *J. Biol. Chem.*, 1993, **268**, 8935.
288. J. B. Hauksson, G. N. La Mar, R. K. Pandey, I. N. Rezzano and K. M. Smith, *J. Am. Chem. Soc.*, 1990, **112**, 6198.
289. J. B. Hauksson, G. N. La Mar, R. K. Pandey, I. N. Rezzano and K. M. Smith, *J. Am. Chem. Soc.*, 1990, **112**, 8315.
290. I. Constantinidis, J. D. Satterlee, R. K. Pandey, H. K. Leung and K. M. Smith, *Biochemistry*, 1988, **27**, 3069.
291. D. L. Budd, G. N. La Mar, K. C. Langry, K. M. Smith and R. Nayyir-Mazhir, *J. Am. Chem. Soc.*, 1979, **101**, 6091.
292. G. N. La Mar and F. A. Walker, *J. Am. Chem. Soc.*, 1973, **95**, 6950.
293. G. N. La Mar, J. S. de Ropp, K. M. Smith and K. C. Langry, *J. Biol. Chem.*, 1981, **256**, 237.
294. S. E. V. Philips and B. P. Shoenborn, *Nature*, 1980, **292**, 81.
295. Y.-C. Fann, T.-L. Ong, J. M. Nocek and B. M. Hoffman, *J. Am. Chem. Soc.*, 1995, **117**, 6109.
296. T. Takano, *J. Mol. Biol.*, 1977, **110**, 537.
297. D. Bashford, C. Chothia and A. M. Lesk, *J. Mol. Biol.*, 1987, **196**, 199.
298. A. E. Eomero-Herrera, M. Goodman, H. Dene, D. E. Bartnicki and H. Mizukami, *J. Mol. Evol.*, 1981, **17**, 140.
299. G. Liljeqvist, G. Paleus and G. Baunitzer, *J. Mol. Evol.*, 1982, **18**, 102.
300. V. S. Sharma, M. E. John and M. R. Waterman, *J. Biol. Chem.*, 1982, **257**, 11887.
301. T. Suzuki, T. Takagi and S. Ohta, *Biochem. J.*, 1989, **260**, 177.
302. J. D. Cutnell, G. N. La Mar and S. B. Kong, *J. Am. Chem. Soc.*, 1981, **103**, 3567.
303. G. N. La Mar, J. Cutnell and S. B. Kong, *Biophys. J.*, 1981, **34**, 217.
304. D. G. Lambright, S. Balasubramanian and S. G. Boxer, *J. Mol. Biol.*, 1989, **209**, 289.
305. N. R. Krishna, D. H. Huang, J. D. Glickson, R. Rowan, III and R. Walter, *Biophys. J.*, 1979, **26**, 345.
306. A. G. Redfield, S. D. Kunz and E. K. Ralph, *J. Magn. Reson.*, 1975, **19**, 114.
307. P. Plateau and M. Guéron, *J. Am. Chem. Soc.*, 1982, **104**, 7310.
308. V. Sklenár and Z. Starcuk, *J. Magn. Reson.*, 1982, **50**, 495.
309. G. M. Clore, B. J. Kimber and A. M. Gronenborn, *J. Magn. Reson.*, 1983, **54**, 170.
310. P. J. Hore, *J. Magn. Reson.*, 1983, **54**, 46.
311. L. Tentori, G. Vivaldi, S. Carta, M. Mariucci, A. Masa, E. Antonini and M. Brunori, *Int. J. Pept. Protein*, 1973, **5**, 182.
312. T. Suzuki, T. Takagi and K. Shikama, *Biochim. Biophys. Acta*, 1981, **669**, 79.
313. T. Takagi, S. Iida, A. Matsuoka and K. Shikama, *J. Mol. Biol.*, 1984, **180**, 1179.
314. T. Suzuki, *J. Biol. Chem.*, 1986, **261**, 3692.
315. J. B. Wittenberg, C. A. Applevy and B. A. Wittenberg, *J. Biol. Chem.*, 1972, **247**, 527.
316. Y. Yamamoto, K. Iwafune, R. Chûjô, Y. Inoue, K. Imai and T. Suzuki, *J. Mol. Biol.*, 1992, **228**, 343.
317. E. Conti, C. Moser, M. Rizzi, A. Mattevi, C. Lionetti, A. Coda, P. Ascenzi, M. Brunori and M. Bolognesi, *J. Mol. Biol.*, 1993, **233**, 498.
318. M. Bolognesi, A. Coda, F. Ferigerio, G. Gatti, P. Ascenzi and M. Brunori, *J. Mol. Biol.*, 1990, **213**, 621.
319. I. Morishima and T. Inubushi, *J. Am. Chem. Soc.*, 1987, **110**, 3568.
320. L. S. Reid, A. R. Lim and A. G. Mauk, *J. Am. Chem. Soc.*, 1986, **108**, 8197.
321. G. N. La Mar, U. Pandey, J. B. Hauksson, R. K. Pandey and K. M. Smith, *J. Am. Chem. Soc.*, 1989, **111**, 485.
322. G. N. La Mar, J. B. Hauksson, L. B. Dugad, P. A. Liddell, N. Venkataramana and K. M. Smith, *J. Am. Chem. Soc.*, 1991, **113**, 1544.
323. D. Morikis, R. Bruschweiler and P. E. Wright, *J. Am. Chem. Soc.*, 1993, **115**, 5237.
324. M. Sette, J. S. de Ropp, G. Hernandez and G. N. La Mar, *J. Am. Chem. Soc.*, 1993, **192**, 133.

325. G. N. La Mar, D. L. Budd, D. B. Viscio, K. M. Smith and K. C. Langry, *Proc. Natl. Acad. Sci. USA*, 1978, **75**, 5755.
326. Q. H. Gibson and E. Antonini, *Biochem. J.*, 1960, **77**, 328.
327. M. Y. Rose and J. S. Olson, *J. Biol. Chem.*, 1983, **258**, 4298.
328. G. N. La Mar, N. L. Davis, D. W. Parish and K. M. Smith, *J. Mol. Biol.*, 1983, **168**, 887.
329. Y. Yamamoto, Nuclear magnetic resonance studies of equilibrated and reconstituted forms of hemoglobin, Ph.D. dissertation, University of California, Davis, CA, 1986.
330. K.-B. Lee, E. Jun, G. N. La Mar, I. N. Rezzano, R. K. Pandey, K. M. Smith, F. A. Walker and D. H. Buttlaire, *J. Am. Chem. Soc.*, 1991, **113**, 3576.
331. J. T. L. Lecomte, R. D. Johnson and G. N. La Mar, *Biochim. Biophys. Acta*, 1985, **829**, 268.
332. G. N. La Mar, Y. Yamamoto, T. Jue, K. M. Smith and R. K. Pandey, *Biochemistry*, 1985, **24**, 3826.
333. Y. Yamamoto and G. N. La Mar, *Biochemistry*, 1986, **25**, 5288.
334. G. N. La Mar, H. Toi and R. Krishnamoorthi, *J. Am. Chem. Soc.*, 1984, **106**, 6395.
335. K. H. Winterhalter and A. Colisimo, *Biochemistry*, 1971, **10**, 621.
336. H. F. Bunn and J. H. Jandl, *J. Biol. Chem.*, 1968, **243**, 4665.
337. G. N. La Mar, K. M. Smith, K. Gersonde, H. Sick and M. Overkamp, *J. Biol. Chem.*, 1980, **255**, 66.
338. G. N. La Mar, P. D. Burns, J. T. Jackson, K. M. Smith, K. C. Langry and P. Strittmatter, *J. Biol. Chem.*, 1981, **256**, 6075.
339. G. N. La Mar, R. R. Anderson, V. P. Chacko and K. Gersonde, *Eur. J. Biochem.*, 1983, **133**, 161.
340. G. N. La Mar, T. Jue, B. M. Hoffman and K. Nagai, *J. Mol. Biol.*, 1984, **178**, 929.
341. J. S. de Ropp, G. N. La Mar, K. M. Smith and K. C. Langry, *J. Am. Chem. Soc.*, 1984, **106**, 4438.
342. M. J. Levy, G. N. La Mar, T. Jue, K. M. Smith, R. K Pandey, W. S. Smith, D. J. Livingston and W. D. Brown, *J. Biol. Chem.*, 1985, **260**, 13694.
343. R. M. Cook and P. E. Wright, *Biochim. Biophys. Acta*, 1985, **832**, 365.
344. S. J. McLachlan, G. N. La Mar, P. D. Burns, K. M. Smith and K. C. Langry, *Biochim. Biophys. Acta*, 1986, **874**, 274.
345. V. P. Ckacko, G. N. La Mar, K. Gersonde and H. Sick, *Eur. J. Biochem.*, 1986, **161**, 375.
346. D. H. Peyton, R. Krishnamoorthi, G. N. La Mar, K. Gersonde, K. M. Smith and D. W. Parish, *Eur. J. Biochem.*, 1987, **168**, 377.
347. H. S. Aojula, M. T. Wilson, G. R. Moore and D. J. Williamson, *Biochem. J.*, 1988, **250**, 853.
348. J. L. McGourty, G. N. La Mar, K. M. Smith, F. Ascoli, E. Chiancone, R. K. Pandey and J. P. Singh, *Eur. J. Biochem.*, 1989, **184**, 53.
349. W. R. Light, R. J. Rohlfs, G. Palmer and J. S. Olson, *J. Biol. Chem.*, 1987, **262**, 46.
350. H. S. Aojula, M. T. Wilson and I. E. G. Morrison, *Biochem. J.*, 1987, **243**, 205.
351. K. Gersonde, H. Sick, M. Overkamp, K. M. Smith and D. W. Parish, *Eur. J. Biochem.*, 1986, **157**, 393.
352. F. A. Walker, D. Emrick, J. E. Rivera, B. J. Hanquet and D. H. Buttlaire, *J. Am. Chem. Soc.*, 1988, **110**, 6234.
353. M. F. Perutz, *Nature*, 1970, **228**, 726.
354. B. R. Gelin, A. W. Lee and M. Karplus, *J. Mol. Biol.*, 1983, **171**, 489.
355. G. N. La Mar and R. Krishnamoorthi, *Biophys. J.*, 1983, **144**, 177.
356. T. Hiroo, G. N. La Mar, R. Margalit, C.-M. Che and H. B. Gray, *J. Am. Chem. Soc.*, 1984, **106**, 6213.
357. R. Krishnamoorthi and G. N. La Mar, *Eur. J. Biochem.*, 1984, **138**, 135.
358. T. Jue and G. N. La Mar, *Biochem. Biophys. Res. Commun.*, 1984, **119**, 640.
359. G. N. La Mar, W. S. Smith, N. L. Davis, D. L Budd and M. J. Levy, *Biophys. Res. Commun.*, 1989, **158**, 462.
360. J. B. Hauksson, G. N. La Mar, U. Pande, R. K. Pandey, D. W. Parish, J. P. Singh and K. M.

Smith, *Biochim. Biophys. Acta*, 1990, **1041**, 186.
361. K.-B. Lee, G. N. La Mar, L. A. Kehres, E. M. Fujinari and K. M. Smith, *Biochemistry*, 1990, **29**, 9623.
362. K.-B. Lee, G. N. La Mar, R. K. Pandey, I. N. Rezzano, K. E. Mansfield and K. M. Smith, *Biochemistry*, 1991, **30**, 1878.
363. K. A. Keating, G. N. La Mar, F.-Y. Shiau and K. M. Smith, *J. Am. Chem. Soc.*, 1992, **114**, 6513.
364. R. Santucci, F. Ascoli, G. N. La Mar, R. K. Pandey and K. M. Smith, *Biochim. Biophys. Acta*, 1993, **1164**, 133.
365. M. J. Cocco, D. Barrick, S. V. Taylor and J. T. J. Lecomte (1992) *J. Am. Chem. Soc.*, 1991, **114**, 11000.
366. G. N. La Mar, N. L. Davis, R. D. Johnson, W. S. Smith, J. B. Hauksson, D. L. Budd, F. Dalichow, K. C. Langry, I. K. Morris and K. M. Smith, *J. Am. Chem. Soc.*, 1993, **115**, 3869.
367. S. Yee and D. H. Peyton, *Biochim. Biophys. Acta*, 1995, **1252**, 295.
368. A. Suzuki, T. Tomizawa, T. Hayashi, T. Mizutani and H. Ogoshi, *Bull. Chem. Soc. Jpn.*, 1996, **69**, 2923.
369. S. Neya, M. Nakamura, K. Imai, H. Hori and N. Fun, *Biochim. Biophys. Acta*, 1996, **1296**, 245.
370. F. A. Walker, *J. Am. Chem. Soc.*, 1980, **102**, 3252.
371. J. G. Gilman, *Biochemistry*, 1979, **18**, 2273.
372. E. Oldfield, R. S. Norton and A. J. Allerhand, *J. Biol. Chem.*, 1975, **250**, 1460.
373. R. B. Visscher and F. R. N. Gurd, *J. Biol. Chem.*, 1975, **250**, 2238.
374. H. C. Lee, J. K. Gard, T. L. Brown and E. Oldfield, *J. Am. Chem. Soc.*, 1985, **107**, 4087.
375. G. N. La Mar, V. Thanabal, R. D. Johnson, K. M. Smith and D. W. Parish, *J. Biol. Chem.*, 1989, **264**, 5428.
376. R. D. Johnson, G. N. La Mar, K. M. Smith, D. W. Parish and K. C. Langry, *J. Am. Chem. Soc.*, 1989, **111**, 481.
377. J. T. L. Lecomte and G. N. La Mar, *Eur. Biophys. J.*, **13**, 373.
378. A. G. Marshall, K. M. Lee and P. W. Martin, *J. Am. Chem. Soc.*, 1980, **102**, 1460.
379. S. D. Emerson, J. T. J. Lecomte and G. N. La Mar, *J. Am. Chem. Soc.*, 1988, **110**, 4176.
380. K. Wüthrich and G. Wagner, *J. Mol. Biol.*, 1979, **130**, 1.
381. G. N. La Mar, D. L. Budd and H. Goff, *Biochem. Biophys. Res. Commun.*, 1977, **77**, 104.
382. G. N. La Mar, K. Nagai, T. Jue, D. L. Budd, K. Gersonde, H. Sick, T. Kagimoto, A. Hayashi and F. Taketa, *Biochem. Biophys. Res. Commun.*, 1980, **96**, 1172.
383. K. Nagai, G. N. La Mar, T. Jue and H. F. Bunn, *Biochemistry*, 1982, **21**, 842.
384. S. Takahashi, A. K. L. C. Lin and C. Ho, *Biophys. J.*, 1982, **39**, 33.
385. S. Miura and C. Ho, *Biochemistry*, 1984, **23**, 2492.
386. S. Takahashi, A. K. L. C. Lin and C. Ho, *Biochemistry*, 1980, **19**, 5196.
387. T. Jue, G. N. La Mar, K.-H. Han and Y. Yamamoto, *Biophys. J.*, 1984, **46**, 117.
388. K.-H. Han and G. N. La Mar, *J. Mol. Biol.*, 1986, **189**, 541.
389. A. Hvidt and S. Nielsen, *Adv. Protein Chem.*, 1966, **21**, 287.
390. E. Antonini and M. Brunori, *Hemoglobin and Myoglobin in Their Reactions with Ligands*, p. 40, North-Holland, Amsterdam, 1971.
391. W. S. Caughey, in *Hemes and Hemoproteins* (ed. B. Chance, R. W. Estarbrook and T. Yonetani), p. 276, Academic Press, New York, 1966.
392. H. Santos, J. J. G. Moura, I. Moura, J. LeGall and A. V. Xavier, *Eur. J. Biochem.*, 1982, **127**, 151.
393. H. Akutsu, K. Fan, Y. Kyogoku and K. Niki, in *Charge and Field in Biosystems II* (ed. M. J. Allen, S. F. Cleary and F. M. Hawkridge), p. 59, Plenum Publishing Corp., New York, 1989.
394. K. Fan, H. Akutsu and K. Niki, *J. Electroanal. Chem.*, 1990, **278**, 295.
395. K. Fan, H. Akutsu, Y. Kyogoku and K. Niki, *Biochemistry*, 1990, **29**, 2257.

396. J.-S. Park, M. Enoki, A. Ohbu, K. Fan, K. Niki, H. Akutsu and Y. Kyogoku, *J. Mol. Struct.*, 1991, **242**, 343.
397. J.-S. Park, K. Kano, Y. Morimoto, Y. Higuchi, N. Yasuoka, M. Ogata, K. Niki and H. Akutsu, *J. Biomol. NMR*, 1991, **1**, 271.
398. J.-S. Park, K. Kano, K. Niki and H. Akutsu, *FEBS Lett.*, 1991, **285**, 149.
399. K. Fan, H. Akutsu and K. Niki, in *Dynamic Interactions and Electronic Processes of Macromolecular Complexes* (ed. E. Tsuchida), p. 251, VHC, New York, 1991.
400. H. Akutsu and M. Hirasawa, *FEBS Lett.*, 1992, **308**, 264.
401. I. B. Coutinho, D. L. Turner, J. LeGall and A. V. Xavier, *Eur. J. Biochem.*, 1992, **209**, 329.
402. D. L. Turner, C. A. Salguerio, J. LeGall and A. V. Xavier, *Eur. J. Biochem.*, 1992, **210**, 931.
403. D. L. Turner, C. A. Salguerio, T. Catarino, J. LeGall and A. V. Xavier, *Biochim. Biophys. Acta*, 1994, **1187**, 232.
404. I. B. Coutinho, D. L. Turner, J. LeGall and A. V. Xavier, *Eur. J. Biochem.*, 1995, **230**, 1007.
405. J.-S. Park, T. Ohmura, K. Kano, T. Sagara, K. Niki, Y. Kyogoku and H. Akutsu, *Biochim. Biophys. Acta*, 1996, **1293**, 45.
406. D. L. Turner, C. A. Salguerio, T. Catarino, J. LeGall and A. V. Xavier, *Eur. J. Biochem.*, 1996, **241**, 723.
407. G. Robillard and R. G. Shulman, *J. Mol. Biol.*, 1972, **71**, 507.
408. Y. Yamamoto, *J. Biochem.*, 1996, **120**, 126.
409. Y. Yamamoto, *Eur. J. Biochem.*, 1996, **243**, 292.

This Page Intentionally Left Blank

Empirical versus Nonempirical Evaluation of Secondary Structure of Fibrous and Membrane Proteins by Solid-state NMR: A Practical Approach

HAZIME SAITÔ, SATORU TUZI and AKIRA NAITO

Department of Life Science, Himeji Institute of Technology, Harima Science Garden City, Kamigori, Hyogo, Japan 678-1297

We describe here an overview of a practical approach to evaluating the secondary structure of fibrous and membrane proteins by means of high-resolution solid-state ^{13}C NMR, both from the empirical and non-empirical points of view. It is emphasized that the local secondary structure of these systems, as viewed from the respective amino acid residues, can be readily evaluated by means of their ^{13}C chemical shifts with reference to the accumulated chemical shift data of amino acid residues with known secondary structure. This approach is not limited to simple fibrous proteins, but is also extended to more complicated systems, together with isotope labelling, as a tool for revealing the initial structure or additional constraints to structural data for the purpose of a non-empirical determination of secondary structure, based on a variety of interatomic distances determined by REDOR (rotational echo double resonance) or other means. Illustrative examples are shown from our data on silk, collagen, bacteriorhodopsin, and some biologically active peptides.

ANNUAL REPORTS ON NMR SPECTROSCOPY
VOLUME 36 ISBN 0-12-505336-3

Copyright © 1998 Academic Press Limited
All rights of reproduction in any form reserved

1. INTRODUCTION

Determination of the three-dimensional structures of fibrous or membrane proteins as well as biologically active peptides as ligand molecules is very important in gaining insight into their biological functions, obtaining a lead compound for drug design, and so on. The standard approaches for this purpose of X-ray diffraction or multidimensional NMR studies are not always straightforwardly applicable to fibrous or membrane proteins because of difficulty in crystallization or in solubility in aqueous solution, respectively. It is natural to explore the application of solid-state NMR because the structural information required is contained in spin interactions in the solid state if one of these interactions can be selectively recovered either by use of pulse techniques or by selective isotope labelling. In particular, three-dimensional structure is available from solid-state NMR on the basis of the accurately determined orientation of the chemical shift tensor with respect to the applied field or the interatomic distances of dipolar pairs of interest, as previously reviewed.[1–6] It seems to be difficult, however, to arrive at the unique structure using these approaches alone when many species with different secondary structures in proteins are present at the same time, even if these methods provide one excellent means for this purpose for simple molecular systems.

In this situation, an empirical approach to exploring the secondary structure of these systems utilizing conformation-dependent ^{13}C chemical shifts with reference to the accumulated chemical shift data of amino acid residues in polypeptides with known local secondary structures provides an invaluable complementary means[7–9] of avoiding meaningless structure in advance. Distinction of polymorphic structures in this way turned out to be very easy and useful for peptides,[10,11] polypeptides[12–15] or fibrous proteins[15–18] in the solid state on the basis of specific displacements[7–9] or splittings of peaks in ^{13}C NMR spectra recorded by high-resolution solid-state NMR, either CP-MAS (cross polarization–magic angle spinning) or DD-MAS (dipolar decoupled–magic angle spinning). This approach was also extended to more complicated globular[19,20] or membrane proteins[21–24] to reveal the initial structure, which could be further refined to the three-dimensional structure once the ^{13}C chemical shifts of particular residues were assigned by means of the sequentially assigned proton NMR signals or specific ^{13}C labelling of certain amino acid residues. In the solid state, local secondary structures of such proteins thus obtained empirically could be further refined on the basis of accurately determined interatomic distances from a selective recoupling of dipolar interactions between selectively isotope-labelled nuclei using either REDOR (rotational echo double resonance for heteronuclear pairs)[25] or RR (rotational resonance for homonuclear pairs),[26] as will be discussed in Section 4.4. This approach is also important and promising in determination of the "active

conformation" of a number of information-carrying molecules such as biologically active peptides bound to certain receptor molecules, to which standard diffraction or multidimensional NMR methods are difficult to apply.

In this review, we demonstrate how effectively the present solid-state NMR approach utilizing empirical or nonempirical evalutation or both is applied to reveal the secondary or three-dimensional structure of fibrous and membrane proteins and also of biologically important peptides.

2. CONFORMATION-DEPENDENT ^{13}C CHEMICAL SHIFTS

It is seen from Table 1 that the ^{13}C chemical shifts of the backbone C_α, C=O and side-chain C_β signals of a variety of amino acid residues in polypeptides are significantly displaced, depending upon their particular local conformations such as α-helix or β-sheet form, irrespective of the variety of neighbouring amino acid residues[7–9] except for the residues followed by proline.[27] In particular, the C_α and C=O ^{13}C chemical shifts of the respective amino acid residues in the right-handed α-helix (α_R- or α_I-) form are displaced upfield by 3.5–8.0 ppm and 2.6–6.1 ppm, respectively, compared with those of the β-sheet form, whereas the C_β signals of the respective amino acid residues in the α-helix are displaced downfield by 3.4–5.2 ppm with respect to those of the β-sheet form. Five other types of conformation—α_{II}-helix, left-handed α-helix (α_L-), collagen-type triple helix and silk I forms, as well as the random coil form—are readily distinguishable on the basis of the conformation-dependent ^{13}C chemical shifts of the respective amino acid residues, as demonstrated, for instance, for the Ala residue in Table 2. This means that the conformation-dependent ^{13}C chemical shifts are not dependent upon the particular peptide sequence, except for the one followed by Pro,[27] but are mainly determined by the local conformation of amino acid residues as defined by a set of torsion angles (ϕ, φ) and the manner of hydrogen-bonding (Fig. 1). Therefore, the transferability of these parameters from the simple model system to more complicated proteins is excellent and can be applied to any type of proteins. The conformation-dependent ^{13}C chemical shifts were theoretically evaluated as a contour map of ^{13}C chemical shift (nuclear shielding constant) for the Ala residue from *N*-acetyl-*N'*-methylalanine amide,[28–30] the Gly residue from *N*-acetyl-*N'*-methylglycine amide,[31] and Ala and Val residues from *N*-formyl-L-alanine amide and *N*-formyl-L-valine amide[32] as a function of the torsion angles based on semi-empirical or *ab initio* molecular orbital methods.

The presence of the α_{II}-helix in which the amide plane is tilted from the helical axis was previously proposed as a major form present in the transmembrane helices of bacteriorhodopsin (bR) by Krimm and Dwivedi,[33] on the basis of IR measurements, as a form similar to that of $(Ala)_n$ dissolved in

Table 1. ^{13}C chemical shifts characteristic of the α-helix and β-sheet forms (ppm from TMS).[9]

Amino-acid residues in polypeptides	C-α			C-β			C=O		
	α-Helix	β-Sheet	Δ^a	α-Helix	β-Sheet	Δ^a	α-Helix	β-Sheet	Δ^a
Ala	52.4	48.2	4.2	14.9	19.9	−5.0	176.4	171.8	4.6
	52.3	48.7	3.6	14.8	20.0	−5.2	176.2	171.6	4.6
	52.8	49.3	3.5	15.5	20.3	−4.8	176.8	172.2	4.6
Leu	55.7	50.5	5.2	39.5	43.3	3.8	175.7	170.5	5.2
	55.8	51.2	4.6	43.7[b]	39.6	(4.1)	175.8	171.3	4.5
Glu(OBzl)	56.4	51.2	5.2	25.6	29.0	−3.4	175.6	171.0	4.6
	56.8	51.1	5.7	25.9	29.7	−3.8	175.4	172.2	3.2
Asp(OBzl)	53.4	49.2	4.2	33.8	38.1	−4.3	174.9	169.8	5.1
	53.6[c]			34.2[c]			174.9		
Val	65.5	58.4	7.1	28.7	32.4	−3.7	174.9	171.8	3.1
		58.2			32.4			171.5	
Ile	63.9	57.8	6.1	34.8	39.4	−4.6	174.9	172.7	2.2
		57.1			33.1			171.0	
Lys[d]	57.4			29.9			176.5		
Lys(Z)	57.6	51.4	6.2	29.3	28.5	−0.8	175.7	170.4	5.3
Arg[d]	57.1			28.9			176.8		
Phe	61.3	53.2	8.1	35.0	39.3	−4.3	175.2	169.0	6.2
Met	57.2	52.2	5.0	30.2	34.8	−4.6	175.1	170.6	4.5
Gly		43.2						168.4	
		44.3						169.2	
							171.6[e]	168.5	3.1

[a]Difference in the ^{13}C chemical shifts of the α-helix form relative to those of the β-sheet form.
[b]This assignment should be reversed.
[c]Erroneously assigned to the left-handed α-helix.
[d]Data taken from neutral aqueous solution.
[e]Averaged values from the data of polypeptides containing ^{13}C-labelled glycine residues.

Table 2. Conformation-dependent ^{13}C chemical shifts of Ala-residues (ppm from TMS).

	α_I-helix (α_R-helix)[a]	α_{II}-Helix[b]	α_L-Helix[a]	β-Sheet[a]	Collagen[a]	Silk I[a]	Random coil[c,d]
C_α	52.4	53.2	49.1	48.2	48.3	50.5	
C_β	14.9	15.8	14.9	19.9	17.6	16.6	16.9
C=O	176.4	178.4	172.9	171.8	173.1	177.1	

[a]H. Saitô and I. Ando, *Annu. Rep. NMR Spectrosc.*, 1989, **21**, 209.
[b]S. Tuzi, A. Naito and H. Saitô, *Biochemistry*, 1994, **33**, 15046.
[c]H. Saitô, M. Kameyama, M. Kodama and C. Nagata, *J. Biochem.*, 1982, **92**, 233.
[d]S. Tuzi, S. Yamaguchi, A. Naito, R. Needleman, J. K. Lanyi and H. Saitô, *Biochemistry*, 1996, **35**, 7520.

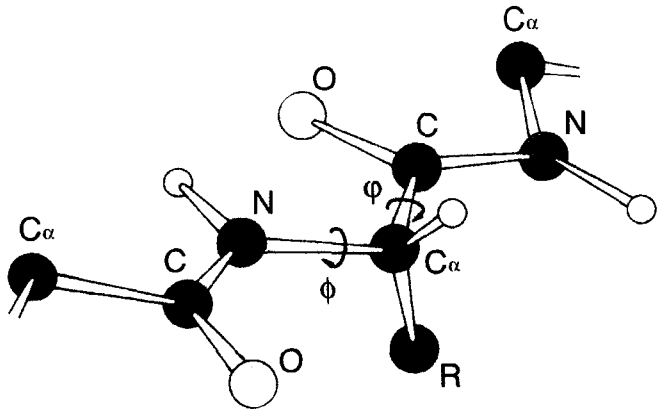

Fig. 1. Definition of torsion angles in the peptide unit.

hexafluoroisopropanol (HFIP) solution.[34] This form (−96°, −16°) is clearly distinguishable from the ordinary α-helix (α_I-helix) form (−57°, −47°) in terms of the conformation-dependent ^{13}C chemical shifts, as summarized in Table 2. It has been shown from this NMR approach[21–23] that the α_{II}-helix is the major conformation of the transmembrane helices in bR, at least as viewed from Ala residues, consistent with the previous findings by IR, Raman, CD, etc.[33–36] It is cautioned here that the aforementioned conformation-dependent ^{13}C chemical shifts could be displaced upfield by ~2 ppm when an amino acid residue under consideration is followed by amino acid-like Pro residues irrespective of the particular conformations.[27]

It is now possible to reveal the local secondary structure of any peptides and proteins, in an empirical manner, as viewed from any amino acid residues, from consideration of their ^{13}C chemical shifts if reference data for the conformation-dependent ^{13}C chemical shifts for the respective amino acid residues are available. In solution state, specific displacements of ^{13}C NMR peaks with respect to those of the random coil form have been utilized as a convenient probe leading to sequential assignment of secondary structures of globular proteins.[19,20]

In Section 3, we demonstrate how this approach can be conveniently applied to reveal the secondary structure of some fibrous or membrane proteins, with illustrative examples from the data of silk fibroin, collagen fibrils, and bR in the purple membrane. In Section 4, we briefly describe the principles and practical aspects of REDOR experiments, and application of this nonempirical approach to reveal the three-dimensional structure of biologically active peptides in combination with the empirical approach.

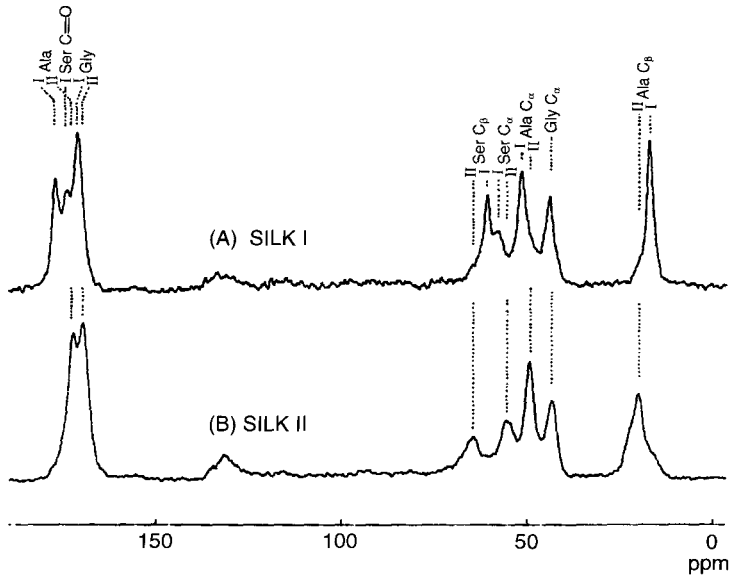

Fig. 2. ^{13}C CP-MAS NMR spectra of silk fibroin from the crystalline fraction of *B. mori* fribroin adopting silk I (A) and silk II (B) forms in the solid state.[17]

3. EMPIRICAL EVALUATION OF SECONDARY STRUCTURE

3.1. Fibrous proteins

The empirical approach was applied[14–18] to reveal the secondary structures of some fibrous proteins such as silk fibroins and collagen fibrils on the basis of the conformation-dependent displacements of ^{13}C chemical shifts. The crystalline silk fibroin exists as one of the polymorphs, either silk I or silk II (β-sheet form) and either α-helix or β-sheet forms, depending on the history of sample preparation and species of silkworms—*Bombyx mori* or *Philosophia cynthia ricini*, etc. It is straightforward, for instance, to distinguish the two polymorphs of silk fibroin[15–17] from *B. mori* of natural abundance by ^{13}C NMR spectra (Fig. 2),[17] since the variety of amino acid residues is limited in this case to Gly (42.9%), Ala (30%), Ser (12.2%) and Tyr (4.8%). It is noteworthy that the C_α signals of Ala and Ser residues of silk I (designated as I) are displaced downfield by about 2 ppm as compared with those of silk II (designated as II), whereas the C_β signals of silk I are displaced upfield by 2.4–4 ppm with respect to those of silk II. Note, however, that the ^{13}C chemical shift of Gly C_α is not always sensitive to the presence of the two types of polymorph, although the ^{13}C chemical shifts of the carbonyl carbons are sensitive. In a similar manner,

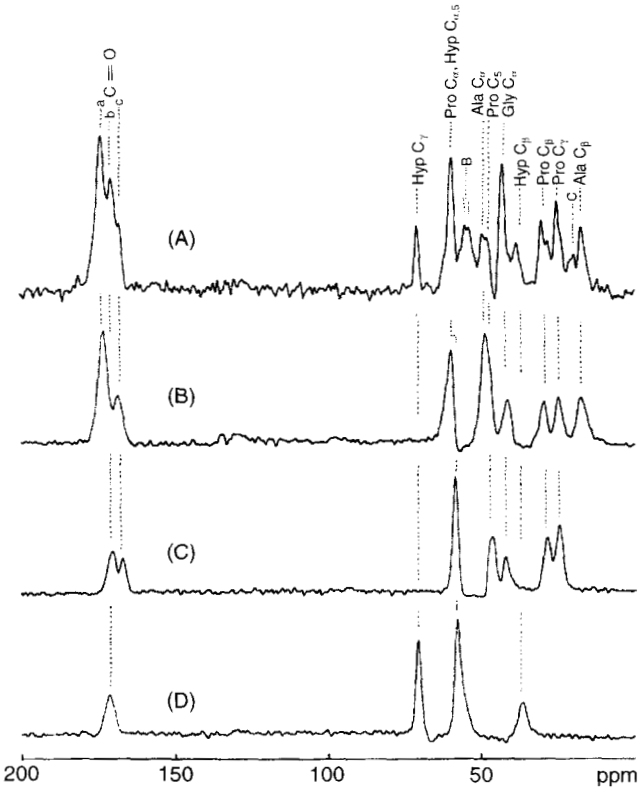

Fig. 3. ^{13}C CP-MAS NMR spectra of collagen from bovine achilles tendon (A) and of model polypeptides taking collagen-like triple helical structures (B–D): B, $(Pro\text{-}Ala\text{-}Gly)_n$; C, $(Pro\text{-}Pro\text{-}Gly)_{10}$; D, $(Hyp)_n$.[18]

the α-helix and β-sheet forms were readily distinguished for the fibroin from *P. c. ricini*.[12] It is pointed out that a major advantage of the present ^{13}C NMR approach is the ability to estimate the relative proportion that is not readily interconverted (20–30%).[37] Recent ^{13}C NMR studies on spider dragline silk by means of the displacements of peaks together with two-dimensional spin-diffusion experiments showed that alanine-rich domains of spider dragline silk fibroin adopt the β-sheet form, whereas the conformation of glycine-rich domains is consistent with the 3_1-helix form.[40,41]

Most of the signals from the ^{13}C NMR signals of collagen fibril (Fig. 3) arose from major amino acid residues, which amount to approximately 65% (Gly, $33 \pm 1.3\%$, Pro $11.8 \pm 0.9\%$, Ala, $10.8 \pm 0.9\%$, Hyp, $9.1 \pm 1.3\%$) and can readily be assigned to the individual amino acid residues (as indicated on the

top of the peaks in the figure) with reference to the peaks of the respective amino acid residues from model polypeptides adopting the similar collagen-like triple helix or 3_1-helix form.[14,18] The remaining unassigned peaks, B and C, were ascribed to the clusters of the C_α and C_γ or C_δ signals of minor amino acid residues (~35%) such as Ser, Glu, Leu, Arg, Lys, etc. In many instances, the C_β signals of peptides or proteins are substantially suppressed because of the presence of inherent low-frequency motions with a time scale of 10^4–10^5 Hz interfering with the proton decoupling frequency.[42] It appears that distinction of the collagen-like triple helix form from the assembly of the single 3_1-helices is not always feasible by means of the ^{13}C NMR data alone because of similarity in the torsion angles (−80°, 150°) and (−72°, 153°), for the 3_1- and collagen-like triple helices, respectively. It turned out, however, that the downfield displacement of the ^{15}N chemical shift of the Gly residue is very sensitive to the presence of (Gly)N−H···O=C interchain hydrogen-bonding, which plays an essential role in stabilization of the collagen-like triple helix[43] and can be utilized as a more sensitive complementary means of distinguishing the collagen-like triple helix from the 3_1-helix. In fact, it was found that the Gly N−H ^{15}N chemical shift of $(Pro\text{-}Pro\text{-}Gly)_{10}$ as a model of the collagen triple helix is displaced downfield by 4.9 ppm as a result of formation of the interchain hydrogen bond stabilizing the triple helix when this peptide is fully hydrated. Naturally, this peak position is very close to that for collagen fibril and $(Pro\text{-}Ala\text{-}Gly)_n$. This is evidently caused by the fact that the ^{15}N chemical shift is generally very sensitive to the manner of hydrogen-bonding.[44]

3.2. Membrane proteins

3.2.1. Three-dimensional crystals: cytochrome C oxidase

Tuzi *et al.* recorded ^{13}C NMR spectra of a three-dimensional crystal of bovine heart cytochrome *c* oxidase,[45] which is a membrane protein of mass 400 kDa containing 70 detergent molecules per protein. The whole three-dimensional structure of this protein was more recently revealed by X-ray diffraction study at 2.8 Å resolution.[46,47] In the three-dimensional crystal, whole membrane lipids are solubilized and replaced by appropriate detergent molecules. It was found that the ^{13}C spectral resolution of the protein moiety in the three-dimensional crystal was not always better than that of the two-dimensional crystal of bR (purple membrane),[23,24] as described later, probably owing to overlaps of many kinds of signals from this high-molecular-mass protein. Therefore, preparation of specifically ^{13}C-labelled protein is preferable for ^{13}C NMR studies, to resolve the peaks of individual residues and to relate the peak position with the respective reference data to reveal the local secondary structure in an empirical manner. It is noteworthy that molecular motions of detergent molecules attached to the protein are highly heterogeneous:[45]

surrounding detergent molecules in the three-dimensional crystals undergo rapid reorientational motions which result in substantial suppression of the peak intensity, although a fraction of molecules undergoing slow motions as a result of interaction with hydrophobic protein surfaces was detected through the proton spin–lattice relaxation times in the rotating frame. Thus, the presence of such detergent signals turned out not always to be serious so far as protein signals are selectively recorded by CP-MAS experiment with a short contact time such as 1 ms.

3.2.2. Two-dimensional crystals: bacteriorhodopsin

Bacteriorhodopsin (bR) is the only protein present in the purple membrane of *Halobacterium salinarium*, which is active as the light-driven proton pump translocating protons from the inside to the outside of the cell.[48,49] In addition to elucidation of its biological function as the proton pump, considerable attention has been paid to this protein as the simplest model system for study of more complicated G-protein-coupled receptors[50] that consist of seven similar transmembrane helices, loops and terminus, and play a crucial role in a variety of signal transductions in biological systems. The three-dimensional structure of bR has been elucidated by cryo-electron microscopy of the two-dimensional crystals at temperatures below −260°C by Henderson and coworkers (Fig. 4)[51,52] because resolution by X-ray diffraction study on the three-dimensional crystals is not yet able to reveal the crystalline structure at atomic resolution. Note that the N- or C-terminal ends are not involved in this representation because of their motions. In this connection, ^{13}C CP-MAS and DD-MAS NMR studies on membrane proteins are very important in clarifying the secondary structure as well as the dynamics at ambient temperature in relation to biological function under physiological condition. ^{13}C-labelled proteins needed for NMR studies are readily available from large-scale culture of *Halobacterium* using synthetic media in which certain unlabelled amino acids are replaced with the respective ^{13}C-labelled species, such as [3-^{13}C]Ala shown as the circled residues in Fig. 5. The boxes within the bilayers depicted the residues involved in the transmembrane helices, as revealed by Henderson and coworkers.[52] It is emphasized that for well-resolved ^{13}C signals fully hydrated samples such as centrifuged pellets are preferable[23,24] to lyophilized samples followed by hydration,[21,22] because dehydration causes substantial conformational disruption even at the transmembrane region, as manifested in considerable broadening and also displacements of peaks.[21,22] Tight sealing of the rotor containing the hydrated sample is strongly advised so as to prevent evaporation of water molecules during sample spinning, either by using a screwed cap with an O-ring or by gluing of caps with epoxy resin.

Regiospecific assignment of ^{13}C NMR signals. From the practical aspect of design of experiments on bR (and other types of membrane proteins in

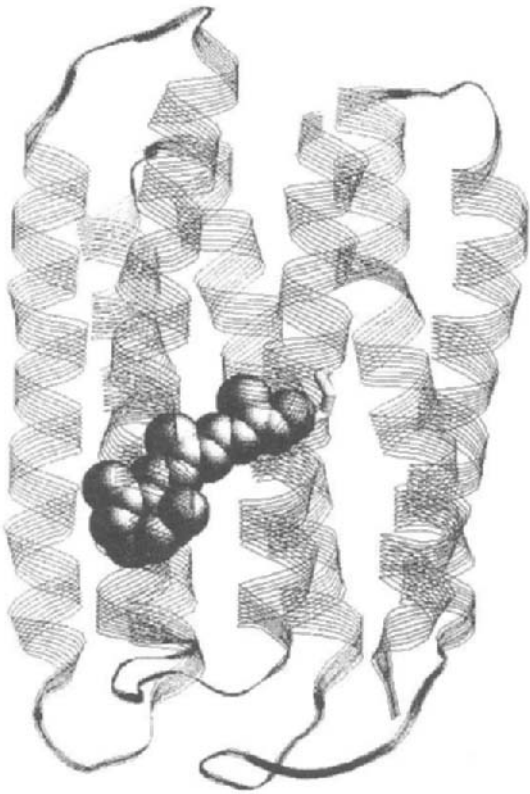

Fig. 4. Three-dimensional structure of bacteriorhodopsin as revealed by cryo-electron microscopy by Henderson *et al.*[51] Note that N- and C-termini are missing in this figure (cytoplasmic site at the top).

general) it is very important to clarify which portion of bR as shown in Figs 4 and 5 can be observed by which types of solid-state NMR technique (DD-MAS or CP-MAS) and also at what temperature. Figures 6A and 6B illustrate the ^{13}C DD-MAS and CP-MAS NMR spectra, respectively, of hydrated [3-^{13}C]Ala-bR. The two types of ^{13}C NMR spectra are not the same because of the presence of portions undergoing rapid conformational fluctuation. Part of the most intense signal at 16.9 and 15.9 ppm, marked as the C-terminus in the former (Fig. 6A), were significantly suppressed in the latter (Fig. 6B).[23] This means that the [3-^{13}C]Ala signals from the C-terminus as well as N-terminus regions are completely suppressed in the CP-MAS experiment because ^{13}C-^{1}H dipolar interactions responsible for the cross polarization are time-averaged owing to the rapid conformational fluctuation with a correlation time shorter than 10^{-8} s. In contrast, all the ^{13}C NMR signals from bR are visible from the

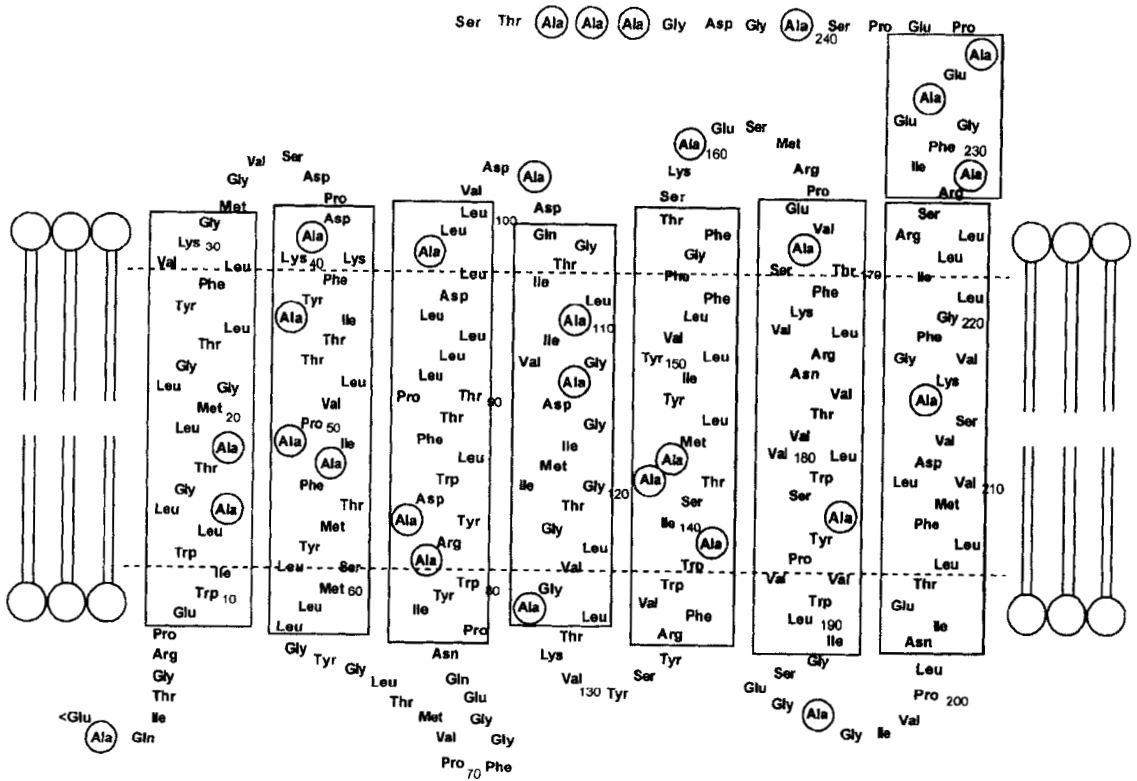

Fig. 5. Schematic representation of the secondary structure of bR after Henderson *et al.*[51] Ala residues are indicated here by circles. Boxes within the bilayer correspond to the transmembane helices.

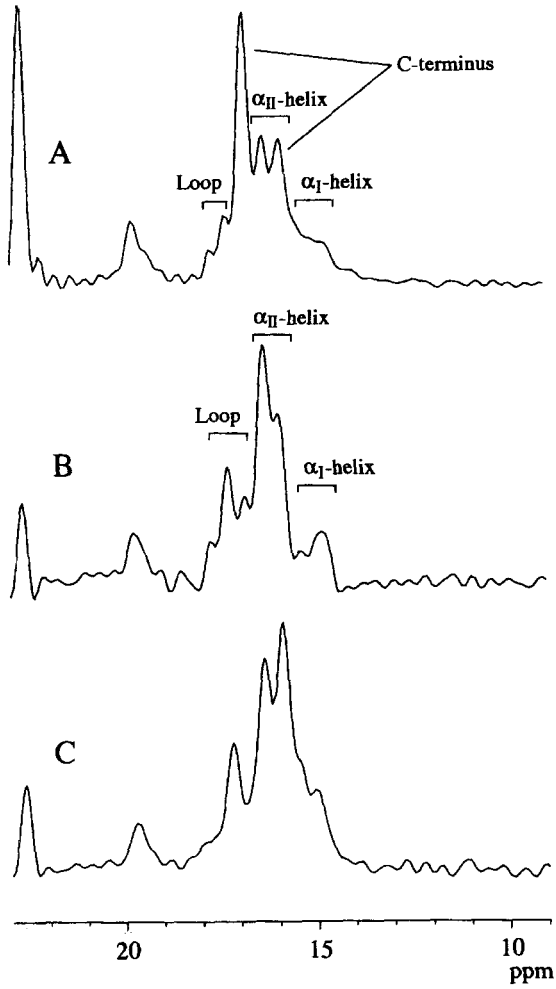

Fig. 6. ^{13}C DD-MAS NMR spectrum of [3-^{13}C]Ala-bR (A) and CP-MAS NMR spectra of [3-^{13}C]Ala-bR (B) and [3-^{13}C]bacterioopsin (bO) (C).[23]

DD-MAS NMR because of their shorter ^{13}C spin–lattice relaxation times (~0.5 s)[23] compared with the standard repetition time (4 s). In fact, the pattern of CP-MAS spectra was unchanged even if the C-terminus moiety containing six Ala residues was cleaved by papain.[22,23] The ^{13}C NMR signals from the N- or C-terminus regions, however, were completely suppressed even in the DD-MAS NMR experiment at temperatures below −20°C as a result of the slower motional frequency that can be interfered with proton decoupling frequency, 10^5 Hz. In short, no NMR signals were visible from these regions by

both DD-MAS and CP-MAS experiments at temperatures from −20° to −110°C.[24]

The seven well-resolved signals (14–18 ppm) in the DD-MAS (Fig. 6A) and CP-MAS NMR (Fig. 6B) spectra of [3-^{13}C]Ala-bR were then ascribed to the C_β signals of all the 29 and 22 Ala residues, respectively. The remaining signals that are visible only by CP-MAS NMR were assigned to Ala residues located at the regions of either the transmembrane helices or loops, depending upon their static or time-averaged torsion angles. The majoritiy of the α-helices in the transmembrane helices in bR are found to be not of the usual type (α_I-helices) but are ascribed to α_{II}-helices, consistent with the proposal by Krimm and Dwivedi based upon their IR experiment.[33] The remaining two peaks at 17.3 and 17.9 ppm and the additional peak at 16.9 ppm in the CP-MAS NMR were then ascribed to the loop region, although no reference data are available for the loop structures in Tables 1 and 2. The peak at 16.9 ppm should be ascribed to Ala residues of random coil located either at the lipid/water interface or at the boundary between the loop and transmembrane helices which undergo conformational fluctuation in anisotropic environment.[63]

The ^{13}C DD-MAS NMR [1-^{13}C]amino acid (Ala, Val, Leu, etc.)-labelled bR appears to detect signals only from the residues at the flexible surface area, as illustrated for [1-^{13}C]Ala-bR in Fig. 7, whereas the CP-MAS NMR detects signals from the transmembrane helices and loops, because the T_1 values for residues at the C-terminus and transmembrane helices as well as loop regions are of the order of 1 s and 10 s, respectively.[23,53] In this connection, Bowers and Oldfield[54] showed that intense carbonyl signals with line widths of 125–150 Hz from [1-^{13}C]Gly-, Val-, Leu-, Ile-, Lys- and Phe-labelled bR are observable by liquid-state high-resolution NMR spectrometry, and those signals are ascribed to the residues at the C-terminus undergoing rapid fluctuation, consistent with their previous finding from ^{2}H NMR spectra.[55] In contrast, Lewis *et al.*[56] observed none of these resonances from [1-^{13}C]Leu-bR under the condition of cross polarization and concluded that the peptide backbone of bR in native bR is extremely rigid even at 40°, consistent with a ^{2}H NMR study of their own.[57] Such a discrepancy can easily be explained in the light of more recent observations;[22–24] the C-terminus regions of fully hydrated bR are not easily detectable by the cross polarization experiment of Lewis *et al.*[56] In addition, Leu residues are located not at the C-terminus but at either the transmembrane helices or loop region. It is noteworthy from Fig. 7B that the ^{13}C NMR signals of the carbonyl region were resolved into 10 peaks for the fully hydrated samples,[58] but broadened peaks from lyophilized samples were not well resolved even if they were equilibrated at 100% relative humidity.[21]

Site-specific assignment of ^{13}C NMR signals. It is important to go on to the assignment of the ^{13}C NMR signals to the individual peaks in a site-specific manner so as to gain insight into the secondary structure as well as the dynamics of such specific sites in relation to biological function. One way is to

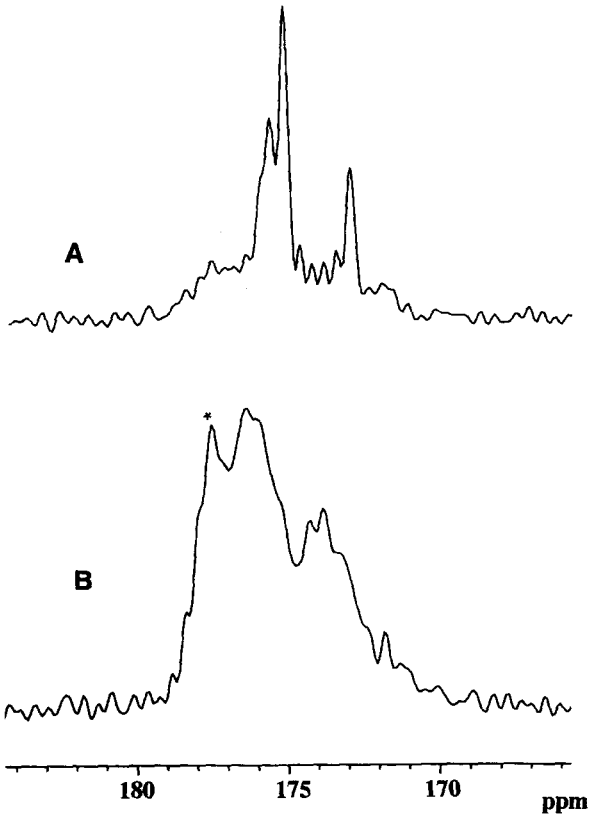

Fig. 7. ^{13}C DD-MAS (A) and CP-MAS NMR(B) spectra of [1-^{13}C]Ala-bR at pH 4.25.

examine a spectral change occurring due to a proteolytic digestion by a variety of proteolytic enzymes. For instance, the signals from Ala-246,247 at the terminal end of the C-terminus (see Fig. 5) were assigned by difference spectra between the intact and cleaved sample using carboxypeptidase A, and the remaining signals of Ala-235, Ala-237, Ala-240 at the C-terminus were assigned by means of cleavage with papain.[22,23] The carbonyl signal of [1-^{13}C]Val-69 was assigned on the basis of a spectral change caused by cleavage at the site of Phe-71–Gly-72 with chymotrypsin.[53] An alternative site-specific assignment compares the ^{13}C NMR spectrum of the wild type with that of a site-directed mutant. As shown in Fig. 8C, the ^{13}C NMR peak of Ala-53 from [3-^{13}C]Ala-bR was assigned to a peak emerging from the difference spectrum between the ^{13}C NMR spectrum of A53V from that of the wild type.[23] The asterisked peak at 177.3 ppm in the ^{13}C CP-MAS NMR spectrum of [1-^{13}C]Ala-bR (Fig. 7B) was assigned unambiguously to Ala-53, with reference to A53V,

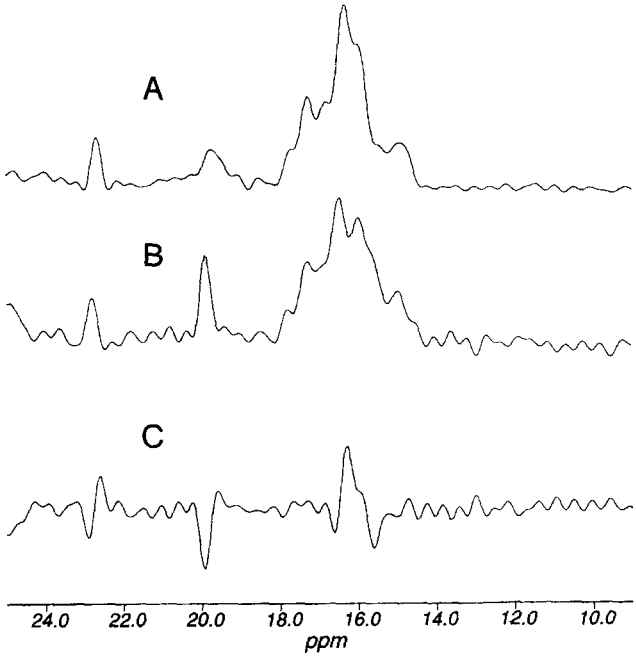

Fig. 8. ^{13}C CP-MAS NMR spectra of wild-type (A) and A53V mutant (B), of [3-^{13}C]Ala-bR, and (C) difference spectrum between A and B.[23]

and turned out to be very close to the peak position of $(Ala)_n$ in HFIP solution adopting the α_{II}-form (see Table 2). The carbonyl ^{13}C peak of Val-49 from [1-^{13}C]Val-bR was assigned in a similar manner using a V49A mutant.[59] This approach can be used as a general means of the peak assignment as long as no further conformational change accompanies site-directed mutagenesis.

The site-specific assignment of peaks is also possible with reference to the ^{13}C NMR spectra of ^{13}C-labelled chemically synthesized fragment of bR inserted into lipid bilayers, as long as the backbone conformation of such fragments does not deviate strongly from that of the corresponding transmembrane helices in bR. For this purpose, [3-^{13}C]Ala-14 and [3-^{13}C]Ala-18 fragments (6–42) and [3-^{13}C]Ala-51 fragment (36–71) of bR (see Fig. 5) were chemically synthesized and incorporated into bilayers of DMPC (dimyristoylphosphatidylcholine) (1:10 mole ratio) as illustrated for the [3-^{13}C]Ala-51 fragment (36–71) in Fig. 9.[60] The observed ^{13}C NMR signals from these peptides at 15.7–16.0 ppm in DMPC bilayers were displaced downfield by 0.4–0.9 ppm compared with those in the solid state and were ascribed to the conformational change to the α_{II}-helix form in the bilayers (see Table 1). This suggests that the α_{II}-helix form of bR as proposed by Krimm and Dwivedi[33] is well reproduced by its fragments on insertion into lipid bilayers at ambient

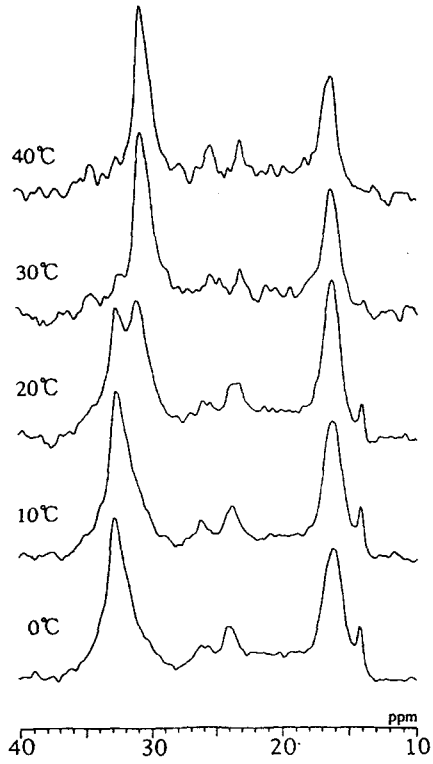

Fig. 9. ^{13}C CP-MAS spectra of [3-^{13}C]Ala^{18}-labelled fragment (36–71) of bR incorporated into DMPC bilayers.[60]

temperature, although no such form was taken into account in a model based on cryo-electron microscopy at low temperature.[51,52] It is emphasized that this approach provides a convenient means for gaining more detailed insight into the structure of α_{II}-helix in terms of whether thermal fluctuation at ambient temperature is responsible.

A pH titration study provides additional evidence of the local conformation. As mentioned above, the inner segment of the C-terminus involving Ala-228–Ala-235 participates in the formation of an α-helical conformation.[22,23,60] It was found that the α-helix domain is stabilized at neutral pH and/or at lower temperature such as 10°C. This helical domain was disrupted by lowering the pH to 4.25, since this is close to the pK_a of a nearby Glu residue which might stabilize the helix by electrostatic interaction.[58] Engelhard *et al.*[61] showed on the basis of ^{13}C CP-MAS NMR of [3-^{13}C]Pro-bR and [4-^{13}C]Pro-bR that the two parts of the C-terminus separated by the Pro residues occupy different

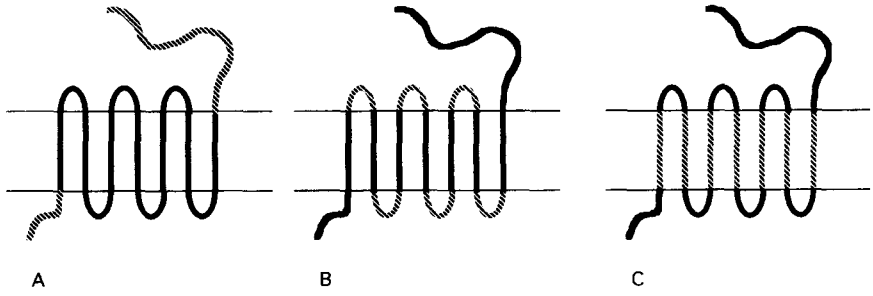

Fig. 10. Schematic representation of areas that are dynamically different (hatched lines): (A) region undergoing rapid fluctuation; (B) region fluctuating on the intermediate time scale; and (C) region undergoing slow fluctuation.

chemical environments and possess different flexibilities: the first part of the C-terminal tail is constrained and the other tail is freely mobile.

Dynamics. It appears convenient to classify the portions with different time scales of backbone motion into the following three kinds: (1) rapid motion with correlation time shorter than 10^{-8} s; (2) intermediate motion with correlation time of the order of 10^{-4}–10^{-5} s; and (3) slow motion with time scale of the order of 10^{-2} s. The presence of such varieties of motional flexibility seems to be characteristic in general of membrane proteins, consisting of seven transmembrane helices, and is closely related to their biological function.

The N- or C-terminal regions of bR (the hatched areas in Fig. 10A) acquire rapid isotropic reorientational motions with correlation times shorter than 10^{-8} s under the condition of full hydration, as demonstrated by the assignment of peaks to the random coil conformation, observation of intense and sharp signals by liquid-state high-resolution spectrometry,[54] ^{13}C spin–lattice relaxation times[22] measured by DD-MAS spectra, suppressed peak intensities owing to the presence of time-averaged dipolar interactions by CP-MAS NMR spectra, and time-averaged isotropic signals from ^{2}H quadrupole echo NMR.[55] The complete absence of the peaks from the C-terminal tail in CP-MAS NMR spectra was easily confirmed by observation of identical spectral profiles between the intact and papain-cleaved bR.[22,23] The Ala-2 signal at the N-terminus was unambiguously assigned to the random coil conformation in view of the ^{13}C NMR spectrum of the C-2 fragment consisting of the transmembrane A and B helices cleaved by chymotrypsin.[59] Nevertheless, the α-helix domain at the C-terminus protruding from the membrane surface is rather rigidly held, consistent with the fluorescence probe study by Renthal *et al.* with time scale of 13–25 ns.[62] It is interesting that no ^{13}C NMR signal from this region was visible even at temperatures below $-20°C$ due to interference with the proton decoupling frequency by either DD-MAS or CP-MAS NMR techniques.

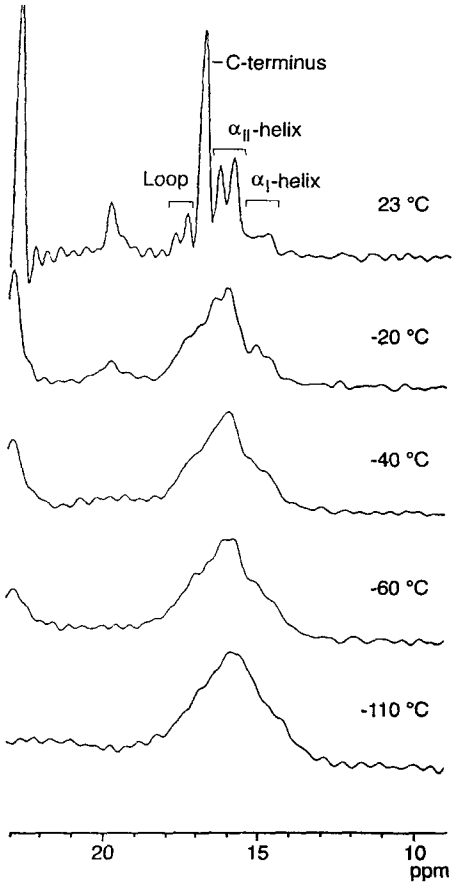

Fig. 11. Temperature-dependent change of ^{13}C DD-MAS NMR spectra of [3-^{13}C]Ala-bR.[24]

The protein backbone undergoing reorientation on the intermediate time scale (Fig. 10B) arises from the loop region, as demonstrated from the proton spin–lattice relaxation times in the rotating frame ($T_{1\rho}$) or partially suppressed peaks due to interference with proton decoupling frequency in both CP-MAS and DD-MAS NMR spectra. We found that the loop region acquired motional freedom on this time scale, as detected by $T_{1\rho}$ experiments, when retinal was removed from bR to yield bacterioopsin (bO). Acquisition of such hinge flexibility in the loop, which seems to be related to further movement of transmembrane helices in bO, seems to be essential for regeneration of bR together with binding of retinal to bO.

It is surprising to note that the well-resolved ^{13}C DD-MAS NMR signals of

bR were observed at ambient temperature and at −20°C but were broadened considerably at temperatures below −40°C, as illustrated in Fig. 11.[24] This situation was interpreted in terms of the presence of exchange processes with time scale of 10^{-2} s at ambient temperature among several slightly different conformations. Such an exchange process was strongly influenced by the manner of organization of the lipid bilayers, depending upon the presence or absence of cations responsible for electric shielding of negative charge at the polar head groups of lipids. In contrast, no such change was noted in the absence of these cations even at a temperature of −110°C. This means that the transmembrane helices are not always rigidly held together to form the trimer in the two-dimensional crystal of bR but undergo conformational fluctuation at ambient temperature.

Conformational changes due to interactions with retinal, lipids, detergents and light. Removal of retinal from bR resulted in substantial spectral change as illustrated in Fig. 6C.[23] The most notable change is that the loop signals split (17.8 and 17.3 ppm in the CP-MAS spectrum) as the peaks (areas of 1:3) in bR were changed to a single peak at 17.2 ppm. This is caused by a conformational change in particular at the loop region. In addition, some peaks in this area were shifted to peaks corresponding to transmembrane α-helices, reflecting the induced conformational change due to removal of retinal. Further, it was demonstrated that the residues at the loops (17.4 ppm) as well as the transmembrane α_{II}-helical region (15.9 ppm) acquired motional freedom of 10^{-5} s, as mentioned above. In a similar manner, we also showed that the resulting spectral change upon formation of complexes with retinal analogues such as retinol or β-ionone appears to differ with the type of complexes, depending on the type of analogues, reflecting the differential conformational change at the transmembrane helices or loops.

As mentioned above, the ^{13}C NMR signals from bR were broadened at temperatures below −20°C in the presence of 10 mmol/l NaCl (see Fig. 11);[24] in contrast, no such broadening was noted for bR suspended without salt even at −110°C. This means that added cations caused neutralization of negatively charged head group of the lipids, leading to more order in the lipid molecules as shown in the differential peak suppression of the terminal methyl groups of fatty acyl chains of the lipids with or without salts. This effect seems, in turn, to result in immobilization and irregular freezing of the protein backbone through the lipid–protein interaction. Thus, no line broadening of bR occurs without cations, as expected. Tanio *et al.*[63] examined how the secondary structure of bR is substantially modified by delipidation using a variety of detergent molecules; about 60–90% of lipids can be extracted by detergents such deoxycholate, CHAPS, and CHAPS–dodecyl maltoside without changing the trimeric structure of bR.[63] They showed[63] that the transmembrane helices and loop structure were appreciably modified by these detergents, as examined by means of ^{13}C chemical shifts. Further, they showed that most of the

secondary structure is retained for bR solubilized in Triton X-100 but that helical content was increased by solubilization with SDS.[63]

Metz and coworkers, from the ^{13}C NMR spectra of [11-^{13}C]Trp-bR,[64] found that the shift of Trp resonances in M state reflect a conformational change of the protein in forming the M intermediate, although detailed information on molecular mechanism is not yet available. Elucidation of the retinal chromophore in relation to the photo-cycle has been reviewed.[65,66] It has been previously demonstrated by diffraction methods[68] that some transmembrane helices move owing to formation of M or N intermediates in the photo-cycle. Such movements were also detected by spin-label experiments at the loop region.[69] Current NMR approaches can be also used to examine such a change following improvement in the site-specific spectral assignment for the loop region.

3.3. Biologically active peptides

The determination of the active conformations of biologically active peptides as information molecules, which may result from binding to a receptor molecule or to lipid bilayers, is of importance because these molecules often take disordered and very flexible forms in solution. Instead, it is more fruitful to study such molecules in the solid or membrane-bound state. In some instances it became clear that the crystalline polymorphs of interest are not always stable, especially when the crystalline form is stabilized by the presence of water or other solvent molecules. That a conformational change is induced by loss or freezing of solvent molecules is shown by a ^{13}C NMR study of Leu- and Met-enkephalins.[10,11] Displacement or splitting of ^{13}C or ^{15}N chemical shifts is useful for examining how the crystalline polymorph is stabilized, since exposure of hydrated samples to a stream of dry air might cause drying of the sample unless the sample rotor is tightly sealed. It is also crucial to grow crystals very carefully and to check by ^{13}C chemical shift what crystalline forms are actually grown.

Finally, it is emphasized that the empirical evaluation of the local conformation on the basis of chemical shift data is important prior to studies aimed at nonempirical evaluation of the three-dimensional structure, since it is easy to exclude in advance inherent errors arising from this method.[38,39]

4. NONEMPIRICAL EVALUATION OF THREE-DIMENSIONAL STRUCTURE

4.1. Recoupling of dipolar interaction

Accurate interatomic distances can be evaluated from dipolar interactions that are normally sacrificed by high-power decoupling and magic angle spinning

techniques.[70,71] Considerable improvement has been established by recoupling the dipolar interaction by either introducing RF pulses synchronized with the MAS rotor period[25] or adjusting the rotor frequency to the difference of chemical shift values of two isotopically labelled homonuclei.[26] REDOR[25,70] was employed to recouple relatively weak heteronuclear dipolar interactions under the MAS condition by applying a π pulse synchronously with the rotor period. Consequently, the transverse magnetization can no longer be refocused completely at the end of the rotor cycle, leading to the reduction of the echo amplitude. The extent of the reduction of the echo amplitude depends on the strength of the heteronuclear dipolar interaction. This method is used extensively to determine the relatively large interatomic distance of 2–8 Å. The rotational resonance (RR) phenomenon[26,72] is a recoupling of the homonuclear dipolar interaction under MAS conditions. When the rotor frequency is adjusted to the difference frequency or integer multiples of the frequency of the chemical shift values of two different resonance lines, line broadening and acceleration of the exchange rate of the longitudinal magnetization are observed. These effects depend strongly on the magnitude of the homonuclear dipolar interaction. Experimentally, homonuclear dipolar interactions can be determined by measuring the exchange rate of the longitudinal magnetization as a function of mixing time. In the RR method, the exchange rate depends not only on the homonuclear dipolar interactions but also on the zero-quantum transverse relaxation times and the anisotropy of the chemical shift interactions of both nuclei.[72] It is, therefore, quite complicated to determine the internuclear distances accurately by the RR method.

In addition to the REDOR and RR methods, many other methods have been developed and are anticipated to be used for the determination of three-dimensional structure. TEDOR (transferred echo double resonance)[73] is a similar method for determining heteronuclear dipolar interactions by observing the build-up of echo amplitude. In this method, the magnetization is transferred from one nucleus to the other through the heteronuclear dipolar interaction. It is, therefore, useful to eliminate natural abundant background signals. DRAMA (dipolar recovery at the magic angle)[74] is used to recouple the homonuclear dipolar interaction, which is normally averaged out by MAS, by applying $90°_x$ and $90°_{-x}$ pulses synchronously with the rotor period and hence internuclear distances between the two homonuclei can be determined. Since DRAMA depends strongly on the offset of carrier frequency, Griffin *et al.* developed MELODRAMA (melding of spin-locking and DRAMA)[75] by combining DRAMA with a spin lock technique. This technique improved reduction of the offset effect. SEDRA (simple excitation for the dephasing of rotational echo amplitude)[76] and RFDR (RF-driven dipolar recoupling)[77] are techniques that apply a π pulse synchronously with the rotor period. These techniques are also applied to determination of the homonuclear dipolar interaction under the MAS condition. Because these techniques are not sensitive to MAS frequency and offset effects, they are useful for determining

dipolar interaction using multidimensional NMR for multiple-site-labelled systems.

4.2. Theoretical background of REDOR experiment

Among the large number of experimental techniques so far described, the REDOR method has been used extensively to determine the secondary structure of biomolecules, because the data analysis required to yield the interatomic distance is the simplest. It is worthwhile describing the formalism of the REDOR experiment compared with use of the density operator to take account of the effect of finite pulse length and the three-spin system which is encountered on many occasions.

4.2.1. Simple description of REDOR experiment[70]

The heteronuclear dipolar interaction between I and S nuclei under MAS conditions can be expressed as

$$\mathcal{H}(t) = -\frac{\gamma_I \gamma_S h}{2\pi r^3}[3\cos^2\theta(t) - 1]I_Z S_Z \tag{1}$$

where γ_I and γ_S are the gyromagnetic ratios of I and S nuclei, respectively; h is Planck's constant; and r is the length of the I–S internuclear vector. $\theta(t)$ is the angle between the static magnetic field and r. When samples rotate with angular velocity ω_r about a direction inclined to the static magnetic field by the magic angle, the two frequencies due to the I–S dipolar interaction are expressed in angular velocity unit as

$$\omega^D(\alpha, \beta, t) = \pm\frac{D}{2}[\sin^2\beta\cos 2(\alpha + \omega_r t) - \sqrt{2}\sin 2\beta\cos(\alpha + \omega_r t)] \tag{2}$$

$$D = \frac{\gamma_I \gamma_S h}{2\pi r^3}$$

where α is the azimuthal angle and β is the polar angle defined by the internuclear vector with respect to the rotor axis. Because the integral of Eq. (2) over one rotor period is zero, the dipolar precession of magnetization returns to the same direction at every rotor period. Consequently, the rotational echo signals are refocused at every rotor period. When a π pulse is applied to the S nucleus that is coupled with the I nucleus in the middle of one rotor period, this pulse inverts the precession direction of the magnetization of the observed I nucleus. Consequently, the magnetization vector of the I nucleus can no longer return to the same direction after one rotor period. Therefore, the amplitude of the echo intensity decreases. The extent of the reduction of rotational echo amplitude will give information on the interatomic

distances. To evaluate REDOR echo amplitude theoretically, one has to average the precession frequency in the presence of a π pulse at the centre of the rotor period over one rotor cycle:

$$\overline{\omega^D(\alpha,\beta)} = \pm\frac{1}{T_r}\left[\int_0^{T_r/2}\omega^D\,dt - \int_{T_r/2}^{T_r}\omega^D\,dt\right]$$
$$= \pm\frac{D}{\pi}\sqrt{2}\sin 2\beta\sin\alpha \tag{3}$$

Therefore, phase angle, $\Delta\Phi(\alpha,\beta)$, for N_c rotor cycles is given by

$$\Delta\Phi(\alpha,\beta) = \overline{\omega^D(\alpha,\beta)}N_c T_r \tag{4}$$

where T_r is the rotor period. Finally, echo amplitude can be obtained by averaging over every orientation:

$$S_f = \frac{1}{2\pi}\int_\alpha\int_\beta \cos[\Delta\Phi(\alpha,\beta)]\,d\alpha\sin\beta\,d\beta \tag{5}$$

Therefore, normalized echo difference, $\Delta S/S_0$, is given by

$$\frac{\Delta S}{S_0} = \frac{S_0 - S_f}{S_0} = 1 - S_f \tag{6}$$

Experimentally, REDOR and full echo spectra were acquired for a variety of $N_c T_r$ values and the respective REDOR(S_f) and full echo(S_0) amplitudes were evaluated.

4.2.2. Rotational echo amplitude calculated by density operator approach

REDOR echo amplitude can be evaluated by density matrix operators using the pulse sequence for the REDOR experiment shown in Fig. 12.[38] The time evolution of the density operator, ρ_0, under heteronuclear dipolar interaction during one rotor period can be considered by taking the pulse length into account. The average Hamiltonian in the rotating frame over one rotor period is

$$\overline{\mathcal{H}} = \frac{1}{T_r}\left[\overline{\mathcal{H}_1(t)}\tau + \overline{\mathcal{H}_2(t)}t_w + \overline{\mathcal{H}_3(t)}\tau\right]$$
$$= \frac{D}{4\pi}\Big\{\sin^2\beta[\sin(2\alpha+\omega_r t_w) + \sin(2\alpha-\omega_r t_w) - 2\sin 2\alpha]$$
$$- 2\sqrt{2}\sin 2\beta[\sin(\alpha+\tfrac{1}{2}\omega_r t_w) + \sin(\alpha-\tfrac{1}{2}\omega_r t_w) + 2\sin 2\alpha]$$
$$- \sin^2\beta[\sin(2\alpha+\omega_r t_w) + \sin(2\alpha-\omega_r t_w)]\frac{4\omega_r^2 t_w^2}{4\omega_r^2 t_w^2 - \pi^2}$$

$$+\sqrt{2}\sin 2\beta[\sin(\alpha+\tfrac{1}{2}\omega_r t_w)+\sin(\alpha-\tfrac{1}{2}\omega_r t_w)]\frac{2\omega_r^2 t_w^2}{\omega_r^2 t_w^2-\pi^2}\Bigg\}I_z S_z$$

$$+\frac{D}{4\pi}\Bigg\{\sin^2\beta[\cos(2\alpha+\omega_r t_w)+\cos(2\alpha-\omega_r t_w)]\frac{2\pi\omega_r t_w}{4\omega_r^2 t_w^2-\pi^2}\Bigg\}I_z S_y$$

$$=aI_z S_z+bI_z S_y \tag{7}$$

where the same notation as in Eqs (1) and (2) is used. $\overline{\mathcal{H}_1(t)}$, $\overline{\mathcal{H}_2(t)}$ and $\overline{\mathcal{H}_3(t)}$ are the average Hamiltonians corresponding to the period shown in Fig. 12. Pulse length, t_w, is also considered in the calculations for the analysis of REDOR results. The density operator, $\rho(T_r)$, at T_r after evolution under the average Hamiltonian can be calculated as

$$\rho(T_r)=\exp(-i\overline{\mathcal{H}}T_r)\rho_0\exp(i\overline{\mathcal{H}}T_r) \tag{8}$$

where ρ_0 is considered to be I_y after the contact pulse. Finally, the transverse magnetization at T_r is given by

$$\langle I_y(T_r)\rangle = T_r\{\rho(T_r)I_y\}=\cos(\tfrac{1}{2}\sqrt{a^2+b^2}\,T_r) \tag{9}$$

Echo amplitude in a powder sample can be calculated by averaging over all orientations as follows:

$$S_f=\frac{1}{2\pi}\int_\alpha\int_\beta\langle I_y(T_r)\rangle\,d\alpha\sin\beta\,d\beta \tag{10}$$

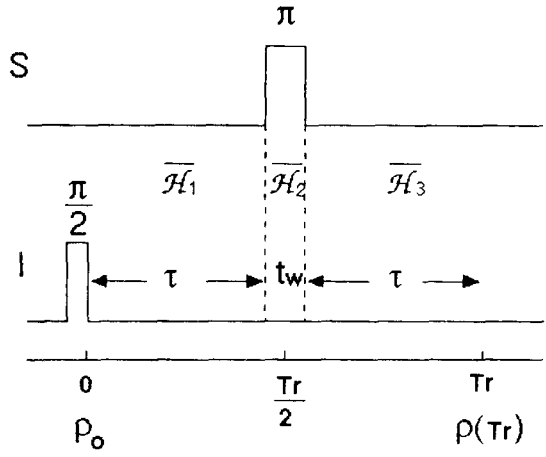

Fig. 12. Pulse sequence and timing chart of the REDOR experiment.

Therefore, normalized echo difference, $\Delta S/S_0$, can be obtained using Eq. (6). When the length of t_w is zero, Eq. (9) can be simplified as

$$\langle I_y(T_r)\rangle = \cos\left(\frac{D}{\pi}\sqrt{2}\sin 2\beta \sin\alpha\, T_r\right) \tag{11}$$

In this case, Eq. (10) is equivalent to Eq. (5) in the case of $N_c = 1$.

4.2.3. Echo amplitude in the three-spin system[39]

It is important to consider the case where the observed nucleus (I_1) is coupled with two other heteronuclei (S_1 and S_2). The Hamiltonian in the three-spin system is

$$\begin{aligned}\mathcal{H}(t) = &-\frac{\gamma_I\gamma_S h}{2\pi r_1^3}[3\cos^2\theta_1(t) - 1]I_{Z1}S_{Z1} \\ &-\frac{\gamma_I\gamma_S h}{2\pi r_2^3}[3\cos^2\theta_2(t) - 1]I_{Z1}S_{Z2}\end{aligned} \tag{12}$$

where r_1 and r_2 are the I_1–S_1 and the I_1–S_2 interatomic distances, respectively. $\theta_1(t)$ and $\theta_2(t)$ correspond to the angles between the magnetic field and the I_1–S_1 and the I_1–S_2 internuclear vectors, respectively. In the molecular coordinate system, the x axis is along the I_1–S_1 internuclear vector, and the S_1–I_1–S_2 plane is laid in the xy plane. The angle between I_1–S_1 and I_1–S_2 is denoted ζ. The coordinate system is transformed from the molecular axis system to the MAS system by applying a rotational transformation matrix $R(\alpha, \beta, \gamma)$ with Euler angles α, β, γ, followed by transformation from the MAS to the laboratory coordinate system by applying $R(\omega_r t, \theta_m, 0)$. Finally, $\cos\theta_1(t)$ and $\cos\theta(t)$ are calculated as

$$\begin{aligned}\cos\theta_1(t) = &(\cos\gamma\cos\beta\cos\alpha - \sin\gamma\sin\alpha)\sin\theta_m\cos\omega_r t \\ &-(\sin\gamma\cos\beta\cos\alpha + \cos\gamma\sin\alpha)\sin\theta_m\sin\omega_r t \\ &+\sin\beta\cos\alpha\cos\theta_m\end{aligned}$$

and

$$\begin{aligned}\cos\theta_2(t) = &[(\cos\gamma\cos\beta\cos\alpha - \sin\gamma\sin\alpha)\cos\zeta\sin\theta_m \\ &+(\cos\gamma\cos\beta\sin\alpha + \sin\gamma\cos\alpha)\sin\zeta\sin\theta_m]\cos\omega_r t \\ &-[(\sin\gamma\cos\beta\cos\alpha + \cos\gamma\sin\alpha)\cos\zeta\sin\theta_m \\ &+(\sin\gamma\cos\beta\sin\alpha - \cos\gamma\cos\alpha)\sin\zeta\sin\theta_m]\sin\omega_r t \\ &+\sin\beta\cos\alpha\cos\theta_m\cos\zeta + \sin\beta\sin\alpha\cos\theta_m\sin\zeta\end{aligned} \tag{13}$$

where θ_m is the magic angle between the spinner axis and the static magnetic field, and ω_r is the angular velocity of the spinner rotating about the magic angle axis. The four resonance frequencies in the system are given by

$$\begin{aligned} \omega^{D_1} &= \tfrac{1}{2}(D_1 - D_2) \\ \omega^{D_2} &= \tfrac{1}{2}(D_1 + D_2) \\ \omega^{D_3} &= -\tfrac{1}{2}(D_1 + D_2) \\ \omega^{D_4} &= -\tfrac{1}{2}(D_1 - D_2) \end{aligned} \tag{14}$$

These dipolar transition frequencies are time dependent and repeat the cycle in the spinning. In the REDOR pulse sequence, a π pulse is applied in the middle of the rotor period. In that case, the averaged angular velocity over one rotor cycle for each resonance is given by

$$\overline{\omega_i(\alpha, \beta, \gamma, T_r)} = \frac{1}{T_r}\left(\int_0^{T_r/2} \omega^{D_i} \mathrm{d}t - \int_{T_r/2}^{T_r} \omega^{D_i} \mathrm{d}t \right) \tag{15}$$

The phase accumulation after N_c cycles is given by

$$\Delta\Phi_i(\alpha, \beta, \gamma, N_c, T_r) = \overline{\omega_i(\alpha, \beta, \gamma, T_r)} N_c T_r \tag{16}$$

Finally, the REDOR echo amplitude after averaging over all Euler angles is calculated as

$$S_f = \frac{1}{8\pi^2} \sum_{i=1}^{4} \int_\alpha \int_\beta \int_\gamma [\cos \Delta\Phi_i(\alpha, \beta, \gamma, T_r)] \mathrm{d}\alpha \sin\beta \mathrm{d}\beta \mathrm{d}\gamma \tag{17}$$

The normalized echo difference, $\Delta S/S_0$, is given by Eq. (6). This relation depends strongly not only on the dipolar couplings of I_1–S_1 and I_1–S_2 but also on the angle S_1–I_1–S_2.[39]

4.3. Practical aspects of the REDOR experiment

Evaluation of accurate interatomic distances is essential to obtain the three-dimensional structure of peptides and proteins. Careful consideration of the following points is important in obtaining reliable interatomic distances by the REDOR experiment, although they have not always been properly taken into account in early papers. In practice, it is advisable to employ a standard sample such as [1-^{13}C, ^{15}N]glycine,[38] whose interatomic distance is determined to be 2.48 Å by neutron diffraction, to verify that the following instrumental conditions of given spectrometer are appropriate for determining accurate interatomic distances prior to every experiment.

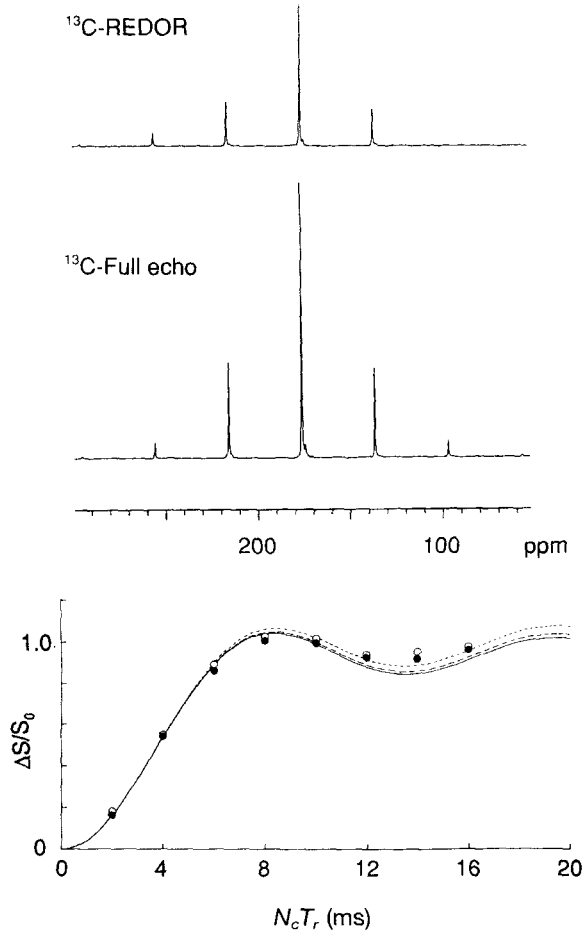

Fig. 13. ^{13}C REDOR and full echo spectra of [1-^{13}C,^{15}N]glycine as recorded with rotor frequency of 4000 Hz and N_cT_r of 4 ms (top) and plots of $\Delta S/S_0$ vs N_cT_r (bottom). Solid and open circles denote experimental points recorded using ^{15}N π pulses of 13.0 and 24.6 μs, respectively. Solid, broken and dotted lines are calculated using π pulses of δ, 13.0 and 24.6 μs, respectively.[38] C–N Interatomic distance was determined as 2.48 Å.

4.3.1. Infinite pulse length[38]

As described in Section 4.2.2, finite pulse length may affect the REDOR factor. In fact, this effect was experimentally observed and calculated using Eq.(10) as shown in Fig. 13. The REDOR parameter, $\Delta S/S_0$, as measured for 20% [1-^{13}C, ^{15}N]Gly was plotted for ^{15}N π pulse lengths of 13.0 μs for the experiment and 24.6 μs (chosen to satisfy 10% rotor cycle) as a function of N_cT_r, with the

calculated lines, using the δ pulse length and finite lengths (13.0 and 24.6 μs) of the π pulse. It turned out that the finite length of the ^{15}N π pulse does not significantly affect the REDOR effect provided that the pulse length is less than 10% of the rotor cycle at the rotor frequency of 4000 Hz.

4.3.2. Compensation of pulse length and power

There are many opportunities for RF power to fluctuate during the acquisition of REDOR experiments. It is therefore very important for the RF power to be stabilized after waiting for a certain time, otherwise the π pulse will not remain an exact π pulse over a long time. Consequently, if the RF power decreases, the REDOR factor is greatly decreased, to yield relatively longer interatomic distances. Compensation of the instability of such RF power by pulse sequence must be free from long-term fluctuations due to amplifiers. Accordingly, *xy*-4 and *xy*-8 pulse sequences were developed, and an *xy*-8 pulse is known to be the best sequence for compensating the fluctuation of the RF power.[78]

4.3.3. Contribution from natural-abundance nuclei

Since the early stages of REDOR experiments, the contribution of natural-abundance nuclei has been considered as the major source of error in distance measurement.[79] The observed dipolar interaction could in principle be modified by the presence of such neighbouring natural-abundance nuclei. This effect was originally taken into account by simply calculating the $\Delta S/S_0$ value as an isolated pair and summing proportionally to the natural-abundance fraction.[79] Careful analysis of the three-spin system as described in Section 4.2.3 indicates that this sort of simple addition may result in serious overestimation of the natural-abundance effect, yielding shorter distances.[39] The most accurate way to consider the natural-abundance effect is, therefore, to treat the whole spin system as a three-spin system by taking account of the neighbouring carbons in addition to the labelled pair. In practice, the contribution from natural-abundance nuclei can be ignored[39] for ^{13}C REDOR but not for ^{15}N REDOR, because the proportional natural abundance of ^{13}C nuclei is higher than that of ^{15}N nuclei.

4.3.4. Contribution from neighbouring labelled nuclei

Doubly labelled samples are usually used in REDOR experiments to determine the interatomic distances between the labelled nuclei. This means that dipolar interaction from the labelled nuclei in the neighbouring molecules should be taken into account with the dipolar interaction of the observed pair. This contribution could be significant if the observed distance is large because of the presence of many contributions from nearby nuclei, but is completely

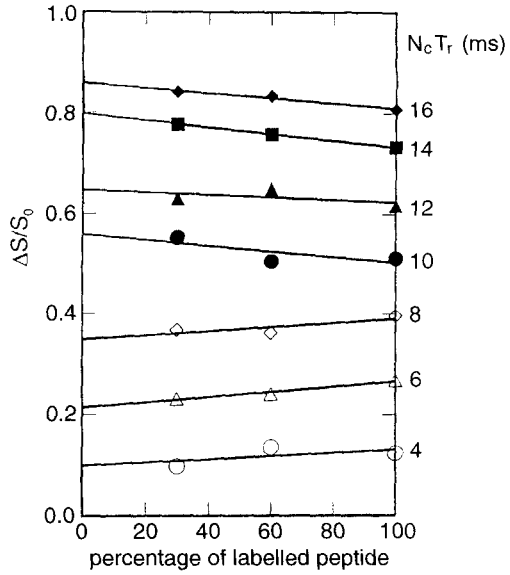

Fig. 14. Plot of $\Delta S/S_0$ against various percentages of a labelled peptide in an unlabelled one. The solid lines were obtained by least-squares fits of the experimental points.[39]

removed by diluting the labelled sample into the sample of natural-abundance molecules. Sensitivity of the signals has to be sacrificed if one wants to remove the effect completely. It is advised to evaluate the REDOR factors at infinite dilution by extrapolating the data of stepwise-diluted samples (60%, 30%, etc.) without losing sensitivity (Fig. 14).[39] Alternatively, the observed plots of $\Delta S/S_0$ values against the corresponding $N_c T_r$ values for the sample without dilution can be fitted with the theoretical curve obtained from three-spin systems, although the accuracy is not always improved to the level of the dilution experiment.

4.3.5. T_2 effect

The transverse magnetization in REDOR experiments decays as a function of ^{1}H decoupling field.[80,81] Dipolar decoupling may be strongly interfered with by molecular motion, if any, when motional frequency is of the same order as the decoupling field, and hence the transverse relaxation times (T_2) are significantly shortened. It was found that the T_2 values of the carbonyl-carbon in Leu-enkephalin were very short because of the presence of backbone motion.[82] This is a serious problem for REDOR, especially for the long-distance pair, because the S/N ratio is significantly degraded. In such a case, it is worth considering measuring the ^{13}C REDOR signal under a strong

decoupling field to lengthen the transverse relaxation times. It is also useful to measure the signals at low temperature to reduce the motional frequency.

4.3.6. Sample packing

In the commercial spectrometer, the rotor is designed to allow as large as possible a sample volume to give better sensitivity. Obviously, this arrangement causes serious problems of H_1 inhomogeneity, which results in a broad distribution of the lengths of the 90° pulses. This problem is especially serious for REDOR experiments, because a number of π pulses are applied in the REDOR pulse sequence. As a result, the pulse error can accumulate during acquisition to give serious error, as shown in Fig. 15. In particular, samples located in the top or bottom part of the sample rotor feel a quite weak RF field.[38,83] This causes a considerable reduction of the REDOR factor. Consequently, the REDOR factor will be reduced when the sample is filled all the way along the sample rotor. This effect should be considered seriously in the case of experiments using commercial spectrometers. It is therefore recommended to fill the sample only in the centre part of the coil, as in a multiple-pulse experiment, to obtain accurate interatomic distances by the REDOR method.

4.4. Three-dimensional structure based on accurately determined interatomic distances

4.4.1. Peptides

Schaefer *et al.*[84] synthesized an emerimicine fragment (Ac-Phe-[1-^{13}C]MeA^2-MeA-MeA-Val-[^{15}N]Gly^6-Leu-MeA-MeA-OBz). ^{13}C–^{15}N interatomic distance four residues apart was determined to be 4.07 Å by the REDOR method. It was concluded that the structure is an α-helix, because the expected distance is 4.13 and 5.87 Å in the cases of an α-helix and a 3_{10}-helix, respectively. In a similar manner, the ^{19}F–^{13}C interatomic distance was measured for the ^{19}F, ^{13}C and ^{15}N triply labelled fragment (^{19}FCH$_2$CO-Phe-MeA-MeA-[1-^{13}C]MeA-[^{15}N]Val-Gly-Leu-MeA-MeA-OBzl)[85] and found to be 7.8 Å by the TEDOR method[73] after transferring the magnetization from ^{15}N to ^{13}C. Because the TEDOR method makes it possible to eliminate background signals due to natural-abundance nuclei, quite remote interatomic distances can be determined. Schaefer *et al.* also attempted to determine the C–N interatomic distances of an ion channel peptide, Val^1-[1-^{13}C]Gly^2-[^{15}N]Ala^3-gramicidin A, in DMPC bilayer.[86] The dipolar interaction of the peptide in the lipid bilayer showed much smaller values than in the powder state, because the helix motions significantly averaged the dipolar interactions. The extent of the scaling of the dipolar interaction shows that gramicidin A consists of the dimer

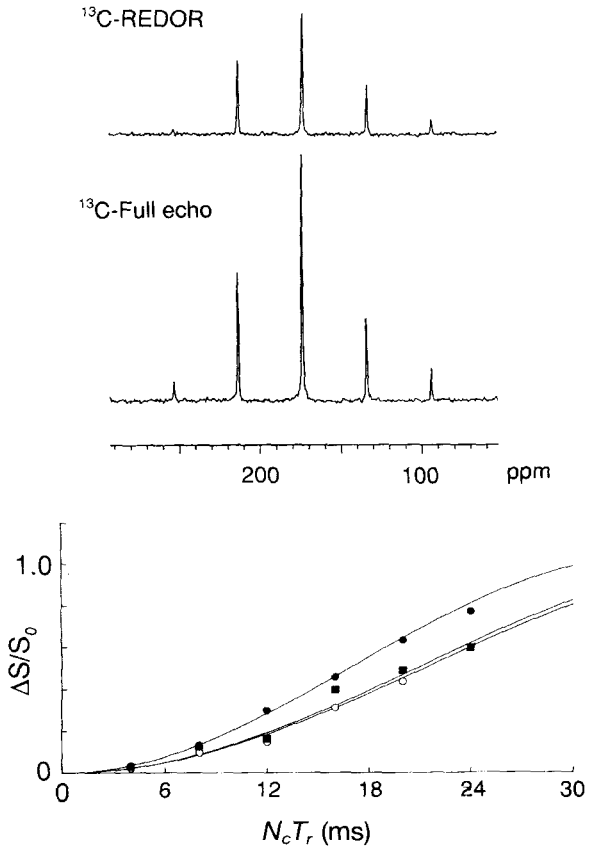

Fig. 15. ^{13}C REDOR and full echo spectra of [1-^{13}C]N-Ac-Pro-Gly-[^{15}N]Phe with an N_cT_r of 16 ms (top) and plots of $\Delta S/S_0$ vs N_cT_r (bottom). Solid circles, solid squares and open circles denote experimental points from samples filled in the central 50% of the total filling volume of a 5 mm o.d. rotor, and the fully packed state of 5.0 and 7.5 mm rotors, respectively. The resulting interatomic distances were determined as 4.07, 4.37 and 4.45 Å, respectively.[38]

with a single helix. A magainin analogue in membrane was investigated by ^{13}C, ^{31}P REDOR.[86a] The result indicates that the α-helical Ala_{19}-magainin 2 amide is bound to the head group of lipid bilayers.

Complete three-dimensional structure can be determined by combining a variety of interatomic distances.[38,86–89] Garbow *et al.* synthesized ^{13}C,^{15}N-labelled peptides labelled at different positions. These interatomic distances were converted to the torsion angles, to yield the secondary structure.[87,88] Naito *et al.* systematically applied this technique to elucidate the three-dimensional structure of *N*-Ac-Pro-Gly-Phe.[38] They proposed that the carbonyl-carbon of

the $(i-1)$ residue and the amino-nitrogen of $(i+1)$ residue should be labelled with ^{13}C and ^{15}N, respectively. Namely, [1-^{13}C]N-Ac-Pro-[^{15}N]Gly-Phe (I), *N*-Ac-[1-^{13}C]Pro-Gly-[^{15}N]Phe (II) and [1-^{13}C]*N*-Ac-Pro-Gly-[^{15}N]Phe (III) were synthesized and the resulting distances were determined to be 3.24, 3.43 and 4.07 Å, respectively, utilizing the REDOR factor obtained for the infinitely diluted state to obviate error from the contribution of neighbouring labelled nuclei. No correction from the contribution of natural-abundance nuclei was necessary. Surprisingly, these distances did not agree well with the values obtained from X-ray diffraction study[90] available at that time, the maximum discrepancy between them being 0.5 Å. This value seemed to be much larger than the expected error in the REDOR experiment(± 0.05 Å). The reason the distances were so different was explained by the fact that the crystal used for the REDOR experiments was different from that reported by X-ray diffraction. To check the accuracy of the REDOR experiment, they performed X-ray diffraction on the same crystals used for the REDOR experiment and found that the distances from the new crystalline polymorph agreed well within the accuracy of 0.05 Å as shown in Table 3. Conformational maps of the possible combinations of the torsion angles of Pro and Gly residues are calculated as shown in Fig. 16a. Further, chemical shift values were measured for C_β and C_γ carbons of Pro residues. According to the relation reported by Siemion,[91] the $\Delta\beta\gamma$ value indicates that the ψ angle is $-13°$. Since ϕ of the Pro residue will be $-75°$, which gives the minimum energy in the residue, the torsion angles of the Pro residue were uniquely determined to be $(-75°, -28°)$. Using these torsion angles, conformational maps were calculated as shown in Fig. 16b. Finally, two pairs of torsion angles were selected as $(-112°, 48°)$ and $(-112°, -48°)$. Energy minimization by molecular mechanics yielded the structure of the β-turn I structure, as shown in Fig. 17. They found that the three-dimensional structure of this peptide was well reproduced by a molecular dynamics simulation taking into account of all the intermolecular interactions in crystals.[38,38a]

Elucidation of the three-dimensional structure of an opioid peptide Leu-enkephalin crystal, Tyr-Gly-Gly-Phe-Leu, grown from MeOH–H_2O mixed solvent by the REDOR method[92] alone poses an additional challenge as to how to reveal the three-dimensional structure of a more complicated system. Six differently labelled Leu-enkephalin molecules were synthesized following the strategy described above, and the interatomic distances were accurately determined. It turned out, however, that the crystalline polymorph under consideration was very easily converted into another form. It was therefore necessary to check whether the six differently labelled samples were all of the same crystalline polymorph by means of the ^{13}C chemical shifts. Meaningless data can be obtained if this precaution is not taken. When the distance data were converted to yield the torsion angles, unique combinations of torsion angles in the corresponding conformational map were determined using the chemical shift data as additional constraints, as discussed in Section 2. The three-dimensional structure was thus determined as shown in Fig. 18 and this

Table 3. C–N Interatomic Distances (Å) determined by REDOR experiments as compared with those by X-ray diffraction and molecular dynamics.

	Experimental			Calculated		
	REDOR	X-ray			Molecular dynamics	
Labelled peptides[a]	Orthorhombic	Orthorhombic	Monoclinic[c]	Energy-minimized[b]	Orthorhombic	Monoclinic
I	3.24 ± 0.05 (3.43 ± 0.05)[d]	3.19	3.76	3.17	3.22 ± 0.10	3.63 ± 0.10
II	3.43 ± 0.05 (3.66 ± 0.05)	3.35	3.21	3.57	3.32 ± 0.10	3.33 ± 0.10
III	4.07 ± 0.05 (4.45 ± 0.05)	3.99	3.91	4.17	3.92 ± 0.12	3.83 ± 0.10

[a] I = [1-^{13}C]*N*-Ac-Pro-[^{15}N]Gly-Phe. II = *N*-Ac-[1-^{13}C]Pro-Gly-[^{15}N]Phe. III = [1-^{13}C]*N*-Ac-Pro-Gly-^{15}N]Phe.
[b] Energy-minimized structure based on REDOR data.
[c] Ref. 90.
[d] Data from Ref. 39 based on fully packed 7.5 mm rotor system.

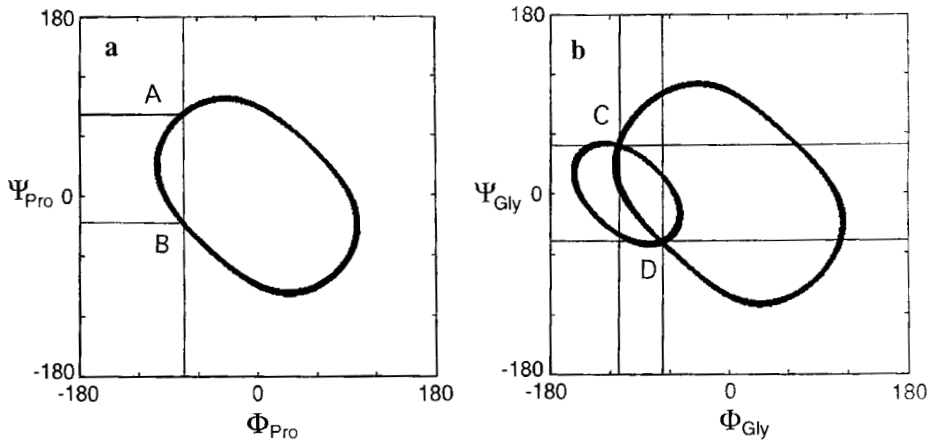

Fig. 16. Conformation maps for the torsion angles in (a) Pro and (b) Gly residues. The A and B regions were obtained from the intersections of the constraint of ϕ angles of the Pro residue. The C and D regions were then obtained by a cross section of the two types of conformation maps.[38]

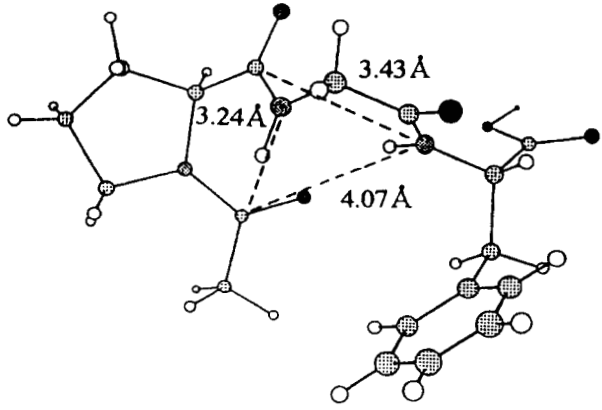

Fig. 17. Optimized conformation of *N*-acetyl-Pro-Gly-Phe as obtained by the minimization of energy from the initial form as deduced from the REDOR experiment.[38]

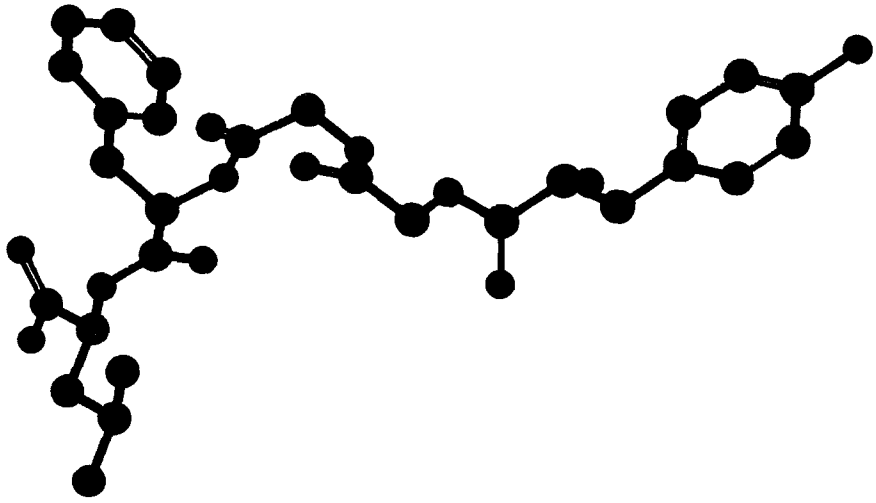

Fig. 18. Three-dimensional structure of Leu-enkephalin crystal determined by the REDOR experiment.[92]

structure was not the same as that previously determined by X-ray diffraction because of the new crystalline polymorph.

The RR method has been used to characterize the structure of fragments of amyloid.[93,94] Griffin *et al.* synthesized a β-amyloid fragment (H_2N-Leu-Met-Val-Gly-Gly-Val-Val-Ile-Ala-CO_2H) that is the C-terminus of the β-amyloid protein. The structure of this molecule was determined from the ^{13}C–^{13}C interatomic distances and the ^{13}C chemical shift values. As shown in Fig. 19, the α-carbon of residue i and the carbonyl-carbon of residue $(i + 1)$ were doubly labelled and the interatomic distance $A[\alpha_i, i + 1]$ was observed using the rotational resonance method. Similarly, interatomic distances of $B[i, \alpha(i + 2)]$, $C[i, \alpha(i + 3)]$ were also determined. Since the rotational resonance signal of A did not show a dilution effect, there is no intermolecular contribution. On the other hand, B and C show strong intermolecular contributions from B^* and C^*. Therefore, it was concluded that the fragment formed an antiparallel β-sheet. Furthermore, the intermolecular contribution shown by the arrow in Fig. 19 indicates that β-strands consist of antiparallel β-sheet forming hydrogen bonds with the position that has slipped from the N-terminus position. It is interesting that the information on the intermolecular contribution made it possible to elucidate the assembly of the amyloid molecule.

4.5.2. Protein–ligand complexes

It is important to determine the structure of the binding sites of ligand protein complexes. This kind of information can also be obtained from interatomic

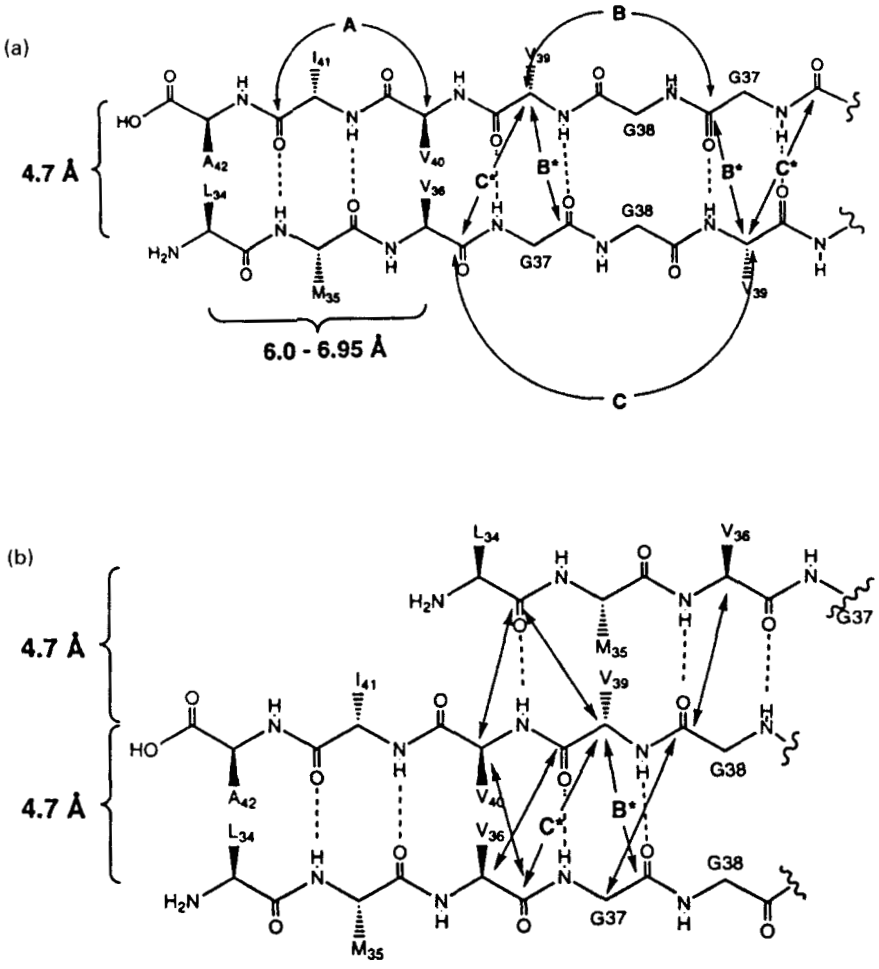

Fig. 19. Intramolecular and intermolecular ^{13}C–^{13}C internuclear distances in β-amyloid peptide fragment determined by the RR experiment. (a) Two idealized antiparallel β-strands. A, B and C denote interatomic pairs of $[\alpha i, i+1]$, $[i, \alpha(i+2)]$ and $[i, \alpha(i+3)]$ of α- and carbonyl-carbons, respectively. B* and C* indicate the distances of the same pairs between strands. (b) Possible interstrand alignment and the interatomic distances between strands.[93]

distances.[95–97] Schaefer *et al.*[95] tried to determine the structure of the binding site of glutamine-binding protein (GlnBP). Although the structure of GlnBP has been determined by X-ray diffraction, that of the complex with L-glutamine had not been determined. This protein was uniformly labelled with ^{15}N isotopes and L-[5-^{13}C]Gln was used as a ligand molecule. In the complex, the

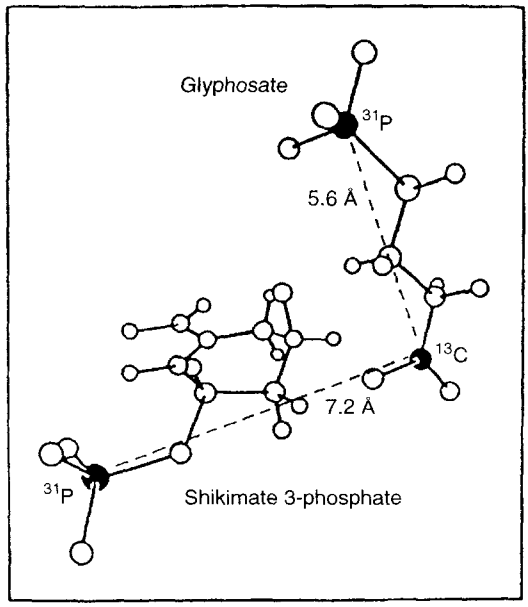

Fig. 20. Possible structure of the S3P–glyphosate complex bound to EPSP synthase.[96a]

interatomic distances between ^{15}N of the imidazole ring of His-156 and C_δ of L-Gln, and $^{15}N_\zeta$ of Lys-115 were determined using the REDOR method. In addition, the interatomic distances between the $^{19}F_{\varepsilon 1}$- and $^{19}F_{\varepsilon 2}$-labelled Tyr-143 and Tyr-185 and ^{15}N of His-156 were also determined. Using this distance information together with molecular dynamics calculations, the three-dimensional structure of the L-Gln complex was reconstructed. It turned out that $N_{\varepsilon 2}$-H of His-156 and N_ζ-H of Lys-115 form hydrogen bonds with L-Gln. It is further revealed that the size of the cavity is small compared with the cavity of the unligated GlnBP.

5-Enolpyruvylshikimate-3-phosphate (EPSP) synthase is an enzyme that catalyses the condensation reaction between shikimate 3-phosphate (S3P) and phosphoenolpyruvate (PEP). The reaction mechanism at the molecular level is not well understood. This reaction can be inhibited in the presence of S3P by glyphosate. The S3P–glyphosate complex is known to be an analogue of the enzyme–substrate transition state. Schaefer *et al.*[96] determined the interatomic distance between ^{13}C and ^{31}P of glyphosate to be 7.2 Å by the REDOR method. As shown in Fig. 20, the glyophosate and S3P are located close to each other. Furthermore, the intramolecular P–C distance was determined to be 5.6 Å, indicating that the molecule is an extended structure in the vicinity of the enzyme molecule. Although it is possible to determine the interatomic distance

by the REDOR method in the case of enzyme–analogue complex because the reaction will not proceed, it is difficult to measure the interatomic distances of the enzyme–substrate complex because they will react in a short time. Evans *et al.*[97] froze the reaction instantaneously and the structure of the intermediate state of the complex could be observed by the REDOR method. The results indicate that the substrate was closely located near both the arginine and lysine residues.

4.5.3. Membrane proteins

Retinal is linked to Lys-216 by formation of a Shiff base and photoisomerization is initiated by absorption of a photon and transfer of the various photointermediates in the photo-cycle of bacteriorhodopsin. A proton pump mechanism was also promoted by the subsequent conformational change of the protein. Griffin *et al.*[98] regenerated the [^{13}C-14]retinal in the [^{13}C]Lys-216-labelled bacteriorhodopsin. They determined the interatomic distance by a rotational resonance method. The interatomic distances of C14–C_ε corresponding to bR555 and bR568 were determined to be 3.0 and 4.1 Å, respectively. This indicates that bR555 adopts a C=N *syn* configuration and bR568 adopts C=N *anti* configuration. The interatomic distance was also determined for the M intermediate to be 3.9 Å, indicating that the M state also adopts C=N *anti* configuration.[99] The N state could be trapped by irradiation at −60°C under high ionic strength (0.1 mol/l NaCl) and at high pH (10.0). The K and L states can be trapped at lower temperature. The ^{15}N chemical shift values of [ε-^{15}N]Lys-216 indicate that retinal adopts the 13-*cis*, C=N *anti* configuration.[100]

5. CONCLUDING REMARKS

We have emphasized practical aspects of the solid-state NMR approach to the problem of determining secondary or three-dimensional structures of fibrous and membrane proteins as well as biologically active peptides. It is demonstrated that local secondary structures of fibrous or membrane proteins are easily evaluated by careful inspection of chemical shift data with reference to the conformation-dependent chemical shifts of the respective amino acid residues as major constraints. We demonstrated several strategies such as selective isotope labelling, either by biosynthesis or chemical synthesis of fragments, site-directed mutagenesis, proteolytic digestion, pH titration, etc., for achieving assignments of individual peaks from membrane proteins to specific amino acid residues of interest, taken from illustrative examples from studies on bacteriorhodopsin. Undoubtedly, accurate determination of the interatomic distances is a prerequisite to provide distance constraints that are only available in the solid state for use in constructing the three-dimensional

structure of peptides and proteins. A protocol for the REDOR experiment for this purpose was described in depth from both theoretical and practical points of view. In addition, an efficient procedure for deriving the three-dimensional structure from these distance constraints was described together with a review of related topics reported to date. We believe that the approach described here is a most promising and valuable tool for revealing the three-dimensional structure of membrane proteins in general.

ACKNOWLEDGEMENTS

The authors are indebted to many collaborators listed in the references, especially to our graduate students, Satoru Yamaguchi, Shigeki Kimura, Michikazu Tanio, Miya Kamihira and Katsuyuki Nishimura, and to Professor Janos Lanyi of University of California, Irvine and Professor Richard Needleman of Wayne State University, for allowing us to cite their collaborative unpublished data.

REFERENCES

1. S. J. Opella, P. L. Stuart and K. G. Valentine, *Q. Rev. Biophys.*, 1987, **91**, 7.
2. S. O. Smith and R. G. Griffin, *Annu. Rev. Phys. Chem.*, 1988, **39**, 511.
3. L. E. Chirlian and S. J. Opella, *Adv. Magn. Reson.*, 1990, **14**, 183.
4. S. J. Opella, *Annu. Rev. Phys. Chem.*, 1994, **45**, 659.
5. S. O. Smith and O. B. Peersen, *Annu. Rev. Biophys. Biomol. Struct.*, 1992, **21**, 25.
6. T. A. Cross, *Annu. Rep. NMR Spectrosc.*, 1994, **21**, 123.
7. H. Saitô, R. Tabeta, A. Shoji, T. Ozaki, I. Ando and T. Asakura, in *Magnetic Resonance in Biology and Medicine* (ed. G. Govil, C. L. Kheterapal and A. Saran), p. 195, Tata McGraw-Hill, New Delhi, 1985.
8. H. Saitô, *Magn. Reson. Chem.*, 1986, **24**, 835.
9. H. Saitô and I. Ando, *Annu. Rep. NMR Spectrosc.*, 1989, **21**, 209.
10. A. Naito, M. Kamihira, S. Tuzi and H. Saitô, *J. Phys. Chem.*, 1995, **99**, 12041.
11. M. Kamihira, A. Naito, K. Nishimura, S. Tuzi and H. Saitô, *J. Phys. Chem.*, submitted.
12. H. Saitô, R. Tabeta, A. Shoji, T. Ozaki and I. Ando, *Macromolecules*, 1983, **16**, 1050.
13. A. Shoji, T. Ozaki, H. Saitô, R. Tabeta and I. Ando, *Macromolecules*, 1984, **17**, 1472.
14. H. Saitô, R. Tabeta, A. Shoji, T. Ozaki, I. Ando and T. Miyata, *Biopolymers*, 1984, **23**, 2279.
15. H. Saitô, R. Tabeta, T. Asakura, Y. Iwanaga, A. Shoji, T. Ozaki and I. Ando, *Macromolecules*, 1984, **17**, 1405.
16. H. Saitô, M. Ishida, M. Yokoi and T. Asakura, *Macromolecules*, 1990, **23**, 83.
17. M. Ishida, T. Asakura, M. Yokoi and H. Saitô, *Macromolecules*, 1990, **23**, 88.
18. H. Saitô and M. Yokoi, *J. Biochem. (Tokyo)*, 1992, **111**, 376.
19. S. Spera and A. Bax, *J. Am. Chem. Soc.*, 1981, **113**, 5490.
20. D. S. Wishart and B. D. Sykes, *Methods Enzymol.*, 1994, **239**, 363.
21. S. Tuzi, A. Naito and H. Saitô, *Eur. J. Biochem.*, 1993, **218**, 837.
22. S. Tuzi, A. Naito and H. Saitô, *Biochemistry*, 1994, **33**, 15046.
23. S. Tuzi, S. Yamaguchi, A. Naito, R. Needleman, J. K. Lanyi and H. Saitô, *Biochemistry*, 1996, **35**, 7520.

24. S. Tuzi, A. Naito and H. Saitô, *Eur. J. Biochem.*, 1996, **239**, 294.
25. T. Gullion and J. Schaefer, *J. Magn. Reson.*, 1989, **81**, 196.
26. D. P. Raleigh, M. H. Levitt and R. G. Griffin, *Chem. Phys. Lett.*, 1988, **146**, 71.
27. D. S. Wishart, C. G. Bigam, A. Holm, R. S. Hodges and B. D. Sykes, *J. Biomol. NMR*, 1995, **5**, 67.
28. I. Ando, H. Saitô, R. Tabeta, A. Shoji and T. Ozaki, *Macromolecules*, 1984, **17**, 457.
29. N. Asakawa, H. Kurosu and I. Ando, *J. Mol. Struct.*, 1994, **323**, 279.
30. A. C. de Dios, J. G. Pearson and E. Oldfield, *Science*, 1993, **260**, 1491.
31. D. Jiao, M. Barfield and V. J. Hruby, *J. Am. Chem. Soc.*, 1993, **115**, 10883.
32. A. C. de Dios and E. Oldfield, *J. Am. Chem. Soc.*, 1994, **116**, 5307.
33. S. Krimm and A. M. Dwivedi, *Science*, 1982, **216**, 407.
34. J. R. Parrish, Jr and E. R. Blout, *Biopolymers*, 1972, **11**, 1001.
35. H. Vogel and W. Gartner, *J. Biol. Chem.*, 1987, **262**, 11464.
36. N. J. Gibson and J. Y. Cassim, *Biochemistry*, 1989, **28**, 2134.
37. T. Asakura, A. Kuzuhara, R. Tabeta and H. Saitô, *Macromolecules*, 1985, **18**, 1841.
38. A. Naito, K. Nishimura, S. Kimura, S. Tuzi, M. Aida, N. Yasuoka and H. Saitô, *J. Phys. Chem.*, 1996, **100**, 14995.
38a. M. Aida, A. Naito and H. Saitô, *J. Mol. Struct. Theochem.*, 1996, **388**, 187.
39. A. Naito, K. Nishimura, S. Tuzi and H. Saitô, *Chem. Phys. Lett.*, 1994, **229**, 506.
40. J. Kummerlen, J. D. van Beek, F. Vollrath and B. H. Meier, *Macromolecules*, 1996, **29**, 2920.
41. D. H. Hijirida, K. G. Do, C. Michal, S. Wong, D. Zax and L. W. Jelinski, *Biophys. J.*, 1996, **71**, 3442.
42. W. P. Rothwell and J. S. Waugh, *J. Chem. Phys.*, 1981, **74**, 2721.
43. A. Naito, S. Tuzi and H. Saitô, *Eur. J. Biochem.*, 1994, **224**, 729.
44. A. Shoji, S. Ando, S. Kuroki, I. Ando and G. A. Webb, *Annu. Rep. NMR Spectrosc.*, 1993, **26**, 55.
45. S. Tuzi, K. Shinzawa-Itoh, T. Erata, A. Naito, S. Yoshikawa and H. Saitô, *Eur. J. Biochem.*, 1992, **208**, 713.
46. T. Tsukihara, H. Aoyama, E. Yamashita, T. Tomizaki, H. Yamaguchi, K. Shinzawa-Itoh, R. Nakashima, R. Yaono and S. Yoshikawa, *Science*, 1995, **269**, 1069.
47. T. Tsukihara, H. Aoyama, E. Yamashita, T. Tomizaki, H. Yamaguchi, K. Shinzawa-Itoh, R. Nakashima, R. Yaono and S. Yoshikawa, 1996, *Science*, **272**, 1136.
48. W. Stoeckenius and R. A. Bogomolni, *Annu. Rev. Biochem.*, 1982, **52**, 587.
49. J. K. Lanyi, *Biochim. Biophys. Acta*, 1993, **1183**, 241.
50. T. M. Savarese and C. M. Fraser, *Biochem. J.*, 1992, **283**, 1.
51. R. Henderson, J. M. Baldwin, T. A. Ceska, F. Zemlin, E. Beckmann and K. H. Downing, *J. Mol. Biol.*, 1990, **213**, 899.
52. N. Grigorieff, T. A. Ceska, K. H. Downing, J. M. Baldwin and R. H. Henderson, *J. Mol. Biol.*, 1996, **259**, 393.
53. T. Tuzi, A. Naito and H. Saitô, unpublished.
54. J. L. Bowers and E. Oldfield, *Biochemistry*, 1988, **27**, 5156.
55. M. A. Keniry, H. S. Gutowsky and E. Oldfield, *Nature*, 1984, **307**, 383.
56. B. L. Lewis, G. S. Harbison, J. Herzfeld and R. G. Griffin, *Biochemistry*, 1985, **24**, 4671.
57. J. Herzfeld, C. M. Mulliken, D. J. Siminovitch and R. G. Griffin, *Biophys. J.*, 1987, **52**, 855.
58. S. Yamaguchi, S. Tuzi, T. Seki, M. Tanio, R. Needleman, J. K. Lanyi, A. Naito and H. Saitô, *J. Biochem. (Tokyo)*, 1998, **123**, 79.
59. T. Tuzi, K. Yokota, A. Naito and H. Saitô, unpublished.
60. A. Naito, S. Kimura, S. Tuzi and H. Saitô, *Peptide Chemistry 1996* (ed. C. Kitada), p. 369, Protein Research Foundation, Osaka, 1997.
61. M. Engelhard, S. Finkler, G. Metz and F. Siebert, *Eur. J. Biochem.*, 1996, **235**, 526.
62. R. Renthal, N. Dawson, J. Tuley and P. Horowitz, *Biochemistry*, 1983, **22**, 5.

63. M. Tanio, S. Tuzi, S. Yamaguchi, H. Konishi, A. Naito, R. Needleman, J. K. Lanyi and H. Saitô, submitted.
64. G. Metz, F. Siebert and M. Engelhard, *FEBS Lett.*, 1992, **303**, 237.
65. L. Zheng and J. Herzfeld, *J. Bioenerg. Biomembrane*, 1992, **24**, 139.
66. M. Engelhard and B. Bechinger, *Israel J. Chem.*, 1995, **35**, 273.
67. N. Grigorieff, E. Beckmann and F. Zemlin, *J. Mol. Biol.*, 1995, **254**, 404.
68. J. Vonck, *Biochemistry*, 1996, **35**, 5870.
69. H.-J. Steinhoff, R. Mollaaghababa, C. Atenbach, K. Hideg, M. Krebs, H. G. Khorana and W. L. Hubbell, *Science*, 1994, **266**, 105.
70. T. Gullion and J. Schaefer, *Adv. Magn. Reson.*, 1989, **13**, 57.
71. E. Bennett, R. G. Griffin and S. Vega, *NMR*, 1994, **33**, 1.
72. M. H. Levitt, D. P. Raleigh, F. Creuzet and R. G. Griffin, *J. Chem. Phys.*, 1990, **92**, 6347.
73. A. W. Hing, S. Vega and J. Schaefer, *J. Magn. Reson.*, 1992, **96**, 205.
74. R. Tycko and G. Dabbagh, *Chem. Phys. Lett.*, 1990, **173**, 461.
75. B.-Q. Sun, P. R. Costa, D. Kocisko, P. T. Lansbury, Jr and R. G. Griffin, *J. Chem. Phys.*, 1995, **102**, 702.
76. T. Gullion and S. Vega, *Chem. Phys. Lett.*, 1992, **194**, 423.
77. A. E. Bennett, J. H. Ok, R. G. Griffin and S. Vega, *J. Chem. Phys.*, 1992, **96**, 8624.
78. T. Gullion and J. Schaefer, *J. Magn. Reson.*, 1991, **92**, 439.
79. Y. Pan, T. Gullion and J. Schaefer, *J. Magn. Reson.*, 1990, **90**, 330.
80. D. Suwelack, W. P. Rothwell and J. S. Waugh, *J. Chem. Phys.*, 1980, **73**, 2559.
81. W. P. Rothwell and J. S. Waugh, *J. Chem. Phys.*, 1981, **74**, 2721.
82. A. Naito, A. Fukutani, M. Uitdehaag, S. Tuzi and H. Saitô, *J. Mol. Struc.*, 1997, in press.
83. O. B. Peersen, M. Groesbeek, S. Aimoto and S. O. Smith, *J. Am. Chem. Soc.*, 1995, **117**, 7728.
84. G. R. Marshall, D. D. Beusen, K. Kociolek, A. S. Redlinski, M. T. Leplawy and J. Schaefer, *J. Am. Chem. Soc.*, 1990, **112**, 963.
85. S. M. Holl, G. R. Marshall, D. D. Beusen, K. Kociolek, A. S. Redlinski, M. T. Leplawy, R. A. Makey, S. Vega and J. Schaefer, *J. Am. Chem. Soc.*, 1992, **114**, 4830.
86. A. W. Hing and J. Schaefer, *Biochemistry*, 1993, **32**, 7593.
86. (a) D. J. Hirsh, J. Hammer, W. L. Maloy, J. Blazyk and J. Schaefer, *Biochemistry*, 1996, **35**, 12733.
87. J. R. Garbow and C. A. McWherter, *J. Am. Chem. Soc.*, 1993, **115**, 238.
88. J. R. Garbow, M. Breslav, O. Antohi and F. Naider, *Biochemistry*, 1994, **33**, 10094.
89. R. C. Anderson, T. Gullion, J. M. Joers, M. Shapiro, E. B. Villhauer and H. P. Weber, *J. Am. Chem. Soc.*, 1995, **117**, 10546.
90. S. K. Brahmachari, T. N. Bhat, V. Sudhakar, M. Vijayan, R. S. Rapaka, R. S. Bhatnagar and V. S. Aranthanarayanan, *J. Am. Chem. Soc.*, 1981, **103**, 1703.
91. von I. Z. Siemion, T. Wieland and K.-H. Pook, *Angew. Chem.*, 1975, **87**, 712.
92. K. Nishimura, A. Naito, C. Hashimoto, S. Tuzi and H. Saitô, manuscript in preparation.
93. P. T. Lansbury, Jr, P. R. Costa, J. M. Griffiths, E. J. Simon, M. Auger, K. J. Halverson, D. A. Kocisko, Z. S. Hendsch, T. T. Ashburn, R. G. S. Spencer, B. Tidor and R. G. Griffin, *Nature, Struct. Biol.*, 1995, **2**, 990.
94. J. M. Griffiths, T. T. Ashburn, M. Auger, P. R. Costa, R. G. Griffin and P. T. Lansbury, Jr, *J. Am. Chem. Soc.*, 1995, **117**, 3539.
95. A. W. Hing, N. Tjandra, P. F. Cottam, J. Schaefer and C. Ho, *Biochemistry*, 1994, **33**, 8651.
96. (a) A. M. Christensen and J. Schaefer, *Biochemistry*, 1993, **32**, 2868.
(b) L. M. McDowell, A. Schmidt, E. R. Cohen, D. R. Studelska and J. Schaefer, *J. Mol. Biol.*, 1996, **256**, 160.
(c) L. M. McDowell, C. A. Klug, D. D. Beusen and J. Schaefer, *Biochemistry*, 1996, **35**, 5395.
97. (a) Y. Li, R. J. Appleyard, W. A. Shuttleworth and J. N. S. Evans, *J. Am. Chem. Soc.*, 1994, **116**, 10799.

(b) Y. Li, F. Krekel, C. A. Ramilo, N. Amrhein and J. N. S. Evans, *FEBS Lett.*, 1995, **377**, 208.

98. L. K. Thompsom, A. E. McDermott, J. Raap, C. M. Van der Wielen, J. Lugtenburg, J. Herzfeld and R. G. Griffin, *Biochemistry*, 1992, **31**, 7931.
99. K. V. Lakshmi, M. Auger, J. Raap, J. Lugtenburg, R. G. Griffin and J. Hetzfeld, *J. Am. Chem. Soc.*, 1993, **115**, 8515.
100. K. V. Lakshmi, M. R. Farrar, J. Raap, J. Lugtenburg, R. G. Griffin and J. Herzfeld, *Biochemistry*, 1994, **33**, 8853.

This Page Intentionally Left Blank

Xenon NMR

CHRISTOPHER I. RATCLIFFE

Steacie Institute for Molecular Sciences, National Research Council of Canada, Ottawa, Ontario, Canada K1A 0R6

This chapter presents an attempt to cover the entire scientific literature of xenon NMR, encompassing physical, chemical and biological applications involving both spectroscopy and imaging, from the earliest days of NMR to the new opportunities afforded by hyperpolarized Xe. The large, polarizable, electron cloud of the Xe atom endows it with a great sensitivity to its local environment, which is reflected in its chemical shift and electric field gradient. Thus the NMR of Xe(0) largely concerns the physical interaction of the Xe atom with other atoms (including other Xe) through collision and overlap, in the gas and in condensed materials including liquids, polymers, clathrates, porous materials and surfaces. Xe NMR has been used extensively to probe pore spaces and other species present in them, such as metal clusters and paramagnetic centres. Much has also been learned in recent years about the dynamics of Xe in porous media, especially through the use of 2D exchange spectroscopy and diffusion experiments. Particular attention has been focused on efforts to understand the origins and to calculate the chemical shift in microporous materials from first principles, and thus go beyond a qualitative picture. The 10^4 gain in sensitivity of hyperpolarized Xe has been exploited for studies of low-surface-area materials, in low-concentration and time resolution experiments, for polarization transfer to other nuclei, and for imaging. ^{129}Xe NMR has also played a very major role in the investigation of Xe chemistry (which is now quite extensive), particularly in following chemical reactions and determining structure and bonding characteristics. An extensive updated tabulation of chemical shifts and J-coupling constants is given.

ANNUAL REPORTS ON NMR SPECTROSCOPY
VOLUME 36 ISBN 0-12-505336-3

Copyright © 1998 Academic Press Limited
All rights of reproduction in any form reserved

1. INTRODUCTION

A number of reviews on xenon NMR have already appeared, some comprehensive[1–3] and others more focused.[4–12] In this chapter an attempt has been made to encompass the entire literature of xenon NMR. Repetition has been avoided as much as possible, except where necessary for completeness of information, and the reader will be referred where necessary to sections of previous reviews for more detail. Since one of the aims of the chapter is to highlight applications of Xe NMR, each of the later sections will give a general, overall view of the research done and then either discuss the most recent work or focus on a few specific topics.

It can be seen from Table 1 that ^{129}Xe has NMR properties that make it very amenable for study, though the quadrupolar nucleus ^{131}Xe has not been entirely neglected. Since Xe is a heavy atom with a large number of electrons, it consequently has a large chemical shift range of over 7500 ppm. The large electron cloud of Xe(0) is also highly polarizable, which makes it very sensitive to its environment. This is reflected in a wide chemical shift range for Xe(0) of several hundred ppm; a "physical shift" if you like. Xenon has approximately the same size as a methane molecule and in its guise as a noble gas it is relatively inert. All these properties make it an ideal material for probing void spaces and surfaces.

Until 1980 work was focused on elemental xenon in the pure gaseous, liquid and solid phases, xenon in gas mixtures and chemical compounds of xenon in solution. Although work in these important areas has continued, the growth of a new major branch of research started at about this time concerning the behaviour of atomic xenon in condensed phases of other materials, namely in

Table 1. Important parameters for Xe NMR.[a]

	^{129}Xe	^{131}Xe
Abundance (%)	26.4	21.2
Spin I	1/2	3/2
Magnetic moment μ (nuclear magnetons)	−0.77247	0.68697
Quadrupole moment Q (m^2)	—	-0.12×10^{-28}
Magnetogyric ratio γ (rad T^{-1} s^{-1})	-7.4003×10^7	2.1939×10^7
NMR frequency at 2.3488 T (MHz) (^{1}H at 100 MHz)	27.66	8.199
Relative sensitivity (^{1}H = 1)	2.12×10^{-2}	2.76×10^{-3}

[a]From Emsley,[13] except for μ from Ref. 14.

solutions, polymers, clathrates and porous materials of all kinds and on surfaces. Studies of Xe chemical compounds have followed the more familiar application of analytical high-resolution NMR for determining molecular structure and bonding characteristics and for following reactions.

The vast majority of solid-state Xe NMR spectra have been obtained by single-pulse excitation of the Xe frequency. However, cross polarization (CP) has been applied where feasible, in particular in studies of clathrates where the Xe is localized in a cage so that ^{1}H–^{129}Xe dipolar interactions are not averaged to zero by dynamics. The use of two-dimensional (2D) exchange spectroscopy (2D EXSY) to study Xe dynamics on relatively long time scales has recently become a very popular technique. Foremost among current areas of activity, hyperpolarized Xe is opening up previously inaccessible areas for study, such as materials with low surface area, low-concentration applications, the possibility of time resolution experiments, transfer of high polarizations to other nuclei, and materials and biomedical imaging applications.

2. NONBONDED XENON: OXIDATION STATE Xe(0)

2.1. Phases of pure elemental xenon

Studies of the fundamental NMR properties of elemental Xe will be discussed in some detail since this will provide the basis for understanding much of what follows. The majority of measurements come from before 1980, though interest has recently reawakened with the advent of hyperpolarized Xe. The need for storage and delivery of this material, especially for imaging uses, requires measurements of relaxation times and a detailed understanding of relaxation mechanisms.

2.1.1. Xe gas

NMR studies of Xe were initiated in 1950 by Proctor and Yu, who determined the magnetic moment for ^{129}Xe, $\mu = -0.7226\mu_N$.[15] Prior to this (in 1934), however, spectroscopic measurements of hyperfine structure had been used to determine the spins of ^{129}Xe ($I = 1/2$) and ^{131}Xe ($I = 3/2$) and the signs and relative magnitudes of the magnetic moments.[16] Other NMR measurements of magnetic moments followed,[17–19] culminating in the work of Brinkmann, whose values are quoted in Table 1.[14] Values of the ^{131}Xe quadrupole moment Q have been given as $-0.15 \times 10^{-28}\ m^2$,[20] or the commonly accepted value $-0.12 \times 10^{-28}\ m^2$.[21]

Chemical shift. Since the NMR of Xe(0) reflects the influence of the environment, the natural reference point is the shift of a lone Xe atom in free space, i.e. no interactions and zero chemical shift anisotropy. In experimental practice

this is taken as the shift of Xe gas extrapolated to zero pressure. Most often shifts are expressed on the δ-scale, increasing downfield, but historically much of the work on elemental Xe is given on the shielding scale σ, increasing upfield.

The temperature (T) and density (ρ) dependence of the Xe chemical shift in the gas phase has been studied repeatedly. Early works showed a linear dependence on pressure,[21–25] though nonlinearity became apparent at higher ρ.[26] Jameson *et al.*[27] were the first to describe the density dependence in terms of virial coefficients using

$$\sigma = \sigma_0 + \sigma_1 \rho + \sigma_2 \rho^2 + \sigma_3 \rho^3 \tag{1}$$

where (at 298 K) σ_0 = reference shift, $\sigma_1 = -0.548 \pm 0.004$ ppm/amagat; $\sigma_2 = (-0.169 \pm 0.02) \times 10^{-3}$ ppm/amagat^2; $\sigma_3 = (0.163 \pm 0.01) \times 10^{-5}$ ppm/amagat^3. (An amagat is the density of the gas at 1 atmosphere at 0°C.)

Later studies[28,29] gave $\sigma_1 = -0.539$ ppm/amagat, $\sigma_2 = -0.161 \times 10^{-3}$ ppm/amagat^2, and the most recent value of σ_1 is -0.553 ppm/amagat at 298 K,[30] although most people refer back to the original paper.[28] Earlier studies, though not expressed originally as σ_1, gave -0.422 ± 0.005 ppm/amagat[23,24] and -0.61 ± 0.02 ppm/amagat.[26] Theory and calculations by Adrian show that the density dependence of the chemical shift arises from exchange interactions during collisions, and he derived the equivalent of Jameson's second virial coefficient = -0.285 ppm/amagat.[31] Below 100 amagat two-body collisions are predominant and the dependence is effectively linear. The nonlinearity at higher pressures, requiring σ_2 and σ_3, arises because of significant contributions from three-body or higher collisions.

A T dependence of the shift was first observed by Kanegsberg *et al.*,[26] and Adrian extended his theory to describe the T, ρ dependence[32] with good agreement with experiment at moderate densities. Jameson *et al.* measured the second virial coefficient σ_1 as a function of T[28,30,33] (Fig. 1) and described the dependence by a polynomial:

$$\sigma_1(T) = -0.553 + 0.1114 \times 10^{-2}\,\tau - 0.765 \times 10^{-5}\,\tau^2 + 0.436 \times 10^{-7}\,\tau^3 - 0.132 \times 10^{-9}\,\tau^4 - 0.545 \times 10^{-12}\,\tau^5 \text{ ppm/amagat} \tag{2}$$

with $\tau = (T - 300)$ K.[30] σ_1 and σ_2 both decrease with increasing T.

These equations (1) and (2) and coefficients are an extremely important resource, since they are frequently used to calibrate the residual Xe gas pressure from the chemical shift in studies of Xe adsorbed on surfaces and in porous media. Note also that the shift extrapolated to zero density (i.e. the isolated Xe atom) is strictly independent of T and thus provides an important chemical shift reference for other nuclei.[29,34]

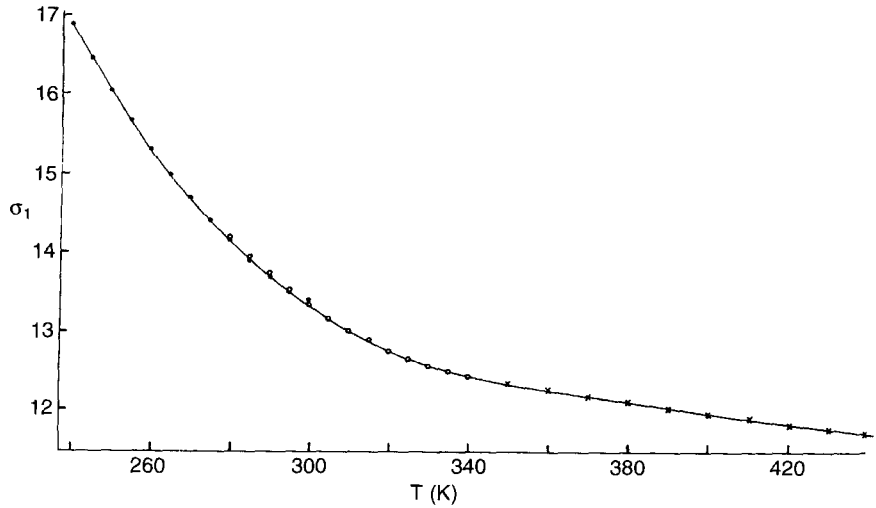

Fig. 1. Temperature dependence of the second virial coefficient $\sigma_1(T)$ in Hz/amagat of ^{129}Xe in the gas phase. (Reprinted with permission from Ref. 28. Copyright 1973 American Institute of Physics.)

Jameson *et al.*,[30] using the accurately determined $\sigma_1(T)$ values, carried out an inversion of the integral equation

$$\sigma_1(T) = 4\pi \int_0^\infty \sigma(R) \exp[-U(R)/kT] R^2 \, dR \tag{3}$$

which describes the shift in terms of the Xe–Xe internuclear separation R and the potential function $U(R)$ for an Xe atom pair, in the first attempt to obtain a functional form for $\sigma(R)$. As will be discussed later, $\sigma(R)$ has a shape similar to that of the Lennard-Jones potential function.

Ab initio calculations. The shielding of an isolated Xe atom is entirely diamagnetic. Paramagnetic contributions from collisions in the gas and electronic overlap interactions with neighbouring atoms in condensed phases reduce the shielding. Malli and Froese[35] in 1967 were the first to calculate the diamagnetic shielding using a Hartree–Fock treatment; with respect to the bare nucleus σ = 5642.32 ppm. Kolb, Johnson and Shorer[36] later included relativistic effects in a coupled Hartree–Fock calculation to give σ = 7040 ppm, which is probably the closest to the real absolute shielding. Bishop and Cybulski[37] used SCF calculations to study the effects of a uniform static electric field on the Xe shift and shielding polarizability. With no field they obtained σ = 5642.4089 ppm and this decreases with increasing electric field.

Relaxation. From the early days it was clear that the spin–lattice relaxation time T_1 of ^{129}Xe in the gas phase was long.[15,19] Streever and Carr[22] showed that T_1 decreases with increasing density ρ or decreasing temperature T. They also pointed out that although T_1 is long it is nevertheless much too short to be accounted for by dipole–dipole interactions between colliding atoms, for which calculations give $T_1 = 3060$ h at 30 atmospheres pressure. An apparent inverse linear dependence on ρ was observed by Brinkmann *et al.*[21] and Hunt and Carr[23,24] and from their results the T_1 values obtained by extrapolation to 1 amagat are 45.9 h and 55.5 h respectively.

Torrey[38] developed a semiempirical formula for T_1 in terms of spin–rotation coupling during binary collisions which, assuming hard-sphere diameters, gave numbers close to those observed. Ramsey's theory[39] of chemical shifts provides the connection between σ and the spin–rotation coupling. Note, however, that if one uses Jameson's second virial coefficient in Torrey's equation, then $T_1 = 34$ h at 1 amagat. More recently, Shizgal also calculated the T dependence of T_1 in the range 200–450 K. His results give $T_1 = 77.8$ h at 1 amagat at 298 K.[40]

Pfeffer and Lutz[41] have determined a T_1 of 13 200 s for pure ^{129}Xe in the gas at 98 kPa in a half-litre sphere using a whole-body imager, and later measured the diffusion profile[42] and obtained $D = 5.3 \pm 0.6 \times 10^{-6}$ m^2 s^{-1}.

The T_1 of ^{131}Xe in the gas is relatively short,[18,19] attributable to the quadrupole interactions. As with ^{129}Xe the T_1 shows an inverse dependence on density,[21] $1/T_1 = 0.0396\rho$ at 298 K (or $T_1 = 25.25$ s at 1 amagat). Early theoretical calculations[20] based on the quadrupole interaction gave a short T_1. Then calculations by Adrian[43] showed that exchange interactions are the principal source of the collision-induced quadrupole interaction that produces the spin–rotation coupling. He calculated a T_1 of 22 s at 1 amagat.

2.1.2. Xe liquid and solid

Early work on liquid[22,25,44–46] and solid[25,44–49] Xe was reviewed by Norberg in 1984.[50] Streever and Carr[22] were the first to observe ^{129}Xe in the liquid. They obtained T_1 values at several temperatures, e.g. $T_1 = 57 \pm 2$ s at 172 K and 112 ± 10 s at 234 K, and gave an approximate shift equivalent to $\delta = 66$ ppm at 198 K and $\rho = 2.87$ g cm^{-2}.

Yen and Norberg[44] studied ^{129}Xe T_2 vs T in the solid and liquid (Fig. 2). They found rigid lattice values ($T_2 = 1.06$ ms) below about 115 K. Line narrowing occurs above this temperature owing to self-diffusion with an activation energy $E_a = 7.4$ kcal mol^{-1} and diffusion constant $D = 7.3 \exp(-7400/RT)$ cm^2 s^{-1}. There is a marked change in T_2 at the melting point and the slope gives an E_a of 1.4 kcal mol^{-1} in the liquid. T_1 was found to be >7000 s at 125 K. They also observed a large linear dependence of the shift on density in the solid of $\Delta H/H\Delta\rho = 2.04$ ppm/amagat. This and a value of 1.82 ± 0.11 ppm/amagat from ^{131}Xe (Ref. 45) were at variance with values determined by Brinkmann and

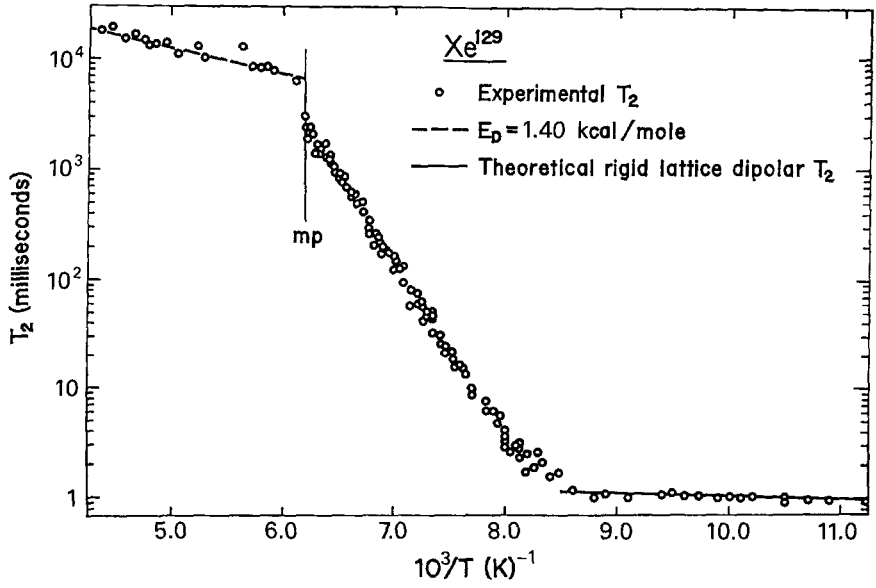

Fig. 2. ^{129}Xe spin–spin relaxation times T_2 in liquid and solid xenon. (Reprinted with permission from Ref. 44. Copyright 1963 American Physical Society.)

Carr[46,47] of 0.53 ± 0.03 and 0.51–0.742 ppm/amagat (the latter showed non-linear dependence). However, later measurements by Cowgill and Norberg[49] gave 0.572 ± 0.036 ppm/amagat. A theoretical calculation by Lurie *et al.*[51] gives about 0.6 ppm/amagat for a similar density range. Results for the liquid are 0.51 ± 0.05[45] and 0.566 ppm/amagat.[46] Pfund *et al.*[52] obtained ^{129}Xe shifts at 297 K in the supercritical fluid at densities between 5×10^{-3} and 2.2×10^{-2} mol cm^{-3} (50–1000 bar). The results exhibit deviations from the second-order virial equation. Chemical shifts in all three phases as a function of density are shown in Fig. 3.

The data of Brinkmann and Carr[46] have often been referred to for the relative shifts in solid and liquid at different temperatures: in the liquid $\delta = 161$ ppm at 244 K, 230 ppm at 161 K. In the solid $\delta = 272$ ppm at 161 K, 299 ppm at 77 K and 311 ppm extrapolated to 0 K. However, much more recent measurements seem to be establishing different values in the solid: Gatzke *et al.*[53] give a shift of 317 ppm at 77 K and Cho *et al.*[54] a value of 316.4 ± 1 ppm at 77 K; Cheung[55] reports 304 ppm at 144 K and Davies *et al.*[56] give 301 ppm at 150 K. Thus it seems that the shift scale of the old data[46] may be offset somewhat as a result of referencing problems.

Warren and Norberg[45] measured ^{131}Xe T_1 in the solid and liquid from 9 to 250 K. In the solid the data can be explained by a quadrupolar relaxation via

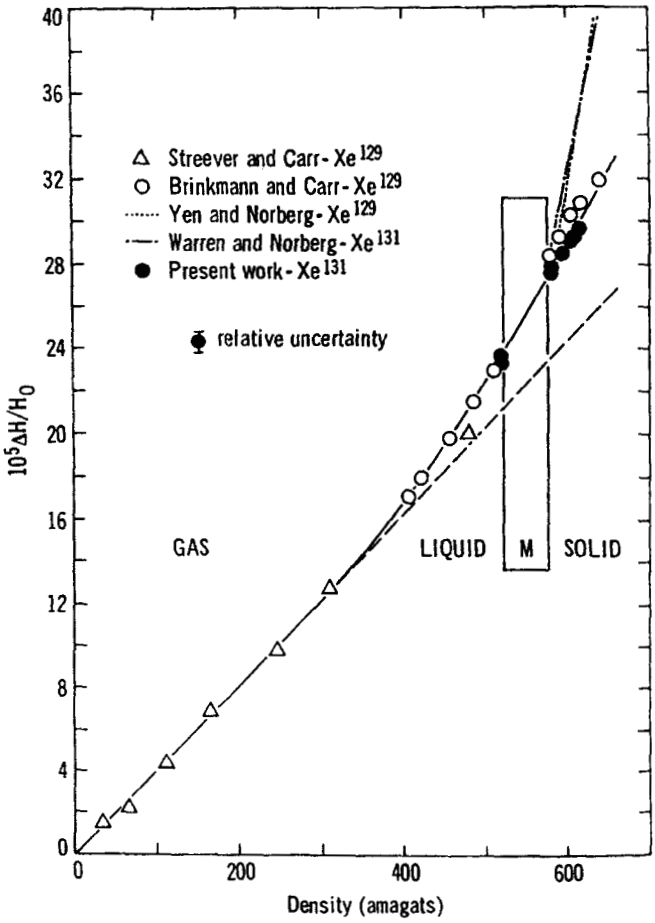

Fig. 3. Chemical shifts in the three phases of xenon as a function of density ρ. (Reprinted with permission from Ref. 49. Copyright 1972 American Physical Society.)

a two-phonon Raman process, based on the theory of Van Kranendonk.[57] T_1 ranges from 390 s at 9 K to 200 ms at the melting point. The T_1 reduces by a factor of about 5 on melting. In the liquid the T_1 increases with increasing T and the relaxation is due to dynamic quadrupolar interactions, ranging from about 40 ms at 161 K to about 84 ms at 250 K.

Norberg[50] also reviewed ^{129}Xe T_1 and $T_{1\rho}$ measurements in the solid by Barroilhet.[58] The $T_{1\rho}$ results yielded $E_a = 7.37$ kcal mol^{-1} for the self-diffusion process. Hunt and Carr[24] reported ^{129}Xe $T_1 = 1000 \pm 200$ s in the liquid from

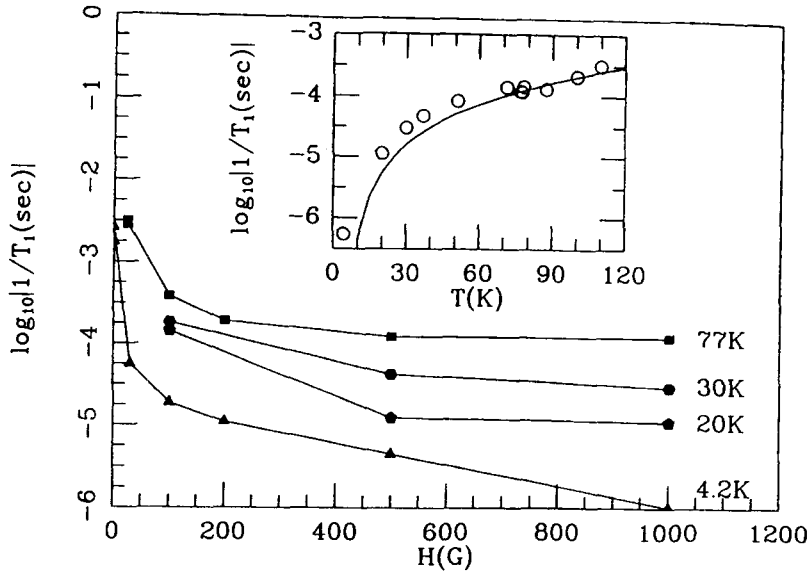

Fig. 4. Magnetic field dependence of ^{129}Xe T_1 in solid xenon at 77, 30, 20 and 4.2 K. The inset shows the temperature dependence at fields of 1 kG or more. (Reprinted with permission from Ref. 53. Copyright 1993 American Physical Society.)

201 to 283 K. The relaxation mechanism is thought to be via the collision-induced spin–rotation interaction.

The most recent relaxation studies on solid ^{129}Xe have utilized the greatly enhanced sensitivity of hyperpolarized Xe (discussed later) by Gatzke *et al.*[53] They found little dependence on field at temperatures above 20 K and no dependence on isotopic composition for fields above 500 G (10^4 Gauss = 1 Tesla). The dominant mechanism of relaxation in the 20–120 K region is thought to arise from inelastic spin–phonon scattering processes resulting from nuclear spin–rotation interaction (from relative angular momentum) between neighbouring atom pairs. They quote a value of $T_1 = 8500 \pm 1800$ s at 77 K in fields above 1 kG. At fields >1 kG, T_1 increases with decreasing T. Above 120 K dipolar relaxation caused by diffusion of vacancies becomes the dominant mechanism. At low magnetic fields below 20 K, T_1 has a strong field dependence (Fig. 4) owing to a new mechanism involving cross relaxation to ^{131}Xe (this process was confirmed by reduction of polarization of ^{129}Xe with concomitant observation of large ^{131}Xe polarization). This relies on a degeneracy of the energy levels of the two magnetic species and the presence of dipolar couplings. The degeneracy results from static ^{131}Xe quadrupolar interactions with imperfections in the lattice, which are large enough to produce cross relaxation even at several kiloGauss. At

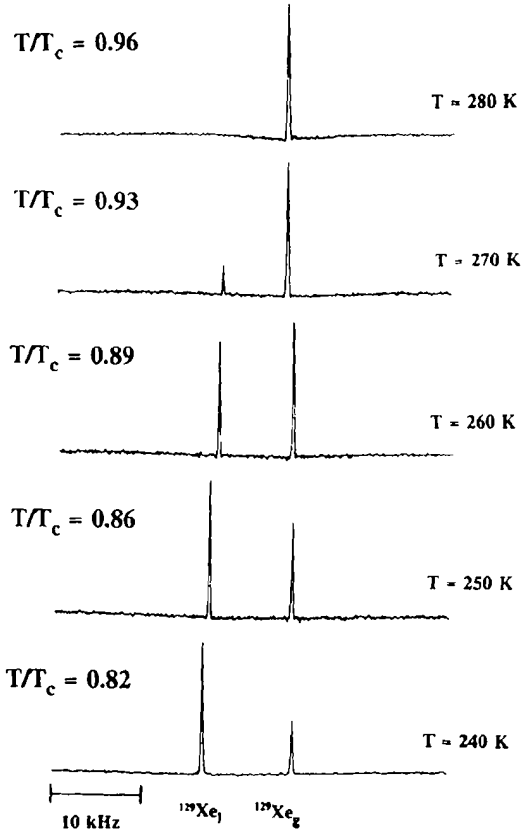
T/T$_c$ = 0.96
T = 280 K
T/T$_c$ = 0.93
T = 270 K
T/T$_c$ = 0.89
T = 260 K
T/T$_c$ = 0.86
T = 250 K
T/T$_c$ = 0.82
T = 240 K
10 kHz
^{129}Xe$_l$
^{129}Xe$_g$

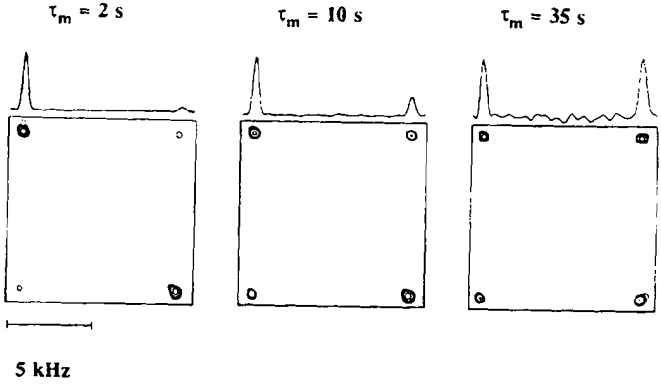
τ_m = 2 s
τ_m = 10 s
τ_m = 35 s
5 kHz

4.2 K and below 1 kG, T_1 depends on the amount of ^{131}Xe present; 80.8% ^{129}Xe with 3.4% ^{131}Xe gives $T_1 = 180$ h, at natural abundances $T_1 = 60$ h, and ^{129}Xe mixed with Kr gives $T_1 = 510$ h.

In an interesting application of ^{129}Xe NMR, Carr *et al.*[59,60] made use of the shift difference between gas and liquid to explore the Xe liquid–vapour coexistence curve near the critical temperature T_c. The shift–density correlation is used to derive the shape of the curve given by $(\rho_L - \rho_V)/\rho_c$, where the subscripts L, V, c refer to liquid, vapour and critical, respectively, which can then be described by a power law $B\varepsilon^{\beta} + B_1\varepsilon^{\beta'}$ where $\varepsilon = (T_c - T)/T_c$. The critical exponents were found to be $\beta = 0.305$ and $\beta' = 0.77$. Ehrlich and Carr[61] determined the self-diffusion constant D using measurements of the decay of the spin-echo amplitudes along the coexistence curve and along the critical isochore. This kind of measurement was extended by Peereboom *et al.*, who studied D over a range of ρ up to 475 amagat and T (248–343 K), using a high-pressure NMR probe and observing ^{129}Xe (Refs 62, 63) and ^{131}Xe (Ref. 63); at 298 K $D = 2.054 \times 10^{-7}$ m^2 s^{-1} at 25.02 amagat and $D = 0.05141 \times 10^{-7}$ m^2 s^{-1} at 475.09 amagat. The density dependence of D at intermediate and high densities could be modelled reasonably well by molecular dynamics calculations using hard spheres. Only qualitative agreement was obtained with MD using Lennard-Jones potentials.

In a graphic demonstration of the power of 2D EXSY NMR, Tomaselli *et al.*[64] were able to observe the exchange of Xe between coexisting gas and liquid phases (Fig. 5). 2D mixing times of $\tau_{mix} = 0.5$–50 s were used at 256 K (where the shifts of the two phases are separated by about 143 ppm) and the relative intensities of the cross peaks were obtained. Analysis of the results suggested that the rate-limiting step in the exchange is the time needed to diffuse to the interface from within the gas phase ($\tau_g = 22 \pm 7$ s) and that there is no apparent interfacial barrier.

2.2. Xe interacting with other nuclei in the gas and liquid phases

2.2.1. Xe with other gases

The chemical shift of Xe mixed with numerous other gases has been thoroughly studied by Jameson *et al.*[27,30,33,65–70] Again the ρ dependence can be expressed in a virial expansion:

$$\sigma = \sigma_0 + \sigma_1(\text{Xe–Xe})\rho_{Xe} + \sigma_1(\text{Xe–A})\rho_A \qquad (4)$$

Fig. 5. ^{129}Xe NMR spectra at several temperatures in the Xe gas–liquid coexistence region (top), and 2D exchange spectra showing gas–liquid exchange at 256 K at the mixing times indicated (bottom). (Reprinted from Ref. 64 with kind permission of Elsevier Science—NL, Sara Burgerhartstraat 25, 1055 KV Amsterdam.)

Table 2. Second virial coefficients σ_1(Xe–A) in ppm/amagat at 298 K for Xe interacting with various gases.

Interacting gas A	σ_1(Xe–A)	Reference[a]
Xe	−0.422	23/24
	−0.61	26
	−0.548	27
	−0.553	33*
	−0.555	30*
Kr	−0.273	27
	−0.293	33*
Ar	−0.140	27
	−0.189	33*
CH_4	−0.278	27
	−0.283	67*
CH_3F	−0.194	27
CH_2F_2	−0.223	27
CHF_3	−0.193	27
CF_4	−0.194	27
	−0.183	67*
C_2H_2	−0.452	69*
C_2H_4	−0.430	69*
C_2H_6	−0.414	69*
SiF_4	−0.197	67*
BF_3	−0.163	69*
HCl	−0.345	27
	−0.337	69*
HBr	−0.489	69*
CO_2	−0.172	27
	−0.193	69*
N_2O	−0.166	69*
CO	−0.252	70*
N_2	−0.210	70*
O_2	−0.945	65
	−1.068	66*
NO	−0.798	65
	−0.687	68*

[a]An asterisk after the reference indicates a value calculated from σ_1(T) data.

With prior knowledge of σ_1(Xe–Xe) the contribution of σ_1(Xe–A), which represents the effects of binary Xe collisions with another gas molecule A, can be determined; Table 2 gives values at 298 K. The density dependence appears to be somewhat dependent on the polarizability of the second gas.

In several cases the temperature dependence of σ_1(Xe–A) has also been obtained (Fig. 6). In almost all cases σ_1(Xe–A) decreases with increasing T, except for CO and N_2 which increase slightly.[70]

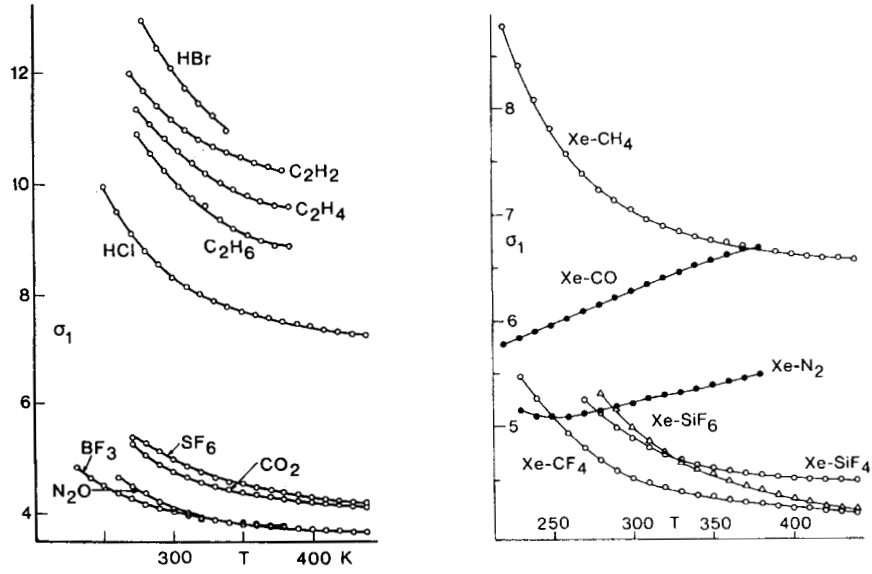

Fig. 6. Temperature dependencies of the second virial coefficients σ_1(Xe–A) in Hz/amagat of ^{129}Xe in various gases. (Reprinted with permission from Refs 69, 70. Copyright 1977, 1978 American Institute of Physics.)

A much stronger interaction (reflected in larger σ_1 values) occurs with the paramagnetic species O_2[65,66] and NO.[65,68] Theoretical calculations by Buckingham and Kollman[71] showed that the Fermi contact interaction via overlap of the Xe (5s) orbital with the O_2 (π_g^*) or NO (π^*) unpaired electron orbitals is the principal cause of the shifts. σ_1(Xe–O_2) also shows a dominant Curie-type $1/T$ dependence, which is expected for a Fermi contact interaction.[66] The T_1 of Xe in O_2[72] is inversely proportional to the density of O_2 and dominated by unpaired electron(O_2)–nuclear(Xe) dipolar coupling with the spin–rotation mechanism negligible in this case.

2.2.2. Xe in solution

The NMR of Xe in liquids was covered thoroughly by Jokisaari[8] in 1994, and more briefly in other reviews.[1–4,6] As with all other situations, the shift of the Xe atom in solution is a complicated function of its interactions with neighbouring atoms and molecules. However, the complications are compounded by the dynamics of the fluid and in most cases a lack of detailed knowledge about the local structure.

Xenon solubility in most solvents is small and the fact that the NMR shifts

are generally found to be independent of concentration indicates that the Xe is in the infinite-dilution limit, i.e. interacting solely with the solvent. The available chemical shift data[73–82] are collected in Table 3. Values range from 58.8 ppm in CO_2 to 335 ppm in CH_2I_2.

Xe NMR shifts in isotropic liquids can be expressed as

$$\sigma = \sigma_0 + \sigma_b + \sigma_a + \sigma_W + \sigma_E \tag{5}$$

where the terms represent reference, bulk susceptibility correction, nonspecific magnetic anisotropy of the solvent molecules, van der Waals interactions and solvent electric dipole interactions, respectively. The major contribution seems to come from the dispersive part of the van der Waals interactions σ_W, for which Rummens developed a model in terms of a "reaction field" in the solvent. The reaction field arises in response to spontaneous electronic fluctuations in the solute.[83] The model relates the shift with the refractive index of the solution through the term

$$f(n) = \left(\frac{n^2 - 1}{2n^2 - 1}\right)^2 \tag{6}$$

This relationship was tested early on[78] for Xe and seems to work well within several homologous series of solvents, e.g. alkanes, cycloalkanes,[75] (Fig. 7) or alcohols,[80] which give linear correlations of $f(n)$ with shift. However, the lines are not coincident and have different intercepts, suggesting that the repulsive part of the van der Waals interactions are similar within a series but contribute to the difference between series. Unfortunately, there is no simple theory for this repulsive contribution. (Muller[84] suggested a variation on this model that takes into account the "cohesive energy density" (CED) of the solvent.) Luhmer *et al.*[85] developed a slightly different model in which they used a pair interaction structureless approximation (PISA) to calculate a good estimate for the Xe–solvent dispersion energy E_{dis}, which also is directly proportional to the shift. This seems to give a better linear correlation than the Rummens model. A very clear linear correlation exists between ^{129}Xe and ^{13}C (in CH_4) shifts in the same solvent,[85] which has been taken as evidence that σ_W is the predominant shift interaction.

n-Alkanes show a larger Xe shift at 273 K than at 298 K; the difference decreases as the chain gets longer, ranging from 7.9 ppm for *n*-pentane to 6.1 ppm for *n*-dodecane,[75] and this can perhaps be related to the increase in density of the solvent at lower T. In mixed organic solvent systems the Xe shift can be nonlinear with composition owing to specific solvent–solvent interactions or short-range liquid order.[86]

Xe in water[78,82,87–90] has an anomalously large shift quite different from that in alcohols, and in water with organic cosolvents (DMSO and alcohols) usually shows an initial sharp increase in the shift at low cosolvent molar ratios and

Table 3. Chemical shifts of Xe(0) in solution.

Solvent	Refractive index n_D[a]	δ (ppm)[b]	Reference
Ethane	1.24	93.2	73[c]
Propane	1.290	125.8	73[c]
n-Butane	1.329	145.4	74
n-Pentane	1.3558	154.1	75
n-Hexane	1.3731	160.9	75
n-Heptane	1.3853	166.0	75
n-Octane	1.3954	169.9	75
n-Nonane	1.4031	173.0	75
n-Decane	1.4096	175.4	75
n-Undecane	1.415	176.0	74
n-Dodecane	1.4198	179.4	75
n-Tridecane	1.423	179.5	74
n-Tetradecane	1.4271	182.4	75
n-Pentadecane	1.430	181.7	74
n-Hexadecane	1.4327	184.5	75
n-Heptadecane	1.435	183.3	74
2,2-Dimethylbutane	1.3674	174.7	75
2,3-Dimethylbutane	1.3733	169.2	75
2-Methylpentane	1.3697	167.4	75
3-Methylpentane	1.3752	165.1	75
2-Methylheptane	1.3934	175.9	75
2,5-Dimethylhexane	1.3910	181.7	75
2,2,4-Trimethylpentane	1.3891	190.5	75
2,2,5-Trimethylhexane		168.0	76
Cyclopentane	1.4044	157.0	75
Cyclohexane	1.4244	163.7	75
Cycloheptane	1.4432	171.4	75
Cyclooctane	1.4568	176.2	75
Cyclodecane	1.4689	182.9	75
Methylcyclohexane		176.7	77
2-Pentene		174.9	76
4-Methyl-1-pentene		185.0	76
Methyl chloride	1.3389	153.0	78
Methyl iodide	1.5288	237.0[d]	79
Methylene chloride	1.4243	192.0	78
Methylene iodide	1.7451	333.0	75
Chloroform	1.4438	215.0	75
Bromoform	1.5977	285.0	78
Carbon tetrachloride	1.4583	221.0	75
		219.7	77

[*Continued*

Table 3—*Continued*

Solvent	Refractive index n_D[a]	δ (ppm)[b]	Reference
Benzene	1.4988	193.0	75
Fluorobenzene	1.4639	174.6	75
Chlorobenzene	1.5225	200.1	75
Bromobenzene	1.5575	217.2	75
Iodobenzene	1.6178	246.7	75
Hexafluorobenzene		85.0	79
Toluene	1.4940	188.5	75
t-Butylbenzene	1.4910	201.6	75
Nitrobenzene	1.5503	187.4	75
Aniline	1.5840	215.8	75
m-Dichlorobenzene	1.5459	207.0	78
Anisole	1.5154	191.1	75
Pyridine	1.5079	203.6	75
n-Propylamine		168.4	80
n-Butylamine		174.3	80
n-Pentylamine		177.6	80
Diethyl ether	1.3505	159.0	75
Ethyl acetate	1.3708	167.0	75
Acetonitrile	1.3440	175.0	81
Acetone	1.3590	175.0	78
Dimethylsulfoxide		245.0	82[e]
p-Dioxane		186.0	82[e]
Oleic acid	1.4582	193.0	78
Olive oil	1.4663	198.0	78
Tetramethylsilane	1.3564	157.0	75
Dimethylformamide		189.4	77
N-Methylformamide		183.9	77
Formamide		216.4	77
Nitromethane		152.9	77
Methanol	1.3286	148.0	78
		147.7	80
Ethanol		161.1	80
		165.0	78
1-Propanol		166.5	80
1-Butanol	1.3990	176.0	78
		171.6	80
1-Pentanol		174.8	80
1-Hexanol		177.4	80
1-Heptanol		179.6	80
1-Octanol	1.4295	187.0	78
		181.4	80

[*Continued*

Table 3—*Continued*

Solvent	Refractive index n_D[a]	δ (ppm)[b]	Reference
1-Nonanol		182.7	80
1-Decanol		183.9	80
1-Undecanol		185.7	80
1-Dodecanol		186.1	80
2-Propanol		178.0	82[e]
t-Butanol		188.0	82[e]
Ethylene glycol	1.4319	199.0	78
Water	1.3330	196.0	78
Carbon dioxide		58.8	73[c]
Carbon disulfide	1.6250	223.0	75
Nitrous oxide		60.6	73[c]
Silicon tetrachloride		193.4	77
Germanium tetrachloride		215.8	77
Tin tetrachloride		238.3	77
Titanium tetrachloride		218.7	77
Magic acid $HFSO_4/SbF_5$	1.092	233.0	81
Trifluoromethanesulfonic acid	1.327	220.0	81
Methanesulfonic acid	1.4300	213.0	81
Dichloroacetic acid	1.4663	210.0	81
Methyl chloroacetate	1.4220	180.0	81
Methyl methanesulfonate	1.4140	183.0	81
Methyl trifluoromethanesulfonate	1.3260	181.0	81

[a]Refractive indices where given in original reference.
[b]Shifts downfield referenced to infinitely dilute Xe gas. All data except for those from Refs 76, 78, 81 have a small correction applied for bulk susceptibility.
[c]Liquids under pressure.
[d]In Ref. 79 it is suggested that an earlier value of 209 ppm[78] is incorrect.
[e]Value read from plot in Ref. 82.

then a steady decrease towards the shift value in the solvent alone[82] (Fig. 8). The T dependence of the shift in water[87] shows a slight increase to a maximum at 318 K then a gradual decrease: 191.5 ppm at 298 K, 192 ppm at 318 K, 189.5 ppm at 358 K. ^{129}Xe pulsed field gradient studies were used to obtain the translational diffusion coefficient of Xe in water; 1.3×10^{-9} to 3×10^{-9} $m^2 s^{-1}$ from 278 to 328 K, roughly the same as that of the water molecules, with an $E_a = 12.8$ kJ mol^{-1}.[90]

Solutions. Studies of the effects of ions on Xe in aqueous solutions[91,92] show that the shifts always increase with ion concentration, but the magnitude of the shift depends on the activity, charge and hydration of the ions.[91]

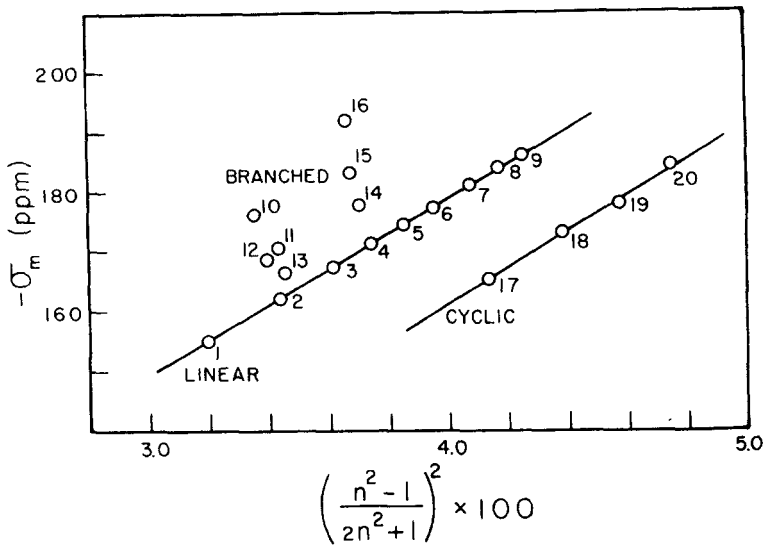

Fig. 7. ^{129}Xe shifts in saturated hydrocarbons at 298 K versus the reaction field parameter $f(n)$ described in the text (Eq. (6)): (1)–(9), linear alkanes with 5, 6, 7, 8, 9, 10, 12, 14, 16 carbons; (10)–(16), various methyl-substituted alkanes with main chains of 4, 5, 6, 7 carbons; (17)–(20), cycloalkanes with 6, 7, 8, 10 carbons. Note the linear and parallel behaviour for the linear and cyclic alkanes. (Reprinted with permission from Ref. 75. Copyright 1981 American Chemical Society.)

Studies of Xe with α-cyclodextrin (α-CD) in water or DMSO solutions show a single line shifted from that in the pure solvent.[93] The shift increases with α-CD concentration, and the presence of a Xe–α-CD complex was demonstrated by observation of a NOE effect. A model involving rapid exchange between three sites (Xe–αCD complex, Xe in close proximity to α-CD, and Xe in bulk solvent) was used to determine equilibrium constants and the shift of Xe in the complex. Similar behaviour was observed for crown ether solutions in $CHCl_3$,[94,95] which contrasted with dioxane, triglyme and tetraglyme which do not form complexes. The fits gave

Xe–α-CD in water	196 ppm
Xe–α-CD in DMSO	195.6 ppm
Xe–12-crown-4–$CHCl_3$	85.3 ppm
Xe–15-crown-5–$CHCl_3$	92.4 ppm

There have been several experimental studies of relaxation times[77,87,89,96–103] as well as with molecular dynamics or Monte Carlo simulations,[104–108] and Jokisaari has tabulated some of the information (Ref. 8, Tables 4 and 5). T_1

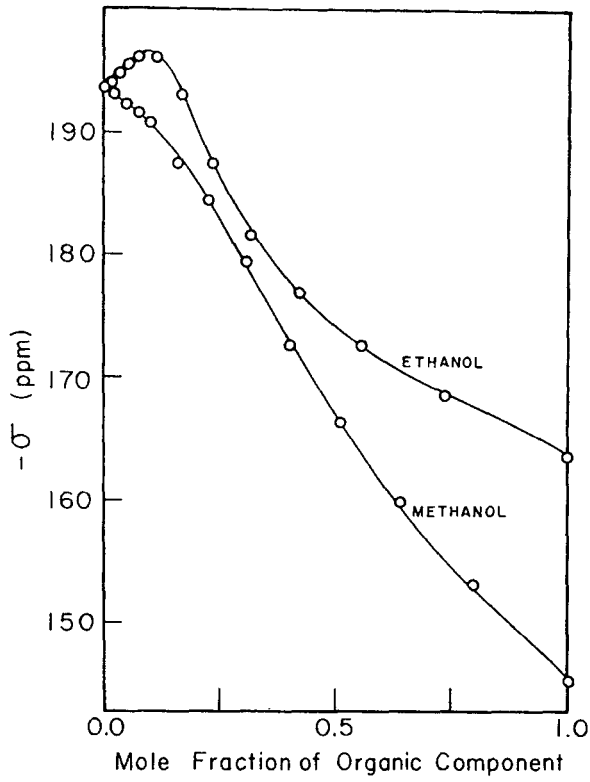

Fig. 8. Chemical shift of ^{129}Xe in mixtures of water and methanol or ethanol. (Reprinted with permission from Ref. 82. Copyright Plenum Publishing Corporation 1984.)

studies in isotropic organics show that ^{129}Xe–^{1}H dipole–dipole coupling is an important relaxation mechanism in hydrogen-containing solvents for which $1/T_1$ increases with T.[97,98] There is a marked difference in relaxation behaviour between C_6H_6, C_6H_{12} and their perdeuterated equivalents; the deuterated solvents have longer T_1 which show very little T dependence. The T_1 of CCl_4 also shows little T dependence. Although it has not been directly demonstrated, it is strongly suspected that spin–rotation interaction is the dominant relaxation mechanism in solvent systems.[97]

^{131}Xe T_1 in polar solvents[77] is quite short, ranging from 0.6 ms for $HCONH_2$ to 6 ms for CH_3CN, owing to rapid fluctuations in the electric field gradient generated by the solvent dipoles. The T_1 is generally significantly longer in nonpolar solvents (20–50 ms) and the dominant relaxation mechanism is not known. Nonpolar benzene is an exception with a T_1 of 4.4 ms thought to be due

to a specific Xe–benzene interaction. Molecular dynamics (MD) and Monte Carlo calculations on the Xe–benzene system[105,107] were used to confirm that there is a significant dipole–dipole contribution to ^{129}Xe T_1, via translational motions, and that ^{131}Xe T_1 depends more on solvent rotational dynamics.

MD calculations have been used to show that the electric field gradient fluctuations at ^{131}Xe in water are largely caused by electrostatic effects involving molecules in the first hydration shell[104] (the calculated T_1 compared very favourably with experiment). MD has also been used to investigate ^{131}Xe T_1 in methanol[106] and dioxanes.[108] *Ab initio* calculations were used to study the origins of the electric field gradient in several other organic solvents.[101]

2.2.3. *Xe in liquid crystals*

There have been numerous studies of Xe in liquid crystals making use of both ^{129}Xe chemical shift anisotropy[96,109–115] and ^{131}Xe quadrupolar coupling[116–119] to probe the anisotropic environment of the Xe and to study the various phase transitions. This topic was reviewed quite extensively by Jokisaari.[8]

^{129}Xe shift studies show abrupt changes in σ on passing through the transitions associated with smectic-A–nematic and nematic–isotropic phases (Fig. 9), and in fact can be used to map out liquid crystal phase diagrams.[109–111] The changes in σ can be interpreted in terms of changes in the orientation of the average chemical shift anisotropy tensor and in its magnitude $\Delta\sigma = \sigma_\parallel + \sigma_\perp$ (for an axially symmetric tensor) in the different phases:

$$\langle\sigma\rangle = \sigma_{iso} + \tfrac{1}{3}\Delta\sigma(3\cos^2\alpha - 1) \qquad (7)$$

where α is the angle between the liquid crystal director (orientation of σ_{zz}) and the magnetic field direction. $\Delta\sigma$ is found to vary with T.[112] Diehl and Jokisaari[96] also found that the ^{129}Xe T_1 in these nematic liquid crystal phases is much faster than in simple organic solvents (23–28 s at 300 K).

Xenon in a nematic liquid crystal phase contained within cylindrical pores (0.1 μm radius) oriented in a membrane showed a $\Delta\sigma$ of 15 ppm owing to random distribution of director axes in a plane perpendicular to the long axis of the cylinder.[115] 2D exchange experiments showed that there was interpore exchange on the time scale of 400 ms, exchange between different average liquid crystal directors within a pore on the 20 ms time scale, and changes in director orientation on a length scale of about 2 μm.

Lowenstein and Brenman[116] were the first to study ^{131}Xe NMR in a liquid crystal (poly(γ-benzyl-L-glutamate) in chloroform). They observed a triplet with a roughly 3:4:3 intensity ratio corresponding to the three transitions of the spin-$\frac{3}{2}$ nucleus in the oriented sample. The splitting of the outer pair of lines was 5.35 kHz, corresponding to a very small average quadrupole coupling. Much later, Diehl, Jokisaari *et al.*[117–119] found much larger quadrupole coupling

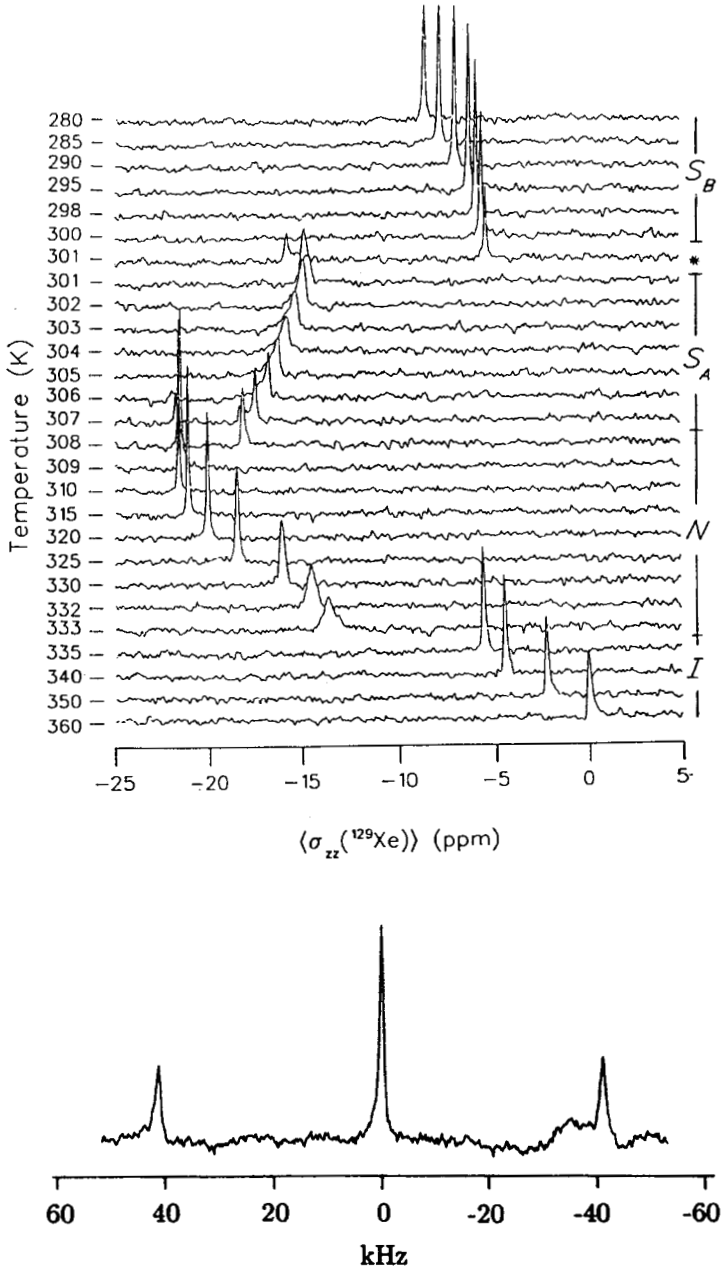

Fig. 9. *Top*: ^{129}Xe NMR spectra of Xe in a binary mixture of nematic liquid crystals as a function of temperature, showing sudden jumps in shift at the various liquid crystal phase transitions. (Reprinted with permission from Ref. 110. Copyright 1990, Gordon and Breach.) *Bottom*: ^{131}Xe spectrum of Xe dissolved in Merck ZLI1167 liquid crystal (a mixture of 4-*n*-alkyl-*trans*,*trans*-bicyclohexyl-4′-carbonitriles) at 325 K, showing a triplet due to quadrupole coupling in the anisotropic medium. (Reprinted with permission from Ref. 118. Copyright 1991, Academic Press Inc.)

constants (see Fig. 9), ranging from 148 to 346 kHz, in nematic liquid crystals (ZLI 1167 and 1132, and EBBA), assuming axially symmetric electric field gradient (EFG) tensors. They attempted to distinguish the EFG generated by the liquid crystal molecules from the EFG arising from distortion of the electron cloud of the Xe due to collisions.

2.2.4. *Solutions of biologically related materials*

Work in this area seems to have been stimulated largely by interest in the anaesthetic properties of Xe and the potential for imaging using hyperpolarized Xe.

Xenon has been studied in various proteins, membranes and vesicles. In the earliest study,[78] data for Xe in solutions of myoglobin suggested that perhaps as many as 10 Xe interact with each myoglobin. There appeared to be fast exchange of Xe between aqueous and organic environments in suspensions of lipid bilayers and membranes in most cases, except for dimyristoyl lecithin vesicles, which showed two separate peaks at 308 K but only one at 323 K. ^{131}Xe T_1 in lecithin vesicles[120] also indicated rapid exchange between free and bound states.

From chemical shift data of Xe in solutions with unilamellar vesicles incorporating gramicidin-A channels[121] it has been suggested that Xe can exchange by transportation through the gramicidin channel.

Xenon will absorb into specific cavities in myoglobin and haemoglobin. More recent studies of ^{129}Xe chemical shifts of these materials in aqueous solution as a function of T[122] indicated one type of Xe site in methaemoglobin, which shows a downfield shift from that in pure water, with an exchange rate of $6 \times 10^{-7}\,m^{-1}\,s^{-1}$ and an E_a of about 13 kcal mol^{-1}. Two sites were indicated in metmyoglobin, one with a large upfield shift (exchange rate $2 \times 10^{-7}\,m^{-1}\,s^{-1}$, and an $E_a \sim 16$ kcal mol^{-1}) and the other a small downfield shift. The sites are in fast exchange with the solvent at room temperature. It was not possible to distinguish any difference between α- and β-haemoglobin using Xe NMR.

In studies using hyperpolarized Xe dissolved in saline for injection into biological samples[123] a T_1 of ~66 s at 9.4 T was obtained in contrast to ~1000 s in D_2O saline. The signal of Xe in red blood cells was found to be ~24 ppm higher than in saline as a result of Xe binding to haemoglobin, and the transfer of Xe from saline to red blood cells was observed. Other biologically interesting materials were also investigated:[123] in "Intralipid" solution $T_1 = 40 \pm 3$ s at 194 ppm and in Fluosol perfluorocarbon $\delta = 110$ ppm. A related study on blood[124] with normal Xe but with HPXe studies in mind looked at T_1 in red blood cells ($\delta = 216$ ppm, $T_1 = 4.5 \pm 1$ s), in plasma ($\delta = 194$ ppm, $T_1 = 9.6 \pm 2$ s) and in water ($T_1 = 26.3 \pm 1.4$ s). The T_1 values are comparable to the transport time of gases in blood.

2.3. Xenon in solid phases of other materials

2.3.1. Polymers

Certain properties peculiar to polymers make them particularly amenable to fruitful study by ^{129}Xe NMR. Amorphous polymers absorb Xe to a significant degree, especially under several atmospheres of pressure, and much more so than crystalline polymers. The absorption is viewed as a dissolution of Xe in the polymer, especially above the glass transition T_g where the polymer chains have considerable mobility.

The usefulness of ^{129}Xe NMR in polymer studies was established by Sefcik *et al.*[125] and Stengle and Williamson.[126] Since then the field has blossomed[127–146] and has been reviewed twice up to 1993,[147,148] so the current discourse will be restricted to describing the salient features and principal uses with detailed reference to a few examples.

(a) The ^{129}Xe chemical shift δ is characteristic of the particular polymer, with values ranging over about 152–250 ppm and with the majority of polymers in the 200–230 ppm region at room temperature.[125–127, 130–134,136,140,142,144–146]

(b) δ decreases with increasing temperature T;[126,132,133,135,143] the changes are usually interpreted in terms of the decreasing density of the polymer.

(c) Plots of δ versus T show two linear regions with a change in the slope at the glass transition T_g.[126,132]

(d) The line widths also show linear T dependence, but with a more pronounced change in slope.[126,131]

(e) Above T_g, the lines are isotropic and can be quite narrow and are generally taken to represent a dynamic average over all site types; the rapid Xe dynamics reflect the increased mobility of the polymer above T_g.[126,133,140,141,145]

(f) Below T_g, motions of the polymer chains are suppressed and Xe is trapped in sites for longer periods. In fact, at temperatures well below T_g, the lines can be very broad.[125,127] This behaviour is interpreted as representing Xe in a distribution of sites, possibly with chemical shift anisotropies, which are not averaged by dynamic exchange. In some cases, however, slow exchange has been noted.[131]

(g) The shift shows very little pressure dependence,[148] except in cases with very high Xe solubility,[132] which is taken to mean that Xe–Xe interactions are not involved, i.e. the Xe atoms are isolated by the polymer matrix.

Polymer mixtures can be characterized either by distinct shifts for Xe in each compound[133] or by differences in line width.[127] Fractional amounts of a component can even be determined from the Xe NMR intensity.[145]

Simpson *et al.*[142,144] have developed a method of determining diffusion

coefficients using polymer microspheres of well-defined size. Using polystyrene beads of sizes 10, 18 and 64 μm, they observed resonances for Xe in the gas and the polymer, and using 2D experiments established that gas–polymer exchange occurs on a time scale of 5 s (smaller beads gave stronger cross peaks). They then selectively saturated the gas-phase Xe resonance and measured the intensity of the Xe resonance in the polymer as a function of the saturation time. The time dependence is readily modelled in terms of the diffusion and T_1. At 25°C, $D = 1.9 \pm 0.4 \times 10^{-9}\,\mathrm{cm^2\,s^{-1}}$, $T_1 = 17.6$ s. From measurements as a function of temperature they were then able to obtain an activation energy for diffusion in glassy polystyrene, $E_a = 36.2\,\mathrm{kJ\,mol^{-1}}$. There was a sharp increase in D above T_g (=100°C); at 115°C, $D = 165 \times 10^{-9}\,\mathrm{cm^2\,s^{-1}}$, $T_1 = 10.3$ s.

The miscibility of polymer blends can be ascertained using Xe NMR. Blends that are truly miscible, i.e. that form a single phase, give rise to a single resonance. Immiscible blends may show two lines arising from Xe in the two regions, but if the domains are small enough to allow rapid exchange on the time scale of the measurement a single line will be observed. The criterion for distinguishing a miscible blend from the latter case is that the observed shift is different from the exchange average calculated from the shifts for the separate polymers. This approach is particularly useful in cases where the T_g is similar in the two components and consequently DSC measurements will not distinguish the two situations; for example, McGrath and Roland[140] observed shifts of 230.5 and 209.8 ppm for Xe in polyepichlorohydrin and poly(vinyl methyl ether), respectively. For a particular blend of these they calculated an exchange average of 214 ppm, significantly different from the observed 217.7 ppm. The blend must therefore be miscible. Walton *et al.*[136] gave a simple demonstration of polymer mixing on the microscopic scale using Xe NMR (Fig. 10). They heated a blend of polybutadiene and polyisoprene (known to be miscible) to 100°C, where phase separation occurred, and then quenched to room temperature. Two Xe signals corresponding to domains of separate polymers were observed immediately after quenching, which gradually coalesced to a single line over a period of days as the components interdiffused. Based on the slow exchange model, a knowledge of the diffusion coefficient and the observed peak separation, they estimated the domain sizes to be about 0.3 μm immediately after quenching.

Several 2D EXSY experiments have been used to study Xe exchange (or the lack of it) between different microdomains and with the gas phase (Fig. 11), to determine the time scales involved and obtain exchange rate constants.[131,134,137,142,143] Effective diffusion constants can then be obtained from the rate constants if the domain sizes are known.

Mansfield and Veeman[137,141] investigated a blend of polypropylene (T_g = 0°C) and polyethylene–polypropylene copolymer (T_g = −50 to −60°C). At 243 K, ^{1}H–^{129}Xe cross polarization and 2D heteronuclear correlation spectra both showed that magnetization transfer was occurring only in the

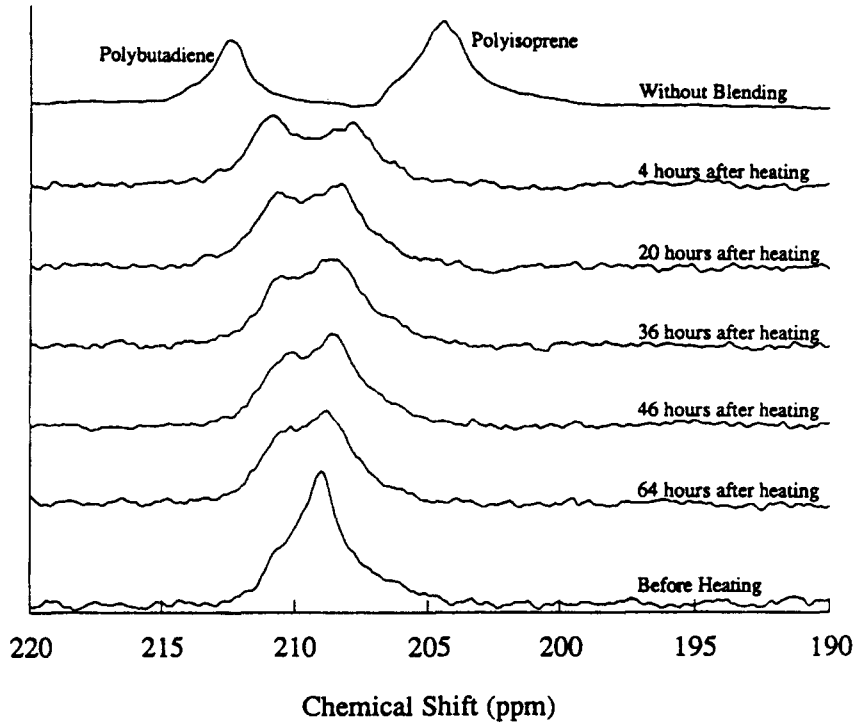

Fig. 10. ^{129}Xe NMR spectra of the miscible polymer blend (34% by volume 1,4-polyisoprene and 66% polybutadiene (8% vinyl content)) at room temperature. *Top*: distinct pieces of the two pure polymers. *Bottom*: The polymer blend before heating. *Middle*: At several times after phase separation induced by heating the blend to 373 K for 30 min. (Reprinted with permission from Ref. 136. Copyright 1993 American Chemical Society.)

glassy polypropylene and not the copolymer. At room temperature, no CP signal was detected from either material. Clearly, when the polymers are above their respective T_g values the enhanced mobility of the chains and of the Xe very effectively reduces the dipolar couplings necessary for CP.

Hyperpolarized ^{129}Xe NMR has been used in two studies of polymer surfaces. (1) HPXe adsorbed on poly(triarylcarbinol), which has a large surface area, at −160°C shows a broad signal, but the main interest here was to demonstrate the ability to selectively transfer polarization from the Xe to the surface protons in high field.[138] (2) HPXe on poly(acrylic acid) was studied at low pressures as a function of temperature.[139] Samples had to be treated at 80°C under vacuum overnight to remove water from the polymer, otherwise very broad signals were observed. Dried samples showed relatively sharp signals which increased in shift as the pressure increased, indicating exchange between

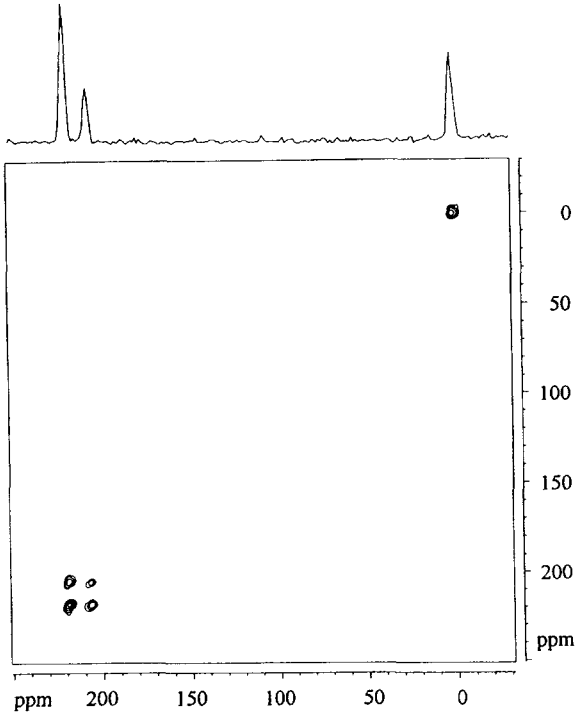

Fig. 11. ^{129}Xe 2D exchange spectrum of Xe in a polymer mixture of 79% polypropylene matrix with 21% copolymer (1/3 polypropylene with 2/3 polyethylene) at room temperature. During the 5 s mixing time exchange occurs between the two phases within the polymer mixture but not between the polymer and the free Xe gas. (Reprinted from Ref. 137 with kind permission of Elsevier Science—NL, Sara Burgerhartstraat 25, 1055 KV Amsterdam.)

the gas and the surface Xe population (at very low pressure at room temperature, resonances may be only a few ppm from the gas line). As the temperature decreases, the shift increases rapidly as more Xe condenses on the surface and its sticking time increases. The shift due to the Xe–surface interaction was determined to be $\delta s = 95$ ppm and δ increases with coverage owing to Xe–Xe interactions on the surface. From the pressure dependence of the shift the surface diffusion coefficient was determined to be $D_s = 3.3 \times 10^{-5}\ \mathrm{cm^2\ s^{-1}}$.

One final observation is that the shift of Xe in polymers is in a range very close to the shift range of 225–242 ppm found for Xe in pentagonal dodecahedral hydrate cages (see following section). These hydrate cages are deemed to be almost a perfect "fit" for the Xe atom in terms of optimum van der Waals interaction. This match perhaps suggests that the average size of the

cavities in polymers is also close to optimum. Presumably the flexibility of the polymer chains allows them to wrap closely about the Xe atom.

2.3.2. Clathrates and inclusion compounds of xenon

Inclusion compounds of xenon are a very important group of materials, especially since they have provided a number of clues relevant to the interpretation of xenon NMR behaviour in other microporous materials.[149–160] (The broader term *inclusion compounds* encompasses clathrates, which are distinguished by having Xe inside closed cages.) In essence they represent one extreme of the range of microporous systems, where the xenon is "locked" into a pore. In many instances they give rise to a measurable chemical shift anisotropy (CSA) (see Table 4). Some of the earliest work done on Xe(0) in solids[149,150] and the first ^{1}H–^{129}Xe cross polarization (CP) and magic angle spinning (MAS) experiments were on xenon clathrates.[151] CP leads to considerable savings in experimental time since ^{129}Xe T_1 in clathrates can be lengthy; compare 800 s recycle times for Xe in D_2O hydrate[149,150] versus 30 s recycle times for CP in H_2O hydrate.[151]

^{129}Xe NMR has been an extremely useful tool for the study of clathrate hydrates,[149–160] which consist of an ice-like network of host water molecules linked together by hydrogen bonds in such a way as to form face-sharing cages that surround single guest molecules. There are three main structural types; cubic structures I and II and hexagonal structure H, each of which can form with numerous different guest molecules. All three have both small and large cages (two types of small cage in structure H) and the dimensions of the principal guest largely determine which structure forms. Xenon alone forms structure I, but it can also be present as a secondary guest in structures II and H. Xe NMR is very sensitive to the sizes, shapes and relative occupancies of the cages: the symmetries of the various cages are known from the hydrates' crystal structures and these are reflected in the ^{129}Xe lineshape anisotropies, which thus can be used to assign the lines to Xe in specific cages;[150,155,157,158] for example, the large cage of structure I has one unique axis and therefore gives an axially symmetric powder pattern. All three hydrate types have pentagonal dodecahedral cages; however, the symmetry is different in each case. In structure I it is pseudospherical and thus gives an isotropic Xe NMR line; structure II gives an axially symmetric lineshape; and structure H gives a nonaxially symmetric lineshape. Assignments can also be based on the line intensities; for example in Xe structure I hydrate there are three times as many large cages as small, so the anisotropic line has more intensity,[149,150,153] and on the relative shifts, since the smaller the cage, the larger the downfield shift.[155]

As a consequence of these properties, each hydrate type has a very characteristic spectrum (Fig. 12), and this has been used to advantage as a

Table 4. Chemical shifts of Xe trapped in cages, inclusions and defects.

Material	T (K)	Site	δ_{iso} (ppm)	Anisotropy (ppm)[a]	Reference
D_2O structure I hydrate	263–293	$5^{12}6^2$ large cage[b]	152	32	149
		5^{12} small cage	242	0	150
Ethylene oxide structure I hydrate	275	$5^{12}6^2$ large cage	150	30	151
		5^{12} small cage	240	0	
Xe structure I hydrate	298	$5^{12}6^2$ large cage	152.1	29.3	[c]
		5^{12} small cage	242.3	0	
Structure II hydrate	77	$5^{12}6^4$ large cage	80	0	155
		5^{12} small cage	225	18	
Tetrahydrofuran structure II hydrate	298	$5^{12}6^4$ large cage			[c]
		5^{12} small cage	232.1	25.2	
Structure H hydrate	77	$4^35^66^3$ small cage	215	~40	155
		5^{12} small cage	232		
Methyl t-butyl ether structure H hydrate	273	$4^35^66^3$ small cage	212.4	47.7	[c]
		5^{12} small cage	230.9	$xx = 1.4$ $yy = 12.2$ $zz = -13.6$	
β-Quinol	298	Single cage	222	−160	151
β-Phenol	298	Small cage	229	−171	151
		Large cage end site	250	−105	
		Large cage middle site	279	−53	
p-Fluorophenol	298		209	−164	152
Dianin's compound	298	1 Xe/cage	134	−84	161
		2 Xe/cage	152	−54	
α-Cyclodextrin	298	Fully hydrated	192	22.4	155
		Dehydrated	199	$xx = 6.8$ $yy = 23.3$ $zz = -30.1$	
Clathrasil D3C structure II					
Cubic	376	Small cage	253	45	155
		Large cage	81	0	
Tetragonal	298		(253)	$xx = 5.1$ $yy = 29.1$ $zz = -34.3$	
Clathrasil DD3R	203	1 Xe/cage	79	~0	361
		2 Xe/cage	142	58	
Zeolite NaA	298	1 Xe/cage	74.8	0	278
Zeolite KA	298	1 Xe/cage	79.5	0	299

[a]Anisotropies given as $(\delta_\perp - \delta_\parallel)$ if axial, or as $\delta_{xx}\,\delta_{yy}\,\delta_{zz}$ relative to δ_{iso} if nonaxial.
[b]Notation for cages: 5^{12} corresponds to a pentagonal dodecahedron, 12×5-sided faces.
[c]Ripmeester and Ratcliffe, new results.

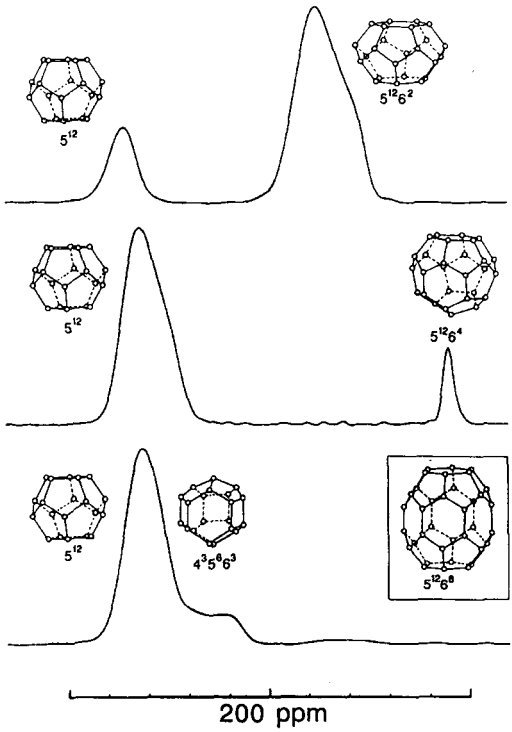

Fig. 12. ^{129}Xe NMR spectra of structures I, II and H clathrate hydrates obtained with ^1H cross polarization at 77 K. *Top*: Pure Xe structure I hydrate. *Middle*: Structure II double hydrate of *n*-butane and Xe. *Bottom*: Structure H double hydrate of bicyclo[2.2.2]oct-2-ene and Xe. The various cages associated with each signal are shown. No signal was found for Xe in the large cage of structure H (inset). (Reprinted with permission from Ref. 157.)

means of identifying potential hydrate-forming molecules.[155] In fact, the Xe spectrum was an important piece of evidence in the discovery of structure H hydrates[154] in 1987. In this hydrate the xenon has been seen only in the two types of small cages, which presumably indicates that the large cage must be fully occupied by the large guest molecule for the structure to be stable. NMR measurements of the small/large cage occupancy ratio in combination with calorimetric measurement of the overall composition of Xe structure I hydrate prepared under 3-phase equilibrium conditions were used to obtain the thermodynamic chemical potential of the empty structure hydrate lattice relative to that of ice, $\Delta\mu_w^\circ = 1297 \pm 110$ J mol^{-1},[153] which is very important in models of hydrate stability.

Pure krypton forms a structure II hydrate; however, from ^{129}Xe NMR, together with powder X-ray diffraction and calorimetry,[156] it was shown that

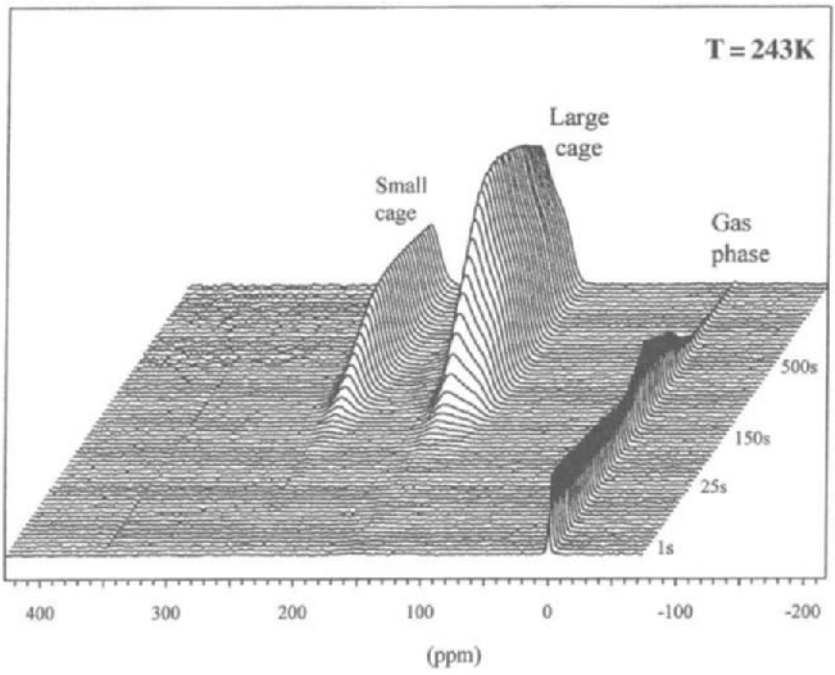

Fig. 13. Hyperpolarized ^{129}Xe NMR spectra as a function of time after absorption of Xe onto D_2O ice at 243 K (Ref. 160).

mixtures of Xe–Kr form exclusively structure I at only 5 mol% Xe. This appears to be driven by Xe having a greater preference for the large cage of structure I than the large cage of structure II.

In recent developments, hyperpolarized Xe has been used to observe the formation of Xe clathrate hydrate on ice surfaces[159,160] as a function of T and time (Fig. 13). In the very early stages of formation there appears to be substantially larger occupation of small cages than is found in bulk equilibrium Xe hydrate.

The clathrasil dodecasil-3C has a structure analogous to structure II hydrate with H_2O replaced by SiO_2. This material, when made with Xe and tetrahydrofuran (THF) guests, displays three phase transitions. There is a progressive lowering of crystal symmetry from the high-temperature cubic lattice to the lower temperature phases, which can be detected by monitoring the ^{129}Xe CSA of the Xe in the small cages.[155] The high-temperature cubic phase shows an axial lineshape, which becomes nonaxial in the room-temperature tetragonal phase. The asymmetry parameter increases in the next phase, and the lowest temperature phase has a lineshape that cannot be described by a single CSA tensor.

Xenon-129 has also been studied in several organic inclusion compounds:

(a) Xe–β-quinol clathrate has a single cage elongated along its symmetry axis and the Xe NMR lineshape correspondingly shows an axially symmetric, negative CSA.[151]
(b) Xe–β-phenol clathrate is more interesting; it has two types of cages but shows a spectrum with three axially symmetric lineshapes, also with negative CSA.[151] The large cage is very elongated and contains 3 Xe atoms, of which the two at each end are equivalent, thus giving rise to two shifts with a 1:2 intensity ratio. The third line arises from a single Xe in the small cage.
(c) Dianin's compound forms a clathrate with hourglass-shaped cages that can contain one Xe in each half of the hourglass. The observed Xe NMR CSAs are again negative, but more interesting here are the results of MAS experiments.[161] With 2 Xe in the cage the shift is roughly 19 ppm downfield from that of half-empty cages with 1 Xe only. Furthermore the 2 Xe line shows fine structure. The origin of this fine structure was determined by CP-MAS studies on mixed Dianin's clathrates made with ethanol and increasing amounts of Xe. The Xe shift was sensitive not only to the second guest in the same cage (either Xe or ethanol) but also to the nearest guest (Xe or ethanol) in the adjacent cage (Fig. 14).
(d) Xe in a α-cyclodextrin inclusion compound is a sensitive probe of the degree of hydration of the macrocycle. In fully hydrated α-CD the Xe NMR lineshape shows positive axial anisotropy. In the driest samples the line shifts downfield and becomes nonaxial, indicating a tighter site with lower symmetry.[155]

Xenon in solid solutions or trapped in defects in a crystal lattice of another solid,[155] although these are not strictly inclusion compounds, behaves in a similar fashion and can give information about the types of trapping site (e.g. Xe in solid H_2S, tetramethylsilane or neopentane) and about phase changes in the host (e.g. Xe in neopentane). A very large shift of about 415 ppm indicates a rather tight fit for Xe in the lattice of H_2S at 77 K.

Table 4 includes values for Xe in the cages of clathrasil DD3R and A zeolites, which are not clathrates since the Xe can diffuse in and out. However, the time scale for this process is such that spectra unaffected by exchange averaging can be obtained, and the chemical shifts reflect encaged Xe.

From these studies on clathrates there has emerged an apparent linear dependence of shift on the van der Waals diameter of the cavity, at least in the region of cage sizes sampled.[155] Another important observation is that positive anisotropies (σ_{zz} at highest field) are associated with oblate cages and, conversely, negative anisotropies (σ_{zz} at lowest field) are associated with prolate cages. There are two ways in which the observed anisotropy of an Xe in a cage might arise:

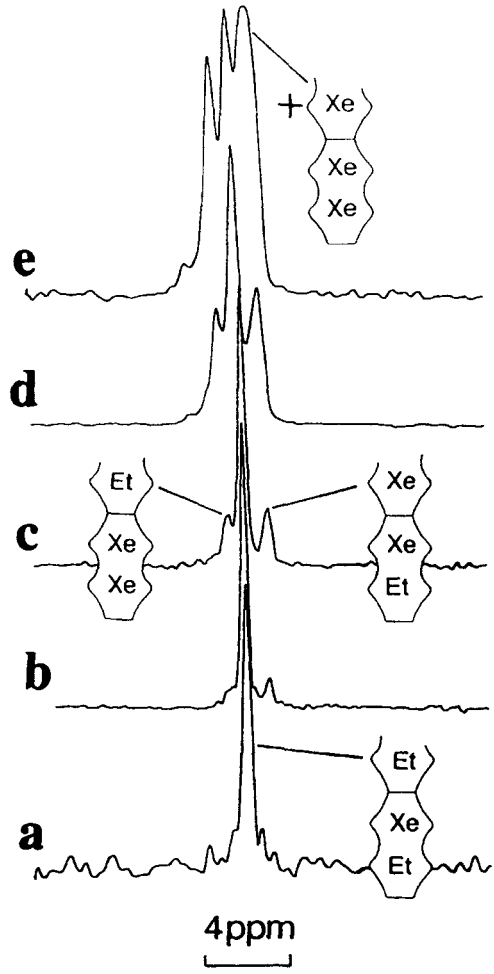

Fig. 14. ^{129}Xe CP-MAS NMR spectra of Dianin's compound clathrate with Xe and ethanol guests. The samples were crystallized from ethanol under different Xe pressures: (a) 0.3; (b) 0.7; (c) 1.5; (d) 3.0; (e) 20.0 atm. The assignments of peaks to Xe with various combinations of neighbours are indicated. (Reprinted with permission from Ref. 161.)

(1) The Xe sits exactly at the cage centre, with the full site symmetry responsible for the axially symmetric anisotropy. The sign of the anisotropy then reflects compression or elongation of the electron cloud along the symmetry axis.
(2) The Xe samples all available space in the cage. At all sites off the cage

centre the Xe must have a shift anisotropy because of the reduction in symmetry, but more importantly the orientation of the shift tensor will be different at each site. The observed anisotropy is then a dynamic average over all site orientations. The change of sign of the anisotropy from prolate to oblate cages is a consequence of this model. Clearly the picture of Xe sitting rigidly at the cage centre is unrealistic because of vibrational motions, and calculations (see later) show that in large cages the Xe prefers to be closer to the walls.

2.3.3. Xenon in porous materials

Xenon NMR has been used to study many kinds of porous solids ranging from very large-pore materials such as Vycor glass to pillared clays and all kinds of zeolites and molecular sieves, some with very small pores. In general the Xe is used to probe pore sizes and adsorption properties, the effects of exchanging H^+ and dealumination, and interaction with different cations or metal clusters, and to probe the effects and locations of other adsorbates, particularly organic molecules in catalytic zeolites and their coking problems. Xenon is roughly the same size as methane and thus is also a model substitute for the study of diffusion of small organic molecules in zeolites. Most of these materials have open channels, which leads to a loading dependence of the chemical shift. They are thus considerably more complicated than the closed cage systems such as the clathrates described above or the A zeolites described later, and the interpretation of Xe NMR results can be fraught with many problems.

There is an extensive literature in this area (the larger part of which pertains to X and Y zeolites), much of which has been reviewed repeatedly, so here we will dwell only on a few specific aspects. However, all the literature pertaining to zeolites, microporous systems and surfaces has been tabulated and grouped according to material type or topic, to provide a useful reference (Table 5). Aside from the more general reviews mentioned earlier,[2,3] there have been several reviews specific to ^{129}Xe NMR in zeolites and microporous materials.[6,7] Fraissard and colleagues have produced several reviews over the years that summarize much of the experimental progress and models current at each time.[5,11,162–167] Dybowski gives a rather more detailed review of a number of the topics mentioned only briefly here.[10]

Chemical shift. Fraissard and coworkers have characterized the shift of Xe in porous media as arising from a sum of various interactions:

$$\delta_{obs} = \delta_0 + \delta_S + \delta_{Xe} + \delta_{SAS} + \delta_E + \delta_M \tag{8}$$

Here δ_0 is the reference shift. δ_S is the shift extrapolated to zero Xe loading. Note, however, that this only has an unambiguous meaning for open pore

Table 5. Catalogue of publications on ^{129}Xe NMR of Xe in zeolites and microporous materials and on surfaces.

Topic	Reference
Zeolites X, Y	
Na^+	168–224
Alkali metal ions	170,173,224–227
Alkaline earth metal ions	168–170,173,176,194,226–228
Transition metal ions	176,226,227,229–240
Cu	224,226,227,241–249
Ag	224,241,250–253
Zn	197,226,227,241,254–257,307
Cd	241,258–260,307
Rare earth ions	170,225,240,261,262
H and dealuminated	168,174,183,197,227,263–273
Zeolite A	
NaA	274–283
NaA calculations	284–296
NaA/Kr	297
NaA/Ar	298
KA	299
AgA	300,301
CaA	168,302–304
Other microporous materials	
ZSM-5	219,220,270,305–311,353
ZSM-11	308–310
ZSM-12	312
ZSM-20	219
Zeolite beta	313,314
Silicalites	315,316
Zeolite Z	308
Nu-10	317
Omega	318
Ferrierite	318
Zeolite Rho	248,249,319–322
Zeolite L	194,308,323,324
H-Ga-MFI	325
MCM-41	326
ETS-10	327
ALPO/SAPO/MAPO	328–339
Mordenites	151,340–342
Clays/pillared montmorillonite	343–345
More specific areas	
Metal clusters in zeolites	192,196,198–218,223,228–237,323,324,346–348,392–397
Surface-coated zeolites	194,349
Inorganics inside zeolites	175,193,239,350
Organics inside zeolites	184–191,351–353

[*Continued*

Table 5—*Continued*

Topic	Reference
More specific areas—*continued*	
Coking of zeolite organics	265–268,270,271,354,355
Pulsed field gradient studies	182,222,356–360
Diffusion	179,180
Models of shifts and exchange	221,361–374
Miscellaneous	
Silicas	54,137,178,181,375–378
Vycor glass	379
Aluminosilicate gels	380
Amorphous silica and alumina	381
Amorphous carbon	382–384
Graphite	385,386
Coal micropores	387,388
Oxide-supported catalysts	389
Pt on alumina	390–395
Heteropolyacids/metallates	396,397

systems and might better be described as the shift arising from interaction of a single Xe with the atoms of the framework, i.e. the shift in the absence of Xe–Xe interactions. δ_{Xe} from Xe–Xe interactions is dependent on loading $\delta_{Xe\text{-}Xe}\rho_{Xe}$. δ_{SAS} is the shift due to strong adsorption sites. δ_E and δ_M shifts are due to electric and magnetic fields (thought to be due to the charge and paramagnetism of the cations). Barrie and Klinowski[7] point out that much earlier theoretical work[31] showed that a point charge should have very little effect on the shift, so that the δ_E term must really represent some other effect.

Figure 15 shows shift versus Xe loading plots for NaY/X and CaY zeolites[168] that are typical of many other systems. Plots can be linear or show various degrees of curvature. The intercept at zero Xe loading gives δ_S and the slope of the linear plots is often taken as largely arising from increasing Xe–Xe interactions, though, as we shall see later, excluded volume and crowding effects must also be considered. Interactions with Na^+ are usually taken to be small and so differences in δ_S for exchanged cations have been interpreted as effects of Xe–cation interaction. Upward curvature, especially at low loadings, has been interpreted as evidence for strong adsorption sites that saturate at higher loadings.

We have already seen in the previous section that there is a general rough correlation between increasing shift and decreasing void space. Although several models have been proposed that attempt to make a more quantitative correlation (the mean free path model of Fraissard *et al.*,[369,372,374] the surface

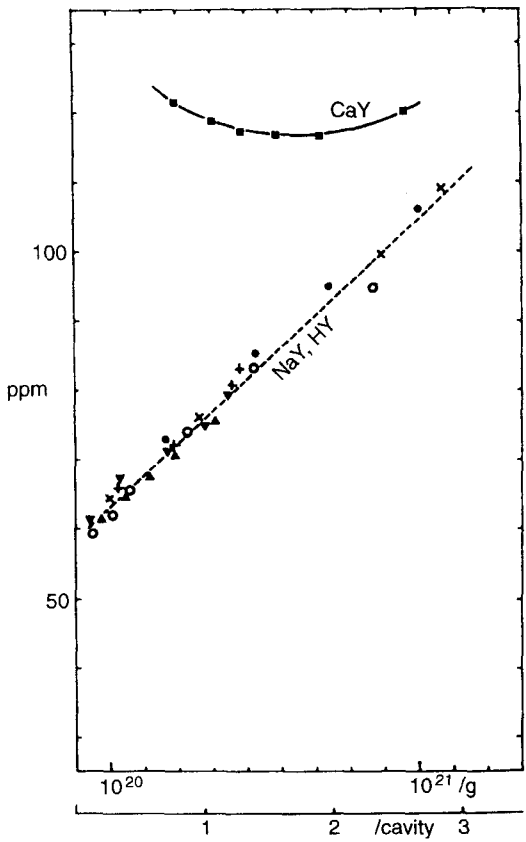

Fig. 15. ^{129}Xe NMR chemical shifts in NaY and CaY zeolites. ▲, $NaY_{54.2}$; ▼, $NaY_{3.2}$; ○, $NaY_{2.42}$; ●, $NaY_{1.35}$; ×, $NaY_{1.28} \equiv NaX$; ■, CaY. The numerical subscript refers to the Si/Al ratio of the zeolite framework. (Reprinted with permission from Ref. 168. Copyright 1982 American Institute of Physics.)

curvature model of Derouane *et al.*[368,371] and the surface area/pore volume ratio model of Johnson and Griffiths[370]), their success and reliability have been questioned.[7,275,334,375] Furthermore, grand canonical Monte Carlo and *ab initio* calculations of Xe shifts in A zeolite cavities, discussed later, show that the shift is a complicated function of many factors. This brings us to a consideration of the effects of Xe dynamics in open pore systems.

Dynamics. One thing that has become very clear over the years is that Xe has a very dynamic personality. Indeed, one must conclude from all available results to date that Xe NMR spectra in whatever medium are strongly influenced by the dynamics of the Xe atom. In general, unless it involves a squeeze into a pocket with a substantial barrier, the various "sites" visited by

the Xe have quite shallow potential wells. The chemical shift must then reflect an average of all the chemical shifts experienced by the Xe weighted by the fraction of time spent at each location during the time frame of the NMR experiment. Obviously this will be influenced by the Boltzmann distribution over the many sites. This also applies to single Xe atoms in zeolite frameworks; the extrapolated shift must still represent an average, unless the Xe is trapped. Even when trapped within a cage, the Xe shift and shielding anisotropy reflect an average over the accessible space.

Pulsed field gradient studies[182,222,356–360] show that the Xe diffuses over large lattice distances on the NMR time scale at ambient temperatures. Of course, rapid Xe exchange among all sites in a cubic framework must give rise to an isotropic NMR lineshape, as observed in X, Y and A zeolites. Numerous 1D experiments have demonstrated intra- and interparticle exchange of Xe (e.g. Refs 223, 300, 301, 360, 362, 364–366). 2D EXSY experiments have been used to demonstrate macroscopic Xe exchange between particles of X and Y zeolites and microscopic exchange between the main channels and side-pockets of mordenite.[195]

In Y zeolites, exchange with the interparticle gas phase is rapid; there is no gas line in the spectrum if the gas space above the sample is excluded from the NMR coil. However, if there is a lot of interparticle gas space, so that some Xe are unable to exchange rapidly enough, a line due to interparticle gas (often broadened) will be observed (inclusion of the gas space above the sample gives a sharp gas line). This interparticle gas phase can give rise to bulk density or aggregate size effects on the shift; i.e. small changes in shift depending on whether the material is compacted or a loose powder (e.g. Refs 176, 362).

There have been several low-temperature studies of Xe, mainly in Y zeolites.[173,220,221,362] Xenon shifts as a function of temperature and loading in NaY[362] are shown in Fig. 16. As T decreases there is an initial sharp rise in shift as more Xe condenses into the pores from the gas phase, then a levelling off when the gas phase is exhausted. At lower temperatures still the shift begins to increase again, suggesting an increase in local Xe density, presumably owing to some kind of phase condensation within the pores. Great care must be taken to equilibrate the samples at each temperature. Cheung[173] observed broad multiple-featured spectra from rapidly cooled samples, and one must also wonder whether his samples slowly cooled to 144 K still gave nonequilibrium spectra in light of other results on NaY at 77 K.[221] Ratcliffe and Ripmeester[221] found that very long equilibration times were needed for samples quenched from room temperature to 77 K (over a year for some samples). However, a crucial observation was that the equilibrium spectra at 77 K were invariably single isotropic lines. This implies that there is still rapid Xe motion among numerous sites in the cubic lattice at 77 K. Multiple anisotropic lines would be expected if the Xe were static. The results were interpreted in terms of rapid intraparticle dynamics, with very slow interparticle exchange at low temperature leading to the very slow equilibration. The complex spectra obtained

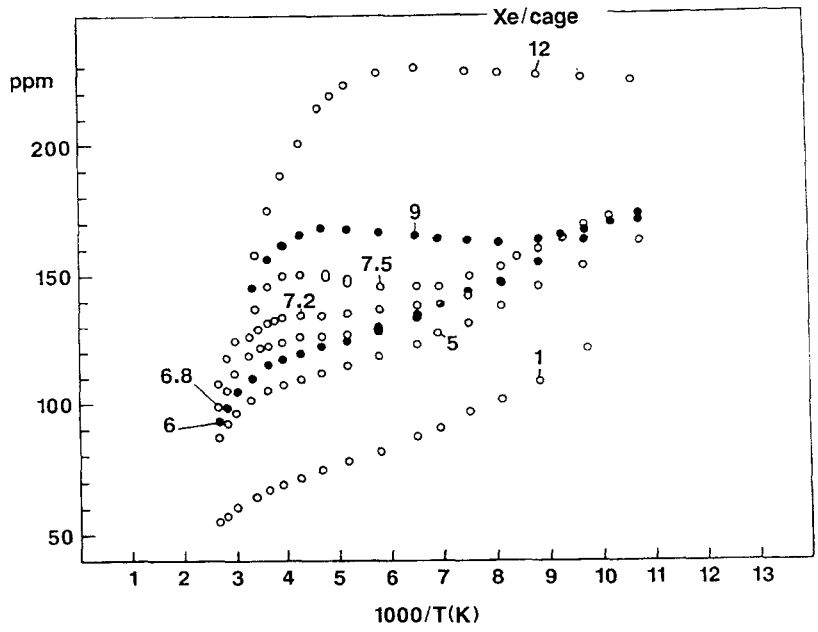

Fig. 16. ^{129}Xe NMR chemical shifts for Xe in NaY zeolite at different average loadings as a function of inverse temperature. (Reprinted with permission from Ref. 362.)

during equilibration arise from a distribution of particles with different Xe loading (brought about in the first place by thermal gradients when the samples were quenched) and hence different Xe shifts.

Chemical shift anisotropy in microporous systems. There have been only a few reports of observations of chemical shift anisotropy for xenon in zeolites and other microporous systems with reduced dimensionality, mainly for the narrow one-dimensional channel aluminophosphate ALPO-11,[7,328,329,332] but also for systems with larger channel sizes such as ZSM-12,[312] Nu-10,[317] ALPO-5,[160,328,332] SAPO-5,[332] SSZ-24 and VPI-5,[160] and for the clathrasil DD3R which has a 2D pore structure.[361] It also seems that in some cases where the anisotropy is small it has been overlooked or misinterpreted, perhaps owing to low magnetic fields where the frequency spread is smaller or because of signal-to-noise problems.[330,334,337,338,374] A key question concerns the origin of this anisotropy, which closely relates to the nature of the observed xenon chemical shifts.

For Xe in the one-dimensional channels of ALPO-11,[329] the anisotropy was found to vary continuously with Xe loading, changing sign in the process (Fig.

17), which was explained in terms of a model involving dynamic exchange between three types of adsorption site:

(a) The channel consists of a chain of interconnected cells.
(b) Each cell can contain only one Xe atom.
(c) Three types of Xe can then exist in this channel, at sites with 0, 1 or 2 neighbouring xenons, i.e. (O<u>Xe</u>O), (O<u>Xe</u>Xe) and (Xe<u>Xe</u>Xe).
(d) Each type of Xe rapidly samples the space available to it and thus has a different chemical shift tensor dependent on its local environment (different Xe–O and Xe–Xe interactions).
(e) The Xe are distributed statistically among the three types of site and thus the site populations vary with loading.
(f) The barrier between cells is sufficiently low that on the time scale of the NMR experiment each Xe experiences fast exchange between the three types of site.
(g) The observed lineshape thus arises from a population-weighted dynamic average of the tensors for the three sites.

ZSM-12[312] has slightly larger channels than ALPO-11, but the behaviour is similar until the higher levels of Xe loading where Xe begins to populate sites of higher energy. In addition to the rapid intracrystallite dynamics, 2D EXSY spectra showed that there is slower exchange of Xe between crystallites and between crystallites and the gas phase. The 2D EXSY spectra shown in Fig. 18 are particularly interesting. At mixing times between 0.5 and 10 ms the anisotropic powder lineshape begins to develop off-diagonal intensity, leading eventually to a novel arrowhead-shaped 2D pattern. This behaviour clearly indicates exchange between different frequency components of the lineshape. If we recall that the anisotropic lineshape is composed of multiple single-frequency lines from crystallites with different orientations, this is unequivocal evidence for slow exchange of xenon between crystallites (estimated lifetime in a crystallite is somewhere between 1 and 10 ms).

2.3.4. Xenon in A zeolites

Studies of Xe in NaA were initiated by Saumant *et al.*,[274] who discovered that NaA dehydrated at 575 K, pressurised with Xe (40 bar/525 K) for several hours and then cooled gave an Xe spectrum consisting of five lines. The resonances arise from Xe in cages containing different numbers of Xe atoms, the chemical shift increasing with the number of Xe from Xe_1 to Xe_5. From here studies of Xe in A zeolites have developed into a very important area. In many respects the Xe–A zeolite system has become a microcosm of the study of Xe in microporous materials, providing a model system for experimental work,[168,275–283,297–304] which, with the aid of established theory and computer

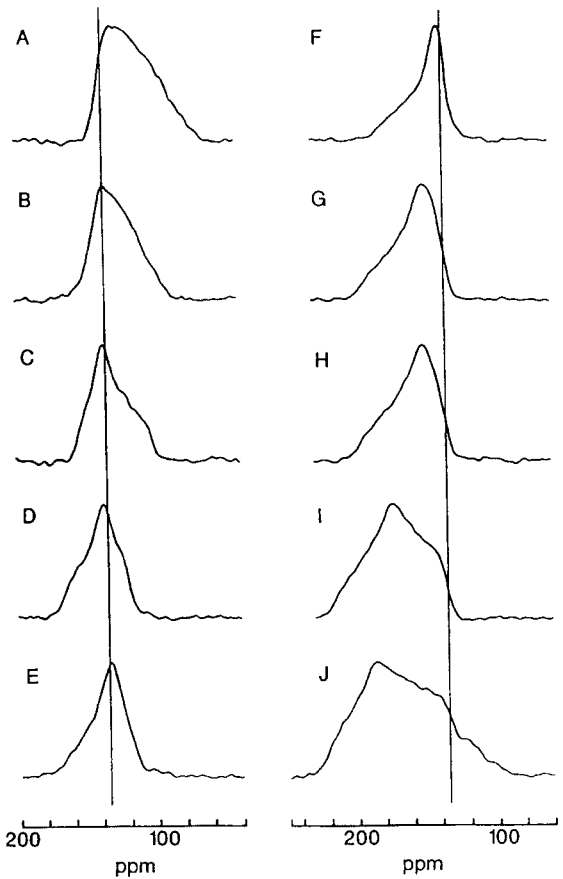
A
B
C
D
E
F
G
H
I
J
200
100
ppm
200
100
ppm

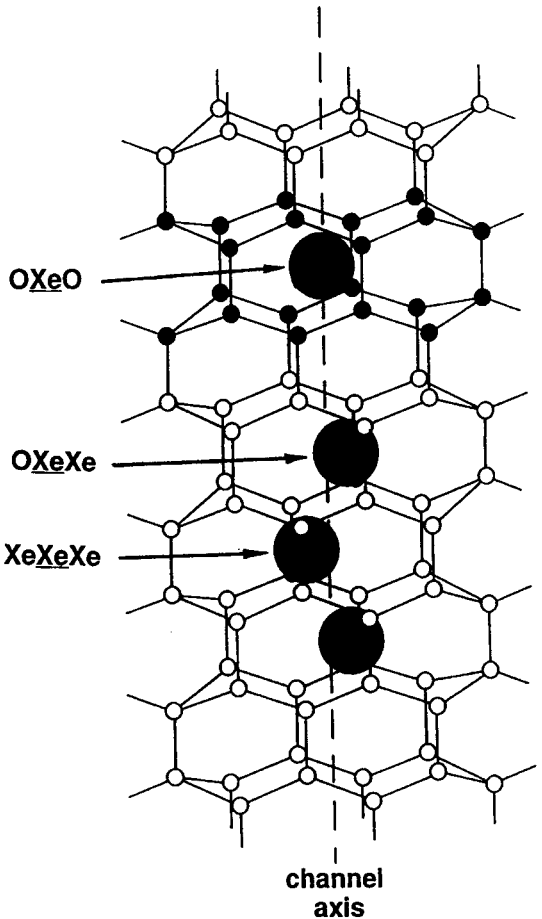
OXeO
OXeXe
XeXeXe
channel
axis

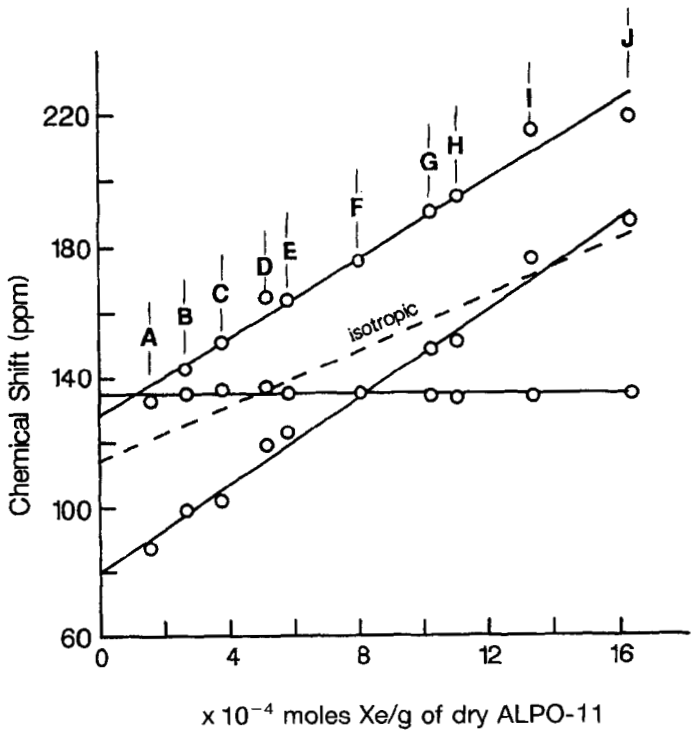

Fig. 17. ^{129}Xe NMR lineshapes for Xe in ALPO-11 as a function of loading at room temperature: spectra (*top left*), chemical shift tensor components (*bottom*). Loading levels from A to J: 1.58, 2.70, 3.80, 5.16, 5.83, 8.05, 10.30, 11.10, 13.40 and 16.40 ($\times 10^{-4}$) moles Xe per gram of dry ALPO-11. The structure of one channel in ALPO-11 (*top right*), indicating the three types of site considered in the model. (Reprinted with permission from Ref. 329.)

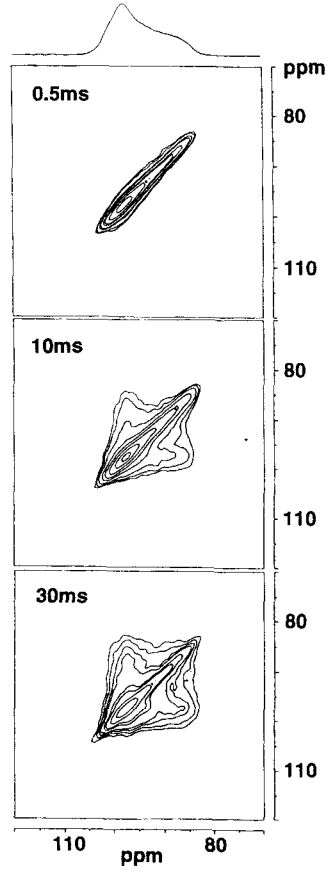

Fig. 18. ^{129}Xe 2D EXSY spectra of Xe in Si-ZSM-12 at room temperature and a loading of 1.676 Xe per unit cell. (Reprinted with permission from Ref. 312.)

modelling,[284–296,298,299,398,399] has helped to increase dramatically our understanding of the chemical shift behaviour of Xe in zeolites.

NaA. The main characteristics of Xe in NaA can be summarized as follows:

(1) Individual resonances are observed for Xe_n clusters of $n = 1$ up to 8 Xe per cage; δ_n = 74.8, 92.3, 111.7, 133.2, 158.4, 183.5, 228.3, 272.3 ppm for Xe_1 to Xe_8, respectively[278] (Table 6). Small variations in shift from one study to another[274–279] probably reflect: (a) different source material; (b) the presence of O_2 or (c) the high- rather than low-temperature structure of the zeolite framework (see later).

Table 6. ^{129}Xe chemical shifts (ppm) for Xe_n clusters in A zeolites

	Na^{+} [278]		K^{+} [299]		Ag^{+} [300,301]	
No. of Xe	δ	$\Delta\delta_{m\rightarrow m+1}$	δ	$\Delta\delta_{m\rightarrow m+1}$	δ	$\Delta\delta_{m\rightarrow m+1}$
1	74.8		79.5		112.3	
		17.5		18.9		17.0
2	92.3		98.4		129.3	
		19.4		21.3		17.8
3	111.7		119.7		147.1	
		21.5		25.7		20.0
4	133.2		145.4		167.1	
		25.2		35.1		25.3
5	158.4		180.5		192.4	
		25.1				28.1
6	183.5				220.5	
		44.8				51.5
7	228.3				272.0	
		44.0				45.6
8	272.3				317.6	

(2) δ_n does not change with the overall loading of Xe; i.e. the shift is not affected by clusters in neighbouring cages.
(3) The shifts increase steadily up to Xe_6, but the increment suddenly doubles for $Xe_6 \rightarrow Xe_7$ and $Xe_7 \rightarrow Xe_8$; $\Delta\delta_{m\rightarrow m+1}$ = 17.5, 19.4, 21.5, 25.2, 25.1, 45.1, 43.7 ppm for $\Delta\delta_{1\rightarrow 2}$ to $\Delta\delta_{7\rightarrow 8}$, respectively[278] (Table 6).
(4) The line intensities give the distribution of Xe_n clusters in the zeolite.
(5) The distribution of clusters depends on the amount of Xe loaded into the zeolite, which in turn depends on the pressure and temperature at which it is equilibrated.
(6) The distribution of clusters changes dramatically with the temperature of equilibration, illustrated in Fig. 19.
(7) Nonequilibrium distributions change slowly with time at room temperature.
(8) With increasing temperature the shifts for 1 or 2 Xe/cage decrease, for 3 Xe/cage it is more or less constant, and for higher loadings the shifts all increase.

Exposure to air[274,279] or addition of small amounts of O_2[276–278,280,281] results in a slight increase in the ^{129}Xe shifts. The O_2 produces a collision-induced contact shift[66] and the effect is strongest for the smallest Xe_n clusters, which have a greater exposure to the O_2 on average.[278] However, an advantage of adding O_2 is that it helps reduce the ^{129}Xe T_1.[276,277,279–282]

If spectra are obtained immediately after cooling from the temperature of

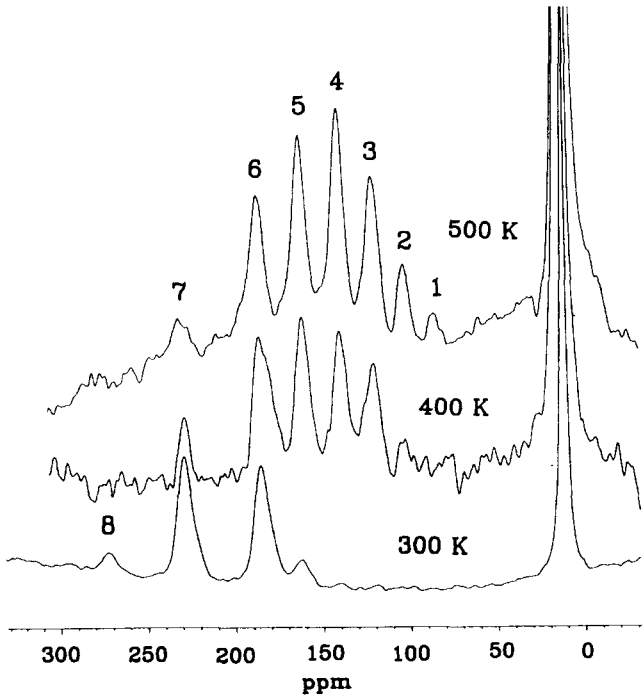

Fig. 19. ^{129}Xe NMR spectra of Xe in dehydrated NaA zeolite obtained at 300 K. The same sample was equilibrated at the different temperatures indicated. The signals from the various Xe_n clusters (n = 1 to 8) are indicated. (Reprinted with permission from Ref. 278. Copyright 1992 American Institute of Physics.)

preparation, then they reflect the distribution at that elevated temperature. Jameson *et al.*[278] have demonstrated the need for long annealing times to establish the equilibrium distribution at room temperatures, and the time needed may be prohibitively long at low temperatures.

Chmelka *et al.*[277] analysed the cluster populations and suggested that they could best be described by hypergeometric distributions, which take into account the finite volumes of the Xe atoms. However, for mean Xe loadings below 3 Xe/cage, where the volume effects are less significant, a binomial distribution also gave an adequate description. They also noted that at the highest loading (5.9 Xe/cage) the distribution was somewhat narrower than the hypergeometric one. Jameson *et al.*[278] later reported that their experimental room-temperature distributions are not fitted very well by the hypergeometric or other statistical distributions, and explained the discrepancies as due to (a) attractive Xe–Xe interactions that favour clustering at low to medium loadings and (b) overcrowding, requiring higher energies, which disfavours the large

Xe_7 and Xe_8 clusters. There is less discrepancy for higher temperature distributions.

The static lines of the Xe_n clusters are inhomogeneously broadened (shown from hole-burning experiments[283]) and T_2 measurements suggest limiting line widths of about 10–20 Hz,[297] so it is not too surprising to find that MAS substantially narrows the lines. MAS also reveals that there may be more than one high-resolution line associated with a particular cluster size. This behaviour varies with NaA obtained from different sources and is thought to arise from variations of the cage structure, possibly due to small amounts of Ca^{2+}. Jameson *et al.*[297] experimented with various *small* amounts of exchanged Ca^{2+} as impurity and were able to produce similar multiline effects. Another two-line effect seems to be associated with the slow relaxation of the zeolite structure from its high-temperature cubic form to its rhombohedral room-temperature form (phase transition at about 335 K); MAS spectra of samples that were not equilibrated after high-temperature preparation initially show resonances with slightly larger shifts than equilibrated samples, but with time lines grow at the equilibrium shift positions at the expense of the initial lines. It was suggested that, aside from overlap of lines from such structural differences, the static line widths arise from disorder of the Na^+ ions which occupy one of twelve III sites in the α-cage, such that each cage has an inherent anisotropy.

Dynamics. The appearance of distinct lines for different populations shows that there is no exchange on the 1 ms time scale (estimated from the smallest line separations). However, the fact that redistribution occurs at room temperature over long time periods shows that there is slow exchange.

2D EXSY experiments[280,281] have been used to demonstrate and quantify this exchange (illustrated for Xe in AgA zeolite in Fig. 20). For NaA at mixing times of 0.2 s very little exchange occurs, but after 0.5 s significant off-diagonal intensity is apparent. Many of the possible cross peaks are observed, but the ones closest to the diagonal have the greatest intensity. This is expected because transfer of just 1 Xe between cages changes not only the chemical shift of the Xe transferred but also the shift of all the Xe in the cages of origin and destination, e.g. for transfer of 1 Xe from a cage containing 8 Xe to one containing 4 Xe:

1 Xe changes from $\delta(Xe_8)$ to $\delta(Xe_5)$
7 Xe change from $\delta(Xe_8)$ to $\delta(Xe_7)$
4 Xe change from $\delta(Xe_4)$ to $\delta(Xe_5)$

After longer mixing times (2 s) multistep Xe exchange processes have to be considered. Rates of microscopic exchange k_{mn} for the exchange process

$$Xe_n + Xe_{(m-1)} \rightarrow Xe_{(n-1)} + Xe_m$$

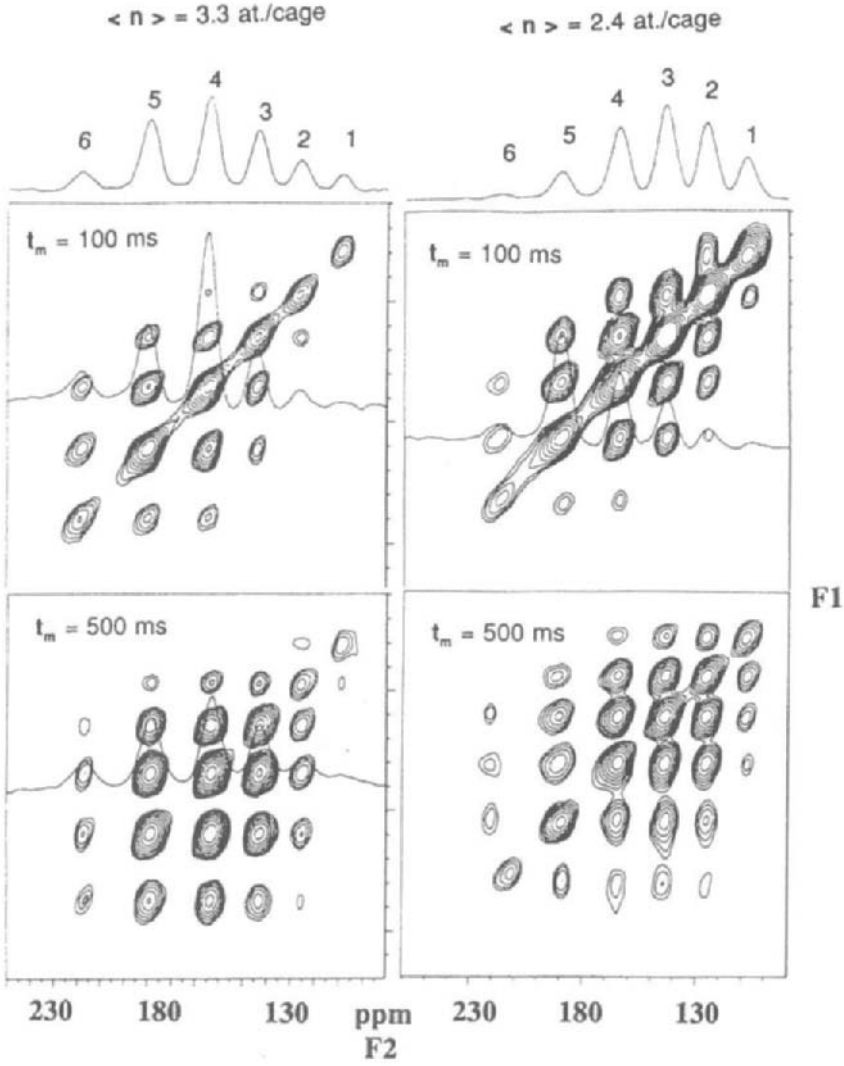

Fig. 20. Typical 2D exchange spectra showing Xe transfer between the α-cages of AgA zeolite, for two different average Xe loading levels at the mixing times indicated. (Reprinted with permission from Ref. 301.)

were obtained from the intensity matrix assuming that the probability of jumping from one particular cluster size n was the same regardless of the size of destination cluster m. Jump rates obtained in this way were $k_{m1} = 0.09$, $k_{m2} = 0.08$, $k_{m3} = 0.05$, $k_{m4} = 0.06$, $k_{m5} = 0.12$, $k_{m6} = 0.26$, $k_{m7} = 0.82\ s^{-1}$. These were then used to determine that the adsorption energy decreases for each addition of an Xe to the cage, owing to increasing repulsive interactions. Variable-temperature experiments were used to estimate an activation energy for the cage-to-cage transfer of $60 \pm 10\ kJ\ mol^{-1}$.

Relaxation measurements are another way of studying the exchange dynamics, though T_1 tends to be quite long; in one study[282] "apparent" T_1 values up to 17.7 s were measured with a recycle of only 5 s. Jameson *et al.*[283] carried out an even more extensive investigation of the microscopic jump rates by means of magnetization transfer experiments, involving selective inversion of the resonances and monitoring of the recovery. They analysed their data without assuming equality of rates to destination cages, and found that the rate constants are relatively independent of the number of Xe in the destination cage $(m - 1)$ except when the population is already high, and then the rate decreases markedly. For starting cage occupancies up to $n = 4$ the rates are similar, and above this they increase steadily. The rates obtained in this way are generally 3–5 times larger than in the 2D study. With the aid of a random walk model incorporating the microscopic rate constants, the diffusion of Xe in NaA at 300 K could be simulated and the self-diffusivity D_s for several different loadings was calculated; $D_s = 0.075, 0.10, 0.13, 0.16 \times 10^{-18}\ m^2\ s^{-1}$ for average loadings of 0, 3.94, 5.80, 6.54 Xe/cage, respectively.

Rehydration. When such dehydrated NaA–Xe samples are rehydrated, the lines initially (up to 10% of the saturated hydration level[276] shift downfield, but eventually the multiline spectrum is replaced by a single line (reported at 187 ppm,[274] 191 ppm[276] or 185 ppm[279]), and some Xe is expelled. At low levels of rehydration the water reduces the space accessible to the Xe causing the downfield shifts, but as more water is introduced the Na^+ is either mobilized or relocated and the Xe can migrate between cages. The assignment of this single line to Xe water clathrate inside the zeolite[274] is surely wrong, as pointed out later;[275,276] the shift is closer to that reported for Xe in aqueous solution (196 ppm)[78] rather than in any of the clathrate hydrate cages (see earlier). However, the similarity to the shift of Xe(aq.) is probably fortuitous since Ryoo *et al.*[279] found that the shift is different for hydrated samples of KA (150 ppm), Cs/KA (178 ppm) and NH_4A (150 ppm), an effect explained as due to changes in the free-space volume available to Xe.

KA. The larger size of the K^+ ion compared to Na^+ means that it is more difficult to get Xe into the α-cages, and after loading and equilibrating a Xe–KA sample at 575 K for 2 days it then takes several months to equilibrate at 300 K. Distributions of Xe_n clusters with $n = 1$–5 give rise to ^{129}Xe NMR

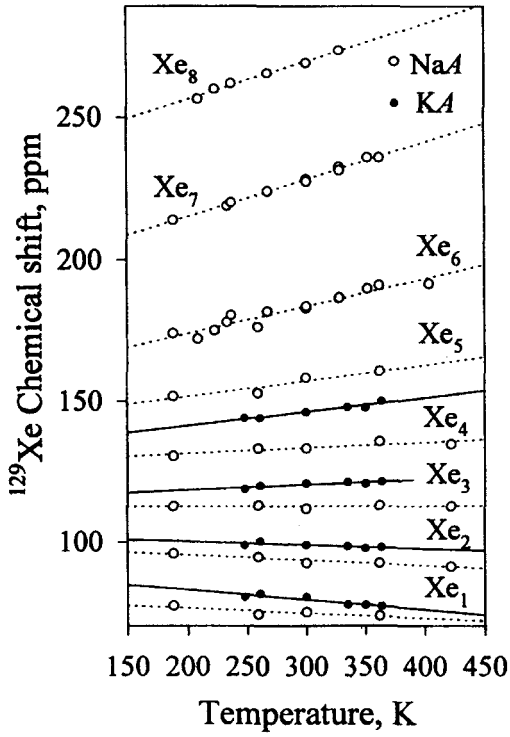

Fig. 21. The temperature dependencies of the ^{129}Xe chemical shifts of Xe_n clusters in zeolites NaA (open circles) and KA (filled circles). (Reprinted with permission from Ref. 299. Copyright 1995 American Institute of Physics.)

resonances[299] with shifts somewhat higher than for the same clusters in NaA: 79.5, 98.4, 119.7, 145.4, 180.5 ppm (Table 6). The increase in shift with each additional Xe is also greater than in NaA. Plots of shift versus temperature (Fig. 21), are qualitatively the same as for NaA, but the changes in slope are more pronounced. Comparison of these results with those for Xe in NaA and CaA together with simulations using grand canonical Monte Carlo calculations (discussed below) provide important insights into the factors that cause shift changes in the presence of these different ions.

AgA. Xe_n clusters in AgA partially dehydrated at temperatures just over 373 K have been studied by Ripmeester *et al.*[300,301] The 8-ring windows are blocked by Ag^+, thought to be associated with some water molecules, and further dehydration at higher temperatures opens the windows. Xenon can enter the cages with greater ease than in NaA, and the loading and equilibration of the Xe into the framework can be monitored at room temperature over

a period of hours to days. Separate resonances for distinct clusters up to Xe_8 are again observed, but all lines are shifted about 20 ppm to lower field than those of Xe in NaA. Apparent anisotropies of the Xe_8 and Xe_7 static lines[300] proved to be due to overlapping lines when MAS spectra were obtained. 2D EXSY spectra gave microscopic rate constants for intercage exchange of about $1\ s^{-1}$ for clusters up to Xe_6, increasing to $4\ s^{-1}$ at Xe_8 (faster than in NaA), and an activation energy of $45 \pm 10\ kJ\ mol^{-1}$, significantly lower than for Xe in NaA. Faster dynamics are also evident in the observation of broadening and coalescence of the lines at higher temperatures.

Coadsorption of Kr or Ar. Jameson *et al.*[297] used the increased resolution that results from MAS to study mixed clusters of Xe and Kr, identifying extra resonances due to Xe_nKr shifted downfield from the pure Xe_n clusters by 9.9, 11.0, 12.8, 15.7, 16.3, 26.5 ppm for $n = 1$–6, respectively. Spectra taken at 298 K immediately after preparation at 623 K showed the equilibrium distributions for Xe at 623 K but for Kr at 298 K, showing that Kr exchanges more rapidly, as expected for its smaller diameter. As the room-temperature Xe equilibrium establishes itself, more Xe is adsorbed from the gas phase and it displaces some of the Kr from the zeolite.

From studies of coadsorbed Xe and Ar in NaA,[298] it is evident that the Ar atom is sufficiently small that it can very rapidly exchange between α-cages and the gas phase: on the time scale of the NMR measurement the Xe atoms do not exchange, but the number of Ar atoms in each cage fluctuates rapidly. The chemical shift for say an Xe_3 cluster is thus an average over the shifts for all possible Xe_3Ar_m clusters weighted according to the distribution of Ar_m/cage. Consequently, the chemical shifts of the Xe_n clusters increase continuously with Ar loading, and carry information regarding the average distribution of the Ar (Fig. 22). The shifts also have a secondary dependence on the average Xe loading because the two types of atoms are competing for sites and their distributions are interdependent.

CaA. CaA was among the first zeolites studied using ^{129}Xe NMR.[168] With the 8-ring windows unblocked, the Xe rapidly samples the void space and gives a single isotropic line. Loading versus shift plots give a zero-loading intercept at 90 ± 2 ppm.

Tsiao *et al.*[302] varied the Na^+/Ca^{2+} ratio. They observed no Xe uptake for $1.2\ Ca^{2+}$ per unit cell, but all samples with higher levels of Ca^{2+} gave single lines, indicating that enough windows were open to allow rapid movement of Xe through the framework. The shift versus loading curves move gradually to lower field as the Ca^{2+} concentration increases up to $4.9\ Ca^{2+}$ per unit cell, while further increases have no effect. This levelling off is accompanied by a slight decrease in Xe uptake and is associated with a decrease in the free volume of the α-cage at high Ca^{2+} levels.

Results for Xe in CaA at 144 K have been questioned;[303] it has been

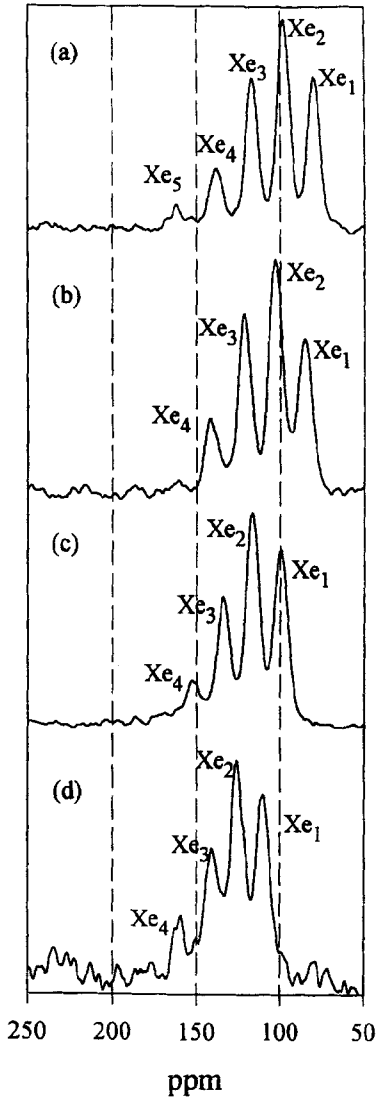

Fig. 22. ^{129}Xe NMR spectra of Xe–Ar mixtures in NaA zeolite at equilibrium. The average Xe and Ar loadings per cage (given as Xe/Ar) are (a) 1.54/0.86; (b) 1.36/1.65; (c) 1.22/3.60; (d) 1.23/4.79. (Reprinted with permission from Ref. 298. Copyright 1996 American Institute of Physics.)

suggested[304] that the broad and asymmetric lineshapes observed at low Xe loading represent nonuniform (nonequilibrium) distributions of Xe over the bulk sample. There is thus also some doubt about the proposed gas–liquid phase transition of the Xe when the loading is above about 6 Xe/cage.

An important finding by Jameson *et al.*[304] from loading dependence versus temperature studies is that the zero-loading intercept is temperature dependent; in fact the shifts at all loadings decrease with increasing temperature. Also there is a downturn evident near maximum loading at 360 K. Equally significant is the fact that they were able to get reasonably good agreement between the experimental shifts for Xe in CaA and those they calculated by averaging over the experimental shifts and distributions of clusters found for NaA. The comparison diverged at very high loadings, leading the authors to suggest that the Xe begin to populate sites in the intersections of cages that are energetically unfavourable except when the cages are full.

Simulations

A zeolites. The majority of simulations of Xe behaviour and chemical shifts in zeolites have concerned zeolite A and for this reason it is appropriate to include a short section at this point. There have been numerous Monte Carlo calculations to varying levels of complexity of clusters of Xe atoms in A zeolite cages by Van Tassel, Davis and McCormick *et al.*,[288–293] molecular dynamics simulations,[295,399] and other models[294,296] made with a view to understanding the adsorption, dynamics and ^{129}Xe NMR behaviour.

Probably the most successful and fruitful work from the NMR perspective, however, has been done by Jameson *et al.*[285,286,298,299] in which a grand canonical Monte Carlo (GCMC) approach was used together with Xe–Xe, Xe–Kr, Xe–Ar, Xe–O, Xe–Na^+ and Xe–K^+ chemical shielding versus internuclear separation functions (see below) to simulate distributions of Xe atoms and their chemical shifts. The experimental observation of a steady increase in shifts from Xe_1 to Xe_6, suggested that a pairwise additivity of contributions to the chemical shift and energies, as a function of position in the cage, be considered as a first approximation. The shift was then calculated as an average of the shifts for all configurations sampled, weighted by an $\exp(-V/kT)$ factor. Clearly the result must depend on the quality of the shielding and potential functions used, and it is especially important to have a good potential in the short contact regions where the shielding functions make large contributions to the average shift. One of the remarkable things about these calculations is that they are able to reproduce a great many experimental results with fairly high fidelity without recourse to adjustable parameters. This gives confidence in the ability of the simulations to provide insight into the different physical effects that ultimately determine the magnitude of the chemical shift. The simulations help corroborate and to some extent quantify the qualitative explanations offered for many of the experimental observations.

The GCMC approach reproduces the experimental distribution of clusters among cages even at the loadings where hypergeometric and other distributions break down, and the shift calculations based on these generally give excellent agreement with experiment. The deviations from the statistical models are found to be due to attractive interactions between Xe–Xe favouring clustering at low to medium loading, and by increasing energies due to close contact Xe–Xe repulsion at high loading. The clusters have a very fluid structure and the Xe atoms prefer to spend more of their time closer to the walls of the cage.

GCMC calculations give insights into the combination of effects that give the total shielding:

(a) Shielding is a highly local property with dramatic distance dependencies.
(b) The shift is shown to be an average over all configurations weighted by the potential function. Averaging just over local minimum energy configurations does not agree nearly so well with experiment.
(c) Xe–Xe shows a much larger shift contribution than Xe–Na, owing to greater interaction.
(d) Shift contributions from Xe–O interactions are reduced as the cation size increases because of "excluded volume effects".
(e) Xe–cation shift effects increase with increasing size of the cation. The larger cations are more polarizable, which leads to a deeper potential well.
(f) The Xe–Xe shift contribution also increases rapidly with loading of Xe. At high loading the Xe atoms are squeezed closer together and begin to sample regions of the shielding function where deshielding is increasing rapidly.
(g) *Temperature effects*: For 1 Xe/cage at low temperature the Xe spends more time close to the walls and thus samples the more deshielded regions of the Xe–O and Xe–cation shielding functions; at high temperature the Xe spends more time away from the walls, sampling more shielded regions. With more Xe in the cage the stronger Xe–Xe interactions dominate the T effects, since as T increases the more deshielded regions of the Xe–Xe shielding function are sampled more often.

Good *ab initio* calculations of the ^{129}Xe NMR shielding functions have historically been prohibitively expensive because of the very large basis sets required, although some attempts are currently being made in this direction.[224,399] However, *ab initio* calculations on shielding functions of ^{39}Ar with various atoms are quite tractable and Jameson *et al.* have found a way to scale these functions to give reasonably good approximations of the shielding functions for atom pairs that include heavier nuclei such as ^{83}Kr and ^{129}Xe.[284,287,398] Such functions were used in the GCMC calculations described above. They calculated the chemical shielding functions for Ar–Ar, Ar–OH_2

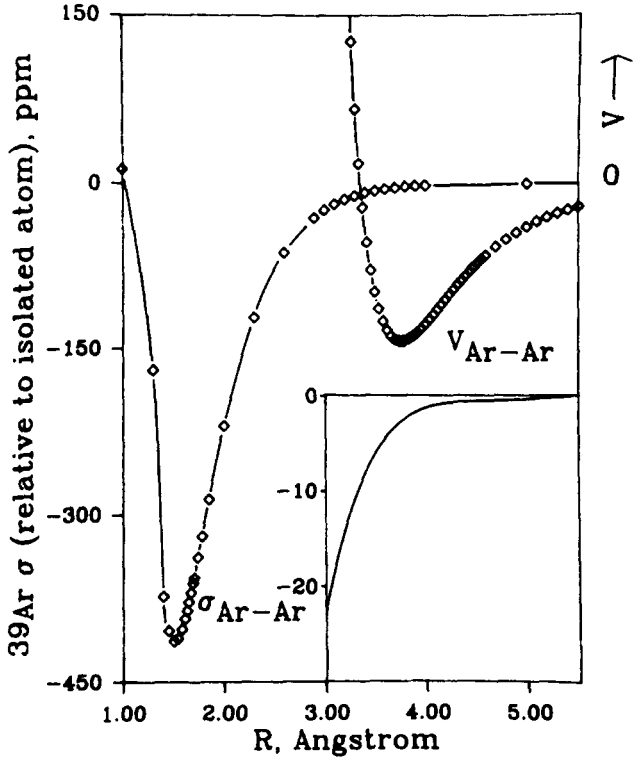

Fig. 23. The results of *ab initio* calculations of the ^{39}Ar chemical shielding σ in an Ar–Ar pair and the potential function V. The inset shows an expansion of the shielding function in the region which gives significant contributions at 100–500 K. (Reprinted with permission from Ref. 284. Copyright 1992 American Institute of Physics.)

and Ar–Na^+ pairs.[284,398] The ^{39}Ar shielding in an Ar–Ar pair (Fig. 23) goes through zero at a very short separation and after passing through a minimum increases towards zero asymptotically as the separation increases. Using scaled functions, the magnitudes and temperature dependences of the second virial coefficients for Xe–Xe, Xe–Kr and Xe–Ar shielding in the gas phase were reproduced moderately well.[284,398] Later calculations for ^{39}Ar with a fragment of an A zeolite cage[287] included chemical shift anisotropy, and gave new Ar–O, Ar–Na^+, Ar–K^+, Ar–Ca^{2+} shielding functions, which show some differences compared to the isolated atom pair functions. The deshielding contribution is a function of the number of electrons on the cation.

Other zeolites and ALPOs. There have been only a few reports of Monte Carlo and molecular dynamics simulations of the ^{129}Xe chemical shift behaviour in other microporous materials: NaY,[177,400,401] silicalite,[400,401]

mordenite,[400,401] ALPOs and SAPOs,[400,401,402] omega, L and ZK-4.[401] These again show the importance of Xe–framework and Xe–Xe interactions. There have also been a number of other simulations (mainly molecular dynamics) of Xe behaviour in Y, silicalite and mordenite which may be of some interest in understanding Xe dynamics, although chemical shifts were not calculated.[403–414]

2.3.5. *Xenon in Cu^+ and Ag^+ exchanged NaX and NaY zeolites*

As we have seen earlier, the behaviour of Xe in the Na^+ form of X or Y zeolites is frequently taken as a benchmark, since the evidence suggests that the interaction of the Xe with the Na^+ is no different from that with the rest of the framework. Virtually all other cation exchanged X and Y zeolites studied show less shielded Xe shifts than the Na^+ form, and the increased shift is usually interpreted as indicating interaction with the cation. Subsequently, in 1991, Gedeon *et al.*[253] observed something very unusual for low loadings of Xe in AgX zeolite dehydrated at 400°C, namely that the Xe nucleus was more shielded than the isolated Xe atom; $\delta(^{129}Xe)$ was as low as -50 ppm at the lowest loadings. δ remained negative up to about 1.5 Xe/α-cage. Even for Xe loadings up to about 5 Xe/α-cage the shifts were more shielded than the Na^+ form. Similar anomalously increased shielding was later observed for AgY, CuX and CuY dehydrated at high temperature,[241,242,244–248,250,251] with observed δ down to about $+4$ ppm, $+52$ ppm and $+18$ ppm, respectively. (N.B., δ values for zero loading determined from *extrapolations* or *model fits* are significantly lower: -50, $+40$ and -70 ppm, respectively). See Fig. 24.

Oxidation treatment at 450°C produced no change in $\delta(^{129}Xe)$ in the case of AgY and a further slight decrease in δ for AgX, whereas samples dehydrated at 26°C or samples reduced at 300°C showed δ greater than for NaY.[250,253] From these observations the authors have suggested that bare Ag^+ might be the species present when the anomalous shifts are observed, rather than polynuclear silver species. Similarly, it has been suggested from various preparation, oxidation and reduction treatments of $Cu^{II}Y,X$ that Cu^I, produced by autoreduction on dehydration, is the ion responsible for anomalously low δ in the copper zeolites.[248] It was postulated that the increased shielding arose from d_π–d_π back-donation to the $Xe(5d^0)$ from $Ag^+(4d^{10})$ or $Cu^+(3d^{10})$. Furthermore, it was proposed that only those Ag^+ [164] or Cu^+ [241] specifically on SIII sites in the α-cages (a fraction of the whole) were involved in the anomalous shielding of Xe through a short-lived complex, with Ag^+ or Cu^+ at SII sites interacting less strongly with the Xe.

While the details of the site, or even the species, have yet to be proven by more direct means, the case for an unusual interaction with Ag^+ or Cu^+ has been strengthened by *ab initio* calculations of the interaction of a xenon atom with singly charged cations, $M^+\cdots Xe$, where M = Li, Na, K, Cu, Ag.[224] The

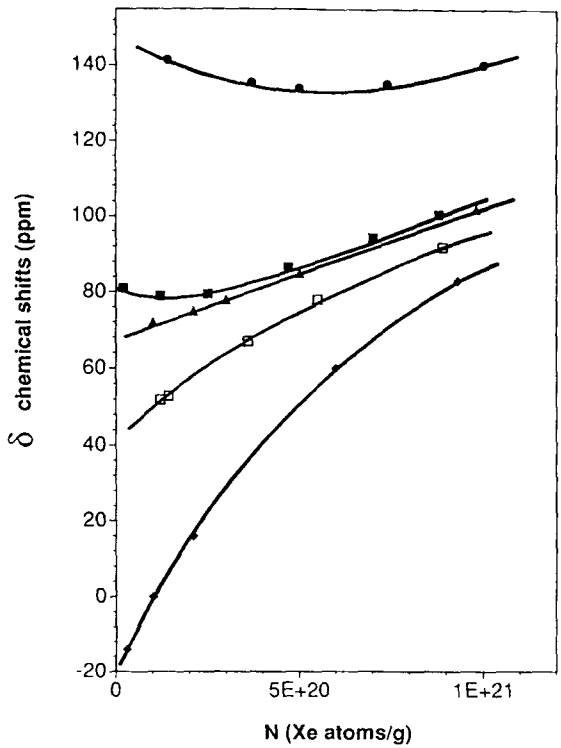

Fig. 24. ^{129}Xe NMR chemical shifts as a function of Xe loading in ion-exchanged X zeolites. From top to bottom: CdX, ZnX, NaX, CuX, AgX. AgX shows negative shifts at low loading and CuX displays a similar downward curving trend. (Reprinted from Ref. 241 with kind permission of Elsevier Science—NL, Sara Burgerhartstraat 25, 1055 KV Amsterdam.)

results show small binding energies for all cases, but whereas the interaction with the alkali cations arises largely from inductive forces, small but distinctly chemical effects occur in the binding of Xe with the d^{10} cations which also produce negative chemical shifts with respect to the isolated Xe atom.

Although the binding energies are small, those for the Cu^+ and Ag^+ are larger than for the alkali metal cations. The d^{10} cations also have equilibrium distances considerably reduced from the sum of van der Waals radii. The positive chemical shifts of ^{129}Xe in the alkali–Xe complexes arise from polarization of the Xe 5s and 5p wavefunctions by the point charge of the cation. The same deshielding effect is present for Cu^+ and Ag^+, but there is also a dominating shielding effect caused by mixing of the Xe 5p, 4p and 3p orbitals with the 3d or 4d orbitals of Cu^+ and Ag^+, respectively, giving rise to an overall negative shift.

Table 7. Summary of *ab initio* results for Xe–M^+ complexes.[224]

Cation	Equilibrium distance (Å)	Binding energy ($kJ\,mol^{-1}$)	δ(Xe)[a] (ppm)
Li^+	2.82 (2.96)[b]	35.43	71
Na^+	3.21 (3.16)	20.28	26
K^+	3.77 (3.51)	10.81	19
Cu^+	2.63 (3.14)	61.02	−24
Ag^+	3.04 (3.31)	36.69	−65

[a]Values calculated for the equilibrium distance.
[b]Values in parentheses give sums of standard van der Waals radii for comparison.

X and Y zeolites exchanged with two other d^{10} cations, Zn^{2+} and Cd^{2+}, and dehydrated at 400°C have also been studied[241,254,258–260] (Fig. 24). Curiously these behave much like other "normal" doubly charged cations, giving ^{129}Xe less shielded than NaY with distinct curvature of the δ versus Xe loading dependence. In view of earlier interpretations, these results were taken to mean that the Zn^{2+} and Cd^{2+} were strong adsorption sites for Xe (to explain the curvature) but that the absence of the extra shielding effects showed they were not on SIII sites.

There have also been studies of the blocking of cation sites in these systems using CO or C_2H_4.[242,245,252,254,258,259] CO appears to be very effective in blocking Xe from the unusual Ag^+ sites, in that the shifts move downfield of those for NaY, whereas C_2H_4 does not have much effect on the Xe shifts, reducing the anomalous shielding only slightly.

Much modelling and fitting of the behaviour of the adsorption isotherms and δ versus Xe loading in these d^{10} cation systems has been carried out,[242,260] involving up to five types of site. However, the number of adjustable parameters involved in these models is troublesome (the systems are underdetermined), and so one must reserve judgement on their validity until the exact nature and number of the sites firmly established by direct means.

2.3.6. Metallic clusters in zeolites

There are over 35 publications concerned with ^{129}Xe NMR of small to nano-sized clusters of metal atoms produced within the pores of zeolites and on supports. The main impetus for studying such materials comes from the interest in the catalytic properties of finely dispersed metal clusters. Work in this area was pioneered by Fraissard *et al.*[199,206,347] and numerous studies have followed, mainly concerned with Pt clusters[198,200,205,207–218,390] and several other transition metals.[201–203,206,217,229–237,346] The ^{129}Xe NMR coupled with adsorption measurements can give a reasonably clear picture of where the metal clusters are situated and an estimate of their sizes.

The penetration of H_2 into beds of Pt–NaY can be followed readily using ^{129}Xe NMR, since zones with and without H_2 give different Xe shifts. In contrast, annealing at 450°C to produce a uniform H_2 distribution gives a single peak.[200,223] The chemisorbed H_2 blocks access of Xe to the Pt particle surface; thus, with increasing H_2 coverage the shift decreases. The adsorption of O_2 on Al_2O_3-supported Pt clusters can be followed in a similar fashion.[392,393] In principle, in conjunction with the measurements of Xe adsorption isotherms with and without H_2 chemisorption and a known Pt content, studies of the Xe shift during progressive chemisorption of H_2 can be used to estimate Pt cluster sizes. Various models have been put forward to give 4–8 Pt atoms,[199] or a larger estimate of about 18 atoms per cluster.[390] However, Ryoo[217] concludes that cluster size determination using Xe NMR is very difficult. This reviewer's own assessment is that, since these estimates make a number of gross assumptions, values of cluster sizes from other techniques are probably more reliable.

Platinum clusters are typically prepared by exchanging NaY zeolite with $Pt(NH_3)_4^{2+}$ and calcining, followed by reduction with H_2. ^{129}Xe NMR has been used as a characterization tool in studies of the preparative conditions, metal loading, and effects of oxidation or reduction. It is used to estimate how much Pt is actually inside the zeolite or on the outside. For example, for 0.8 wt% Pt in NaY, when reduced in H_2 at 300°C, 93% of the Pt remains inside the zeolite, but reduction at 650°C causes migration of all the Pt to the outside.[198] Expulsion of the metal gives rise to Xe chemical shifts equivalent to those for pure NaY, whereas the presence of an internal Pt clusters gives significantly higher shifts, which increase with Pt loading.[209]

One remarkable property of such clusters is that they cause some of the largest (deshielded) Xe(0) chemical shifts. First observed for Pt/NaY,[199,206,347] it was found that as the Xe loading decreases towards zero the chemical shift increases very rapidly. Similar effects occur for clusters of Pd, Ir, Ru, Rh produced within the pores of NaY zeolite (Fig. 25 and Table 8). Decarbonylation of molybdenum carbonyl in NaY was shown by EXAFS to give Mo_2 at 200°C and Mo_{3-4} at 400°C, but no large shifts were observed.[201] Shifts after complete decarbonylation were almost the same as for NaY, suggesting that the Mo clusters were in either the sodalite cages or hexagonal prisms.[203]

Platinum clusters in zeolite KL,[323,324] which is used to convert linear alkanes to aromatics, have not shown any very large ^{129}Xe shifts, though the shift increases with Pt content, and the Xe helps to verify that the clusters (determined by EXAFS to be about 5–7 atoms) occupy the main channel of the zeolite. Large shifts up to ~600 ppm were reported for Pt in EMT zeolite after H_2 reduction at 573 K.[348]

Platinum clusters have also been investigated on Al_2O_3[390–395] and SiO_2;[390] large shifts were observed on Al_2O_3 at low Xe loading and −60°C (~580 ppm at 1×10^{20} Xe/g).[394]

Significantly, the large shifts do not occur when Xe is prevented from contacting the Pt surface by chemisorbed H_2 or CO,[211,212] or when the material

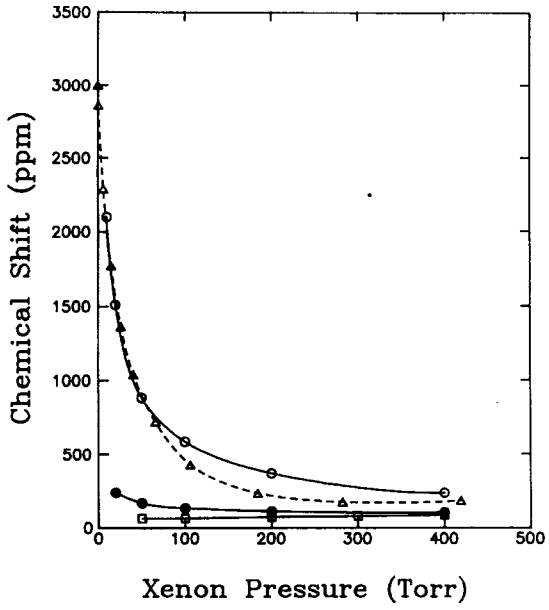

Fig. 25. ^{129}Xe NMR chemical shifts as a function of Xe pressure in NaY (□), Pd-exchanged NaY (○), Pd–NaY chemisorbed with oxygen (●) and Pd–NaY simulation assuming a limiting δ = 3000 ppm (△). (Reprinted with permission from Ref. 346. Copyright 1991 American Chemical Society.)

Table 8. Giant Xe(0) chemical shifts on metals in zeolites.

Metal/support	Largest observed[a] shift (ppm)	Shift at zero Xe loading[b] (ppm)	Reference
Pt/NaY	1300		212,217
Pt/EMT	600		348
Pt/Al_2O_3	580		394
Pd/NaY	2150	3000	346
58%Ni/NaY 500°C	2070		233
Ir/NaY		800	206,217
Rh/NaY		3200	217
Ru/NaY	820	950	217

[a]Values in some (most) cases estimated from published figures.
[b]Values from fits extrapolated to zero Xe loading.

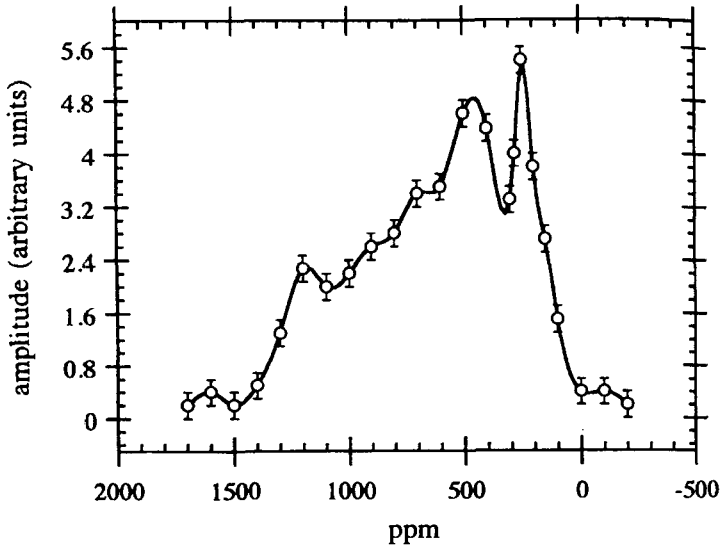

Fig. 26. ^{129}Xe NMR spectrum of Xe adsorbed on Pt–NaY zeolite at 80 K, obtained using a frequency-swept spin-echo. The peak at 250 ppm is assigned to Xe adsorbed on the surface of the zeolite while the remaining broad spectrum (300–1300 ppm) is assigned to Xe interacting with the Pt clusters. (Reprinted with permission from Ref. 212. Copyright 1995 American Physical Society.)

is reoxidized.[209] Adsorption measurements show that Xe is more strongly adsorbed on the metal clusters than the zeolite framework, with ΔH_{ads} ~45 kJ mol^{-1}.[217] (Note this is somewhat higher than the isosteric heat of adsorption of 27.32 kJ mol^{-1} for an Xe atom on a Pt(111) surface.[415]) Ryoo *et al.*[217,346] fit the Xe δ vs P plots using data from adsorption measurements:

$$\delta = \frac{n_{Pt}\,\delta_{Pt} + n_{sup}\,\delta_{sup}}{n_{Pt} + n_{sup}}$$

where n_{Pt} = number of Xe on Pt, δ_{Pt} = 1300 ppm from fitting, n_{sup} = number of Xe on zeolite, δ_{sup} = taken as δ_{NaY} at specific pressure. n_{sup} is obtained from the Xe adsorption isotherm after H_2 chemisorption $n_{Pt} = n_{ads} - n_{sup}$, with n_{ads} obtained from the Xe adsorption isotherm. The origin of the large shifts was early on ascribed to Xe interacting with the metal particles, in terms of electronic charge transfer from the Xe to the metal, though interaction with paramagnetic centres was also considered.[347] More recent work on a sample with 15 wt% Pt in NaY as a function of temperature has suggested that the shifts could arise from interaction with conduction electrons on a metallic surface;[212] above 163 K they observed a single resonance with very short Xe

T_1 values (a minimum of less than 1 ms was reached at 213 K). Below 163 K very broad-structured spectra developed covering 300–1300 ppm (Fig. 26). This indicates a distribution of Xe/Pt surface sites, with the Xe condensed onto the metal and no longer in rapid exchange with other sites in the zeolite. The T_1 of the 1300 ppm component showed a linear dependence on temperature consistent with Korringa-like behaviour characteristic of metals.

Ryoo *et al.* have also investigated a number of systems containing bimetallic clusters.[210,215,218,228] Ag/Pt–NaY[215] and Cu/Pt–NaY[210] show a decreasing ^{129}Xe shift as the Ag or Cu loading increases; the second metal, which on its own does not show the large shift behaviour, appears to decrease access of the Xe to the Pt cluster perhaps by covering it. Variable temperature studies of Ir/Pt–NaY[218] were used to show that it is truly a bimetallic cluster: physical mixtures of Ir–NaY and Pt–NaY give two lines at 163 K (a single line at 295 K), whereas the bimetallic case gives one line not at the average position of the two in the mix.

In passing it should be pointed out that in most of these studies there seems to be little doubt that clusters of metal atoms are present, but there has been very little discussion of whether they are charged or neutral and whether they are even large enough to have metallic properties.

Nickel clusters? Studies of Xe in Ni^{2+} exchanged NaY are also very interesting.[230–234,236,237] In the most recent report[233] Ni exchanged up to 58% and heated at up to 500°C also gave some very large shifts for Xe, with values quoted up to 2070 ppm, and up to 1700 ppm for 300°C treatment. The authors interpreted the large shift in terms of contact with paramagnetic Ni^{2+} rather than metallic Ni^0 clusters. This may be valid but it is not clear that the exact state of the Ni has been established. Lower loadings of Ni do not show this large shift; Dybowski *et al.*[232,234,236] established that at <15 wt% the Ni appears to be in the sodalite cages to which Xe has no access, and that reduction with H_2 causes the Ni to migrate out of the zeolite and reoxidation does not reverse this. These authors talk in terms of Ni^0 after reduction but did not observe any Xe resonances at large shifts. At intermediate Ni loadings >15% and up to 300°C treatment, the ^{129}Xe results suggested that there is some Ni in the supercages but still with at least a partial hydration sphere preventing close Xe contact with the Ni^{2+} (and hence no large shifts). More recent papers have dealt with the use of ^{129}Xe NMR to study sulfidation of Ni exchanged Y zeolite.[230,231,237] The lower shifts observed after sulfidation were interpreted to mean that S is more effective than O or H_2O at shielding Xe from Ni^{2+}. However, since the shifts are still larger than for pure NaY, this was interpreted in terms of smaller void spaces due to the presence of Ni_3S_2 in the α-cages or slight interaction with paramagnetic Ni^{2+}. Very large shifts were not seen in these experiments as might be expected.

Sodium vapour deposits. It is well-known that when sodium metal vapour is deposited into anhydrous zeolites paramagnetic "clusters" are formed inside

the sodalite cages, such as Na_4^{3+} from $Na^0 + 3Na^+$.[416–418] There is also evidence for other unusual species besides Na^+ in the supercages.[419] Trescos *et al.*[192,196,204] have investigated this material using ^{129}Xe NMR, and identified a signal from Xe in the supercages at significantly larger shifts than in pure NaY. The shift increases further as the Na content of the zeolite increases. The shifts extrapolated to zero Xe pressure (from a linear P dependence) range from 103 to 123 ppm for the samples studied, compared to 61 ppm for empty NaY. The lines are also an order of magnitude broader than in pure NaY, interpreted as indicating a distribution of Na cluster sizes. The shift itself was thought to arise from contact with paramagnetic sodium clusters in the supercage. When sufficient oxygen is admitted into the system to oxidize the Na^0, the samples lose their colour, the Xe shift decreases by ~47 ppm and the line width decreases. The latter two features are thought to be due to disappearance of the paramagnetic species, and a second factor which may contribute to the decrease in shift is a volume reduction on going from a Na cluster to a much denser Na_2O, i.e. an increase in the volume available to the Xe.

The shifts observed here contrast markedly with the much larger shifts observed at low Xe pressures with Pt, Ni, etc., discussed above, and though the full picture will not be known until the particles in the cages in all these systems have been satisfactorily identified, one must wonder whether in the case of the Na–NaY the paramagnetic interaction may in fact be longer range, i.e. with the known Na_4^{3+} clusters in the sodalite cages which are not directly accessible to the Xe.

2.4. Hyperpolarized xenon

The past few years have seen a steadily growing interest in the exciting field of hyperpolarized xenon (HP Xe) NMR. An optical pumping technique is used to generate polarizations of 40% or so. To put this in perspective, in a normal NMR experiment at room temperature in a field of 7.05 T (300 MHz ^1H, 82.98 MHz ^{129}Xe), the ^{129}Xe polarization from the Boltzmann distribution between the two nuclear spin states is 6.6×10^{-4}%. Thus 40% represents a sensitivity enhancement of 6×10^4. This is also about 340 times greater sensitivity than for a normal ^1H NMR experiment. Furthermore, when one considers that signal to noise grows as the square root of the number of scans, a 40% polarization represents a huge advantage over conventional NMR. Of course, following the preparation of the HP Xe one of the main challenges is to be able to utilize the hyperpolarization before it is lost to relaxation processes. In the gas phase T_1 is quite long (see Section 2.1.1), but relaxation from interactions with the walls of the container can reduce this considerably and much effort has been expended in finding materials with which to coat the walls to reduce this effect.

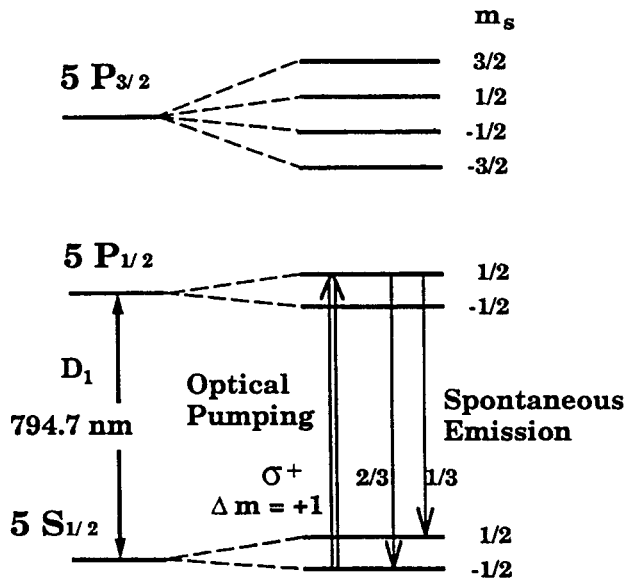

Fig. 27. Schematic electronic energy levels of Rb showing optical pumping using right circularly polarized light from the $m_s = -\frac{1}{2}$ ground state to the $m_s = +\frac{1}{2}$ excited state, followed by excited state mixing and emission back to both ground states. (Reprinted with permission from Ref. 3. Copyright 1994 Springer-Verlag.)

A detailed description of the optical pumping method used to obtain highly polarized xenon has been given in the review by Raftery and Chmelka,[3] so only a brief description of the important aspects will be given here. Pietrass and Gaede[12] have also recently reviewed applications of HP ^{129}Xe NMR. Optical pumping techniques for NMR in general have been reviewed by Tycko and Reimer,[420] who include an excellent short section on HP Xe.

The basic idea is to generate a highly polarized *electronic* state in gaseous alkali metal atoms by optical pumping and then transfer some of this polarization to Xe nuclei: in practice a mixture of vaporized Rb and Xe (sometimes in a nitrogen or helium buffer gas) contained in a heated glass cell is irradiated with polarized light in a low magnetic field. The resulting HP Xe is then transferred via vacuum line to the sample in the high-field magnet, where the NMR experiment is performed. This sounds remarkably simple, but the constraints required to make the technique work efficiently are considerable. At present Rb seems to be the metal of choice, although Cs has also been used.[421,422]

(a) *Rb optical pumping.*[3] The electronic $5S_{1/2}$ (ground) and $5P_{1/2}$ (first excited) states of the Rb atom each split into two levels $\pm 1/2$ in the low magnetic field (<100 G) (Fig. 27). Right circularly polarized light of

wavelength 794.7 nm (852.13 nm for Cs) propagating along the field direction causes transitions from $5S_{-1/2}$ to $5P_{+1/2}$. In isolation the excited atom would decay to both ground states within about 30 ns, with probabilities of 1/3 to $5S_{+1/2}$ and 2/3 to $5S_{-1/2}$, but at the gas pressures used (~1 atm) collisions cause state mixing before de-excitation, with the result that the ground states are repopulated with roughly equal probabilities. Since the relaxation rate restoring equilibrium between the two ground states is about 1 s, the net result of the optical pumping is to leave the $5S_{+1/2}$ level (in the case of right circularly polarized light) highly polarised. The Rb polarization is found to build up close to 100% within about 100 μs.

(b) *Polarization transfer to Xe.* The next step relies on the fact that Rb and Xe can briefly form an RbXe van der Waals complex. During the short lifetime of the atom pair, of the order of 10^{-7} to 10^{-9} s before it is broken up by collisions, spin exchange occurs between the Rb electron and the Xe nucleus via the Fermi contact interaction. The Xe polarization takes several minutes to reach its maximum.

(c) *Reduction of Xe polarization loss.* (i) Rb electron spin polarization couples to the rotational angular momentum of the RbXe pair (spin–rotation interaction) and is lost when the complex breaks up. The application of moderate magnetic fields reduces this coupling. (ii) During de-excitation the Rb atoms emit some photons with left circular polarization which can be absorbed by other Rb atoms and bring about their depolarization. A buffer gas helps to quench this. (iii) Following the optical pumping, the Xe polarization can be lost via reverse spin exchange with the Rb, so the Rb must be quickly condensed out by cooling. (iv) Xe relaxation thought to be due to interaction with paramagnetic centres in the cell walls can be reduced by silicone or paraffin wall coatings.

Historically, optical pumping using polarized light originated with Kastler,[423,424] who also suggested the possibility of creating nonequilibrium nuclear spin states of atoms in a magnetic field. Numerous developments including optical pumping of alkali metal atoms, transfer of polarization, the observation of alkali metal–noble gas van der Waals complexes, and relaxation of polarization due to collisions with the vessel walls[425–429] culminated in the first NMR detection of enhanced ^{129}Xe polarization by Grover in 1978.[430] Since then several groups, but principally Happer and coworkers, have worked towards a complete understanding of all the physics involved:[431–445] spin-exchange of Rb–^{131}Xe[431,433] and Rb–^{129}Xe,[432,434,435,437,438] wall interactions with ^{131}Xe[439–442] and ^{129}Xe.[443,444] Then in 1991 Zeng *et al.*[421] and Pines and coworkers[446] began to exploit the capabilities of HP Xe for high-field ^{129}Xe NMR.

One should also briefly note that an alternative method of obtaining HP Xe nuclei (metastability exchange collision) was investigated during the 1960s but it does not appear to have been developed further: polarized Xe nuclei can be produced by collision of electronic ground-state Xe atoms with metastable

excited electronic states of Xe atoms already polarized by either electron-impact or optical pumping techniques.[447–449]

Augustine and Zilm have shown that high Xe polarization is possible by optical pumping in high field.[450,451] The mechanism is similar to that in low field except that the increased spectral dispersion of the Rb optical transitions, arising from the Zeeman shifts of the electronic levels, permits direct frequency selection of the pumping transition without the need for circularly polarized light, as the other transitions lie outside the typical laser bandwidth. They observed reduction of the H_0 inhomogeneity relaxation processes.

With MRI imaging requirements in mind, Driehuys *et al.* have developed a method for large-volume production of HP Xe.[452] The Xe is polarized in a continuous gas flow system pressurized to 10 atm with ^{4}He, which broadens the Rb absorption, allowing a more efficient use of the laser's broad spectral output. The HP Xe is then frozen out and stored at 77 K. Cates *et al.*[453] had earlier shown that HP Xe can be frozen to 77 K with little effect on the polarization. Their measured T_1 at 77 K was about 3 h. Driehuys *et al.*[444] showed that although relaxation times for Xe gas are increased by coating the vessel walls with silicone, the relaxation is nevertheless dominated by ^{129}Xe–^{1}H dipolar couplings while the Xe is stuck in or on the coating.

Both ^{129}Xe and ^{131}Xe can be polarized by the optical pumping, though once again only ^{129}Xe has been used in studies of materials, and the radioactive NMR nuclei ^{133}Xe (I = 3/2), ^{133m}Xe (I = 11/2) and ^{131m}Xe (I = 11/2) have also been hyperpolarized and their magnetic moments determined.[454] One very interesting result from ^{131}Xe studies, however, is the observation of very small but nonzero quadrupole coupling constants for the gas contained in nonspherical vessels,[439,440,442] (Fig. 28). The effect is due to interaction of the atoms with the walls, where they experience substantial fluctuations of the electric field gradient and hence of the quadrupole coupling. This is reminiscent of the microscopic site averaging of the chemical shift anisotropy of ^{129}Xe in nonspherical cages (Section 2.3.2), except here the asymmetry is for a cell on the macroscopic scale.

One of the most exciting applications for HP Xe with a great deal of potential is the possibility of transferring the polarization to other nuclei, and a limited number of studies have demonstrated its feasibility. However, an efficient and routine method remains something of a Holy Grail.

Cross polarization (CP) has been achieved in three different ways:

(a) *Low-field thermal mixing.* This requires low enough field and long enough interaction time so that energy-conserving spin flip-flops can occur. Gatzke *et al.*[53] studying HP ^{129}Xe T_1 in the solid state found that the relaxation below 20 K is dominated by cross relaxation to ^{131}Xe. Large ^{131}Xe polarizations were observed when the field was momentarily reduced to low values (<100 G), with a concomitant reduction of ^{129}Xe polarization. Bowers *et al.*[455] obtained CP between 80% ^{129}Xe and 99% $^{13}CO_2$ mixed as gases at room temperature and then cocondensed into a solid at 77 K. The thermal mixing

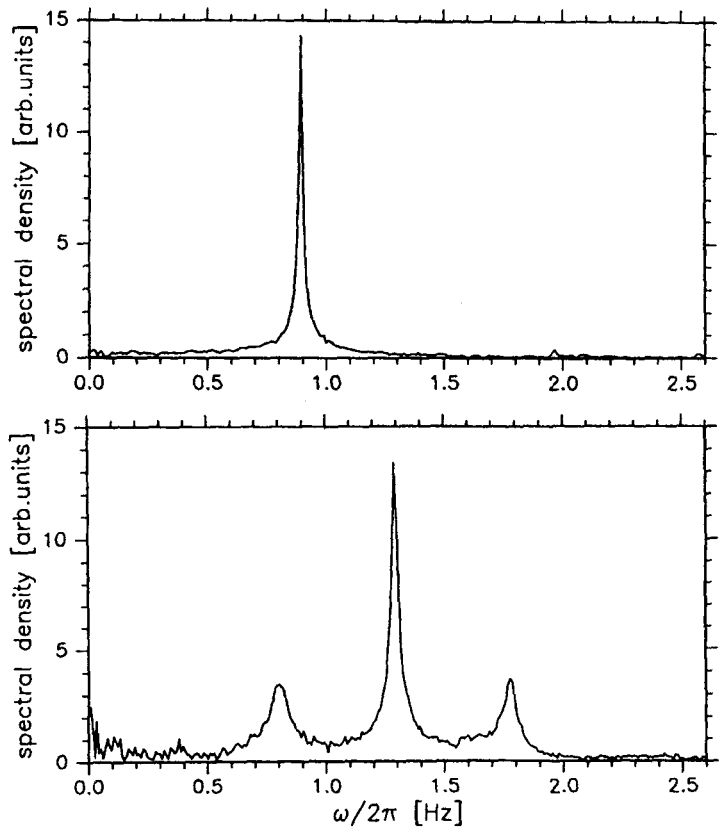

Fig. 28. ^{131}Xe NMR spectra of hyperpolarized Xe gas in spherical (top) and cylindrical (bottom) sample cells at very low field (260 nT). The lower spectrum was obtained with the field parallel to the cylinder axis and shows a small quadrupole splitting due to anisotropic averaging of the quadrupole interactions of the Xe with the cell walls. (Reprinted with permission from Ref. 442. Copyright 1994 American Institute of Physics.)

parameters were varied (0.1 G/200 ms, 10 G/200 ms, 35 G/10 s), with little effect on the polarization transfer. Enhancement of the CO_2 CSA powder pattern of ~200 was observed, but also of significance was the observation of inversion of the signal when light of the opposite circular polarization was used in the initial optical pumping stage (Fig. 29). The low enhancement may simply mean that many CO_2 are not in contact with Xe. Driehuys *et al.*[456] observed large transfer of polarization from ^{129}Xe to ^{1}H in silicone wall coatings (^{1}H enhancement of 10^4–10^5 in a 0.2 T field) (Fig. 29). Efficient spin-exchange requires a minimum sticking time of $\tau \sim T_2 \sim 10^{-4}$ s. This sticking time is related to the adsorption energy $\tau = \tau_0 \exp(E_a/kT)$, where $\tau \sim 10^{-12}$ s;

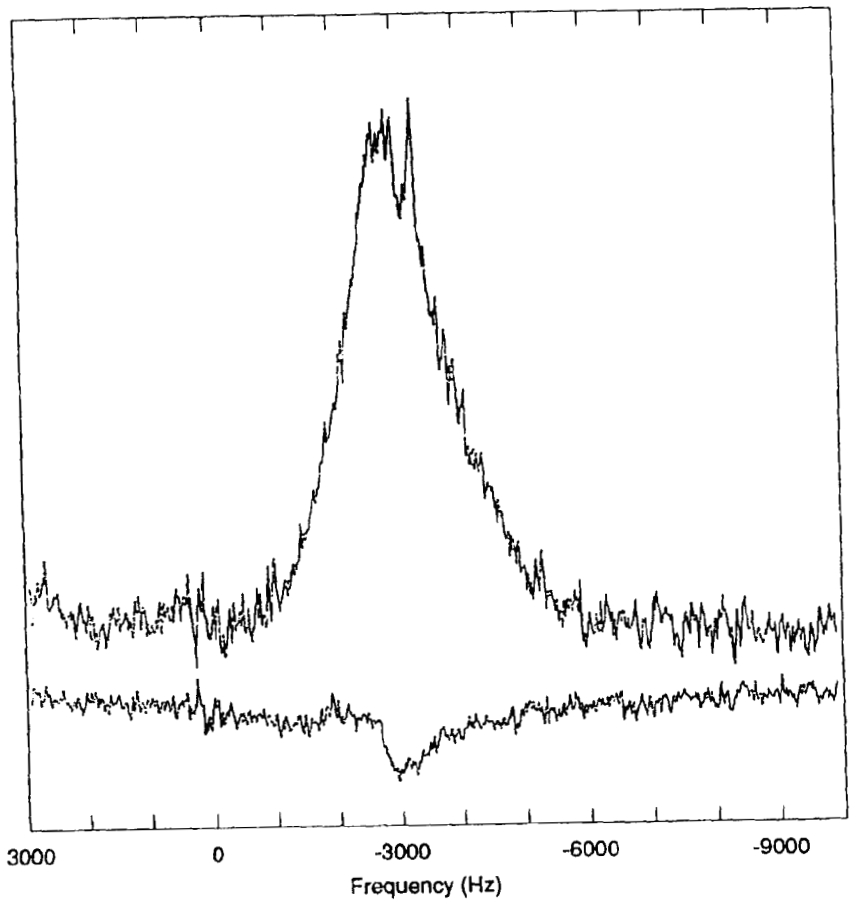
3000
0
-3000
-6000
-9000
Frequency (Hz)

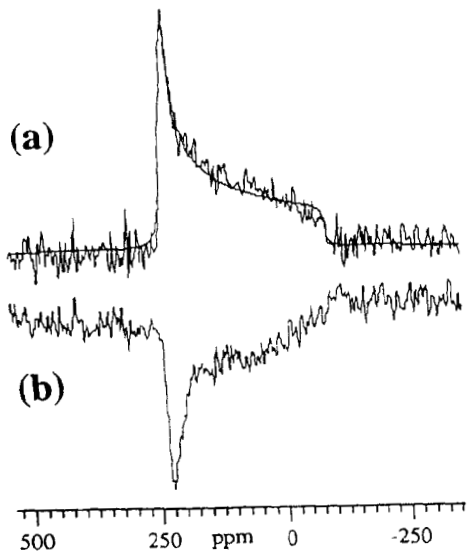
(a)
(b)
500
250
ppm
0
-250

consequently, cooling to <190 K is required. In practice the cell was cooled to 77 K for 10 s in 40 G, then removed to the earth's field of ~0.5 G for 3 s to allow rapid spin exchange. They also observed transfer of ^{1}H polarization into the bulk solid either from Xe penetrating to lower levels or via ^{1}H–^{1}H spin-diffusion.

(b) *High-field Hartman–Hahn coupling.* Gaede *et al.*[457] obtained a 10^3 enhancement for surface ^{1}H on ultra-high surface area microporous poly(triarylcarbinol) or poly(tetrabiphenylsilane). They also investigated an aerosil, R812, with much lower surface ^{1}H. They were able to do repeated CP sequences (up to 8) while the Xe was spin locked before polarization was lost. An earlier experiment by Long *et al.*[138] on poly(triarylcarbinol) showed the feasibility of the method but achieved only an estimated ^{1}H enhancement of 70.

(c) *SPINOE (spin polarization-induced NOE).* Navon *et al.*[458] observed transfer of polarization from HP Xe to ^{1}H spins in solution via NOE without RF irradiation. The ^{1}H signal shows positive or negative NOE depending on the sign of the Xe polarization (Fig. 30). The enhanced ^{1}H polarization was then also used to image the progress of the polarization into the solution when exposed to Xe.

Generally one tries to utilize HP Xe in areas where sensitivity is normally a problem, i.e. in low concentrations and on surfaces, and several such applications have been discussed in earlier sections.[53,56,123,138,139,159] Other examples of HP Xe on surfaces may be mentioned. One early experiment to demonstrate the feasibility of surface studies was the observation of Xe on the surface of a benzanthracene crystal (0.5 m^2/g).[446] Raftery *et al.*[459] produced 1 μm thin films of solid HP Xe coating vessels of various shapes and obtained some unusual lineshapes, which could be explained in terms of the bulk diamagnetic susceptibility effects. HP Xe was also used to study the distribution of thiophenol capping groups on the surface of CdS nanocrystals;[460] at 123 K completely capped particles show only one Xe signal, whereas partial coverage gives two overlapping signals indicating that the capping groups form islands rather than distributing homogeneously. HP Xe made it possible to study the adsorption properties of porous silicon at low pressures.[461] Saturation coverage of the hydrogen-terminated silicon was found to occur at 33 torr. Samples prepared with non-hydrogen-terminated surfaces also showed rapid relaxation, owing to interaction of the Xe with the dangling Si bonds. Raftery

---

Fig. 29. Cross-polarization from hyperpolarized ^{129}Xe via low-field thermal mixing. *Left*: ^{1}H NMR CP signal from protons in a silicone surface coating (top) and without CP (bottom) (from Ref. 456). Right: ^{13}C NMR CP signal of 99% ^{13}C-enriched CO_2 in a matrix of solid HPXe prepared using right (a) or left (b) circularly polarized light (from Ref. 455). (Reprinted from Refs 456, 455 with kind permission of Elsevier Science—NL, Sara Burgerhartstraat 25, 1055 KV Amsterdam.)

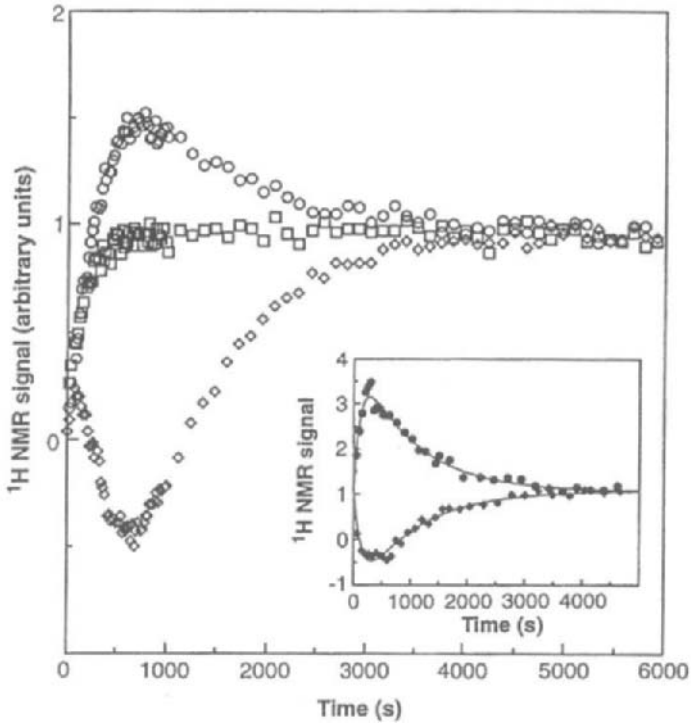

Fig. 30. Cross polarization from hyperpolarized (HP) ^{129}Xe via SPINOE. Time dependence of ^{1}H NMR signals in solutions of Xe in 25%C_6D_5H–75%C_6D_6: Positive (○) or negative (◇) NOE observed depending on sign of HP ^{129}Xe polarization; (□) unpolarized Xe. The samples were exposed to Xe in low field and the initial rise in the signal is due to spin–lattice relaxation. The inset shows the result when the ^{1}H magnetization was first allowed to equilibrate at high field before exposure to HP Xe. (Reprinted with permission from Ref. 458. Copyright 1996 American Association for the Advancement of Science.)

et al.[462] also developed some multiple-pulse experiments for both HP ^{129}Xe and HP ^{131}Xe to reduce the effects of inhomogeneity at low fields.

Reports are now appearing of the first trials of HP Xe as a magnetic resonance imaging probe of inorganic and biological cavities, e.g. in materials[458,463] and lungs.[464–469] Projecting ahead, one can envision that one of the greatest applications of HP Xe will probably be in the medical imaging of lungs and regions of the body to which HP Xe can be transported by the blood or injectable fluids. This was clearly the stimulus for the studies of the behaviour of HP Xe in blood, saline and other medical solutions discussed earlier.[123]

We can probably look forward to interesting developments in the field of HP Xe for some years to come.

3. CHEMICALLY BONDED XENON: OXIDATION STATES Xe(II, IV, VI AND VIII)

^{129}Xe NMR has played a vital role in the detection of new xenon compounds, in their bonding and structural characterization, and in following the course of reactions in synthesis and decomposition.

Many aspects of the NMR have been reviewed very thoroughly by Schrobilgen in 1978,[1] and by Jameson.[2] The latter reviewed materials investigated up until 1984 and in the meantime the number of compounds studied by NMR has more than doubled. The chemistry of compounds containing Xe–N linkages, including NMR aspects, was recently reviewed by Schrobilgen.[470]

Xenon compounds were studied by ^{19}F NMR virtually from the time the first compound was prepared by Bartlett in 1962[471] and numerous ^{1}J(Xe–F) values were obtained. Double resonance experiments allowed indirect measurement of a few ^{129}Xe shifts, through effects on the ^{19}F spectra.[472,473] Direct ^{129}Xe NMR studies were initiated by Seppelt and Rupp in 1974.[474,475] To date there have been no reports either of solid-state NMR or of ^{131}Xe NMR studies of xenon compounds. The majority of measurements in pure liquids or in solution have concentrated on isotropic chemical shifts and spin–spin coupling constants. Trends in these parameters give information about bonding, and the multiplicites arising from J coupling provide information about connectivities and hence structure. Table 9 provides a comprehensive listing of all compounds studied by NMR,[476–528] the experimental conditions and the chemical shifts and J-couplings measured. Table 10 summarizes the ranges of ^{129}Xe chemical shifts, listed according to oxidation state, valence shell electron pair repulsion theory (VSEPR) description and the ligand atoms attached to the Xe. The VSEPR theory[529,530] appears to work well in predicting the geometries of xenon compounds.

Referencing. In compiling such a table it quickly becomes apparent that the comparison of ^{129}Xe chemical shifts in different compounds is complicated by different choices of reference material and different solvents and temperatures. In the majority of cases chemical shifts have been referenced to liquid $XeOF_4$ at room temperature (24/25°C), but in other cases XeF_2, usually but not always in CH_3CN solution at room temperature, or Xe gas in an organic solvent have been used as reference. This poses a few problems if precise comparisons are desired, though an approximate common scale (referenced to $XeOF_4$ on the δ-scale) can be established from the following pieces of information.

(A) Seppelt and Rupp[475] place XeF_2 in CH_3CN at +3508 ppm and $XeOF_4$ at +5331 ppm with respect to Xe(0) in n-C_6F_{14} or $CFCl_3$.
(B) Jameson[2] estimated Xe(0) in n-C_6F_{14} to be at 130 ppm with respect to the isolated Xe atom.

Table 9. Chemical compounds of xenon: ^{129}Xe NMR parameters.

Compound	Solvent	T (K)	δ(Xe) (ppm)[a]	$J(^{129}\text{Xe-L})$ (Hz)[b] L = ^{19}F	L = ^{13}C, ^{14}N, ^{15}N, ^{17}O, ^{125}Te	Reference[c]
Xe(0)						
Xe atom		298	−5426			See text
Xe(II)						
XeF^+	SbF_5	299	−574	7594		476
				7210		477 (478, 480)
$XeOTeF_5^+$	SbF_5	278	−1481.9			481
$XeOTeF_5^+$	SbF_5	299	−1472	^{3}J/18.5		482, 477
cis-FXeO—TeF_4—OXe^+/ AsF_6^-	HF	273	−913			483
XeF_2	CD_3CN	293	−1818*[d]	5643		484
XeF_2	CH_3CN	298	−1823*	5550		475
XeF_2	CH_3CN	297	−1813.3			485
XeF_2	SO_2ClF	298	−1905	5630		486
XeF_2	SO_2ClF	299	−1913	5621		477
XeF_2	BrF_5	298	−1750	5616		476,486
XeF_2	BrF_5	233	−1708	5583		486
XeF_2	HF	298	−1592	5652		486,476 (478)
XeF_2	$CFCl_3$	299	−2009	5579		477
XeF_2	HSO_3F	193		6025		(478,487)
$F_tXeF_b^+XeF_t$	BrF_5	213	−1059	4828 br[e]		482
				6662 t		
$FXeFXe'OTeF_5^+$	BrF_5	213	−1146	5747		482
			−1633′			
$FXeFBrOF_2^+$	BrF_5	214	−1359	5680		482
$FXeF\cdots MoOF_4$	BrF_5	193	−1383	5117 br		476,486,488
				6139 t		
$FXeF\cdots MoOF_4$	SO_2ClF	155	−1441	5076 br		486,488
				6058 t		
$FXeF\cdots MoOF_4(MoOF_4)$	SO_2ClF	155	−1338	5036 br		486,488
				6159 t		
$FXeF\cdots MoOF_4(MoOF_4)_2$	SO_2ClF	155	−1321	5029 br		486,488
				6156 t		
$FXeF\cdots WOF_4$	BrF_5	207	−1331	5051 br		476,486,488
				6196 t		(489)
$FXeF\cdots WOF_4$	SO_2ClF	158	−1315	5000 br		486,488
				6127 t		
$FXeF\cdots WOF_4(WOF_4)$	SO_2ClF	158	−1189	4964 br		486,488
				6268 t		(489)
$FXeF\cdots WOF_4(WOF_4)_2$	SO_2ClF	158	−1170	4996 br		486,488
				6304 t		

[*Continued*

Table 9—*Continued*

Compound	Solvent	T (K)	δ(Xe) (ppm)[a]	$J(^{129}Xe–L)$ (Hz)[b] L = ^{19}F	L = ^{13}C, ^{14}N, ^{15}N, ^{17}O, ^{125}Te	Reference[c]
Xe(II)—*continued*						
$FXeOSO_2F$	BrF_5	233	−1666	5830		486
	SO_2ClF	268	−1725	5837		490
$FXeOSO_2F$	HSO_3F	189	−1467	5975		486 (478)
$FXeOSO_2F$	HSO_3F	183	−1416	6012		486
		173	−1407	6051		
$FXeOSO_2F$	BrF_5	233	−1666	5830		486
		196	−1613	5848		476
$(FXeO)_2SOF$	BrF_5	196	−1258	6428		476
$FXeOSOF(OMoOF_4)$	HSO_3F	173	−1342	5971		486,488
$FXeOSOF(OWOF_4)$	HSO_3F	183	−1335	6131		486,488
$FXeOWF_5(OWOF_4)$	SO_2ClF	158	−955	6373		486,488
$FXeOWF_5(OWOF_4)_2$	SO_2ClF	158	−906	6373		486,488
$FXeOSeF_5$	$CFCl_3$	293	−1947*	5630 ^3J/37		474
$FXeOTeF_5$	SO_2ClF	299	−2051	5743		477
$FXeOTeF_5$	$CFCl_3$	293	−2062*	5670 ^3J/30	^2J/Te 540	474
$FXeOSO_2CF_3$	CD_3CN	243	−1597*	5873		484
$FXeOSO_2CF_3$	CH_2Cl_2	243	−1759*	5786		484
$FXeOSO_2C_4F_9$	CD_3CN	243	−1577*	5880		484
$FXeOCOCF_3$	CD_3CN	243	−2172*	5500		484
$(CF_3)_2SOXeF^+/SbF_6^-$	HF	203	−1679.3*	6343		491
$CF_3C(OXeF)NH_2^+/AsF_6^-$	BrF_5	220	−1578	5991		492
$CF_3C(OXeF)NH_2^+/AsF_6^-$	BrF_5	211	−1578	5991		493
FXe—*trans*-$(OIOF_4)$	SO_2ClF	268	−1741.2	5913 ^3J/42		490
		233	−1701.5	5893		
	$CFCl_3$	297	−1853.6	5880 ^3J/43		
	BrF_5	273	−1720.5	5910		
		233	−1702.8	5868		
FXe—*cis*-$(OIOF_4)$	SO_2ClF	268	−1865.0	5870		490
		233	−1824.4	5851		
	$CFCl_3$	297	−1962.0	5849		
	BrF_5	273	−1823.5	5803		
		233	−1798.2	5814		
Xe—*tr,tr*-$(OIOF_4)_2$	SO_2ClF	268	−1860.7	^3J/38		490
		233	−1802.7			
	$CFCl_3$	297	−1994.6	^3J/38		
	BrF_5	273	−1871.4			
Xe—*cis,tr*-$(OIOF_4)_2$	SO_2ClF	268	−1987.0	^3J/19		490
		233	−1929.8			
	$CFCl_3$	297	−2120.0			
	BrF_5	273	−1929.2			
Xe—*cis,cis*-$(OIOF_4)_2$	SO_2ClF	268	−2105.8			490
		233	−2076.0			
	$CFCl_3$	297	−2235.7			
	BrF_5	273	−2059.5			

[*Continued*

Table 9—*Continued*

Compound	Solvent	T (K)	δ(Xe) (ppm)[a]	$J(^{129}Xe–L)$ (Hz)[b] L = ^{19}F	L = ^{13}C, ^{14}N, ^{15}N, ^{17}O, ^{125}Te	Reference[c]
Xe(II)—*continued*						
(OSO_2F)—Xe—*tr*-$(OIOF_4)$	SO_2ClF	268	−1834.2			490
(OSO_2F)—Xe—*cis*-$(OIOF_4)$	SO_2ClF	268	−1956.4			490
cis-$Xe(OTeF_5)(OIOF_4)$	$CFCl_3$	278	−2298.7			490
		297	−2315.7			
trans-$Xe(OTeF_5)(OIOF_4)$	$CFCl_3$	278	−2205.3			490
		297	−2217.5			
$Xe(OSO_2F)_2$	HSO_3F	189	−1613			486
$Xe(OSO_2F)_2$	HSO_3F	183	−1572			486
$Xe(OSeF_5)_2$		298	−2200*	^3J/37		474
$Xe(OTeF_5)_2$		298	−2379*	^3J/31	^2J/Te 470	474
$Xe(OTeF_5)_2$	$CFCl_3$	299	−2447.2	^3J/31		477
$Xe(OTeF_5)_2$	SO_2ClF	299	−2327	^3J/30		477
$Xe(OSeF_5)(OTeF_5)$		298	−2289*		^2J/Te 480	474
$CD_3CN.XeF^+/BF_4^-$	CD_3CN	243	−1677*	5895	^{14}N 313	484
$H^{13}C^{15}NXeF^+/AsF_6^-$	HF	263	−1552	6161	^{15}N 471 $^3J/^1H$ 24.7 $^2J/^{13}C$ 84	494
$H^{13}C^{15}NXeF^+/AsF_6^-$	BrF_5	223	−1570	6176	^{15}N 483 $^3J/^1H$ 26.8	494
$HCNXeF^+/AsF_6^-$	HF	263	−1552	6150	^{14}N 334 $^3J/^1H$ 26.8 $^2J/^{13}C$ 84	495
$HCNXeF^+/AsF_6^-$	BrF_5	215	−1569	6181		495
CH_3CN—XeF^+/AsF_6^-	HF	263	−1708	6020	^{14}N 313 $^2J/^{13}C$ 79	495
CH_2FCN—XeF^+/AsF_6^-	HF	263	−1541	6163	^{14}N 333	495
CH_2ClCN—XeF^+	HF	243 to 263	−1583	6147	^{14}N 331	470
C_2H_5CN—Xe—F^+/AsF_6^-	HF	263	−1717	6017	^{14}N 311	495
CH_2FCH_2CN—XeF^+	HF	243 to 263	−1662	6063	^{14}N 322	470
$CH_3CH_2CH_2CN$—XeF^+	HF	243 to 263	−1718	6020	^{14}N 309	470
$CH_2FCH_2CH_2CN$—XeF^+	HF	243 to 263	−1663	6065	^{14}N 321	470
CH_3CHFCH_2CN—XeF^+	HF	243 to 263	−1700	6038	^{14}N 315	470

[*Continued*

Table 9—*Continued*

Compound	Solvent	T (K)	δ(Xe) (ppm)[a]	$J(^{129}Xe-L)$ (Hz)[b] L = ^{19}F	L = ^{13}C, ^{14}N, ^{15}N, ^{17}O, ^{125}Te	Reference[c]
Xe(II)—*continued*						
$C_4H_9CN—XeF^+$	HF	243 to 263	−1720	6022	^{14}N 309	470
$CH_2FC_3H_6CN—XeF^+$	HF	243 to 263	−1703	6027	^{14}N 311	470
$CH_3CHFC_2H_4CN—XeF^+$	HF	243 to 263	~−1705	6015		470
$(CH_3)_2CHCN—XeF^+$	HF	243 to 263	−1721	6016	^{14}N 309	470
$(CH_3)_3CCN—XeF^+$	HF	243 to 263	−1721	6024	^{14}N 309	470
$CH_2FC(CH_3)HCN—XeF^+$	HF	243 to 263	−1669	6027	^{14}N 301	470
$CH_2ClC(CH_3)HCN—XeF^+$	HF	243 to 263	−1703	6027	^{14}N 314	470
$C_6F_5CN—Xe—F^+/AsF_6^-$	HF	263	−1426	6610		495
$(C_5F_5N)—Xe—F^+$	HF	243	−1871.9	5936	^{14}N 236	496
	BrF_5	243	−1922.5	5926		
$p\text{-}CF_3—(C_5F_4N)—Xe—F^+$	HF	258	−1802.6	5977	^{14}N 238	496
	BrF_5	223	−1853.4	5963		
$s\text{-}(C_3N_3F_3)—Xe—F^+$	HF	268	−1807.9	5909	^{14}N 245	497
	BrF_5	223	−1862.4	5932		
$CF_3CN—Xe—F^+$	BrF_5	209	−1337.1	6397		497
$C_2F_5CN—Xe—F^+$	BrF_5	209	−1293.7	6437		497
$C_3F_7CN—Xe—F^+$	BrF_5	209	−1294.2	6430		497
F_3SNXeF^+/AsF_6^-	?	213	−1661	6248		492
$XeNH(TeF_5)^+/AsF_6^-$	HF	240	−2840			493
	BrF_5	215	−2902		^{15}N 138	
$XeNH(SO_2F)^+/AsF_6^-$	BrF_5	212	−2660		^{15}N 109	493
$XeN(SO_2F)_2^+$	SbF_5	298	−1943		^{15}N 91.7	498
$FXeN(SO_2F)_2$	BrF_5	215	−1997.3	5586 ^3J/18.7	^{15}N 307.4	499,500
$FXeN(SO_2F)_2$	BrF_5	233	−2016	5572 ^3J/18		486
$FXeN(SO_2F)_2$	BrF_5	268	−2053	5624 ^3J/18		501
	SO_2ClF	233	−2009	5664		502
$[XeN(SO_2F)_2]_2F^+/AsF_6^-$	BrF_5	268	−1933			501
$Xe[N(SO_2F)_2]_2$	SO_2ClF	233	−2257		^{15}N 259	502
		233	−2248			

[*Continued*

Table 9—*Continued*

Compound	Solvent	T (K)	δ(Xe) (ppm)[a]	$J(^{129}Xe\text{–}L)$ (Hz)[b] L = ^{19}F	$J(^{129}Xe\text{–}L)$ (Hz)[b] L = ^{13}C, ^{14}N, ^{15}N, ^{17}O, ^{125}Te	Reference[c]
Xe(II)—*continued*						
$Xe[N(SO_2F)_2]_2$	BrF_5	268	−2101			501
$Xe(CF_3)_2$[f]	CH_2Cl_2	188		^2J/1940		(503)
4-FC_6H_4—Xe^+/BF_4^-	CD_3CN	243	−3714*		^{13}C 104	504
2-FC_6H_4—Xe^+/BF_4^-	CD_3CN	243	−3857*	^3J/48	^{13}C 78	504
2,4,6-$F_3C_6H_2$-Xe^+/BF_4^-	CD_3CN	243	−3891*	^3J/54	^{13}C 103.6	505,504
2,6-$F_2C_6H_3$-Xe^+/BF_4^-	CD_3CN	243	−3933*	^3J/52	^{13}C 99	504
2,6-$F_2C_6H_3$-Xe^+/BF_4^-	CD_3CN/ CH_2Cl_2	243	−3907*	^3J/52		506
2,6-$F_2C_6H_3$-$Xe^+/CF_3SO_3^-$	CH_3CN	294	−3943*	^3J/54		506
4-F-$C_6H_4Xe^+/BF_4^-$	CH_3CN/ C_2H_5CN 1:3	193	−3733*			485
3-F-$C_6H_4Xe^+/BF_4^-$	CH_3CN/ C_2H_5CN 1:3	193	−3693*			485
4-CF_3-$C_6H_4Xe^+/BF_4^-$	CH_3CN/ C_2H_5CN 1:3	193	−3675*			485
3-CF_3-$C_6H_4Xe^+/BF_4^-$	CH_3CN/ C_2H_5CN 1:3	193	−3675*			485
3-CF_3-$C_6H_4Xe^+$/ $CF_3C_6H_4BF_3^-$	CH_3CN	229	−3702*			485
$C_6F_5Xe^+/(C_6F_5)_2BF_2^-$	CH_3CN/ C_2H_5CN 1:3	193	−3806*			485
$C_6F_5Xe^-/AsF_6^-$	CH_3CN/ C_2H_5CN 1:3	193	−3811*			485
$C_6F_5Xe^-/AsF_6^-$	CH_3CN	229	−3830*			485
$C_6F_5Xe^-/AsF_6^-$	CH_3CN	243	−3828*	^3J/69		507
$C_6F_5Xe^+/AsF_6^-$/CsF mixture	CH_3CN	238	−3835*	^3J/75		507
$C_6F_5Xe^+$	CH_3CN	243	−3768*	^3J/69.1 ^4J/19.5		508
C_6F_5-Xe^+/BF_4^-	CD_3CN	261	−3798*	^3J/67.8 ^4J/18.6 ^5J/4.2	^{13}C 119	509
$[CH_3CN\text{-}Xe\text{-}C_6F_5]^+/[(C_6F_5)_2BF_2]^-$	CH_3CN	243	−3774	^3J/68.8 ^4J/18.7		510
4-Cl-$C_6H_4Xe^+/BF_4^-$	CD_3CN/ CH_2Cl_2 1:1	223	−3739*			511

[*Continued*

Table 9—*Continued*

Compound	Solvent	T (K)	δ(Xe) (ppm)[a]	$J(^{129}Xe\text{-}L)$ (Hz)[b] L = ^{19}F	L = ^{13}C, ^{14}N, ^{15}N, ^{17}O, ^{125}Te	Reference[c]
Xe(II)—*continued*						
2,6-Cl_2-$C_6H_3Xe^+/BF_4^-$	CH_3CN	237	−3686*			511
2,4,6-Cl_3-$C_6H_2Xe^+/BF_4^-$	CH_3CN	237	−3671*			511
2,4,6$F_3C_6H_2Xe^+/CF_3SO_3^-$	CD_3CN	253	−3901*	^3J/57		513
3,5$(CF_3)_2C_6H_3Xe^+/CF_3SO_3^-$	CD_3CN	238	−3634*		$^3J/^1$H 27	513
2F,5$(CF_3)C_6H_3Xe^+/CF_3SO_3^-$	CD_3CN	238	−3796*	^3J/48.1		513
2F,5$(NO_2)C_6H_3Xe^+/CF_3SO_3^-$	CD_3CN	253	−3769*	^3J/47.8		513
$C_6F_5Xe^+/CF_3SO_3^-$	$(CF_3CO)_2O$	238	−3911*			513
2,4,6-$Cl_3C_6H_2Xe^+/CF_3SO_3^-$	$(CF_3CO)_2O$	238	−3742*			513
$C_6F_7Xe^+/AsF_6^-$ (1,4-cyclohexadien-1-yl)	HF	243	−3941**	^3J/68.5		514
$C_6F_7Xe^+/AsF_6^-$ (1,4-cyclohexadien-1-yl)	CD_3CN	243	−3793*	^3J/82.1		514
$C_6F_9Xe^+/AsF_6^-$ (cyclohexen-1-yl)	HF	243	−3887**	^3J/69.7		514
$C_6F_9Xe^+/AsF_6^-$ (cyclohexen-1-yl)	CD_3CN	243	−3732*	^3J/83.1		514
$(CH_3)_3C{-}C{\equiv}C{-}Xe^+/BF_4^-$	$CDCl_3$	233			^{13}C 120 $^2J/^{13}$C 79	515
$(CH_3)_3Si{-}C{\equiv}C{-}Xe^+$	CD_2Cl_2	228				515
$C_2H_5{-}C{\equiv}C{-}Xe^+$	CD_2Cl_2	228				515
n-$C_3H_7{-}C{\equiv}C{-}Xe^+$	CD_2Cl_2	228				515
$C_6F_5{-}Xe{-}OOCC_6F_5$	CD_2Cl_2	263	−3848*	^3J/86.3		516
Xe(IV)						
XeF_3^+	SbF_5	301	595	2384 (F′, eq)[e] 2609 (F_2, ax)		476 (480)
$F_2Xe(OTeF_5)^+$	SbF_5	278	22.4	2893		481
$FXe(OTeF_5)_2^+$	SbF_5	278	−178.4	2900		481
$Xe(OTeF_5)_3^+$	SbF_5	278	−341.9			481
XeF_4	CH_3CN	297	316.9	3895		517
XeF_4	BrF_5	298	259*	3900		475
XeF_4	BrF_5	301	253	3823		476, 486
XeF_4	$CFCl_3$	297	166.1	3801		477
XeF_4	$CFCl_3$	297	202.9	3817		518
$FXe(OTeF_5)_3$	$CFCl_3$	297	−436.5	3506 ^3J/66	^2J/Te 1032 (eq) 1292 (ax)	518
cis-$FXe(OTeF_5)_3$	$CFCl_3$	297	−242.6	3714 ^3J/69	^2J/Te 1059	518
trans-$FXe(OTeF_5)_3$	$CFCl_3$	297	−215.9	3503 ^3J/69	^2J/Te 1166	518

[*Continued*

Table 9—*Continued*

Compound	Solvent	T (K)	δ(Xe) (ppm)[a]	$J(^{129}Xe–L)$ (Hz)[b] L = ^{19}F	L = ^{13}C, ^{14}N, ^{15}N, ^{17}O, ^{125}Te	Reference[c]
Xe(IV)—*continued*						
$F'F_2Xe(OTeF_5)$	$CFCl_3$	297	−25.5	3552 (F_2) ^3J/71 3733 (F′)	^2J/Te 1192	518
$Xe(OTeF_5)_4$	$C_4F_9SO_2F$		−637*	^3J/67	^2J/Te 1107	519
$Xe(OTeF_5)_4$	$CFCl_3$	297	−662.8	^3J/63	^2J/Te 988	477
$Xe(OTeF_5)_4$	$CFCl_3$	297	−646.5	^3J/66	^2J/Te 1008	518
$XeF_5^-/N(CH_3)_4^+$	CH_3CN	297	−527	3400		517
Xe(VI)						
$XeF_5^+/Sb_2F_{11}^-$	HF	298	12.7	1400 (F′, ax) 159 (F_4, eq)		486
$XeF_5^+/Sb_2F_{11}^-$	SbF_5	298	131.8	1507 (F′, ax) 145 (F_4, eq)		486
XeF_5^+	HSO_3F	193	−23.9	1377 (F′, ax) 165 (F_4, eq)		476 486(520, 521,522)
$XeOF_3^-/SbF_6^-$	XeF_2/SbF_5	303	237.4/ ^{16}O 238/ ^{18}O	1012 (F′, eq) 464 (F_2, ax)		523
$XeOF_3^+/SbF_6^-$	SbF_5	298	238	1018 (F′, eq) 434 (F_2, ax)		486
$XeOF_3^+$	SbF_5	278	242.8	1021 (F′, eq) 496 (F_2, ax)		481
$XeOF_3^-$	$HF.AsF_5$	303	200.8/ ^{16}O 200.1/ ^{18}O		^{17}O 619	523 (520,480)
$F_2XeO(OTeF_5)^+$	SbF_5	278	121.3	796		481
$FXeO(OTeF_5)_2^+$	SbF_5	278	60.6	1089		481
XeO_2F^+	SbF_5	278	704.3	95		481
XeO_2F^+	SbF_5	298	600	95		486(520, 480)

[*Continued*

Table 9—*Continued*

Compound	Solvent	T (K)	δ(Xe) (ppm)[a]	$J(^{129}Xe-L)$ (Hz)[b] L = ^{19}F	L = ^{13}C, ^{14}N, ^{15}N, ^{17}O, ^{125}Te	Reference[c]
Xe(VI)—*continued*						
$XeO_2(OTeF_5)^+$	SbF_5	278	543			481
XeF_6	BrF_5	298	−45*			475
XeF_6	n-C_6F_{14}	298	−35*			475
XeF_6	$(SF_5)_2O$	298	−35*			475,524
$(XeF_6)_4$	$(SF_5)_2O$	155	−39*	325 (dynamic)		475,524, 525 (526)
$(XeF_6)_4$	SO_2ClF/ CF_2Cl_2 1:1	128	−60.8	331.7		486
$XeOF_4$	Liquid	297	0 ref	1123		477
$XeOF_4$	CH_3CN	298	5*	1116		475
$XeOF_4$	SO_2ClF/ CF_2Cl_2 1:1	128	−0.1	1127		486
$XeOF_4$	Liquid			1163		(472)
$Xe^{17}OF_4$	Liquid				^{17}O 692	527
$Xe^{17}OF_4$	HF	223	23.7	1146		518
		297			^{17}O 704	
$XeOF'F_2(OTeF_5)$	$CFCl_3$	297	−66.3	1148 (F_2) ^3J/53 931 (F′)		518
$XeOF_3(OTeF_5)$	$C_2F_4Cl_2$	298	−40*	1145 (F_2) ^3J/50 945 (F′)		519
cis-$XeOF_2(OTeF_5)_2$	$C_2F_4Cl_2$	298	−92*	990 ^3J/51		519,518
cis-$XeOF_2(OTeF_5)_2$	$CFCl_3$	297	−117.8	1074 ^3J/51	^2J/Te 1536	518
trans-$XeOF_2(OTeF_5)_2$	$CFCl_3$	297	−106.4	984 ^3J/53	^2J/Te 1535	518
trans-$XeOF_2(OTeF_5)_2$	$C_2F_4Cl_2$	298	−81*	1231 ^3J/53		519,518
$XeOF(OTeF_5)_3$	$C_2F_4Cl_2$	298	−133*	^3J/52		519
$XeOF(OTeF_5)_3$	$CFCl_3$	297	−157	1206 ^3J/52		518
$XeO(OTeF_5)_4$	$C_2F_4Cl_2$	298	−210*	^3J/55 ^3J/4	^2J/Te 1281	519
$XeO(OTeF_5)_4$	$CFCl_3$	297	−211.8	^3J/54	^2J/Te 1304	477
$XeO(OTeF_5)_4$	$CFCl_3$	297	−204.1	^3J/52	^2J/Te 1351	518
$Xe^{17}O_2F_2$	HF	223	171	1213		518
		297	173.2	1217	^{17}O 521	486
$XeO_2F(OTeF_5)$	SO_2ClF	199	154.1	1046 ^3J/37	^2J/Te 1856	518
$XeO_2(OTeF_5)_2$	SO_2ClF	199	131	^3J/34	^2J/Te 1684	518
XeO_3	H_2O	298	217*			475
Xe(VIII)						
XeO_6^{4-}/Na^+	H_2O	298	2077			486

[*Continued*

Table 9—*Continued*

[a]Referenced with respect to neat $XeOF_4$ at 24°C.
[b]One-bond coupling constants (^1J) except where indicated, e.g. ^3J.
[c]References given in brackets imply certain parameters from the NMR of other nuclei, e.g. ^1J(Xe–F) from ^{19}F measurements.
[d]An appended asterisk indicates modified values as follows: for all cases referenced to XeF_2 in solution, $\delta^* = [\delta(\text{given}) - 1818]$; for all cases referenced to Xe(0) in solution $\delta^* = [\delta(\text{given}) - 5331]$. **Two cases referenced to XeF_2 in HF, $\delta^* = [\delta(\text{given}) - 1592]$.
[e]Abbreviations: br = bridging, t = terminal, ax = axial, eq = equatorial.
[f]Material not fully characterized.

(C) Frohn[485] gives the shift of XeF_2 in CH_3CN at 24°C as +3402.1 ppm with respect to 2.36 mmol. Xe(0) in CH_3CN at 24°C, and (referring to a private communication with Schrobilgen) as −1813.3 ppm with respect to neat $XeOF_4$ at 24°C.
(D) Arnett and Wernett[77] give Xe(0) in CH_3CN at +175 ppm relative to Xe gas extrapolated to zero pressure.

From A–D, relative to $XeOF_4$ at 24°C:

(a) XeF_2 in CH_3CN is at −1823 ppm (from A, B) or −1813.3 ppm (from C, D), in fairly close agreement.
(b) The isolated Ce(0) atom is at −5461 ppm (from A, B) or −5390.4 ppm (from C, D), showing more of a discrepancy. (Average value of −5426 ppm assumed for comparison in Tables 9 and 10.)
(c) Xe(0) in n-C_6F_{14} is at −5331 ppm (from A) and in CH_3CN is at 5215.4 ppm (from C). The difference here is 115.6 ppm instead of the 45 ppm expected from B and D.

Consequently in Table 9 all values originally referenced to XeF_2 under various conditions have been adjusted by subtracting 1818 ppm. Values originally referenced to Xe(0) in n-C_6F_{14} have likewise been adjusted by subtracting 5331 ppm. The adjusted values have been indicated by a trailing asterisk * to alert the reader of the approximate nature of these values.

Schrobilgen[518] has given the precise absolute frequency of pure liquid $XeOF_4$ as 27.810184 MHz at 24°C, quoted relative to a ^1H frequency of exactly 100 MHz for neat $(CH_3)_4Si$ at 24°C (magnetic field of 2.3488 T). As Jameson has previously suggested,[2] there is still a clear need to establish the exact shift difference between $XeOF_4$ and the isolated Xe(0) atom.

With reference to Tables 9 and 10 one can see that most of the trends and general behaviour noted in the earlier reviews are still valid. These and other points are included in the following summary:

Table 10. ^{129}XE NMR chemical shift ranges grouped according to type.

VSEPR type[a]	Ligands	$\delta(^{129}Xe)$ range	
Xe(0)			
E_4		−5009	−5476
Xe(II)			
AE_3^+	F	−574	
	O	−913	−1482
A_2E_3	F_2	−1059	−2009
	F, O	−906	−2172
	F, N	−1294	−2257
	O_2	−1613	−2447
	N_2	−2101	−2257
	C, N	−3761	−3933
	C, O	−3848	
Xe(IV)			
$A_3E_2^+$	F_3	+595	
	F_2, O	+22	
	F, O_2	−178	
	O_3	−342	
A_4E_2	F_4	+166	−317
	F_3, O	−26	
	F, O_3	−216	−437
	O_4	−637	−663
$A_5E_2^-$	F_5	−527	
Xe(VI)			
A_5E^+	F_5	+132	−24
A_3BE^+	F_3, (=O)	+243	+200
AB_2E^+	F_2, O, (=O)	+121	
	F, O_2, (=O)	+61	
	F, $(=O)_2$	+704	+600
	O, $(=O)_2$	+543	
A_6E	F_6	−35	−61
A_4BE	F_4, (=O)	+5	−0.1
A_2B_2E	F_3, O, (=O)	−40	−66
B_3E	F_2, O_2, (=O)	−81	−118
	F, O_3, (=O)	−133	−157
	O_4, (=O)	−204	−212
	F_2, $(=O)_2$	+173	+171
	F, O, $(=O)_2$	+154	
	O_2, $(=O)_2$	+131	
	$(=O)_3$	+217	
Xe(VIII)			
$A_4B_2^4-$	O_4, $(=O)_2$	+2077	

[a]A = single bond; B = double bond; E = lone pair.

(1) Oxidation state

(a) The xenon nucleus is progressively more deshielded (δ and frequency increase) as the oxidation state increases, although the ranges for the IV and VI states overlap considerably. This general trend was suggested by early calculations[531] and is also common to numerous transition metals.[532]

(b) Similarly $^{1}J(^{129}Xe–^{19}F)$ decreases with increasing oxidation state: Xe(II)(4828–7594) > Xe(IV)(2384–3900) > Xe(VI)(95–1507) (Hz).

(c) $^{2}J(^{129}Xe–^{125}Te)$ for $OTeF_5$ ligands increases with oxidation state: Xe(II)(470–540) < Xe(IV)(988–1292) < Xe(VI)(1281–1856) (Hz).

(2) Charge effects

(a) It appears that removal of any ligand to produce a cation always results in deshielding (Jameson noted this for removal of F). Conversely, in the one case studied, addition of a ligand to produce the anion leads to increased shielding, $\delta(^{129}Xe)$: XeF_3^+ (+595) > XeF_4 (+166 to −317) > XeF_5^- (−527) (ppm).

(b) $^{1}J(^{129}Xe–^{19}F)$ increases from XeF_2 to XeF^+, but for Xe(IV) and Xe(VI) states there is usually, but not always, a decrease upon cation formation.

(3) Physical effects of solvent and temperature

(a) Physical effects on δ increase with the number of lone pairs. We have seen earlier the range of effects on δ of Xe(0) which are all physical shifts. For this reason it is always preferable to make comparisons between materials in the same solvent at the same temperature, if this is feasible. In fact, Schrobilgen has suggested that δ is more sensitive to solvent effects than can be explained by nonchemical interactions, implicating weak, labile F or O bridges to solvent molecules, particularly for Xe(II) species such as XeF^+.[1]

(b) The coupling constants can also be quite sensitive to solvent and temperature effects,[2,486] although there are exceptions. For example, measurements on XeF_2 in CD_3CN have shown a strong linear dependence of δ on temperature, $\Delta\delta/\Delta T = -0.497$ ppm K^{-1}; however $^{1}J(^{129}Xe–^{19}F)$ is independent of T over 243–303 K.[533]

(4) Ligands

(a) Replacing 2F with =O is always deshielding, whereas replacing F with −O, −N or −C is always shielding.

(b) In Xe(II) cases with a bridging and a terminal F, $^{1}J(^{129}Xe–^{19}F)$ is always

larger for the terminal F: terminal F (6058–6662) > bridging F (4828–5117) (Hz).

(5) Covalency of bonds

(a) The increasing covalency of terminal Xe—F bonds (and decreasing bond length) is associated with increasing δ and increasing $^1J(^{129}Xe–^{19}F)$. (The ^{19}F shift decreases at the same time. In fact there is a general correlation of $\delta(^{19}F)$ with $^1J(^{129}Xe–^{19}F)$.[521,534])
(b) The deshielding effect of =O substitution is thought to be due to ionic character in the double bond, i.e. $Xe{=}O \leftrightarrow Xe^+{-}O^-$.
(c) In F—Xe—L compounds of Xe(II), separate linear correlations exist between $\delta(^{129}Xe)$ and $\delta(^{19}F_{terminal})$ for L with an F or an O bridge. Both shifts are more deshielded for O bridges, interpreted as indicating greater covalent character in the Xe—O bond than the Xe—F bond.[486]

A number of one-bond ^1J couplings to ^{17}O, ^{14}N, ^{15}N and ^{13}C have now been observed (Table 9), but there are too few to draw any conclusions about trends.

Secondary isotope effects have been observed for oxygens on xenon ($^1\Delta\,^{129}Xe(^{18,16}O)$: $XeOF_4$, −0.58 ppm;[518] $XeOF_3^+$, −0.69 ppm;[523] XeO_2F_2, −0.52 ppm[518]) and for nitrogen on xenon ($^1\Delta\,^{129}Xe(^{15,14}N)$: $XeN(SO_2F)_2^+$, −0.56 ppm[498]). A larger vibrational amplitude for the lighter isotope causes the slight deshielding of the Xe relative to the heavier isotope.[535]

Jameson[2] has also tabulated quadrupole coupling constants measured largely from Mössbauer studies of the excited ^{129}Xe nucleus.[536,537] Except for the symmetrical XeO_6^{4-} ion all the quadrupole coupling constants for Xe compounds are very large, ranging up to 2650 MHz. Although no chemical shift anisotropies have been measured directly for xenon compounds, all indications are that these are likely to be very large: (i) calculations;[531] (ii) correlation with the qudrupole coupling constants; (iii) known large anisotropies for nuclei of similar atomic number; and (iv) sizable anisotropies even from physical effects for Xe(0) in cages (see earlier). From T_1 versus temperature and field studies of XeF_2 in CD_3CN it was ascertained that the relaxation is dominated by shielding anisotropy and spin–rotation interactions, from which one analysis gave a value of $|\Delta\sigma| = 2416$ ppm with $|C_{Xe}| = 340$ kHz.[538] Other measurements of T_1 are sparse and have generally been obtained at only one temperature.[474,475]

Specific examples

(1) Many of the Xe–N compounds are weak donor–acceptor complexes of the Lewis acid $Xe{-}F^+$ with R—CN Lewis bases. Schrobilgen *et al.*[470] have studied many of these complexes including $[HCN{-}Xe{-}F]^+$, whose solution structure

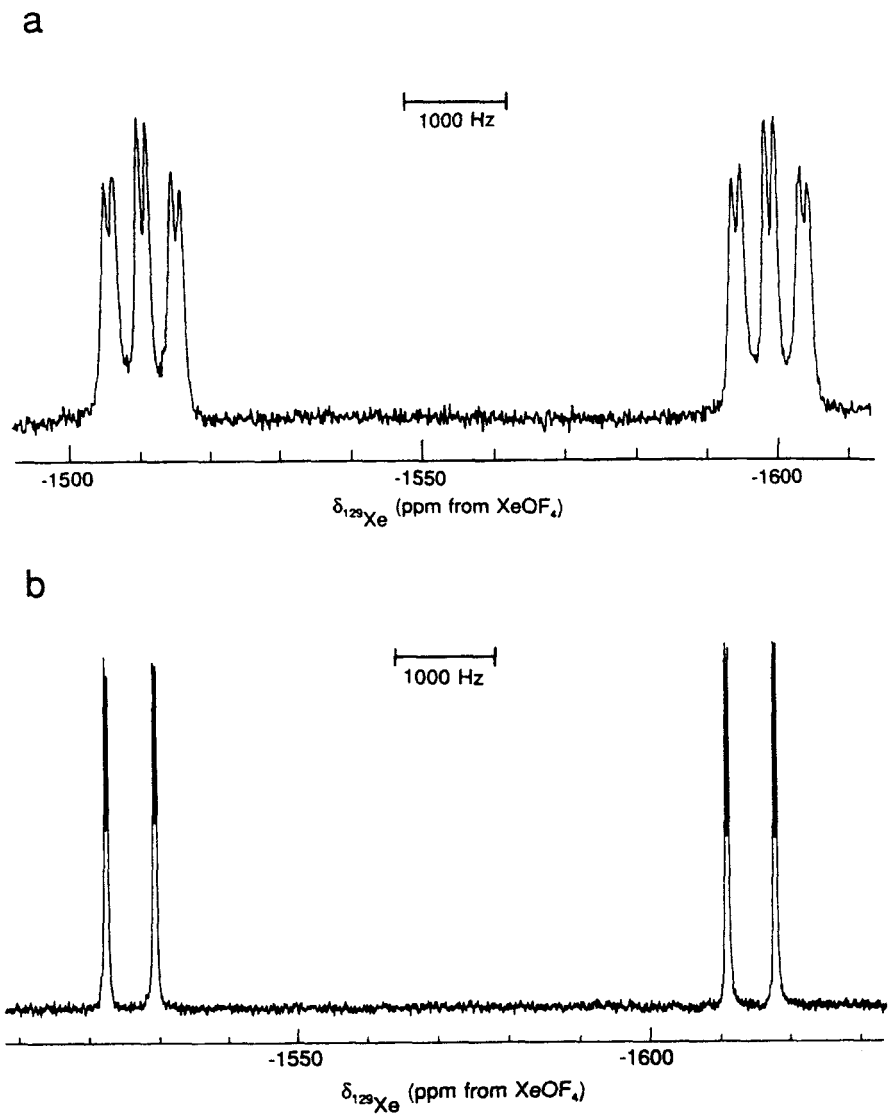

Fig. 31. ^{129}Xe NMR spectra of $HCNXeF^{+}AsF_6^{-}$: (a) 99.2% ^{13}C-enriched, HF solvent, 263 K; (b) 99.5% ^{15}N-enriched, BrF5 solvent, 223 K; expansions A and B are without and with ^{1}H decoupling. (Reprinted with permission from Ref. 494. Copyright 1992 American Chemical Society.)

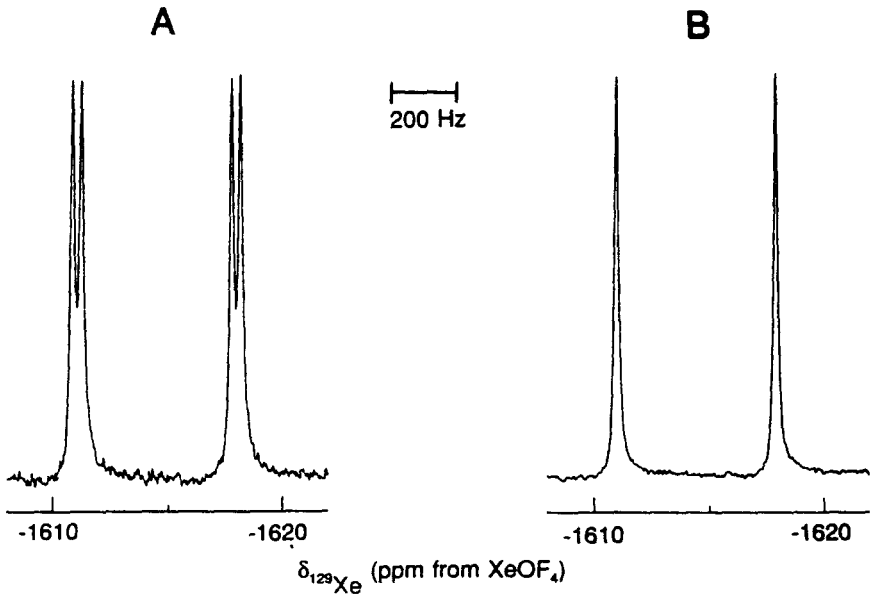

Fig. 31. (continued)

was determined using multinuclear NMR. The same techniques indicated that the Xe–N bond is weakly covalent. ^{129}Xe J couplings to all the nuclei in the molecule, including ^{14}N, were observed[494] (Fig. 31). The observation of $^1J(^{129}Xe–^{14}N)$ coupling is a result of low viscosity of the HF solvent, axial symmetry and a much reduced quadrupole coupling constant for the ^{14}N. In BrF_5, with increased viscosity, the spectrum is quadrupole collapsed.

(2) XeF_5^- turns out from X-ray diffraction and solution NMR work[517] to be completely planar with five-fold symmetry, just as would be predicted from the VSEPR theory for a molecule with five ligands and two lone pairs. The NMR shows a sextet for Xe attached to five equivalent F atoms.

(3) XeF_6 is a fascinating species, as its NMR shows considerable dynamic behaviour. Both the ^{19}F and ^{129}Xe NMR spectra show multiplets at 155 K in $O(SF_5)_2$ solution[475,524] and at 129 K in 50:50 $SO_2ClF–CF_2Cl_2$ solution,[486] which have been interpreted as consistent with tetrameric units $(XeF_6)_4$ in which all four Xe are equivalent as are all 24 F, with the Fs undergoing rapid intra-tetramer exchange (Fig. 32). in the ^{19}F spectra only seven lines have been seen in the natural-abundance spectra, but nine are seen when the ^{129}Xe is enriched to 61%[486] or 62.5%.[525] The observed intensities are consistent with over-lapped J multiplets corresponding to the statistical distribution of ^{129}Xe in tetramers. Coupling to the ^{131}Xe was not observed. The ^{129}Xe NMR multiplet

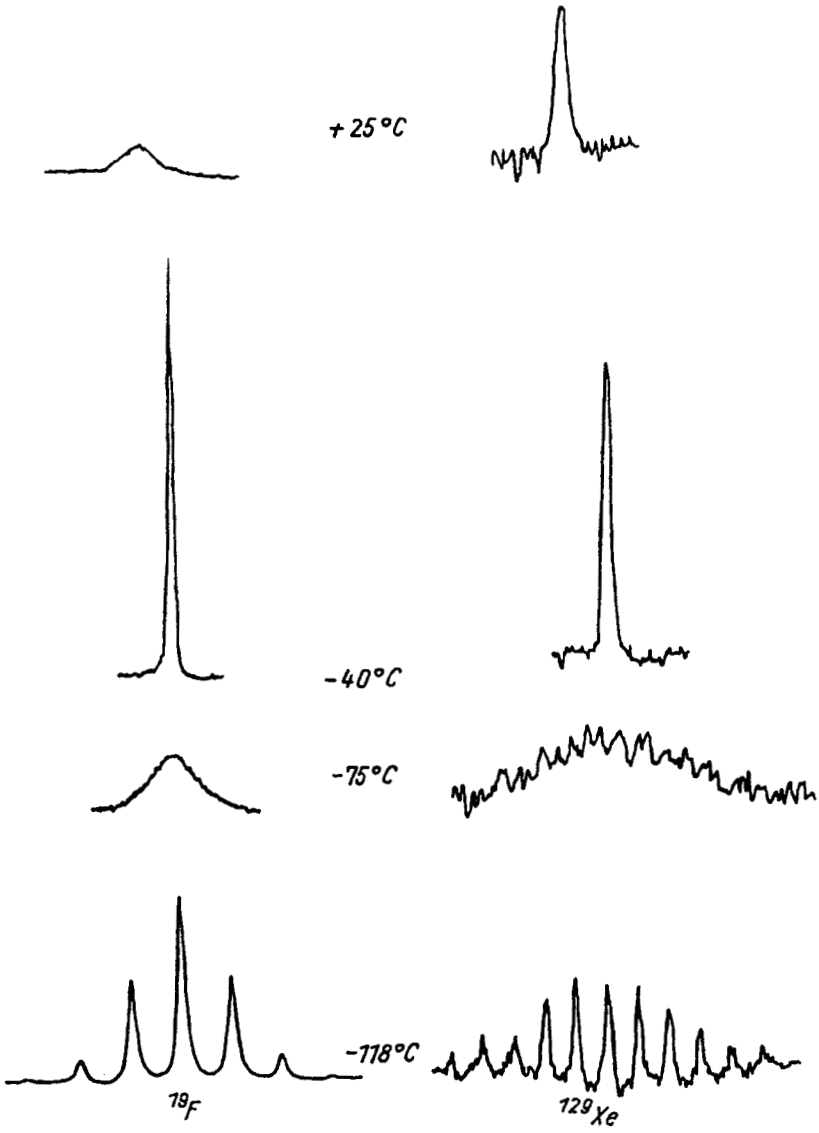

Fig. 32. XeF_6 tetramer. (*Top*) ^{19}F and ^{129}Xe NMR spectra at 298, 233, 198 and 155 K in F_5SOSF_5 solution. (Reprinted with permission from Ref. 475. Copyright 1974 Hüthig.) (*Bottom*) ^{129}Xe spectrum at 128 K in 50/50 SO_2ClF/CF_2Cl_2 solution. (Reprinted with permission from Ref. 486. Copyright 1978 American Chemical Society.)

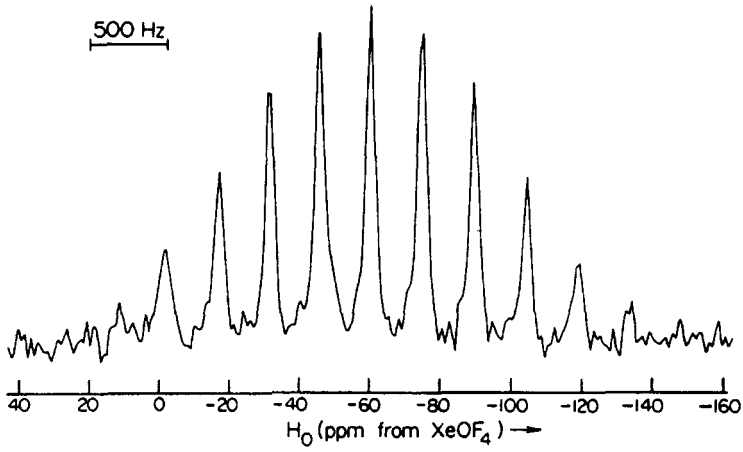

Fig. 32. (continued)

corresponding to such a tetramer should contain 25 lines; the relative intensities of the limited number of lines observed (11 to 13) were found to be consistent with those calculated for such a multiplet. At higher temperatures the multiplets collapse and by 228 K the spectra narrow to single lines, interpreted in terms of rapid inter-tetramer exchange of F. By room temperature the lines are still single but much broader, and indications are that there is an equilibrium between monomers and polymers.

(4) All the Xe—C compounds studied are shielded quite significantly relative to all other Xe compounds, and all involve Xe attached to a substituted aromatic ring, with a few exceptions that involve bonds to alkene or alkyne groups.[514,515] The unusual shifts are attributed to a reduction of the positive charge density at the Xe(II) through resonance structures with π-bond character and electron donation from *ortho*-F atoms (when present). This effect may be enhanced by solvents such as CH_3CN forming weak complexes, aryl—Xe^+—$NCCH_3$.

4. CONCLUSION

This review has traversed the whole spectrum of Xe NMR activity, from the early days of NMR itself to the promise of new frontiers with hyperpolarized Xe. The broad scope has limited the coverage of certain topics in detail, but it is hoped the flavour has come across and the interested reader will be able to delve into other reviews and publications listed here. Finally, I think one can say that xenon the "stranger" (from the Greek *xenos*) is a stranger no more.

ACKNOWLEDGEMENTS

I thank my colleagues Dr John Ripmeester and Dr Igor Moudrakovski for many years of stimulating Xe NMR experimentation and discussion, and Professor Cynthia Jameson for numerous discussions.

Published as NRCC No. 40847.

REFERENCES

1. G. J. Schrobilgen, in *NMR and the Periodic Table* (ed. R. K. Harris and B. E. Mann), Ch. 14, Academic Press, London, 1978.
2. C. J. Jameson, in *Multinuclear NMR* (ed. J. Mason), Ch. 18, Plenum Press, London, 1987.
3. D. Raftery and B. F. Chmelka, *NMR Basic Principles and Progress*, 1994, **30**, 111.
4. J. Reisse, *Nouveau J. Chim.*, 1986, **10**, 665.
5. J. Fraissard and T. Ito, *Zeolites*, 1988, **8**, 350.
6. C. Dybowski, N. Bansal and T. M. Duncan, *Annu. Rev. Phys. Chem.*, 1991, **42**, 433.
7. P. J. Barrie and J. Klinowski, *Prog. NMR Spectrosc.*, 1992, **24**, 91.
8. J. Jokisaari, *Prog. NMR Spectrosc.*, 1994, **26**, 1.
9. J. H. Walton, *Polym. Polym. Compos.*, 1994, **2**, 35.
10. C. Dybowski, *J. Incl. Phenom. Mol. Recog. Chem.*, 1995, **21**, 113.
11. M.-A. Springuel-Huet, J.-L. Bonardet and J. Fraissard, *Appl. Magn. Reson.*, 1995, **8**, 427.
12. T. Pietrass and H. C. Gaede, *Adv. Mater.*, 1995, **7**, 826.
13. J. Emsley, *The Elements*, 2nd edn, Clarendon Press, Oxford, 1991.
14. D. Brinkmann, *Helv. Phys. Acta*, 1963, **36**, 413.
15. W. G. Proctor and F. C. Yu, *Phys. Rev.*, 1950, **78**, 471.
16. H. Kopfermann and E. Rindal, *Z. Phys.*, 1934, **87**, 460.
17. W. G. Proctor and F. C. Yu, *Phys. Rev.*, 1951, **81**, 20.
18. E. Brun, J. Oeser, H. H. Staub and C. G. Telschow, *Phys. Rev.*, 1954, **93**, 904.
19. E. Brun, J. Oeser, H. H. Staub and C. G. Telschow, *Helv. Phys. Acta*, 1954, **27**, 173.
20. H. Staub, *Helv. Phys. Acta*, 1956, **29**, 246.
21. D. Brinkmann, E. Brun and H. H. Staub, *Helv. Phys. Acta*, 1962, **35**, 431.
22. R. L. Streever and H. Y. Carr, *Phys. Rev.*, 1961, **121**, 20.
23. E. R. Hunt and H. Y. Carr, *Bull. Am. Phys. Soc.*, 1962, **7**, 293.
24. E. R. Hunt and H. Y. Carr, *Phys. Rev.*, 1963, **130**, 2302.
25. D. Brinkmann, *Helv. Phys. Acta*, 1968, **41**, 367.
26. E. Kanegsberg, B. Pass and H. Y. Carr, *Phys. Rev. Lett.*, 1969, **23**, 572.
27. A. K. Jameson, C. J. Jameson and H. S. Gutowsky, *J. Chem. Phys.*, 1970, **53**, 2310.
28. C. J. Jameson, A. K. Jameson and S. M. Cohen, *J. Chem. Phys.*, 1973, **59**, 4540.
29. A. K. Jameson and C. J. Jameson, *J. Am. Chem. Soc.*, 1973, **95**, 8559.
30. C. J. Jameson, *J. Chem. Phys.*, 1975, **63**, 5296.
31. F. J. Adrian, *Phys. Rev.*, 1964, **136**, A980.
32. F. J. Adrian, *Chem. Phys. Lett.*, 1970, **7**, 201.
33. C. J. Jameson, A. K. Jameson and S. M. Cohen, *J. Chem. Phys.*, 1975, **62**, 4224.
34. C. J. Jameson, A. K. Jameson and S. M. Cohen, *J. Magn. Reson.*, 1975, **19**, 385.
35. G. Malli and C. Froese, *Int. J. Quantum. Chem.*, 1967, **1**, 95.
36. D. Kolb, W. R. Johnson and P. Shorer, *Phys. Rev. A*, 1982, **26**, 19.
37. D. M. Bishop and S. M. Cybulski, *J. Mag. Reson., Ser. A*, 1994, **107**, 99.
38. H. C. Torrey, *Phys. Rev.*, 1963, **130**, 2306.
39. N. F. Ramsey, *Phys. Rev.*, 1950, **78**, 699.
40. B. Shizgal, *Chem. Phys.*, 1974, **5**, 464.

41. M. Pfeffer and O. Lutz, *J. Magn. Reson., Ser. A*, 1994, **108**, 106.
42. M. Pfeffer and O. Lutz, *J. Mag. Reson., Ser. A*, 1995, **113**, 108.
43. F. J. Adrian, *Phys. Rev.*, 1965, **138**, A403.
44. W. M. Yen and R. E. Norberg, *Phys. Rev.*, 1963, **131**, 269.
45. W. W. Warren Jr and R. E. Norberg, *Phys. Rev.*, 1966, **148**, 402.
46. D. Brinkmann and H. Y. Carr, *Phys. Rev.*, 1966, **150**, 174.
47. D. Brinkmann, *Phys. Rev. Lett.*, 1964, **13**, 187.
48. W. W. Warren Jr and R. E. Norberg, *Phys. Rev.*, 1967, **154**, 277.
49. D. F. Cowgill and R. E. Norberg, *Phys. Rev. B*, 1972, **6**, 1636.
50. R. E. Norberg in *Rare Gas Solids*, p. 59. Springer-Verlag, Berlin, 1984.
51. J. Lurie, J. L. Feldman and G. K. Horton, *Phys. Rev.*, 1966, **150**, 180.
52. D. M. Pfund, T. S. Zemanian, J. C. Lineham, J. L. Fulton and C. R. Yonker, *J. Phys. Chem.*, 1994, **98**, 11846.
53. M. Gatzke, G. D. Cates, B. Driehuys, D. Fox, W. Happer and B. Saam, *Phys. Rev. Lett.*, 1993, **70**, 690.
54. G. Cho, L. B. Moran and J. P. Yesinowski, *Appl. Mag. Reson.*, 1995, **8**, 549.
55. T. T. P. Cheung, *J. Phys. Chem.*, 1990, **94**, 376.
56. G. R. Davies, T. K. Halstead, R. C. Greenhow and K. J. Packer, *Chem. Phys. Lett.*, 1994, **230**, 237.
57. J. Van Kranendonk, *Physica*, 1954, **20**, 781.
58. L. E. Barroilhet, NMR Relaxation Study of Atomic Transport Properties in Solid and Liquid Xenon. PhD thesis, University of Wisconsin, 1973.
59. L. M. Stacey, B. Pass and H. Y. Carr, *Phys. Rev. Lett.*, 1969, **23**, 1424.
60. C. E. Hayes and H. Y. Carr, *Phys. Rev. Lett.*, 1977, **39**, 1558.
61. R. S. Ehrlich and H. Y. Carr, *Phys. Rev. Lett.*, 1970, **25**, 341.
62. P. W. E. Peereboom, H. Luigjes, K. O. Prins and N. J. Trappeniers, *Physica*, 1986, **139&140B**, 134.
63. P. W. E. Peereboom, H. Luigjes and K. O. Prins, *Physica A*, 1989, **156**, 260.
64. M. Tomaselli, B. H. Meier, P. Robyr, U. W. Suter and R. R. Ernst, *Chem. Phys. Lett.*, 1993, **214**, 1.
65. C. J. Jameson and A. K. Jameson, *Mol. Phys.*, 1971, **20**, 957.
66. C. J. Jameson, A. K. Jameson and S. M. Cohen, *Mol. Phys.*, 1975, **29**, 1919.
67. C. J. Jameson, A. K. Jameson and S. M. Cohen, *J. Chem. Phys.*, 1976, **65**, 3401.
68. C. J. Jameson, A. K. Jameson and S. M. Cohen, *J. Chem. Phys.*, 1976, **65**, 3397.
69. C. J. Jameson, A. K. Jameson and S. M. Cohen, *J. Chem. Phys.*, 1977, **66**, 5226.
70. C. J. Jameson, A. K. Jameson and H. Parker, *J. Chem. Phys.*, 1978, **68**, 3943.
71. A. D Buckingham and P. A. Kollman, *Mol. Phys.*, 1972, **23**, 65.
72. C. J. Jameson, A. K. Jameson and J. K. Hwang, *J. Chem. Phys.*, 1988, **89**, 4074.
73. Y.-H. Lim, N. E. Nugara and A. D. King Jr., *J. Phys. Chem.*, 1993, **97**, 8816.
74. Y.-H. Lim and A. D. King Jr, *J. Phys. Chem.*, 1993, **97**, 12173.
75. T. R. Stengle, N. V. Reo and K. L. Williamson, *J. Phys. Chem.*, 1981, **85**, 3772.
76. J. H. Walton, J. B. Miller and C. M. Roland, *Appl. Mag. Reson.*, 1995, **8**, 535.
77. T. R. Stengle, N. V. Reo and K. L. Williamson, *J. Phys. Chem.*, 1984, **88**, 3225.
78. K. W. Miller, N. V. Reo, A. J. M. Schoot Uiterkamp, D. P. Stengle, T. R. Stengle and K. L. Williamson, *Proc. Natl. Acad. Sci. USA*, 1981, **78**, 4946.
79. P. Diehl, R. Ugolini, N. Suryaprakash and J. Jokisaari, *Magn. Reson. Chem.*, 1991, **29**, 1163.
80. Y.-H. Lim, N. Nugara and A. D. King Jr, *Appl. Magn. Reson.*, 1995, **8**, 521.
81. E. M. Arnett and P. C. Wernett, *J. Am. Chem. Soc.*, 1993, **115**, 12187.
82. T. R. Stengle, S. M. Hosseini, H. G. Basiri and K. L. Williamson, *J. Soln. Chem.*, 1984, **13**, 779.
83. F. H. A. Rummens, *NMR Basic Principles and Progress*, 1975, **10**, 1.

84. N. Muller, *J. Phys. Chem.*, 1982, **86**, 2109.
85. M. Luhmer, A. Dejaegere and J. Reisse, *Magn. Reson. Chem.*, 1989, **27**, 950.
86. T. R. Stengle, S. M. Hosseini and K. L. Williamson, *J. Soln. Chem.*, 1986, **15**, 777.
87. R. K. Mazitov, K. M. Enikeev and A. V. Ilyasov, in *Interactions of Water in Ionic and Nonionic Hydrates*, p. 137 (ed. H. Kleeberg), Springer-Verlag, Berlin, 1987.
88. R. Haselmeier, M. Holz, W. Marbach and H. Weingartner, *J. Phys. Chem.*, 1995, **99**, 2243.
89. H. Weingartner, R. Haselmeier and M. Holz, *J. Phys. Chem.*, 1996, **100**, 1303.
90. H. Weingartner, R. Haselmeier and M. Holz, *Chem. Phys. Lett.*, 1991, **195**, 596.
91. S. McKim and J. F. Hinton, *J. Magn. Reson., Ser. A*, 1993, **104**, 268.
92. R. K. Mazitov, H. G. Hertz, V. F. Garanin, K. M. Enikeev, A. V. Ilyasov and V. F. Sukhoverkhov, *Dokl. Akad. Nauk. SSSR*, 1983, **273**, 131.
93. K. Bartik, M. Luhmer, S. J. Heyes, R. Ottinger, J. Reisse, *J. Magn. Reson., Ser. B*, 1995, **109**, 164.
94. J. Reisse, M. Claessens, O. Fabre, G. Michaux, M. L. Stien and D. Zimmermann, *Bull. Soc. Chim. Belg.*, 1983, **92**, 819.
95. M. Claessens, O. Fabre, D. Zimmermann and J. Reisse, *Bull. Soc. Chim. Belg.*, 1984, **93**, 983.
96. P. Diehl and J. Jokisaari, *J. Magn. Reson.*, 1990, **88**, 660.
97. A. Moschos and J. Reisse, *J. Magn. Reson.*, 1991, **95**, 603.
98. K. Oikarinen and J. Jokisaari, *Appl. Magn. Reson.*, 1995, **8**, 587.
99. M. Luhmer, M.-L. Stien and J. Reisse, *Heterocycles*, 1994, **37**, 1041.
100. A. Dejaegere, M. Luhmer, M.-L. Stien and J. Reisse, *J. Magn. Reson.*, 1991, **91**, 362.
101. J. Vaara, J. Jokisaari, T. T. Rantala and J. Lounila, *Mol. Phys.*, 1994, **82**, 13.
102. M. Holz, R. Haselmeier, A. Klein and R. K. Mazitov, *Appl. Magn. Reson.*, 1995, **8**, 501.
103. R. K. Mazitov, K. M. Enikeev and A. V. Ilyasov, *Radiospektroskopia* (ed. Schaposchnikov), p. 106, Perm University Press, Perm, 1988.
104. J. Schnitker and A. Geiger, *Z. Phys. Chem. N.F.*, 1987, **155**, 29.
105. M. Luhmer, D. van Belle, J. Reisse, M. Odelius, J. Kowalewski and A. Laaksonen, *J. Chem. Phys.*, 1993, **98**, 1566.
106. M. Odelius, *J. Phys. Chem.*, 1994, **98**, 12108.
107. M. Luhmer, A. Moschos and J. Reisse, *J. Magn. Reson., Ser. A*, 1995, **113**, 164.
108. M. Luhmer and J. Reisse, *J. Magn. Reson., Ser. A*, 1995, **115**, 197.
109. J. P. Bayle, J. Courtieu and J. Jullien, *J. Chim. Phys. Phys.-Chim. Biol.*, 1988, **85**, 147.
110. J. Jokisaari, P. Diehl and O. Muenster, *Mol. Cryst. Liq. Cryst.*, 1990, **188**, 189.
111. J. Jokisaari and P. Diehl, *Liq. Cryst.*, 1990, **7**, 739.
112. O. Muenster, J. Jokisaari and P. Diehl, *Mol. Cryst. Liq. Cryst.*, 1991, **206**, 179.
113. J. Lounila, O. Muenster, J. Jokisaari and P. Diehl, *J. Chem. Phys.*, 1992, **97**, 8977.
114. R. Seydoux, O. Muenster and P. Diehl, *Mol. Cryst. Liq. Cryst.*, 1994, **250**, 99.
115. H. W. Long, M. Luzar, H. C. Gaede, R. G. Larsen, J. Kritzenberger, A. Pines and G. P. Crawford, *J. Phys. Chem.*, 1995, **99**, 11989.
116. A. Loewenstein and M. Brenman, *Chem. Phys. Lett.*, 1978, **58**, 435.
117. P. Diehl and J. Jokisaari, *Chem. Phys. Lett.*, 1990, **165**, 389.
118. P. Ingman, J. Jokisaari and P. Diehl, *J. Magn. Reson.*, 1991, **92**, 163.
119. J. Jokisaari, P. Ingman, J. Lounila, O. Pulkkinen, P. Diehl and O. Muenster, *Mol. Phys.*, 1993, **78**, 41.
120. R. F. Tilton Jr. and I. D. Kuntz Jr, *Biochemistry*, 1982, **21**, 6850.
121. G. Saba, M. Casu and A. Lai, *Int. J. Quantum Chem.*, 1996, **59**, 343.
122. S. McKim and J. F. Hinton, *Biochim. Biophys. Acta*, 1994, **1193**, 186.
123. A. Bifone, Y.-Q. Song, R. Seydoux, R. E. Taylor, B. M. Goodson, T. Pietrass, T. F. Budinger, G. Navon and A. Pines, *Proc. Natl. Acad. Sci. USA*, 1996, **93**, 12932.
124. M. S. Albert, V. D. Schepkin and T. F. Budinger, *J. Computer Assisted Tomography*, 1995, **19**, 976.

125. M. D. Sefcik, J. Schaefer, J. A. E. Desa and W. B. Yelon, *Polym. Prepr. Am. Chem. Soc. Div. Polym. Chem.*, 1983, **24**, 85.
126. T. R. Stengle and K. L. Williamson, *Macromolecules*, 1987, **20**, 1428.
127. S. K. Brownstein, J. E. L. Roovers and D. J. Worsfold, *Magn. Reson. Chem.*, 1988, **26**, 392.
128. E. J. Cain, W.-Y. Wen, R. D. Jost, X. Liu, Z. Dong, A. A. Jones and P. T. Inglefield, *Polym. Mater. Sci. Eng.*, 1989, **61**, 512.
129. E. J. Cain, W.-Y. Wen, R. D. Jost, X. Liu, Z. P. Dong, A. A. Jones and P. T. Inglefield, *J. Phys. Chem.*, 1990, **94**, 2128.
130. G. J. Kennedy, *Polym. Bull.*, 1990, **23**, 605.
131. A. P. M. Kentgens, H. A. van Boxtel, R.-J. Verweel and W. S. Veeman, *Macromolecules*, 1991, **24**, 3712.
132. T. T. P. Cheung and P. J. Chu, *J. Phys. Chem.*, 1992, **96**, 9551.
133. J. H. Walton, J. B. Miller and C. M. Roland, *J. Polym. Sci., Part B*, 1992, **30**, 527.
134. M. Tomaselli, B. H. Meier, P. Robyr, U. W. Suter and R. R. Ernst, *Chem. Phys. Lett.*, 1993, **205**, 145.
135. J. B. Miller, J. H. Walton and C. M. Roland, *Macromolecules*, 1993, **26**, 5602.
136. J. H. Walton, J. B. Miller, C. M. Roland and J. B. Nagode, *Macromolecules*, 1993, **26**, 4052.
137. M. Mansfield and W. S. Veeman, *Chem. Phys. Lett.*, 1993, **213**, 153.
138. H. W. Long, H. C. Gaede, J. Shore, L. Reven, C. R. Bowers, J. Kritzenberger, T. Pietrass and A. Pines, *J. Am. Chem. Soc.*, 1993, **115**, 8491.
139. D. Raftery, L. Reven, H. Long, A. Pines, P. Tang and J. A. Reimer, *J. Phys. Chem.*, 1993, **97**, 1649.
140. K. J. McGrath and C. M. Roland, *Rubber Chem. Technol.*, 1994, **67**, 629.
141. M. Mansfield and W. S. Veeman, *Chem. Phys. Lett.*, 1994, **222**, 422.
142. J. H. Simpson, W.-Y. Wen, A. A. Jones, P. T. Inglefield and J. T. Bendler, *Appl. Magn. Reson.*, 1995, **8**, 349.
143. M. Mansfield, A. Flohr and W. S. Veeman, *Appl. Magn. Reson.*, 1995, **8**, 573.
144. J. H. Simpson, W.-Y. Wen, A. A. Jones and P. T. Inglefield, *Macromolecules*, 1996, **29**, 2138.
145. F. M. Mirabella Jr. and D. C. McFaddin, *Polymer*, 1966, **37**, 931.
146. C. Urban, E. F. McCord, O. W. Webster, L. Abrams, H. W. Long, H. Gaede, P. Tang and A. Pines, *Chem. Mater.*, 1995, **7**, 1325.
147. J. B. Miller, *Rubber Chem. Technol.*, 1993, **66**, 455.
148. J. H. Walton, *Polym. Polym. Compos.*, 1994, **2**, 35.
149. J. A. Ripmeester and D. W. Davidson, *Bull. Magn. Reson.*, 1981, **2**, 139.
150. J. A. Ripmeester and D. W. Davidson, *J. Mol. Struct.*, 1981, **75**, 67.
151. J. A. Ripmeester, *J. Am. Chem. Soc.*, 1982, **104**, 289.
152. D. W. Davidson and J. A. Ripmeester, in *Inclusion Compounds* (ed. J. L. Atwood, J. E. D. Davies and D. D. MacNicol), Vol. 3, Ch. 3, p. 78, Academic Press, London, 1984.
153. D. W. Davidson, Y. P. Handa and J. A. Ripmeester, *J. Phys. Chem.*, 1986, **90**, 6549.
154. J. A. Ripmeester, J. S. Tse, C. I. Ratcliffe and B. M. Powell, *Nature*, 1987, **325**, 135.
155. J. A. Ripmeester, C. I. Ratcliffe and J. S. Tse, *J. Chem. Soc., Faraday Trans. 1*, 1988, **84**, 3731.
156. Y. P. Handa, C. I. Ratcliffe, J. A. Ripmeester and J. S. Tse, *J. Phys. Chem.*, 1990, **94**, 4363.
157. J. A. Ripmeester and C. I. Ratcliffe, *J. Phys. Chem.*, 1990, **94**, 8773.
158. J. A. Ripmeester and C. I. Ratcliffe, in *Inclusion Compounds* (ed. J. L. Atwood, J. E. D. Davies and D. D. MacNicol), Vol. 5, Ch. 2, p. 37, Oxford University Press, Oxford, 1991.
159. T. Pietrass, H. C. Gaede, A. Bifone, A. Pines and J. A. Ripmeester, *J. Am. Chem. Soc.*, 1995, **117**, 7520.
160. I. L. Moudrakovski, C. I. Ratcliffe and J. A. Ripmeester, unpublished results.
161. F. Lee, E. Gabe, J. S. Tse and J. A. Ripmeester, *J. Am. Chem. Soc.*, 1988, **110**, 6014.
162. J. Fraissard, T. Ito, M. Springuel-Huet and J. Demarquay, *Stud. Surf. Sci. Catal.*, 1986, **28**, 393.

163. J. Fraissard, *Z. Phys. Chem. N.F.*, 1987, **152**, S.159.
164. J. Fraissard, *Z. Phys. Chem.*, 1988, **269**, S.657.
165. J. Fraissard, T. Ito and M. A. Springuel-Huet, *J. Chim. Phys.*, 1988, **85**, 747.
166. Q. Chen, J. B. Nagy, J. Fraissard, J. El Hage-Al Asswad, Z. Gabelica, E. G. Derouane, R. Aiello, F. Crea, G. Giordano and A. Nastro, *NATO ASI Series, Ser. B*, 1990, **221**, 87.
167. M. A. Springuel-Huet and J. Fraissard, *Petrole et Techniques*, 1991, **361**, 90.
168. T. Ito and J. Fraissard, *J. Chem. Phys.*, 1982, **76**, 5225.
169. T. Ito and J. Fraissard, *J. Chim. Phys.*, 1986, **83**, 441.
170. T. Ito and J. Fraissard, *J. Chem. Soc., Faraday Trans. 1*, 1987, **83**, 451.
171. A. Gedeon, T. Ito and J. Fraissard, *Zeolites*, 1988, **8**, 376.
172. M. L. Smith and C. Dybowski, *J. Phys. Chem.*, 1991, **95**, 4942.
173. T. T. P. Cheung, C. M. Fu and S. Wharry, *J. Phys. Chem.*, 1988, **92**, 5170.
174. K.-J. Chao and D.-S. Shy, *J. Chem. Soc., Faraday Trans.*, 1993, **89**, 3841.
175. J. Thoret, C. Marchal, C. Doremieux-Morin, P. P. Man, M. Gruia and J. Fraissard, *Zeolites*, 1993, **13**, 269.
176. C. Tway and T. Apple, *J. Catal.*, 1992, **133**, 42.
177. V. Gupta, H. T. Davis and A. V. McCormick, *J. Phys. Chem.*, 1996, **100**, 9824.
178. W. F. Maier, I.-C. Tilgner, M. Wiedorn and H.-C. Ko, *Adv. Mater.*, 1993, **5**, 726.
179. N. Bansal and C. Dybowski, *J. Magn. Reson.*, 1990, **89**, 21.
180. J. Karger, *J. Magn. Reson.*, 1991, **93**, 184.
181. W. L. Earl, Y.-W. Kim and D. M. Smith, *Stud. Surf. Sci. Catal.*, 1994, **87**, 301.
182. J. Fraisard and J. Karger, *Zeolites*, 1989, **9**, 351.
183. J. Pires, M. Brotas de Carvalho, F. Ramoa Ribeiro, J. B. Nagy and E. G. Derouane, *Appl. Catal. A: General*, 1993, **95**, 75.
184. B. F. Chmelka, J. V. Gillis, E. E. Petersen and C. J. Radke, *AIChE J.*, 1990, **36**, 1562.
185. R. Ryoo, S.-B. Liu, L. C. de Menorval, K. Takegoshi, B. Chmelka, M. Trecoske and A. Pines, *J. Phys. Chem.*, 1987, **91**, 6575.
186. L. C. de Menorval, D. Raftery, S.-B. Liu, K. Takegoshi, R. Ryoo and A. Pines, *J. Phys. Chem.*, 1990, **94**, 27.
187. J.-F. Wu, T.-L. Chen, L.-J. Ma, M.-W. Lin and S.-B. Liu, *Zeolites*, 1992, **12**, 86.
188. S.-B. Liu, J.-F. Wu, L.-J. Ma, M.-W. Lin and T.-L. Chen, *A.C.S. Symp. Ser.*, 1993, **517**, 272.
189. S.-B. Liu, L.-J. Ma, M.-W. Lin, J.-F. Wu and T.-L. Chen, *J. Phys. Chem.*, 1992, **96**, 8120.
190. B. F. Chmelka, J. G. Pearson, S. B. Liu, R. Ryoo, L. C. de Menorval and A. Pines, *J. Phys. Chem.*, 1991, **95**, 303.
191. T. T. P. Cheung, *J. Phys. Chem.*, 1992, **96**, 5505.
192. E. Trescos, L. C. de Menorval and F. Rachdi, *Appl. Magn. Reson.*, 1995, **8**, 489.
193. A. Seidel, U. Tracht and B. Boddenberg, *J. Phys. Chem.*, 1996, **100**, 15917.
194. J.-G. Kim, L. Ch. de Menorval, R. Ryoo and F. Figueras, *Stud. Surf. Sci. Catal.*, 1995, **94**, 226.
195. I. L. Moudrakovski, C. I. Ratcliffe and J. A. Ripmeester, *Appl. Magn. Reson.*, 1995, **8**, 385.
196. L. C. de Menorval, E. Trescos, F. Rachdi, F. Fajula, T. Nunes and G. Feio, *Stud. Surf. Sci. Catal.*, 1995, **98**, 136.
197. A. Seidel and B. Boddenberg, *Chem. Phys. Lett.*, 1996, **249**, 117.
198. K. I. Pandya, S. M. Heald, J. A. Hriljac, L. Petrakis and J. Fraissard, *J. Phys. Chem.*, 1996, **100**, 5070.
199. L.-C. de Menorval, J. P. Fraissard and T. Ito, *J. Chem. Soc., Faraday Trans. 1*, 1982, **78**, 403.
200. M. Boudart, M. G. Samant and R. Ryoo, *Ultramicroscopy*, 1986, **20**, 125.
201. J. M. Coddington, R. F. Howe, Y.-S. Yong, K. Asakura and Y. Iwasawa, *J. Chem. Soc., Faraday Trans.*, 1990, **86**, 1015.
202. C. Pak, S. J. Cho, J. Y. Lee and R. Ryoo, *J. Catal.*, 1994, **149**, 61.
203. C. L. Tway and T. M. Apple, *Inorg. Chem.*, 1992, **31**, 2885.
204. E. Trescos, L. C. de Menorval and F. Rachdi, *J. Phys. Chem.*, 1993, **97**, 6943.

205. B. F. Chmelka, R. Ryoo, S.-B. Liu, L. C. de Menorval, C. J. Radke, E. E. Petersen and A. Pines, *J. Am. Chem. Soc.*, 1988, **110**, 4465.
206. J. Fraissard, T. Ito, L. C. de Menorval and M. A. Springuel-Huet, *Stud. Surf. Sci. Catal.*, 1982, **12**, 179.
207. O. B. Yang, S. I. Woo and R. Ryoo, *J. Catal.*, 1990, **123**, 375.
208. B. F. Chmelka, L. C. de Menorval, R. Csencsits, R. Ryoo, S.-B. Liu, C. J. Radke, E. E. Petersen and A. Pines, *Stud. Surf. Sci. Catal.*, 1989, **48**, 269.
209. B. F. Chmelka, G. T. Went, R. Csencsits, A. T. Bell, E. E. Petersen and C. J. Radke, *J. Catal.*, 1993, **144**, 506.
210. D. H. Ahn, J. S. Lee, M. Nomura, W. M. H. Sachtler, G. Moretti, S. I. Woo and R. Ryoo, *J. Catal.*, 1992, **133**, 191.
211. L.-C. de Menorval, J. P. Fraissard, T. Ito and M. Primet, *J. Chem. Soc., Faraday Trans. 1*, 1985, **81**, 2855.
212. A. Bifone, T. Pietrass, J. Kritzenberger, A. Pines and B. F. Chmelka, *Phys. Rev. Lett.*, 1995, **74**, 3277.
213. L. Petrakis, M. A. Springuel-Huet, T. Ito, T. R. Hughes, I. Y. Chan and J. Fraissard, *Proc. 9th Int. Congr. Cat.*, 1988, **1**, 348.
214. J. Karger, H. Pfeifer and J. Fraissard, *Z. Phys. Chem. Leipzig*, 1987, **268**, 195.
215. R. Ryoo, C. Pak and S. J. Cho, *Jpn. J. Appl. Phys.*, 1993, **32** (Suppl. 32-2), 475.
216. G. Moretti and W. M. H. Sachtler, *Catal. Lett.*, 1993, **17**, 285.
217. R. Ryoo, S. J. Cho, C. Pak, J.-G. Kim, S.-K. Ihm and J. Y. Lee, *J. Am. Chem. Soc.*, 1992, **114**, 76.
218. O. B. Yang, S. I. Woo and R. Ryoo, *J. Catal.*, 1992, **137**, 357.
219. T. Ito, J. Fraissand, J. B. Nagy, N. Dewaele, Z. Gabelica, A. Nastro and E. G. Derouane, *Stud. Surf. Sci. Catal.*, 1990, **49**, 579.
220. Q. J. Chen and J. Fraissard, *J. Phys. Chem.*, 1992, **96**, 1809.
221. C. I. Ratcliffe and J. A. Ripmeester, *J. Am. Chem. Soc.*, 1995, **117**, 1445.
222. F. Stallmach, J. Karger, K. P. Datema, J. A. Bolt-Westerhoff and A. K. Nowak, *Z. Phys. Chem.*, 1995, **189**, 43.
223. R. Ryoo, C. Pak and B. F. Chmelka, *Zeolites*, 1990, **10**, 790.
224. A. Freitag, Ch. van Wullen and V. Staemmler, *Chem. Phys.*, 1995, **192**, 267.
225. K. J. Chao, S. H. Chen and S. B. Liu, *Stud. Surf. Sci. Catal.*, 1991, **60**, 123.
226. S. B. Liu, C. S. Lee, P. F. Shiu and B. M. Fung, *Stud. Surf. Sci. Catal.*, 1994, **83**, 233.
227. S.-B. Liu, B. M. Fung, T.-C. Yang, E.-C. Hong, C.-T. Chang, P.-C. Shih, F.-H. Tong and T.-L. Chen, *J. Phys. Chem.*, 1994, **98**, 4393.
228. C. Pak and R. Ryoo, *Appl. Magn. Reson.*, 1995, **8**, 475.
229. S. J. Cho, S. M. Jung, Y. G. Shul and R. Ryoo, *J. Phys. Chem.*, 1992, **96**, 9922.
230. T. I. Koranyi, L. J. M. van de Ven, W. J. J. Welters, J. W. de Haan, V. H. J. de Beer and R. A. van Santen, *Colloids Surf. A: Phys. Eng. Asp.*, 1993, **72**, 143.
231. T. I. Koranyi, L. J. M. van de Ven, W. J. J. Welters, J. W. de Haan, V. H. J. de Beer and R. A. van Santen, *Catal. Lett.*, 1993, **17**, 105.
232. N. Bansal and C. Dybowski, *Stud. Surf. Sci. Catal.*, 1987, **38**, 243.
233. A. Gedeon, J. L. Bonardet and J. Fraissard, *J. Phys. Chem.*, 1989, **93**, 2563.
234. N. Bansal and C. Dybowski, *J. Phys. Chem.*, 1988, **92**, 2333.
235. R. Shoemaker and T. Apple, *J. Phys. Chem.*, 1987, **91**, 4024.
236. E. W. Scharpf, R. W. Crecely, B. C. Gates and C. Dybowski, *J. Phys. Chem.*, 1986, **90**, 9.
237. W. J. J. Welters, G. Vorbeck, H. W. Zandbergen, J. W. de Hahn, V. H. J. de Beer and R. A. van Santen, *J. Catal.*, 1994, **150**, 155.
238. J. L. Bonardet, A. Gedeon and J. Fraissard, *Stud. Surf. Sci. Catal.*, 1995, **94**, 139.
239. W. J. J. Welters, G. Vorbeck, H. W. Zandbergen, L. J. M. van de Ven, E. M. van Oers, J. W. de Haan, V. H. J. de Beer and R. A. van Santen, *J. Catal.*, 1996, **161**, 819.
240. Q. J. Chen, T. Ito and J. Fraissard, *Zeolites*, 1991, **11**, 239.

241. A. Gedeon and J. Fraissard, *Chem. Phys. Lett.*, 1994, **219**, 440.
242. M. Hartmann and B. Boddenberg, *Microporous Mater.*, 1994, **2**, 127.
243. B. Boddenberg and M. Hartmann, *Chem. Phys. Lett.*, 1993, **203**, 243.
244. A. Gedeon, J. L. Bonardet and J. Fraissard, *J. Phys. Chem.*, 1993, **97**, 4254.
245. M. Hartmann and B. Boddenberg, *Stud. Surf. Sci. Catal.*, 1994, **84**, 509.
246. S.-B. Liu, T.-S. Lin, T.-C. Yang, T.-H. Chen, E.-C. Hong and R. Ryoo, *J. Phys. Chem.*, 1995, **99**, 8277.
247. S. B. Liu, T. C. Yang, R. Y. Lin, E. C. Hong and T. S. Lin, *Stud. Surf. Sci. Catal.*, 1994, **84**, 789.
248. A. Gedeon, J. L. Bonardet, C. Lepetit and J. Fraissard, *Solid State Nucl. Magn. Reson.*, 1995, **5**, 201.
249. A. Gedeon and J. Fraissard, *Stud. Surf. Sci. Catal.*, 1995, **98**, 83.
250. R. Grosse, R. Burmeister, B. Boddenberg, A. Gedeon and J. Fraissard, *J. Phys. Chem.*, 1991, **95**, 2443.
251. R. Grosse, A. Gedeon, J. Watermann, J. Fraissard and B. Boddenberg, *Zeolites*, 1992, **12**, 909.
252. B. Boddenberg and J. Watermann, *Chem. Phys. Lett.*, 1993, **203**, 531.
253. A. Gedeon, R. Burmeister, R. Grosse, B. Boddenberg and J. Fraissard, *Chem. Phys. Lett.*, 1991, **179**, 191.
254. B. Boddenberg and A. Seidel, *J. Chem. Soc., Faraday Trans.*, 1994, **90**, 1345.
255. F. Rittner, A. Seidel and B. Boddenberg, *Chem. Phys. Lett.*, 1995, **243**, 140.
256. A. Seidel, F. Rittner and B. Boddenberg, *J. Chem. Soc., Faraday Trans.*, 1996, **92**, 493.
257. A. Seidel, F. Rittner and B. Boddenberg, *J. Chem. Soc., Faraday Trans.*, 1996, **92**, 1815.
258. B. Boddenberg and T. Sprang, *J. Chem. Soc., Faraday Trans.*, 1995, **91**, 163.
259. T. Sprang and B. Boddenberg, *J. Chem. Soc., Faraday Trans.*, 1995, **91**, 555.
260. T. Sprang and B. Boddenberg, *Appl. Magn. Reson.*, 1995, **8**, 415.
261. J.-G. Kim, T. Kompany, R. Ryoo, T. Ito and J. Fraissard, *Zeolites*, 1994, **14**, 427.
262. S.-B. Liu, Y.-J. Shu and C.-T. Chang, *J. Chinese Chem. Soc.*, 1994, **41**, 53.
263. P. V. Shertukde, W. K. Hall and G. Marcelin, *Catal. Today*, 1992, **15**, 491.
264. T. Yoshida, J. Koizumi and Y. Akai, *Bull. Chem. Soc. Jpn*, 1988, **61**, 989.
265. J. L. Bonardet, M. C. Barrage and J. Fraissard, *A.C.S. Symp. Ser.*, 1994, **571**, 230.
266. M. C. Barrage, J. L. Bonardet and J. Fraissard, *Catal. Lett.*, 1990, **5**, 143.
267. T. Ito, J. L. Bonardet, J. Fraissard, J. B. Nagy, C. Andre, Z. Gabelica and E. G. Derouane, *Appl. Catal.*, 1988, **43**, L5.
268. J. T. Miller, B. L. Meyers and G. J. Ray, *J. Catal.*, 1991, **128**, 436.
269. T. T. P. Cheung and C. M. Fu, *J. Phys. Chem.*, 1989, **93**, 3740.
270. J. L. Bonardet, M. C. Barrage and J. Fraissard, *J. Mol. Catal. A: Chem.*, 1995, **96**, 123.
271. J. L. Bonardet, M. C. Barrage, J. Fraissard, M. A. Ferrero and W. C. Connor, *Stud. Surf. Sci. Catal.*, 1994, **88**, 265.
272. N. Bansal, D. R. Corbin and C. Dybowski, *Appl. Magn. Reson.*, 1995, **8**, 337.
273. R. L. Cotterman, D. A. Hickson, S. Cartlidge, C. Dybowski, C. Tsiao and A. F. Venero, *Zeolites*, 1991, **11**, 27.
274. M. G. Samant, L.-C. de Menorval, R. A. Dalla Betta and M. Boudart, *J. Phys. Chem.*, 1988, **92**, 3937.
275. J. A. Ripmeester and C. I. Ratcliffe, *J. Phys. Chem.*, 1990, **94**, 7652.
276. A. V. McCormick and B. F. Chmelka, *Mol. Phys.*, 1991, **73**, 603.
277. B. F. Chmelka, D. Raftery, A. V. McCormick, L. C. de Menorval, R. D. Levine and A. Pines, *Phys. Rev. Lett.*, 1991, **66**, 580.
278. C. J. Jameson, A. K. Jameson, R. Gerald II and A. C. de Dios, *J. Chem. Phys.*, 1992, **96**, 1676.
279. R. Ryoo, L.-C. de Menorval, J. H. Kwak and F. Figueras, *J. Phys. Chem.*, 1993, **97**, 4124.
280. R. G. Larsen, J. Shore, K. Schmidt-Rohr, L. Emsley, H. Long and A. Pines, *Chem. Phys. Lett.*, 1993, **214**, 220.

281. M. Janicke, B. F. Chmelka, R. G. Larsen, J. Shore, K. Schmidt-Rohr, L. Emsley, H. Long and A. Pines, *Stud. Surf. Sci. Catal.*, 1994, **84**, 519.
282. S. S. Nivarthi and A. V. McCormick, *Microporous Mater.*, 1994, **3**, 47.
283. A. K. Jameson, C. J. Jameson and R. E. Gerald II, *J. Chem. Phys.*, 1994, **101**, 1775.
284. C. J. Jameson and A. C. de Dios, *J. Chem. Phys.*, 1992, **97**, 417.
285. C. J. Jameson, A. K. Jameson, B. I. Baello and H.-M. Lim, *J. Chem. Phys.*, 1994, **100**, 5965.
286. C. J. Jameson, A. K. Jameson, H.-M. Lim and B. I. Baello, *J. Chem. Phys.*, 1994, **100**, 5977.
287. C. J. Jameson and H.-M. Lim, *J. Chem. Phys.*, 1995, **103**, 3885.
288. P. R. Van Tassel, H. T. Davis and A. V. McCormick, *Mol. Phys.*, 1991, **73**, 1107.
289. P. R. Van Tassel, H. T. Davis and A. V. McCormick, *Mol. Phys.*, 1992, **76**, 411.
290. P. R. Van Tassel, C. Hall, H. T. Davis and A. V. McCormick, *Pure Appl. Chem.*, 1992, **64**, 1629.
291. P. R. Van Tassel, J. C. Phillips, H. T. Davis and A. V. McCormick, *J. Mol. Graphics*, 1993, **11**, 180.
292. P. R. Van Tassel, H. T. Davis and A. V. McCormick, *J. Chem. Phys.*, 1993, **98**, 8919.
293. P. R. Van Tassel, H. T. Davis and A. V. McCormick, *Langmuir*, 1994, **10**, 1257.
294. T. T. P. Cheung, *J. Phys. Chem.*, 1993, **97**, 8993.
295. F.-Y. Li and R. S. Berry, *J. Phys. Chem.*, 1995, **99**, 2459.
296. P. R. Van Tassel, H. T. Davis and A. V. McCormick, *AIChE J.*, 1994, **40**, 925.
297. A. K. Jameson, C. J. Jameson, A. C. de Dios, E. Oldfield, R. E. Gerald II and G. L. Turner, *Solid State Nucl. Magn. Reson.*, 1995, **4**, 1.
298. C. J. Jameson, A. K. Jameson and H.-M. Lim, *J. Chem. Phys.*, 1996, **104**, 1709.
299. C. J. Jameson, A. K. Jameson, R. E. Gerald II and H.-M. Lim, *J. Chem. Phys.*, 1995, **103**, 8811.
300. J. A. Ripmeester and C. I. Ratcliffe, *Proc. 9th Int. Zeolite. Conf., Montreal 1992* (ed. R. von Ballmoos *et al.*), p. 571, Butterworth-Heinemann, 1993.
301. I. L. Moudrakovski, C. I. Ratcliffe and J. A. Ripmeester, *Stud. Surf. Sci. Catal.*, 1995, **97**, 243.
302. C. Tsiao, D. R. Corbin and C. R. Dybowski, *J. Phys. Chem.*, 1990, **94**, 867.
303. T. T. P. Cheung, *J. Phys. Chem.*, 1990, **94**, 376.
304. C. J. Jameson, A. K. Jameson, R. Gerald II and A. C. de Dios, *J. Chem. Phys.*, 1992, **96**, 1690.
305. R. Ryoo, H. Ihee, J. H. Kwak, G. Seo and S.-B. Liu, *Microporous Mater.*, 1995, **4**, 59.
306. M.-A. Springuel-Huet, A. Nosov, J. Karger and J. Fraissard, *Preprints Am. Chem. Soc. Div. Pet. Chem.*, 1996, **41**, 373.
307. F. Rittner, A. Seidel, T. Sprang and B. Boddenberg, *Appl. Spectrosc.*, 1996, **50**, 1389.
308. T. Ito, L. C. de Menorval, E. Guerrier and J. P. Fraissard, *Chem. Phys. Lett.*, 1984, **111**, 271.
309. Q. Chen, M. A. Springuel-Huet, J. Fraissard, M. L. Smith, D. R. Corbin and C. Dybowski, *J. Phys. Chem.*, 1992, **96**, 10914.
310. S. M. Alexander, J. M. Coddington and R. F. Howe, *Zeolites*, 1991, **11**, 368.
311. G. Seo and R. Ryoo, *J. Catal.*, 1990, **124**, 224.
312. I. L. Moudrakovski, C. I. Ratcliffe and J. A. Ripmeester, *Appl. Magn. Reson.*, 1996, **10**, 559.
313. S.-B. Liu, J.-F. Wu, L.-J. Ma, T.-C. Tsai and I. Wang, *J. Catal.*, 1991, **132**, 432.
314. R. Benslama, J. Fraissard, A. Albizane, F. Fajula and F. Figueras, *Zeolites*, 1988, **8**, 196.
315. C. Tsiao, D. R. Corbin, V. Durante, D. Walker and C. Dybowski, *J. Phys. Chem.*, 1990, **94**, 4195.
316. Q. J. Chen, J. L. Guth, A. Seive, P. Caullet and J. Fraissard, *Zeolites*, 1991, **11**, 798.
317. C. Pellegrino, T. Ito, Z. Gabelica, J. B. Nagy and E. G. Derouane, *Appl. Catal.*, 1990, **61**, L1.
318. T. Ito, M.-A. Springuel-Huet and J. Fraissard, *Zeolites*, 1989, **9**, 68.

319. T. Ito and J. Fraissard, *Zeolites*, 1987, **7**, 554.
320. C. Tsiao, J. S. Kauffman, D. R. Corbin, L. Abrams, E. E. Carroll Jr and C. Dybowski, *J. Phys. Chem.*, 1991, **95**, 5586.
321. M. L. Smith, D. R. Corbin and C. Dybowski, *J. Phys. Chem.*, 1993, **97**, 9045.
322. M. L. Smith, D. R. Corbin, L. Abrams and C. Dybowski, *J. Phys. Chem.*, 1993, **97**, 7793.
323. S. J. Cho, W.-S. Ahn, S. B. Hong and R. Ryoo, *J. Phys. Chem.*, 1996, **100**, 4996.
324. M. Sugimoto, H. Katsuno, T. Hayasaki, K.-I. Hirasawa, *Appl. Catal. A.*, 1993, **106**, 9.
325. S. M. Bradley and R. F. Howe, *Microporous Mater.*, 1995, **4**, 131.
326. J. M. Kim, J. H. Kwak, S. Jun and R. Ryoo, *J. Phys. Chem.*, 1995, **99**, 16742.
327. X. Yang and R. E. Truitt, *J. Phys. Chem.*, 1996, **100**, 3713.
328. P. J. Barrie, Synthesis and Characterisation of Aluminophosphate-based Molecular Sieves, PhD thesis, University of Cambridge, 1990.
329. J. A. Ripmeester and C. I. Ratcliffe, *J. Phys. Chem.*, 1995, **99**, 619.
330. M. E. Davis, C. Saldarriaga, C. Montes and B. E. Hanson, *J. Phys. Chem.*, 1988, **92**, 2557.
331. N. Dumont, T. Ito and E. G. Derouane, *Appl. Catal.*, 1989, **54**, L1.
332. Q. J. Chen, M. A. Springuel-Huet and J. Fraissard, *Chem. Phys. Lett.*, 1989, **159**, 117.
333. M. A. Springuel-Huet and J. Fraissard, *Chem. Phys. Lett.*, 1989, **154**, 299.
334. M. J. Annen, M. E. Davis and B. E. Hanson, *Catal. Lett.*, 1990, **6**, 331.
335. R. Ryoo, C. Pak, D. H. Ahn, L.-C. de Menorval and F. Figueras, *Catal. Lett.*, 1990, **7**, 417.
336. L. Maistriau, E. G. Derouane and T. Ito, *Zeolites*, 1990, **10**, 310.
337. J. A. Martens, E. Feijen, J. L. Lievens, P. J. Grobet and P. A. Jacobs, *J. Phys. Chem.*, 1991, **95**, 10025.
338. Q. J. Chen, J. Fraissard, H. Cauffriez and J. L. Guth, *Zeolites*, 1991, **11**, 534.
339. R. L. Bedard, C. L. Bowes, N. Coombs, A. J. Holmes, T. Jiang, S. J. Kirkby, P. M. Macdonald, A. M. Malek, G. A. Ozin, S. Petrov, N. Plavac, R. A. Ramik, M. R. Steele and D. Young, *J. Am. Chem. Soc.*, 1993, **115**, 2300.
340. J. A. Ripmeester, *J. Magn. Reson.*, 1984, **56**, 247.
341. J. T. Miller, P. D. Hopkins, B. L. Meyers, G. J. Ray, R. T. Roginski, G. W. Zajac and N. H. Rosenbaum, *J. Catal.*, 1992, **138**, 115.
342. M. A. Springuel-Huet and J. P. Fraissard, *Zeolites*, 1992, **12**, 841.
343. G. Fetter, D. Tichit, L. C. De Menorval and F. Figueras, *Appl. Catal.*, 1990, **65**, L1.
344. G. F. McCann, I. Gameson, W. J. Stead, T. Rayment, P. J. Barrie and J. Klinowski, *Mater. Res. Soc. Symp. Proc.*, 1991, **233**, 273.
345. P. J. Barrie, G. F. McCann, I. Gameson, T. Rayment and J. Klinowski, *J. Phys. Chem.*, 1991, **95**, 9416.
346. J.-G. Kim, S.-K. Ihm, J. Y. Lee and R. Ryoo, *J. Phys. Chem.*, 1991, **95**, 8546.
347. T. Ito, L.-C. de Menorval and J. P. Fraissard, *J. Chim. Phys.*, 1983, **80**, 573.
348. H. Ihee, T. Becue, R. Ryoo, C. Potvin, J.-M. Manoli and G. Djega-Mariadassou, *Stud. Surf. Sci. Catal.*, 1994, **84**, 765.
349. R. Ryoo, J. H. Kwak and L.-C. de Menorval, *J. Phys. Chem.*, 1994, **98**, 7100.
350. T. T. P. Cheung, *J. Catal.*, 1990, **124**, 511.
351. M. E. Davis, P. Hathaway, D. Morgan, T. Glass and H. Dorn, *Stud. Surf. Sci. Catal.*, 1987, **38**, 263.
352. C. Tsiao, C. Dybowski, D. Walker, V. Durante and D. R. Corbin, *Langmuir*, 1988, **4**, 1219.
353. M.-A. Springuel-Huet, A. Nosov, J. Karger and J. Fraissard, *J. Phys. Chem.*, 1996, **100**, 7200.
354. C. Tsiao, C. Dybowski, A. M. Gaffney and J. A. Sofranko, *J. Catal.*, 1991, **129**, 520.
355. M. C. Barrage, F. Bauer, H. Ernst, J. Fraissard, D. Freude and H. Pfeifer, *Catal. Lett.*, 1990, **6**, 201.
356. T. Ito, J. Fraissard, J. Karger and H. Pfeifer, *Zeolites*, 1991, **11**, 103.
357. J. Karger, H. Pfeifer, F. Stallmach and H. Spindler, *Zeolites*, 1990, **10**, 288.
358. W. Heink, J. Karger, H. Pfeifer and F. Stallmach, *J. Am. Chem. Soc.*, 1990, **112**, 2175.

359. J. Karger, H. Pfeifer, F. Stallmach, N. N. Feoktistova and S. P. Zhdanov, *Zeolites*, 1993, **13**, 50.
360. J. Karger, H. Pfeifer, T. Wutscherk, S. Ernst, J. Weitkamp and J. Fraissard, *J. Phys. Chem.*, 1992, **96**, 5059.
361. J. A. Ripmeester and C. I. Ratcliffe, *Mater. Res. Soc. Symp. Proc.*, 1991, **233**, 281.
362. J. A. Ripmeester and C. I. Ratcliffe, *Anal. Chim. Acta*, 1993, **283**, 1103.
363. D. Fenzke and J. Karger, *Z. Phys. D*, 1993, **25**, 345.
364. J. Fraissard, A. Gedeon, Q. Chen and T. Ito, *Stud. Surf. Sci. Catal.*, 1991, **69**, 461.
365. Q. J. Chen and J. Fraissard, *J. Phys. Chem.*, 1992, **96**, 1814.
366. Q. J. Chen and J. Fraissard, *Chem. Phys. Lett.*, 1990, **169**, 595.
367. A. Gedeon, J. L. Bonardet and J. Fraissard, *J. Chim. Phys.*, 1988, **85**, 871.
368. E. G. Derouane and M. E. Davis, *J. Mol. Catal.*, 1988, **48**, 37.
369. M. Springuel-Huet, J. Demarquay, T. Ito and J. Fraissard, *Stud. Surf. Sci. Catal.*, 1988, **37**, 183.
370. D. W. Johnson and L. Griffiths, *Zeolites*, 1987, **7**, 484.
371. E. G. Derouane and J. B. Nagy, *Chem. Phys. Lett.*, 1987, **137**, 341.
372. J. Demarquay and J. Fraissard, *Chem. Phys. Lett.*, 1987, **136**, 314.
373. T. T. P. Cheung, *J. Phys. Chem.*, 1995, **99**, 7089.
374. Q. Chen, M. A. Springuel-Huet and J. Fraissard, *Stud. Surf. Sci. Catal.*, 1991, **65**, 219.
375. V. V. Terskikh, I. L. Moudrakovski and V. M. Mastikhin, *J. Chem. Soc., Faraday Trans.*, 1993, **89**, 4239.
376. V. V. Terskikh, I. L. Moudrakovski, V. M. Mastikhin and L. G. Simonova, *React. Kinet. Catal. Lett.*, 1993, **49**, 13.
377. W. C. Conner, E. L. Weist, T. Ito and J. Fraissard, *J. Phys. Chem.*, 1989, **93**, 4138.
378. D. M. Smith, D.-W. Hua and W. L. Earl, *MRS Bull.*, 1994, **19**, 44.
379. V. Pasquier, P. Levitz and A. Delville, *J. Phys. Chem.*, 1996, **100**, 10249.
380. J. B. Nagy, I. Ivanova, R. Aiello, F. Crea, A. Nastro and F. Testa, *Zeolites*, 1995, **15**, 421.
381. T. T. P. Cheung, *J. Phys. Chem.*, 1989, **93**, 7549.
382. H. C. Foley, N. Bansal, D. S. Lafyatis and C. Dybowski, *Prepr. Am. Chem. Soc., Div. Pet. Chem.*, 1991, **36**, 502.
383. N. Bansal, H. C. Foley, D. S. Lafyatis and C. Dybowski, *Catal. Today*, 1992, **14**, 305.
384. D. J. Suh, T.-J. Park, S. K. Ihm and R. Ryoo, *J. Phys. Chem.*, 1991, **95**, 3767.
385. G. Neue, *Z. Phys. Chem. N.F.*, 1987, **152**, 13.
386. T. Shibanuma, H. Asada, S. Ishi and T. Matsui, *Jpn. J. Appl. Phys.*, 1983, **22**, 1656.
387. P. C. Wernett, J. W. Larsen, O. Yamada and H. J. Yue, *Energy and Fuels*, 1990, **4**, 412.
388. C. Tsiao and R. E. Botto, *Energy and Fuels*, 1991, **5**, 87.
389. J. Kritzenberger, H. C. Gaede, J. S. Shore, A. Pines and A. T. Bell, *J. Phys. Chem.*, 1994, **98**, 10173.
390. M. Boudart, R. Ryoo, G. P. Valenca and R. Van Grieken, *Catal. Lett.*, 1993, **17**, 273.
391. S. V. Filimonova, V. M. Mastikhin, M. D. Smolikov, S. S. Belyi and V. K. Duplyakin, *React. Kinet. Catal. Lett.*, 1992, **48**, 209.
392. G. P. Valenca and M. Boudart, *J. Catal.*, 1991, **128**, 447.
393. M. Boudart, L.-C. de Menorval, J. Fraissard and G. P. Valenca, *J. Phys. Chem.*, 1988, **92**, 4033.
394. D. Rouabah and J. Fraissard, *Solid State Nucl. Magn. Reson.*, 1994, **3**, 153.
395. G. P. Valenca, PhD thesis, Stanford University, 1991 (*Diss. Abstr.*, **52**, 1469).
396. J. L. Bonardet, G. B. McGarvey, J. B. Moffat and J. Fraissard, *Colloids Interfac. A*, 1993, **72**, 191.
397. J. L. Bonardet, J. Fraissard, G. B. McGarvey and J. B. Moffat, *J. Catal.*, 1995, **151**, 147.
398. C. J. Jameson and A. C. de Dios, *J. Chem. Phys.*, 1993, **98**, 2208.
399. J.-H. Kantola, J. Vaara, T. T. Rantala and J. Jokisaari, *Mater. Res. Soc. Symp. Proc.*, 1996, **408**, 599.

400. F. Vigne-Maeder, *J. Phys. Chem.*, 1994, **98**, 4666.
401. V. Gupta, D. Kim, H. T. Davis and A. V. McCormick, *J. Phys. Chem. B*, 1997, **101**, 129.
402. T. Koskela, M. Ylihautala, J. Vaara and J. Jokisaari, *Chem. Phys. Lett.*, 1996, **261**, 425.
403. F. Vigne-Maeder, S. El Amrani and P. Gelin, *J. Catal.*, 1992, **134**, 536.
404. R. L. June, A. T. Bell and D. N. Theodorou, *J. Phys. Chem.*, 1990, **94**, 8232.
405. S. D. Pickett, A. K. Nowak, J. M. Thomas, B. K. Peterson, J. F. P. Swift, A. K. Cheetham, C. J. J. den Ouden, B. Smit and M. F. M. Post, *J. Phys. Chem.*, 1990, **94**, 1233.
406. F. Vigne-Maeder, *J. Catal.*, 1989, **117**, 566.
407. S. Yashonath, *Chem. Phys. Lett.*, 1991, **177**, 54.
408. S. Yashonath, *J. Phys. Chem.*, 1991, **95**, 5877.
409. P. Santikary, S. Yashonath and G. Ananthakrishna, *J. Phys. Chem.*, 1992, **96**, 10469.
410. G. Schrimpf, M. Schlenkrich, J. Brickmann and P. Bopp, *J. Phys. Chem.*, 1992, **96**, 7404.
411. S. El Amrani, F. Vigne-Maeder and B. Bigot, *J. Phys. Chem.*, 1992, **96**, 9417.
412. P. Santikary and S. Yashonath, *J. Solid State Chem.*, 1993, **106**, 184.
413. S. Yashonath and P. Santikary, *J. Phys. Chem.*, 1994, **98**, 6368.
414. S. S. Nivarthi, P. R. Van Tassel, H. T. Davis and A. V. McCormick, *Zeolites*, 1995, **15**, 40.
415. J. A. Barker, C. T. Rettner and D. S. Bethune, *Chem. Phys. Lett.*, 1992, **188**, 471.
416. P. P. Edwards, P. A. Anderson and J. M. Thomas, *Acc. Chem. Res.*, 1996, **29**, 23.
417. L. J. Woodall, P. A. Anderson, A. R. Armstrong and P. P. Edwards, *J. Chem. Soc., Dalton Trans.*, 1996, 719.
418. N. P. Blake and G. D. Stucky, *J. Inclusion Phenom.*, 1995, **21**, 299.
419. H. Nakayama, D. D. Klug, C. I. Ratcliffe and J. A. Ripmeester, *J. Am. Chem. Soc.*, 1994, **116**, 9777.
420. R. Tycko and J. A. Reimer, *J. Phys. Chem.*, 1996, **100**, 13240.
421. X. Zeng, C. Wu, M. Zhao, S. Li, L. Li, X. Zhang, Z. Liu and W. Liu, *Chem. Phys. Lett.*, 1991, **182**, 538.
422. Z. Liu, M. Zhao, C. Wu, L. Li, S. Li, X. Zeng and W. Xiong, *Chem. Phys. Lett.*, 1992, **194**, 440.
423. J. Brossel and A. Kastler, *Compt. Rend.*, 1949, **229**, 1213.
424. A. Kastler, *J. Phys. Radium*, 1950, **11**, 255.
425. M. A. Bouchiat, T. R. Carver and C. N. Varnum, *Phys. Rev. Lett.*, 1960, **5**, 373.
426. R. M. Herman, *Phys. Rev.*, 1965, **137**, A1062.
427. R. L. Gamblin and T. R. Carver, *Phys. Rev.*, 1965, **138**, A946.
428. C. C. Bouchiat, M. A. Bouchiat and L. C. L. Pottier, *Phys. Rev.*, 1969, **181**, 144.
429. M. A. Bouchiat, J. Brossel and L. C. Pottier, *J. Chem. Phys.*, 1972, **56**, 3703.
430. B. C. Grover, *Phys. Rev. Lett.*, 1978, **40**, 391.
431. C. H. Volk, T. M. Kwon, J. G. Mark, Y. B. Kim and J. C. Woo, *Phys. Rev. Lett.*, 1980, **44**, 136.
432. C. H. Volk, T. M. Kwon and J. G. Mark, *Phys. Rev. A*, 1980, **21**, 1549.
433. T. M. Kwon, J. G. Mark and C. H. Volk, *Phys. Rev. A*, 1981, **24**, 1894.
434. X. Zeng, Z. Wu, T. Call, E. Miron, D. Schreiber and W. Happer, *Phys. Rev. A*, 1985, **31**, 260.
435. N. D. Bhaskar, W. Happer and T. McClelland, *Phys. Rev. Lett.*, 1982, **49**, 25.
436. W. Happer, E. Miron, S. Schaefer, D. Schreiber, W. A. van Wijngaarden and X. Zeng, *Phys. Rev. A*, 1984, **29**, 3092.
437. G. D. Cates, R. J. Fitzgerald, A. S. Barton, P. Bogorad, M. Gatzke, N. R. Newbury and B. Saam, *Phys. Rev. A*, 1992, **45**, 4631.
438. N. D. Bhaskar, W. Happer, M. Larsson and X. Zeng, *Phys. Rev. Lett.*, 1983, **50**, 105.
439. Z. Wu, W. Happer and J. M. Daniels, *Phys. Rev. Lett.*, 1987, **59**, 1480.
440. Z. Wu, S. Schaefer, G. D. Cates and W. Happer, *Phys. Rev. A*, 1988, **37**, 1161.
441. Z. Wu, W. Happer, M. Kitano and J. Daniels, *Phys. Rev. A*, 1990, **42**, 2774.
442. R. Butscher, G. Wackerle and M. Mehring, *J. Chem. Phys.*, 1994, **100**, 6923 (correction, 1995, **102**, 8681).

443. X. Zeng, E. Miron, W. A. Van Wijngaarden, D. Schreiber and W. Happer, *Phys. Lett. A*, 1993, **96**, 191.
444. B. Driehuys, G. D. Cates and W. Happer, *Phys. Rev. Lett.*, 1995, **74**, 4943.
445. S. R. Schaefer, G. D. Cates, T.-R. Chien, D. Gonatas, W. Happer and T. G. Walker, *Phys. Rev. A*, 1989, **39**, 5613.
446. D. Raftery, H. Long, T. Meersmann, P. J. Grandinetti, L. Reven and A. Pines, *Phys. Rev. Lett.*, 1991, **66**, 584.
447. T. Hadeishi and C.-H. Liu, *Phys. Rev. Lett.*, 1967, **19**, 211.
448. L. D. Shearer, *Phys. Lett.*, 1969, **28A**, 660.
449. L. D. Shearer, *Phys. Rev.*, 1969, **188**, 505.
450. M. P. Augustine and K. W. Zilm, *J. Chem. Phys.*, 1996, **105**, 2998.
451. M. P. Augustine and K. W. Zilm, *Mol. Phys.*, 1996, **89**, 737.
452. B. Driehuys, G. D. Cates, E. Miron, K. Sauer, D. K. Walter and W. Happer, *Appl. Phys. Lett.*, 1996, **69**, 1668.
453. G. D. Cates, D. R. Benton, M. Gatzke, W. Happer, K. C. Hasson and N. R. Newbury, *Phys. Rev. Lett.*, 1990, **65**, 2591.
454. F. P. Calaprice, W. Happer, D. F. Schreiber, M. M. Lowry, E. Miron and X. Zeng, *Phys. Rev. Lett.*, 1985, **54**, 174.
455. C. R. Bowers, H. W. Long, T. Pietrass, H. C. Gaede and A. Pines, *Chem. Phys. Lett.*, 1993, **205**, 168.
456. B. Driehuys, G. D. Cates, W. Happer, H. Mabuchi, B. Saam, M. S. Albert and A. Wishnia, *Phys. Lett. A*, 1993, **184**, 88.
457. H. C. Gaede, Y.-Q. Song, R. E. Taylor, E. J. Munson, J. A. Reimer and A. Pines, *Appl. Magn. Reson.*, 1995, **8**, 373.
458. G. Navon, Y.-Q. Song, T. Room, S. Appelt, R. E. Taylor and A. Pines, *Science*, 1996, **271**, 1848.
459. D. Raftery, H. Long, L. Reven, P. Tang and A. Pines, *Chem. Phys. Lett.*, 1992, **191**, 385.
460. C. R. Bowers, T. Pietrass, E. Barash, A. Pines, R. K. Grubbs and A. P. Alivisatos, *J. Phys. Chem.*, 1994, **98**, 9400.
461. T. Pietrass, A. Bifone and A. Pines, *Surf. Sci.*, 1995, **334**, L730.
462. D. Raftery, H. W. Long, D. Shykind, P. J. Grandinetti and A. Pines, *Phys. Rev. A*, 1994, **50**, 567.
463. Y.-Q. Song, H. C. Gaede, T. Pietrass, G. A. Barrall, G. C. Chingas, M. R. Ayers and A. Pines, *J. Magn. Reson., Ser. A*, 1995, **115**, 127.
464. M. S. Albert, G. D. Cates, B. Driehuys, W. Happer, B. Saam, C. D. Springer Jr and A. Wishnia, *Nature*, 1994, **370**, 199.
465. B. Schwarzschild, *Physics Today*, 1995, 17.
466. M. S. Albert, PhD thesis, S.U.N.Y. Stonybrook, 1993 (*Diss. Abstr.*, 1994, **55**, 435).
467. M. E. Wagshul, T. M. Button, H. F. Li, Z. Liang and A. W. Wishnia, *Proc. Soc. Magn. Reson. 3rd Meeting and Eur. Soc. Magn. Reson. Med. Biol., Nice*, 1995, p. 1194.
468. G. A. Johnson, R. D. Black, G. Cates, G. Cofer, R. Gunther, W. Happer, L. W. Hedlund, H. Middleton and J. Swartz, *Proc. Soc. Magn. Reson. 3rd Meeting and Eur. Soc. Magn. Reson. Med. Biol., Nice*, 1995, p. 392.
469. S. Pele, F. A. Jolesz, M. S. Albert and R. L. Walsworth, *Proc. Soc. Magn. Reson. 3rd Meeting and Eur. Soc. Magn. Reson. Med. Biol., Nice*, 1995, p. 1192.
470. G. J. Schrobilgen, in *Synthetic Fluorine Chemistry* (ed. G. A. Olah, R. D. Chambers and G. K. S. Prakash), Ch. 1, p. 1, Wiley, New York, 1992.
471. N. Bartlett, *Proc. Chem. Soc.*, 1962, 218.
472. T. H. Brown, E. B. Whipple and P. H. Verdier, *J. Chem. Phys.*, 1963, **38**, 3029.
473. T. H. Brown, E. B. Whipple and P. H. Verdier, in *Noble Gas Compounds* (ed. H. H. Hyman), p. 263. University of Chicago Press, Chicago, 1963.
474. K. Seppelt and H. H. Rupp, *Z. Anorg. Allg. Chem.*, 1974, **409**, 338.

475. K. Seppelt and H. H. Rupp, *Z. Anorg. Allg. Chem.*, 1974, **409**, 331.
476. J. H. Holloway, G. J. Schrobilgen, P. Granger and C. Brevard, *C.R. Acad. Sci. Paris, Ser. C*, 1976, **282**, 519.
477. T. Birchall, R. D. Myers, H. de Waard and G. J. Schrobilgen, *Inorg. Chem.*, 1982, **21**, 1068.
478. R. J. Gillespie, A. Netzer and G. J. Schrobilgen, *Inorg. Chem.*, 1974, **13**, 1455.
479. P. Boldrini, R. J. Gillespie, P. R. Ireland and G. J. Schrobilgen, *Inorg. Chem.*, 1974, **13**, 1690.
480. R. J. Gillespie and G. J. Schrobilgen, *Inorg. Chem.*, 1974, **13**, 2370.
481. R. G. Syvret, K. M. Mitchell, J. C. P. Sanders and G. J. Schrobilgen, *Inorg. Chem.*, 1992, **31**, 3381.
482. N. Keller and G. J. Schrobilgen, *Inorg. Chem.*, 1981, **20**, 2118.
483. L. Turowsky and K. Seppelt, *Inorg. Chem.*, 1990, **29**, 3226.
484. B. Cremer-Lober, H. Butler, D. Naumann and W. Tyrra, *Z. Anorg. Allg. Chem.*, 1992, **607**, 34.
485. H. J. Frohn and C. Rossbach, *Z. Anorg. Allg. Chem.*, 1993, **619**, 1672.
486. G. J. Schrobilgen, J. H. Holloway, P. Granger and C. Brevard, *Inorg. Chem.*, 1978, **17**, 980.
487. R. J. Gillespie and G. J. Schrobilgen, *Inorg. Chem.*, 1974, **13**, 1694.
488. J. H. Holloway and G. J. Schrobilgen, *Inorg. Chem.*, 1980, **19**, 2632.
489. J. H. Holloway, G. J. Schrobilgen and P. Taylor, *J. Chem. Soc., Chem. Commun.*, 1975, 40.
490. R. G. Syvret and G. J. Schrobilgen, *Inorg. Chem.*, 1989, **28**, 1564.
491. R. Minkwitz and W. Molsbeck, *Z. Anorg. Allg. Chem.*, 1992, **612**, 35.
492. G. J. Schrobilgen and J. M. Whalen, *Inorg. Chem.*, 1994, **33**, 5207.
493. J. M. Whalen and G. J. Schrobilgen, *J. Fluorine Chem.*, 1995, **71**, 225.
494. A. A. A. Emara and G. J. Schrobilgen, *Inorg. Chem.*, 1992, **31**, 1323.
495. A. A. A. Emara and G. J. Schrobilgen, *J. Chem. Soc., Chem. Commun.*, 1987, 1644.
496. A. A. A. Emara and G. J. Schrobilgen, *J. Chem. Soc., Chem. Commun.*, 1988, 257.
497. G. J. Schrobilgen, *J. Chem. Soc., Chem. Commun.*, 1988, 1506.
498. R. Faggiani, D. K. Kennepohl, C. J. L. Lock and G. J. Schrobilgen, *Inorg. Chem.*, 1986, **25**, 563.
499. J. F. Sawyer, G. J. Schrobilgen and S. J. Sutherland, *J. Chem. Soc., Chem. Commun.*, 1982, 210.
500. J. F. Sawyer, G. J. Schrobilgen and S. J. Sutherland, *Inorg. Chem.*, 1982, **21**, 4064.
501. D. D. DesMarteau, R. D. LeBlond, S. F. Hossain and D. Nothe, *J. Am. Chem. Soc.*, 1981, **103**, 7734.
502. G. A. Schumacher and G. J. Schrobilgen, *Inorg. Chem.*, 1983, **22**, 2178.
503. L. J. Turbini, R. E. Aikman and R. J. Lagow, *J. Am. Chem. Soc.*, 1979, **101**, 5833.
504. D. Naumann, H. Butler, R. Gnann and W. Tyrra, *Inorg. Chem.*, 1993, **32**, 861.
505. H. Butler, D. Naumann and W. Tyrra, *Eur. J. Solid State Inorg. Chem.*, 1992, **29**, 739.
506. D. Naumann, R. Gnann, V. Padelidakis and W. Tyrra, *Fluorine Chem.*, 1995, **72**, 79.
507. H. J. Frohn, A. Klose, V. V. Bardin, A. J. Kruppa and T. V. Leshina, *J. Fluorine Chem.*, 1995, **70**, 147.
508. H. J. Frohn and S. Jakobs, *J. Chem. Soc., Chem. Commun.*, 1989, 625.
509. D. Naumann and W. Tyrra, *J. Chem. Soc., Chem. Commun.*, 1989, 47.
510. H. J. Frohn, S. Jakobs and G. Henkel, *Angew. Chem. Int. Ed. Engl.*, 1989, **28**, 1506.
511. D. Naumann, W. Tyrra and D. Pfolk, *Z. Anorg. Allg. Chem.*, 1994, **620**, 987.
512. J. Reuben, D. Samuel, H. Selig and J. Shamir, *Proc. Chem. Soc.*, 1963, 270.
513. D. Naumann, W. Tyrra, R. Gnann and D. Pfolk, *J. Chem. Soc., Chem. Commun.*, 1994, 2651.
514. H. J. Frohn and V. V. Bardin, *J. Chem. Soc., Chem. Commun.*, 1993, 1072.
515. V. V. Zhdankin, P. J. Stang and N. S. Zefirov, *J. Chem. Soc., Chem. Commun.*, 1992, 578.
516. H. J. Frohn, A. Klose and G. Henkel, *Angew. Chem. Int. Ed. Engl.*, 1993, **32**, 99.

517. K. O. Christe, E. C. Curtis, D. A. Dixon, H. P. Mercier, J. C. P. Sanders and G. J. Schrobilgen, *J. Am. Chem. Soc.*, 1991, **113**, 3351.
518. G. A. Schumacher and G. J. Schrobilgen, *Inorg. Chem.*, 1984, **23**, 2923.
519. E. Jacob, D. Lentz, K. Seppelt and A. Simon, *Z. Anorg. Allg. Chem.*, 1981, **472**, 7.
520. R. J. Gillespie, B. Landa and G. J. Schrobilgen, *J. Chem. Soc., Chem. Commun.*, 1972, 607.
521. R. J. Gillespie and G. J. Schrobilgen, *Inorg. Chem.*, 1974, **13**, 765.
522. D. D. Desmarteau and M. Eisenberg, *Inorg. Chem.*, 1972, **11**, 2641.
523. H. P. A. Mercier, J. C. P. Sanders, G. J. Schrobilgen and S. S. Tsai, *Inorg. Chem.*, 1993, **32**, 386.
524. H. Rupp and K. Seppelt, *Angew. Chem. Int. Ed. Engl.*, 1974, **13**, 612.
525. K. Seppelt, *Acc. Chem. Res.*, 1979, **12**, 211.
526. K. Seppelt and N. Bartlett, *Z. Anorg. Allg. Chem.*, 1977, **436**, 122.
527. J. Shamir, H. Selig, D. Samuel and J. Reuben, *J. Am. Chem. Soc.*, 1965, **87**, 2359.
528. H. J. Frohn, *Nachr. Chem. Tech. Lab.*, 1993, **41**, 956.
529. R. J. Gillespie, *Molecular Geometry*, p. 62, Van Nostrand-Rheinhold, London, 1972.
530. R. J. Gillespie and R. S. Nyholm, *Q. Rev. Chem. Soc.*, 1957, **11**, 339.
531. C. J. Jameson and H. S. Gutowsky, *J. Chem. Phys.*, 1964, **40**, 2285.
532. R. G. Kidd, *Annu. Rep. NMR Spectrosc.*, 1991, **23**, 85.
533. J. P. Jokisaari, L. P. Ingman, G. J. Schrobilgen and J. C. P. Sanders, *Magn. Reson. Chem.*, 1994, **32**, 242.
534. H. D. Frame, *Chem. Phys. Lett.*, 1969, **3**, 182.
535. C. J. Jameson, *Bull. Magn. Reson.*, 1980, **3**, 3.
536. G. J. Perlow and M. R. Perlow, *J. Chem. Phys.*, 1968, **48**, 955.
537. H. DeWaard, S. Bukshpan, G. J. Schrobilgen, J. H. Holloway and D. Martin, *J. Chem. Phys.*, 1979, **70**, 3247.
538. L. P. Ingham, J. Jokisaari, K. Oikarinen and R. Seydoux, *J. Magn. Reson., Ser. A*, 1994, **111**, 155.

This Page Intentionally Left Blank

Index

Note: Figures and Tables are indicated [in this index] by *italic page numbers*